UNIVERSITY OF SOUTHAMPTON

AN INVESTIGATION INTO THE AERODYNAMICS OF A WING IN GROUND EFFECT IN GENERIC RACING CAR WAKE FLOWS

by

Michael D. Soso

Thesis submitted for the degree of
Doctor of Philosophy

Fluid Structure Interaction Research Group
School of Engineering Sciences
Faculty of Engineering, Science and Mathematics

May 2005

Abstract

Wind tunnel experiments and CFD simulations were carried out in an attempt to shed light on the aerodynamic changes that a leading open-wheeled racing car would induce on a following car of similar specifications. The leading car was idealised as a bluff body that was equipped with a rear wing and a diffuser, while the following car was represented by a front wing that was located further downstream.

The tests entailed varying the height and angle of attack of the front wing above a moving ground, while changing the oncoming flow conditions. The oncoming conditions were generated by a stand alone rear wing, the bluff body with different diffuser angles and the bluff body at different heights. The results from these cases were compared to the results obtained from the undisturbed freestream. Data collection methods included force and pressure measurements, in conjunction with flow visualisation images from the surface of the wing. Velocity flow field measurements were taken with PIV and LDA.

The investigations showed that the wing experienced a decrease in downforce when downstream of the idealised leading car. The decrease was found to vary with the height of the wing above the ground. The investigations also showed that the wing experienced an increase in drag at the downstream location, and that its efficiency increased as the diffuser angle was decreased. The aerodynamic changes were linked to the flow field generated by the upstream configurations.

To my family

Acknowledgements

I would like to express my sincere thanks to Prof. Wilson and to the School of Engineering Sciences for making it possible for me to perform the type of research that I always wished to do. The support that was provided has been an integral to the successful completion of this document.

I also wish to thank my family for their continued unconditional support in the pursuit of my goals. Their love and encouragement has been indispensable. A heart felt thank you is also extended to the Forbes' for making me a part of their family in Southampton. It would not have happened without you.

I would like to say a special thank you to my girlfriend, Mona. You have constantly stood by my side, and it is appreciated more than you would know.

Finally, I must also express gratitude to the wind tunnel technicians. They provided a great deal of help and information, which was necessary for the successful completion of the experiments.

Table of Contents

List of Tables

List of Figures

Nomenclature

b	Wing span
c	Wing chord
$\bar{c}_f$	Average skin friction coefficient
c_p	Specific heat at constant pressure
C_D	Coefficient for the horizontal component of the resultant force on the wing
C_l	2-D sectional lift coefficient
C_L	Coefficient for the vertical component of the resultant force on the wing
C_p	Pressure coefficient
d	Diffuser half width
e	Internal energy per unit mass
$\mathbf{f}$	Body force per unit mass
$FC1$	Flow condition 1: freestream flow
$FC2$	Flow condition 2: flow generated by upstream wing
$FC3$	Flow condition 3: flow generated by upstream diffuser bluff body
h_r	Ride height
i, j, k	Tensor indices
k	Thermal conductivity
k	Turbulent kinetic energy
l	Length of diffuser bluff body
p	Static pressure
P_{TOT}	Total pressure

$\dot{q}$	Heat flux
Re	Reynolds number
Re_L	Reynolds number based on length
t	Time
T	Temperature
u, v, w	Cartesian velocity components
u_τ	Friction velocity
U_e	Boundary layer edge velocity
U_∞	Freestream velocity
V	Scalar velocity
$\mathbf{V}$	Velocity vector
x, y, z	Cartesian coordinates
y_1	Distance from solid boundary to center of first grid cell
y^+	Boundary layer inner variable
$2z/b$	Normalised coordinate in the spanwise direction
α	Angle of attack
α	Scaling factor
δ_{ij}	Kronecker delta
λ	Second viscosity coefficient
μ	Coefficient of viscosity
ρ	Density
τ_w	Wall shear stress
τ_{ij}	Viscous stress tensor
ν	Kinematic viscosity
ν_τ	Turbulent viscosity
Φ	Dissipation function
Ω	Streamwise vorticity

$\overline{\quad}$	Denotes a time averaged quantity
$'$	Denotes a fluctuating quantity

Chapter 1

Introduction

One of the most important factors affecting the performance of modern opened-wheeled racing cars is aerodynamics [1, 2]. At high speeds, the aerodynamic features of the racing car are responsible for generating the necessary downforce that holds the vehicle to the ground, thereby allowing it to negotiate corners at a faster rate, and also providing increased braking ability [3, 4, 5]. Aerodynamic design also influences the drag experienced by the vehicle, which directly affects the overall speed for a given power. The aerodynamic development of a racing car is usually carried out in a wind tunnel, as consistent freestream conditions can constantly be produced. The car is therefore designed to perform well when in an undisturbed uniform air stream. However, if the oncoming flow were to change, as it does on the race track, the efficiency of the original design may be compromised, thus resulting in an unintended loss in performance.

In general, when a following race car approaches a leading car, the change in the freestream conditions experienced by the following car can have both positive [6] and negative [7, 8] effects on its aerodynamic characteristics. A positive effect is the resulting reduction in drag, while a negative effect is the reduction in downforce. Furthermore, for an open wheeled racing car, the loss of downforce can make it difficult to overtake the leading car, a situation that can produce dull racing if the cars continuously circulate the track in the form of a procession. If it were possible to routinely develop the aerodynamics of a generic car so as to allow it to travel in both undisturbed and disturbed freestream conditions without adversely affecting its performance, then racing may become more exciting, as more opportunities for overtaking may be created.

1.1 Background

On a typical open wheeled racing car, a major part of the aerodynamic downforce is developed by the system of wings present at either end of the vehicle. Of these, the front wing can be considered as being more important since it operates in ground effect and since the remainder of the vehicle operates in the wake that it generates.

Ground effect refers to the change in aerodynamic characteristics that a wing experiences as it approaches a solid boundary. The phenomenon manifests itself as a reduction in the induced drag and an increase in the lift curve slope of the wing [9, 10, 11, 12]. The changes are irrespective of whether the suction surface or the pressure surface is closest to the boundary. For racing cars, the configuration employed is to have the suction surface closest to the ground in order to generate downforce.

As previously stated, the remainder of the vehicle operates in the wake generated by the front wing. Consequently, not only is it necessary to have a thorough understanding of the physics of the flow produced by the device, but it is also necessary to understand how this flow changes when the device is placed in non uniform flow conditions; conditions such as those produced by the wake of a preceding vehicle.

In the process of designing an open-wheeled racing car, one of the main goals is to achieve an optimum distribution between the downforce generated at the front and at the rear of the vehicle. Designers strive to achieve this goal because the difference in the forces from both ends of the vehicle influences the location of its centre of pressure (the point through which the resultant force acts), which directly affects its mechanical characteristics [3, 13]. If the centre of pressure is located too far to the rear of the vehicle, then it experiences understeer, whereas if it is located too far to the front, oversteer develops. In the former condition, the vehicle tends not to turn a corner and drifts to its outer edge. In the latter, it turns too much, resulting in the back end rotating to the outer edge of the corner.

In racing conditions, a following car approaching the rear of a leading car normally experiences a reduction in its downforce levels, with the reduction being unevenly distributed about either end of the vehicle. Usually a greater loss in front downforce occurs, which then leads to a rearward shift in the centre of pressure. The net result is then understeer, a common complaint of drivers when following a leading car in high speed corners [14]. In order to avoid drifting to the outer edge of the corner, the driver has to reduce speed, which allows the leading car to pull further ahead, and reduces any available opportunity to perform an overtaking manoeuvre.

It therefore follows that a car having aerodynamics suited for running in undisturbed freestream conditions, and also for running in the disturbed flow produced by a leading car, may be able to gain a significant advantage during a race since it may not be plagued by major changes in its handling characteristics.

1.2 Research Aim

The aim of the current research is to perform a generic study of the aerodynamic interaction that occurs when a following open wheeled racing car approaches a leading car and operates in its wake. Ultimately, in order to shed light on the fundamental aspects of more robust aerodynamic packages, both quantitative and qualitative information from two different flow fields in which the following car is to operate, will be presented.

1.3 Contribution to Existing Knowledge

The findings to be outlined in this document will fill gaps in the existing level of knowledge by providing a more detailed insight into the aerodynamic interaction experienced by a downstream wing when in the wake of an upstream racing car. The generic approach to studying the topic is unique. Furthermore, a wide range of the data has not previously been presented in the public domain. New contributions are:

1. The loss in the downforce that was experienced by the downstream wing depended on the height of the wing above the ground.
2. The loss in downforce varied across the span of the wing, with more downforce being lost from sections close to the midspan, than was the case from sections close to the tips.
3. The disturbed flow emanating from the upstream body had the ability to significantly alter the surface flow patterns on the downstream wing.
4. Lower diffuser angles promote an increase in the efficiency of the downstream wing.
5. Varying the angle of the diffuser, and varying its height above the ground, appeared to influence the development of the wake of the downstream wing.
6. CFD computations predicted the correct force and pressure trends, thus providing confidence for performing more complex simulations.

Chapter 2

Literature Review

2.1 Introduction

In this chapter, a review of the literature that was relevant to the research investigation will be described. The relevant databases were searched, as were the internet and other related print media.

2.2 Vehicle Aerodynamic Interaction

Aerodynamic interaction studies aimed at quantifying the effect of one racing car on another were carried out in the early nineteen seventies. Romberg et al. [6] initiated a series of experiments aimed at investigating the steady state aerodynamic forces of NASCAR racing cars in a variety of drafting and passing positions. They used scaled models of a Dodge Charger, Dodge Coronet and Plymouth Road Runner. Wind tunnel restrictions limited the maximum distance between two vehicles to approximately two car lengths. Within this range, their force results showed that there was as much as a 37% reduction in the drag of the following car, while it was possible for the leading car to experience as much as a 30% reduction. They also reported significant changes in the distribution of lift forces at the front and rear axles of both vehicles.

Howell [7] also carried out steady state experimental investigations into the aerodynamic forces of lift, drag and pitching moment occurring when two Can-Am racing cars without wheels, were in close proximity to each other. His main objective was to show that the following car could experience sufficient aerodynamic changes to cause it to overturn. As part of his investigation, he provided plots showing that it experienced reduced drag and downforce values, while showing increased pitching moment, when in the wake of the car ahead.

Dominy [15] has by far carried out the most complete investigation of the aerodynamic effects occurring when one open-wheeled race car follows in the wake of another. His experiments were performed using quarter scale models of 1989 Formula 1 cars, and were carried out for positions that the the author considered as being representative of an initial overtaking manoeuvre with no yawing of the vehicle. Owing to wind tunnel restrictions, the distance between the two models was fixed to less than a car length. Measurements for the following car were taken on a moving ground, while the leading car was placed on the wind tunnel floor ahead. The aerodynamic data obtained from the model was later used as the input to a circuit performance prediction code, partially developed by the author, which was capable of modelling the behaviour of a car around typical race tracks.

In the measurements of lift and drag that were presented, it was shown that when fully immersed in the wake of the leading car, downforce on the following car was reduced by 36% and drag by 23%. As the lateral offset between the two cars increased, both variables commenced to recover to their freestream values, with the drag taking much longer to do so than did the downforce. Information was also provided to show that the centre of pressure changed from 68% wheelbase to 90% wheelbase when directly behind the leading car, but then recovered to freestream values with increasing offset.

Duncan [16] performed experiments that used pressure tap data to deduce the aerodynamic changes that occurred on racing cars that experienced body modifications, changes in yaw and interactions with other cars. The vehicles under consideration were stock cars, an IMSA GTS race car and an NHRA Funny Car. Of main interest, an interference study was carried out using two stock cars. With measurements taken on the following car, the author indicated that the reduction in drag was about 50% when its front bumper was 150 mm behind the rear bumper of the leading car. No such estimate was given for the downforce values.

From an internet search, it is also known that aerodynamic interaction studies were carried out at Imperial College, encompassing scaled models of open-wheeled racing cars. However, no references to published information were given. The author though, was able to ascertain the nature of some of the tests from Ref. [17]. It appears that the research was sponsored by the FIA in order to investigate if changes to the Formula 1 technical regulations would make it easier to follow a leading car, and probably increase overtaking opportunities. The test was reported to focus on variations such as changes to the height of the floor (flat bottom of the car), and changes to the front and rear wing heights. Some of the results of the tests were summarised by current F1 engineer, Ross Brawn. "You lose performance and you particularly lose front-end performance and whatever we did it didn't seem to make much difference. We tried a few packages of technical regulations and couldn't really influence it."

In summary, the literature survey on vehicle aerodynamic interaction has highlighted the fact that the aerodynamic characteristics of both a leading car and a following car can be affected by the presence of the other vehicle. The majority of the research on the subject, however, was carried out for closed-wheeled, stock car type vehicles, which have very little in common with their open-wheeled counterparts. Some of the aerodynamic effects reported may therefore not apply to the latter. The published case that focussed exclusively on open-wheeled racing cars only began to scratch the surface, in terms of producing insight into the fundamental changes that were taking place. Consequently, there remains a wide scope for innovative research to be performed.

2.3 Vehicle Wakes

The disturbed flow emanating from the rear of a leading vehicle is termed the wake. It is a region of low momentum fluid that arises from the different flow separations that occur from the surfaces of solid bodies as they move relative to a fluid. The flow field in a wake is usually very complicated as it is three-dimensional and unsteady. However, over time, distinct features such as vortices are clearly discernable. Vehicles can be considered as being bluff bodies in ground effect since their aerodynamic characteristics are greatly influenced by the flow separation that they produce [18]. As such, a great deal of the work relating to vehicle wakes is performed with the use of approximate bluff body representations of the true vehicle.

Some of the first investigations into automobile wakes commenced in the early seventies, with work published by Morel [19]. His intent was to investigate the drag of 3-D bluff bodies for automotive purposes. His initial experiments were carried out first on a slender axisymmetric cylinder with a slanted base, and then on a vehicle type body with a slanted rear. He obtained results showing that the drag of the body was dependent on the slope angle of the slanted base portion. More importantly though, he described the presence of two flow regimes depending on slant angle, one in which the flow was fully separated from the rear of the body and the other in which the flow was attached to the slanted portion.

Morel's work was followed by experimental work carried out by Ahmed [20, 21]. Ahmed's experiments were aimed at correlating the wake structure with the drag properties of typical vehicle shapes. Consequently, detailed flow visualisations of the developing flow behind the models had to be performed. The shapes investigated included Estate, Fastback and Notchback vehicles. His results showed that the flow near the model base was characterised by an oval separation bubble, with flow inside the bubble consisting of two separate recirculation regions. Downstream of this initial zone, by measuring velocity profiles perpendicular to the longitudinal axis of the vehicle, he identified the presence of a pair of counter rotating vortices that induced an upwash in the case of the Estate model and a downwash for the Fastback and Notchback models.

Work carried out by Hamidy [22] provided more detail of the near wake region of 3-D bluff bodies in ground effect. He took measurements of such variables as pressure coefficient, cross flow velocity vectors, streamwise velocity vectors, vorticity distribution, turbulent kinetic energy distribution and Reynolds stress distribution. He too described the presence of a separation bubble, along with the eventual formation of two streamwise vortices.

Bearman [23] also provided a summary of the near wake flow present behind three-dimensional bluff bodies. Using results from Particle Image Velocimetry (PIV) measurements of a previous study, he showed that there can be a marked difference between the instantaneous and time averaged flow structures present in the near wake. The instantaneous velocity field consisted of a large number of vortex structures. Time averaging a number of the instantaneous velocity fields then produced results similar to Ahmed's, which identified the presence of two counter rotating vortices in the far wake. In this case, only 10 instantaneous velocity measurements were averaged. He mentioned that averaging larger numbers should produce more distinct vortex cores.

In recent work completed by Lienhart et al. [24], a Laser Doppler Anemometry (LDA) investigation of the wake of an Ahmed body with its slanted rear facing upwards was performed to obtain data for numerical turbulence models. Measurements were taken at the longitudinal centreline of the body, and in cross flow planes up to a distance of half of a body length downstream. Even at the furthest distance downstream at which data was taken, velocity vector plots show the presence of two vortices inducing a downwash to the flow.

With the advances in computational power and Computational Fluid Dynamics (CFD), computational modelling of wakes has become fairly advanced, the aim being to reproduce the results obtained from experimental investigations. Alajbegovic et al. [25] used a new CFD method, DIGITAL PHYSICS, to predict the wake flow of the Morel body in ground effect. For this body (as with the Ahmed body), the wake flow is either dominated by a pair of counter rotating vortices or by full flow separation, depending on the angle of the slanted back portion. Importantly, after showing the good agreement between experiment and the computational lift and drag values predicted by DIGITAL PHYSICS, the authors went on to state that up to that time, traditional CFD codes were not able to capture all the salient features of the flow field, resulting in drag values that were about 30% too high.

In a similar study, Bayraktar et al. [26] carried out an experimental and computational investigation of a full scale Ahmed body in ground effect. The body was of a size representative of a car or light truck. In this case, the computational analysis was carried out using a Reynolds Averaged Navier-Stokes (RANS) code. At the Reynolds numbers and back slant angles tested, the authors obtained good agreement between the experimental and computational lift and drag values by taking a time average of the results of their unsteady calculations.

Basara et al. [27] performed CFD simulations of the external aerodynamics of several industrial vehicle benchmarks in an effort to ascertain the effectiveness of the standard κ–ϵ model and the Reynolds-stress model (RSM). The investigations were carried out on reference bodies obtained from Peugeot, the SAE and Volkswagen. The bodies encompassed flow regimes with small separation, moderate separation and a case where the flow over the car was heavily influenced by the wake vortices formed on the surface of the body. The authors had previously pointed out the fact that some CFD methods and turbulence models give encouraging results in cases of small separation, but totally fail for cases of large separation. For their comparison, the CFD code used was AVL SWIFT, which was based on finite volume discretisation methods. Results from the three benchmarks showed that the RSM predicted more accurate flow conditions than the κ–ϵ model.

Krajnovic and Davidson [28] used a more advanced turbulence model in their wake investigation studies. They performed a LES of the flow around a vehicle type bluff body in ground effect. Their computational results were compared with experimental investigations carried out on the same model by different authors. They indicated that good agreement was attained between the the results, with regard to velocity profiles taken downstream of the bluff body.

In summary, the literature survey on vehicle wakes has highlighted the fact that bluff body models can be used to study and to reproduce the flow generated by actual vehicles. It is possible for the models to generate a separation bubble region close to the bluff body base. Further downstream of this region, there is the eventual formation of streamwise vortices. The models being used, however, should still mimic the major features of the original vehicle, since the shape of the body can influence the direction in which the downstream vortices rotate. Bluff bodies are characterised by large flow separations, which can pose significant problems for the use of CFD codes in modelling their flow physics. If prior experimental data is not available as a guide, the CFD can give erroneous information regarding the specific areas from which important flow features may be generated. Higher order turbulence models in the CFD codes appear to produce more reliable results for cases involving complex flows.

2.4 Wings in Ground Effect

The aerodynamics of inverted wings in ground effect has been investigated both experimentally and computationally, in an effort to gain a more fundamental understanding of the parameters that could lead to successful racing car designs. Ranzenbach and Barlow [29, 30, 31] carried out a series of comparative computational and experimental studies of a symmetric and cambered airfoil in ground effect. Their work centred on the investigation of the force coefficients as the height of each airfoil was varied. They also investigated the effect of a moving ground in the computational simulations. Their results showed that as the distance between the airfoil and the ground was reduced, the downforce experienced by the wing increased to a maximum, and then decreased with further height reduction. In general, drag was shown to rise monotonically, except for the computational case of the symmetric airfoil above a moving ground. The authors also obtained fairly good agreement between the computational and experimental coefficients. They then used vorticity contours from one of the computational solutions to postulate that the region of force reduction was caused by the merging of the airfoil and ground boundary layers. With regard to the ground boundary, they showed that the airfoil experienced greater downforce coefficients when that particular surface moved with the freestream velocity, as opposed to when it was stationary.

Knowles et al. [32] carried out an experimental, and limited computational study of a GA(W)-1 wing with endplates in ground effect. The experimental facility was equipped with a rolling road. They varied the angle of attack of the wing at different heights above the ground to generate lift curves, while recording force and pressure data. They obtained results showing that the lift curve slope of the wing increased, while the angle of stall was reduced, as the ground was approached. They also indicated that there was more drag at lower ride heights and that there was less induced drag at low ride heights. The computational comparisons, which were carried out with a 2-D airfoil in a panel method, were limited to pressure distribution plots. The plots showed fairly good agreement at low angles of attack and large ride heights.

Jasinski and Selig [33] performed an experimental ground effect study of wing and endplate combinations representative of Champ Car and Formula 1 front wings at the time. A rolling road was not used. They specifically looked at the effect of Reynolds number, flap deflection, flap planform shape and endplate shape. The measurements that were taken included forces, pressures and flow field data (extracted with a seven-hole probe). They obtained results showing that the drag coefficient at constant C_L was relatively unaffected while increasing flap deflection, and that flap planform and endplate shape had a large effect on the wing's aerodynamics. Their flow field data clearly highlighted the presence of two vortices, the larger emanating from the bottom of the endplate and the smaller from the top. Reynolds number was found to have the least effect on the aerodynamics.

Zerihan and Zhang [34, 35, 36] performed extensive experimental investigations of a single element, then a double element wing in ground effect, in facilities equipped with rolling roads. A variety of experimental techniques were used, including force and pressure measurements, flow visualisation, PIV and LDA investigations of the flow field. To supplement the experimental techniques, a 2-D computational investigation was also performed. Their results confirmed the trends that had previously been established, while shedding light on new areas of ground effect aerodynamics. Among the important conclusions to be drawn from the single element wing investigation were that there was no indication of force reduction being caused by the merging of the boundary layers of the wing and the ground, and that an increase in the wing's angle of attack engendered greater maximum downforce, while reducing its sensitivity to changes in downforce. Transition fixing was shown to produce less downforce on the wing and to produce force reduction at a greater ride height. With regard to the double element wing, it was found that most of the downforce was generated by the main element and that the flow from this element dominated the downstream wake.

More recently, a comparison between PIV and CFD velocity profile data from a GA(W)-1 wing in ground effect was provided by Lawson et at. [37]. The PIV images were taken on the suction surface of the wing, in the chordwise direction. A 2-D Fluent computational model was constructed for the comparison. As indicated by the authors, with appropriate reasons, the experiments were performed at 25 m/s, while the computations were carried out at 20 m/s. The authors indicated that there was a good match between the experimental and computational velocity profiles at an angle of attack of 0 deg and ride heights of $h/c = 0.1$ and 0.47. The data did not match well at the higher angle of attack of 15 deg.

Up to the present time, the research carried out on wings in ground effect has been focussed on establishing the baseline aerodynamic characteristics for this type of component. It was reported that the downforce generated by a typical wing increased to a maximum, and then decreased, as the distance between the wing and the ground boundary was reduced. The data supporting these results was gathered in oncoming flow conditions that replicated uniform freestream flow. The fact that the wings may have to operate in disturbed oncoming flow was not addressed. It is likely that the disturbed conditions would have the potential to alter the aerodynamic characteristics that have been established to date. An opportunity therefore exists to carry out novel research in this area.

2.5 Vortex Wakes

Vortices dominate the wakes of wings in ground effect, and vehicle wakes in general. Therefore, it is also essential to have an idea of the work performed in this more specific area. A thorough description of the physics of vortex wakes as applied to wings can be found in Ref. [38]. The author describes how a difference in the velocity from the pressure and suction surfaces at the trailing edge of the wing results in the generation of vorticity, which then gets convected downstream within a thin free shear layer, eventually rolling up into concentrated vortex cores due to 3-D induced effects. Among other things, the author has also divided the vortex wake into three distinct regions. The first, the roll-up region, is the initial portion of the wake where the cores of the vortices are formed. Next is the vortex region, where the vortex cores drift downwards (in the case of a conventional wing), and vortex breakdown initially commences. Finally, there is the decay region, where the vortices are totally eliminated owing to the action of viscous dissipation.

A great driver for vortex wake research is for air traffic control purposes [39]. Vortex structures can remain in the atmosphere for a long period of time, having possible detrimental effects on following aircraft [40, 41]. If an effective and suitable means of vortex alleviation can be found [42, 43, 44, 45], then aircraft safety can be improved, and the technology may also be applicable to racing car design.

Huenecke [46] investigated experimentally, near wake (up to 95% of wing half span) of a half model of a medium range transport aircraft in a high-lift configuration. Data was taken with a five-hole probe. He looked at such areas as the structure of the cross flow and streamwise velocity fields, the structure of the wake vorticity and total pressure losses in the wake.

De Bruin et al. [47] performed an experimental study of the roll-up of a trailing vortex wake of an aircraft model with flaps extended, up to a distance of 5 wing spans downstream of the wing. Both flow visualisations using a laser light sheet and measurements with five-hole probes were taken. For the model under consideration, their results showed that the tip vortex rotated around the flap vortex before eventually merging with it further downstream.

In an attempt to assess the ability of computational methods for predicting the roll-up region of a vortex wake, Stumpf et al. [48] used an Euler code for the calculation of the nearfield wake vortex of a narrow-body airliner in take-off configuration. The calculations were performed up to a distance of half a span behind the trailing edge of the wing tip. The results were compared with PIV data for the same model obtained from wind tunnel tests. The authors state that generally good agreement with the experimental data was obtained, but at a reduced angle of attack. That is, the Euler code over predicted the lift and vortex development at the original angle of attack, a consequence of the neglect of viscosity.

Using a more complex CFD code, Eaton [49] carried out a computational analysis of a low aspect ratio wing in a wind tunnel to assess the performance of different turbulence models. The models were the κ–ϵ and the Differential Reynolds Stress Model (DSM). Experimental data on the same wing was used as a baseline. His results showed that the DSM compared better to the experimental values than did the κ–ϵ since it took into account the anisotropic nature of turbulence. Inspection of the data presented showed that the core of the experimental vortex was much more concentrated than the cores of the corresponding CFD vortices, and that the κ–ϵ vortex was the more diffused of the two computational representations.

Senior and Zhang [50] and Ruhrmann and Zhang [51] measured forces and pressures on a diffuser bluff body in ground effect. Their investigations encompassed different ramp angles, which were constructed to be 5, 10, 15, 17 and 20 deg to the horizontal. As a result of their work, they confirmed that the downforce curve of a typical diffuser was similar to that of a wing in ground effect, in that there was a region of force increase, followed by a region of force reduction. In the region of force increase, a pair of counter-rotating vortices emanated from the diffuser, while in the region of force reduction, asymmetric flow was present, owing to the bursting of one of the vortices. They further identified different operating regions on the downforce curve and showed that there were distinctive flow regimes for low angle (5, 10 deg) and for high angle (15, 17, 20 deg) diffusers. It was reported that force reduction was caused by vortex breakdown, in the case of low angle diffusers and by a combination of flow separation and vortex breakdown in the case of high angle diffusers.

Zhang et al. [52] measured vortices downstream of a diffuser equipped bluff body in ground effect, above a rolling road, using LDA. The diffuser ramp angle was set to 17 deg to the horizontal. In their work, they linked changes in the downstream vortex flow to different regions identified from the diffuser's downforce curve. At large ride heights, corresponding to the first portion of the region of force increase, the vortices were found to be symmetrical and highly concentrated, with high axial speed cores. Closer to the ground, and at lower ride heights in the region of force increase, the vortices had increased in size, with a low axial speed in their cores. In the region of diffuser force reduction, they identified vortex breakdown, accompanied by asymmetric flow and flow reversal.

In summary, the literature review for vortex wakes has shown that a great deal of research was carried out for aircraft configurations. These cases typically involved symmetrical vortex flow in the downstream flow field. This data can provide some guidance, but ultimately, the vortices may be much more powerful than those generated in automotive circumstances. Additionally, vortices generated by extended wing flaps served to further complicate the flow field. The vortex wakes of bluff bodies in ground effect were shown to consist either of symmetrical vortex flow or asymmetrical vortex flow, depending on the height of the body above the ground. It is conceivable to expect that these wakes would have different effects on any downstream components.

2.6 Effect of Turbulence

A set of experiments aimed at investigating the effects of oncoming freestream turbulence on the aerodynamic performance of an airfoil was carried out by Hoffmann [53]. The turbulence was generated by a set of unidirectional rods, spanning the cross section of the wind tunnel test facility, upstream of the airfoil. The intensities investigated ranged from 0.25% to 12%, the lowest being the original wind tunnel value. The wing tested was a rectangular NACA 0015 section with a chord of 154 mm and an aspect ratio of 2.9. The test Reynolds number was 250 000. Results were obtained showing that the lift curve slope of the wing remained unchanged with increasing turbulence intensity. It was also shown that at 9% turbulence intensity, C_{Lmax} had increased by 30% – the greatest value in the series of tests – over its value at 0.25% turbulence intensity. The drag coefficient data showed a trend of increasing values with increasing freestream turbulence. A peak in the coefficient occured at 9% turbulence intensity. The increase in drag was deemed to be small, however, as it was within the uncertainty of the measurements. Oil flow visualisation presented for 9% turbulence intensity confirmed delayed separation and elimination of the laminar separation bubble.

For wind turbine applications, Devinant et al. [54] carried out an experimental investigation of a NACA $65_4 - 421$ airfoil in turbulence intensities ranging from 0.5% to 16%, for Reynolds numbers from 100 000 to 700 000. Again, the turbulence was produced by grids placed upstream of the test section. From their tests, they obtained results that indicated that there was a reduction in the lift curve slope as the turbulence was increased, in addition to a delay in separation and an increase in the maximum lift coefficient. For the case of the drag coefficient, the authors indicated that there was slightly increased drag in the linear portion of the lift curve.

In summary, the literature review on the effect of turbulence has highlighted a conflict in the results to be expected for the lift curve slope of a wing. One publication indicated that there was no change in the slope, while the other indicated that there was a reduction in the slope as the turbulence level was increased. For the cases under consideration, the turbulence was generated by grids placed upstream of the wind tunnel test section. This turbulence may be different from the turbulence generated behind vehicles or vehicle-like bluff bodies.

2.7 Conclusion

From the literature reviewed, it has become clear that a following racing car travelling in the wake of a leading car can experience significant changes to its aerodynamic characteristics. These changes seem to be induced at least partly, by the presence of vortices and turbulent flow in the wake. It is also evident that the interaction studies published so far seemed to have concentrated on a systems approach to the problem. That is, measurements were taken on entire vehicles in the wake of another. In an effort to obtain a more fundamental understanding of what is taking place, it would be worthwhile to concentrate on the changes experienced by the major aerodynamic components of the following car. For an open wheeled racing car, the front wing then becomes a prime candidate for such a study because it is the foremost point of the car and because the remainder of the vehicle operates in the wake that it produces.

Although a great deal of research has been carried out on the subject of wings in ground effect, no one has as yet made an attempt to quantify the aerodynamic effects that occur when the wing in ground effect operates in the flow produced by an upstream vehicle. Suitable experimental techniques for the investigation include force measurements, pressure measurements and flow visualisation on the wing itself, while five-hole probe, PIV and LDA data can be taken of the flow field. Computational modelling can be performed with an appropriate RANS code, using more advanced turbulence models than the κ-ϵ model.

Chapter 3

Experimental Methodology

3.1 Introduction

This chapter presents the experimental techniques, models and facilities used to carry out the research. A detailed description of each area is provided, with appropriate figures where necessary.

3.2 Flow Configurations

The experimental tests involved placing a single element wing in different oncoming flow conditions that were produced in the University of Southampton's large scale wind tunnel facilities. The baseline flow condition, "FC1" or "clean air," was a uniform freestream, such as that produced in a typical test section. The remaining flow conditions fell under the category of "dirty air." This label was used to refer to cases where a body was placed upstream of the wing, thus disturbing the oncoming flow.

The "dirty air" flow condition was developed in a series of incremental steps. Each step was designed to add a physical component that would produce a wake that would more closely resemble that of a generic racing car. As a result, the following subdivisions were used:

- FC2 – A wing used to simulate the rear wing of a typical open-wheeled racing car was placed upstream of the test wing.

- FC3 – A diffuser bluff body was added to the rear wing.

Owing to limits placed on the time available in the wind tunnel facility, it was only possible to investigate FC1 and FC3 in an in depth manner. FC2 was investigated to a lesser extent.

The physical procedure undertaken was to vary the height and angle of attack of the test wing when placed in the different oncoming flow conditions. The height of the endplate above the tunnel floor ranged from 2 mm to 169.6 mm. The angle of attack ranged from -5 deg to 30 deg in order to ensure that the wing's region of stall was covered. For some test conditions, the angle of the diffuser ramp was changed in order to generate downstream flow typical of high angle and low angle diffusers. For other test conditions, the height or lateral position of the diffuser was varied, while keeping the ramp angle constant. Techniques such as force measurements, flow visualisation, pressure tapping, PIV and LDA were then used to extract the relevant data from the wing and its flow field, in order to shed light on changes to its aerodynamic performance.

3.3 Models

There were several wind tunnel models constructed for the experimental investigation. These included two versions of the test wing, a separate wing used to produce flow condition FC2, and a diffuser bluff body with removable ramp wedges. In attempting to find a compromise between: (1) the working length of the test section, (2) generating a bluff body wake as far downstream as possible, (3) performing the experiments at as high a Reynolds number as possible, it was decided to scale the models to 40% of the dimensions of a current Formula 1 racing car as outlined in Ref. [55]. All models were constructed by the technicians in the workshops at the University of Southampton.

3.3.1 Test Wing

The wing on which the tests were performed was of an untwisted, untapered, single element LS(1)-0417 profile (otherwise known as GA(W)-1) [56]. Two versions were constructed, one for force measurement and flow visualisation tests, and the other tapped for the pressure distribution tests. Applying the scale factor to its dimensions resulted in a chord of 220 mm and a span of 550 mm. The trailing edge thickness was 1.5 mm. Endplates of thickness 5 mm were attached to each end of the wing. The model was constructed from wood, and was covered with paint to provide a smooth finish. The endplates were made of perspex. The wing was specifically designed to pivot at the quarter chord point, while allowing the endplates to remain parallel to the ground at all times. A side view of the model is presented in Fig. 3.1, while its coordinates and the coordinates of the pressure taps are tabulated in Appendix A.

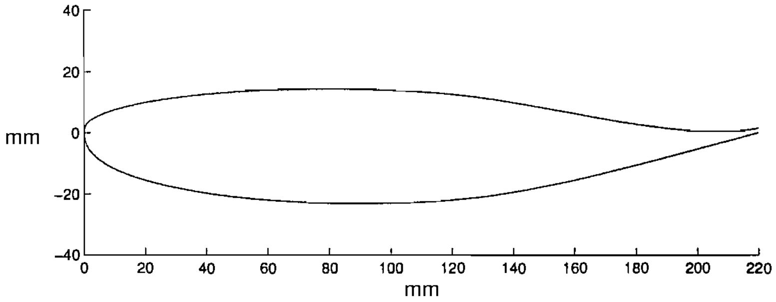

Figure 3.1: The profile of the LS(1)-0417 wing on which the tests were performed.

A single element wing configuration was adopted because it provided fewer variables to be manipulated during a particular experiment, thus effectively maximising the use of time. Additionally, it was thought that attempting to understand the aerodynamic changes experienced by a single element would be a necessary precursor to understanding the changes experienced by a multi element wing. That is, a database will be compiled gradually, in a step by step manner.

3.3.2 Upstream Rear Wing

In order to generate the wake flow expected from the rear wing of a typical F1 car, a second wing to be placed upstream of the test wing was constructed. The profile selected for this wing was an Eppler E420 high lift airfoil because of its highly cambered design. The wing had a chord of 140 mm and a span of 400 mm. It was again constructed of wood, and was untapered and untwisted. A trip strip was located at 10% chord in order to ensure that the flow was turbulent at the test Reynolds number. The trip strip was sized according to the information provided in Refs. [57, 58, 59]. A special sting was constructed for the wing in order to attach it to the roof of the wind tunnel. No endplates were constructed, as it was deemed more appropriate to have the trailing vortices rolling up from the edges of the wing. The profile is depicted in Fig. 3.2, at the same scale as Fig. 3.1 for comparison. Coordinates are tabulated in Appendix A.

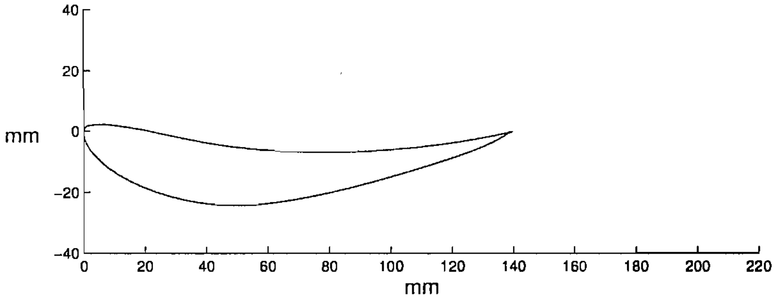

Figure 3.2: The Eppler E420 profile used for the upstream rear wing.

3.3.3 Diffuser Bluff Body

A diffuser equipped bluff body was constructed as a generic means of representing a leading racing car. The bluff body was meant to represent the vehicle itself, while the diffuser was used to produce the vortex dominated downstream flow typical of a modern open wheeled racing car. In general, it was not possible to scale all dimensions of the bluff body to 40% of the standard size, owing to restrictions imposed by the working length of the wind tunnel test section. The length and height of the bluff body were 0.9 m and 0.18 m respectively, while its 40% scaled width was 400mm. The diffuser ramp was constructed in a manner that allowed for 3 different angles to the horizontal to be set. The angles were 5, 10 and 16.7 deg. The baseline ramp angle was taken to be 16.7 deg, a value that was very close to the angle used in the experimental tests outlined in Ref. [50]. The height of the diffuser was adjustable in three 10 mm increments, from a minimum of 40 mm to a maximum of 60 mm. The baseline height was 60 mm. The model was again constructed of wood. A trip strip was located at x/l = 0.1 in order to ensure that the flow was turbulent. The rear wing was attached to the diffuser bluff body via endplates, as shown in Fig. 3.3. As a result of the limited test section length, a ground board with a sharp leading edge was constructed in order to extend the floor and to mount the bluff body.

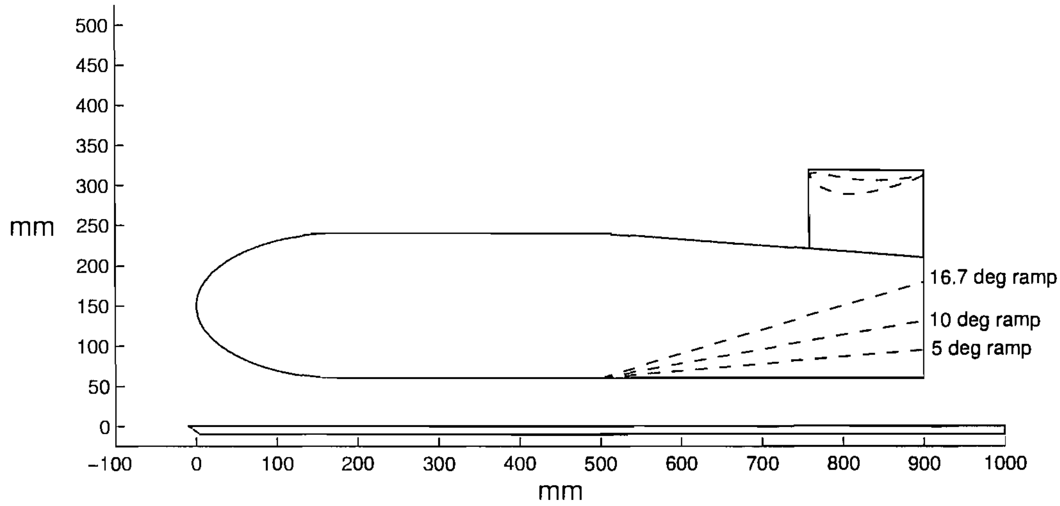

Figure 3.3: The diffuser bluff body and associated ground board that were used in the experimental tests.

3.4 Wind Tunnel Facilities

The experimental tests were carried out in the low speed wind tunnel facilities at the University of Southampton. The facilities included both the 2.1 m × 1.5 m wind tunnel and the 3.5 m × 2.5 m R. J. Mitchell wind tunnel. Both wind tunnels are of the closed circuit, single return type, and are equipped with rolling roads. The rolling road allows for the speed of the ground to be matched with the oncoming freestream velocity for correct simulation of wings in ground effect. Each tunnel also contains a 3 component balance for the measurement of forces on models. Additionally, the R. J. Mitchell facility is equipped with a 3-component LDA system.

3.5 Model Installation

Figure 3.4 provides a visual representation of the experimental configuration adopted for the 2.1 m × 1.5 m wind tunnel. The diffuser bluff body, which is shown in the foreground, was mounted to a fixed ground board that was positioned just ahead of the rolling road. Physical attachment of the bluff body to the board was achieved with the use of angled brackets that were secured to the side of the model. The brackets allowed for the bluff body height to be adjusted in 10 mm increments, from a minimum of 40 mm, to a maximum of 60 mm above the board.

The board was made level with the top of the tunnel's boundary layer suction box via 4 specially constructed studding adjusters that passed through the board and into the floor of the tunnel. Each bit of studding contained bolts that when screwed, caused a particular corner of the board to be raised or lowered. A digital inclinometer was then placed on the top surface in order to ensure that it was horizontal to within a tenth of a degree.

The test wing was located further downstream, above the rolling road. It was hung from the overhead balance via struts that connected to pivots at its quarter chord point. The struts had machined slots along their top ends that allowed a degree of freedom in the vertical direction in order to raise and lower the wing. Machined blocks of varying thickness were then placed between the bottom of the endplates and the top of the rolling road surface to set specific ride heights. To adjust the angle of attack, a tail wire connection was fixed to the wing trailing edge. Exact angular values were set by placing

Figure 3.4: The diffuser bluff body and associated ground board that were used in the experimental tests.

the inclinometer on a flat surface that was designed to be parallel to the chord of the wing when placed on its upper profile. Angles were usually double checked before and after each test run. The relative positions of the bluff body and the test wing, along with the area covered by the ground board are outlined in the sketch in Fig. 3.5. The distance from the base of the bluff body to the leading edge of the wing was 2160 mm, a value that approximates to 1.5 car lengths at full scale.

In the larger 3.5 m × 2.5 m facility, both the test wing and the bluff body were mounted using the same strategy. The only difference was an increase in the distance between the two models, owing to the longer moving ground belt system in that tunnel. The distance from the base of the bluff body to the leading edge of the wing was 3100 mm in this tunnel (approximately 2.2 car lengths at full scale).

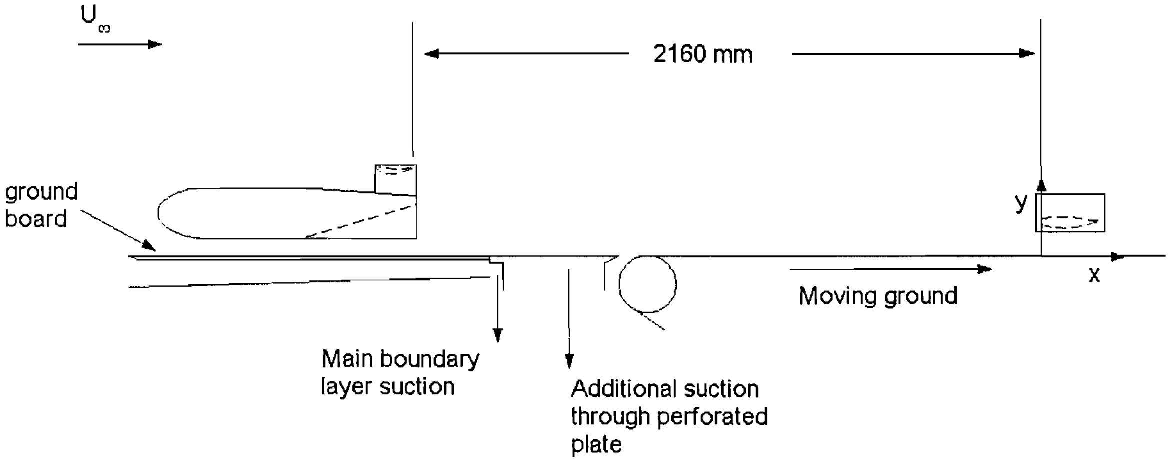

Figure 3.5: A partial wind tunnel schematic, showing the relative positions of the diffuser bluff body and the test wing.

3.6 Test Conditions

The experimental investigations were carried out at two constant wind tunnel dynamic pressures; 25 and 39 mm water. These dynamic pressures corresponded to freestream velocities of approximately 20 and 25 m/s respectively. Owing to variations in the ambient pressure and in the temperature of the wind tunnel, the corresponding Reynolds numbers, based on the test wing chord, vary from 300 000 to 309 000 at 20 m/s and from 375 000 to 387 000 at 25 m/s.

3.7 Force Measurements

Forces were measured on the over-head mechanical balances present in each wind tunnel. The system in the 2.1 m × 1.5 m facility is a 3-component balance of a weigh-beam design, with stepper motors used to drive the weights. The maximum load ranges for lift, drag and pitching moment are 1800 N, 450 N and 450 N.m respectively. The system in the 3.5 m × 2.5 m facility is a Nutem 6-component balance. The maximum loads on this balance are adjustable, and are as follows: lift (300 – 11000 N), drag (256 – 5000 N), side force (645 – 3350 N), yawing moment (83 – 830 N.m), pitching moment (83 – 3500 N.m), and rolling moment (165 – 2500 N.m). Further information on both balances can be found in Ref. [63].

Typically, a series of 75 samples were taken at each ride height configuration. An average was then calculated and output by the controlling software. As it was not possible to obtain each of the individual samples, a slightly different procedure had to be used for error analysis purposes. For these cases, 15 individual samples were taken, following theory outlined in [64]. This value allowed for large-sample statistics to be applied to the calculation of confidence intervals. Appendix B provides detailed error analysis.

3.8 Flow Visualisation

For the flow visualisation studies, a mixture of invisible blue fluorescent pigment, parafin and oleic acid was used. It was then applied to the model with a paint roller or paintbrush. When dried, the mixture formed a white flaky coating that highlighted the flow of the air around the object. Typical drying times range from 0.5 to 1 hour, depending on the temperature of the wind tunnel.

3.9 Pressure Acquisition

Pressure data from the wing was acquired in the 2.1 m × 1.5 m wind tunnel. The pressure taps were located in the direction of the oncoming flow, at 3 separate spanwise stations. There were 44 taps at each station, 24 on the suction surface and 20 on the pressure surface. The taps were constructed in such a manner as to minimise the number of flexible tubes emanating from the wing, and passing across the tunnel to the external transducers.

Small hollow metal tubes were placed just underneath the skin of the wing. The metal tubes were laid in the spanwise direction, and protruded out of a hole in the side of the wing and endplate. Small holes were then drilled through the surface of the wing into each tube, at the appropriate spanwise station. With this design, only 44 flexible tubes connected the wing to the transducers, even though there were 3 times as many pressure taps. Any spanwise station not in use was covered with tape.

A ZOC pressure transducer system was used to take the measurements [65]. The ZOC was located external to the tunnel test section in order to minimise the effect of temperature changes on the transducer. As the 2.1 m × 1.7 m facility has no cooling system, the temperature within the confines of the tunnel can vary by more than 15 deg in a matter of hours. The ZOC itself was connected to PI software [66], which allowed for a number of measurement runs to be programmed at each ride height. For the data obtained in this document, 22 values were recorded at each tap for each ride height investigated. An average was then calculated to provide the most representative value.

3.10 Particle Image Velocimetry

PIV is a non intrusive measurement technique used to obtain instantaneous velocities in a region of a fluid flow under investigation. The flow must be seeded with particles so that instantaneous image pairs can be taken a short time interval apart. From the distance that the particles have travelled in the time that the successive images were taken, velocities can be calculated. The main components necessary for this technique are a laser source and its associated optics, a Charged Coupled Device (CCD) camera and a controlling computer with the associated software.

For a typical 2-D PIV test, the laser and camera are set up at right angles to each other in such a manner that the light sheets produced by the former, pass through the camera focal plane at the point of interest. The light sheets emanating from the laser are pulsed so as to produce a stroboscopic effect, which essentially freezes the movement of the particles for the images to be taken. This implies that the pulsing and the image capture have to be synchronised so that the positions of the particles at the time of the first pulse are captured on the first image, while their positions at the time of the second pulse are captured on the second image. The particles show up as specks of light on the dark background of the image. The background of the image is dark because all external light sources have to be eliminated from the experimental region. The recorded image pairs can then be post processed by the supplied software.

Post processing takes the form of performing a cross correlation between the image pairs in order to identify the relative position of each particle in both frames. To achieve this goal accurately, the software divides each image into rectangular interrogation regions. The cross correlation is then carried out between the corresponding interrogation regions on each frame, from which average particle displacement vectors may be produced. Special algorithms can then be applied to validate the vector maps in order to eliminate spurious vectors.

The system used at the University of Southampton was obtained from Dantec Dynamics. The apparatus consisted of New Wave Gemini Nd:Yag lasers, capable of producing 120 mJ at 532 nm. Both laser components were contained within a single casing, with the associated internal optics used to direct each beam to an external lens for final projection. A Dantec HiSense CCD camera was supplied for image collection. The camera had a resolution of 1280 × 1024 pixels, and has three different lenses. The 105 mm lens was used, since it provided the highest flow field resolution. The laser and camera were controlled by Dantec FlowMap software [67] via the associated PC. The software allowed for the adjustment of both the laser and the camera parameters, while also collecting the acquired images for post-processing.

In order to obtain 2-D data on a plane that was parallel to the trailing edge of the wing, it was necessary to mount the camera inside and to the rear of the tunnel test section. Conversely, the laser was mounted outside the test section, with the beams projected through the glass at the side. To obtain data on planes parallel to the tunnel

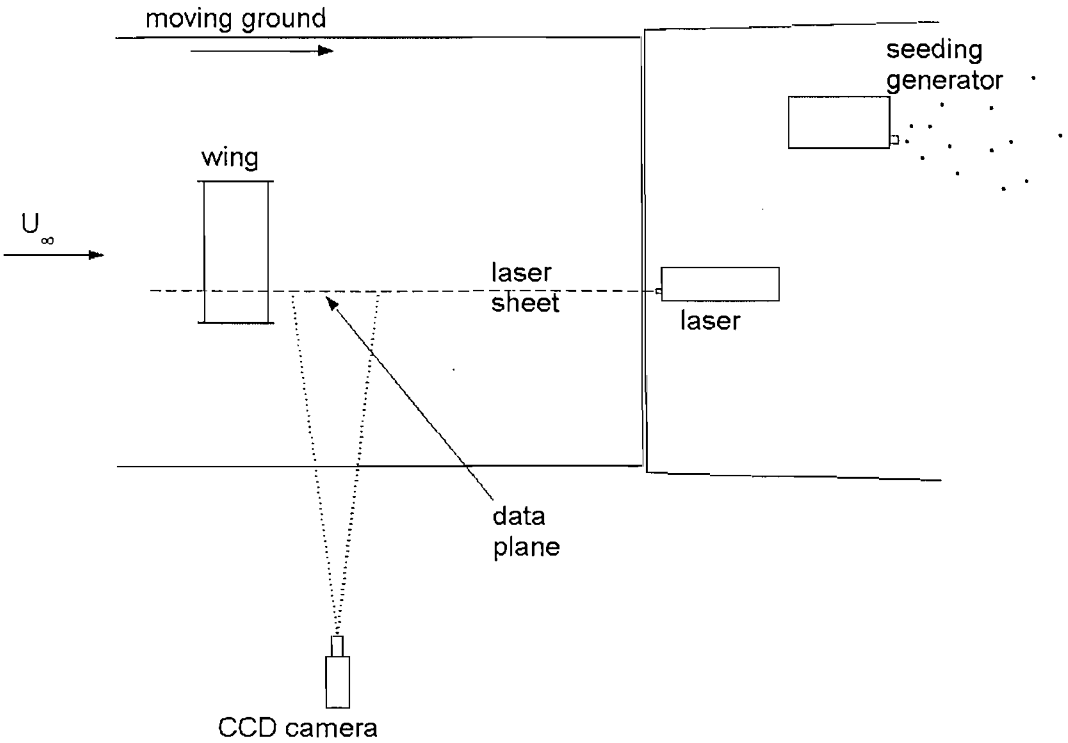

Figure 3.6: A plan view showing the PIV experimental configuration.

centreline, the laser and camera positions were reversed, as in Fig. 3.6. A smoke generator was also placed downstream of the test section. The ejected particles travelled around the tunnel before passing through the measurement plane. Since the tunnel's boundary layer suction mechanism had to be in operation, it was necessary to eject particles from the generator at frequent intervals. As outlined in Appendix B, the uncertainty in the PIV measurements were estimated to be ±1.6% in u, and less than ±1% in v.

3.11 Laser Doppler Anemometry

LDA is a non-intrusive measurement technique in which light beams are used to acquire the velocity at a point in a flow field. The light beams overlap to form a measurement volume that consists of interference fringes. When seeding particles that are introduced to the flow pass through this volume, they scatter some of the light, which is collected and post processed. Underlying frequency patterns that are extracted from the collected light then allow for the velocities to be deduced.

The three-component LDA system at the University of Southampton was supplied by Dantec [68]. It consists of a continuous wave argon-ion laser, optics for the transmission, manipulation and collection of the laser beams, two probe modules and signal processing equipment. In order to measure one component of velocity, two overlapping, monochromatic, coherent light beams are required. Thus for three components, the system emits six beams, four of which originate from one probe module.

For the three-component system, the beam of light that is emitted from the laser is directed to a Bragg cell via internal optics. The Bragg cell is an acousto-optical modulator that serves to split the original beam into two new beams of equal intensity, introducing a frequency shift to one of them as it does so. The pair of beams are then separated into three colours – green, blue and violet – which are then focussed into optical fibres before being emitted by a particular probe module. Each pair of colours is of a different wavelength, with one colour being used to measure one velocity component.

All six beams are then focussed to a particular spatial location, which creates a measurement volume in the shape of an ellipsoid. Owing to the overlap of each coloured beam, interference fringes are produced, with the distance between the fringes being a function of the wavelength and the angle between the beams. When a seed particle passes through the fringe patterns, it scatters light. The scattered light contains a Doppler shift [69] that is proportional to the velocity component along the measurement axis of the particular pair of beams. The scattered light is collected by receiving optics and processed by spectrum analysers to produce the resultant velocity component. As outlined in Appendix B, the uncertainty in the LDA measurements were estimated to be ±0.10 m/s.

Chapter 4

The Effect of Upstream Bodies on a Single Element Wing in Ground Effect

4.1 Introduction

This chapter presents results that highlight the changes to the aerodynamic characteristics of the single element wing when placed behind upstream bodies. The upstream bodies included a wing attached to a sting (FC2), and a diffuser equipped bluff body that incorporated the previous wing (FC3). Forces, flow visualisation images, pressure distribution plots and flow field measurements were used to decipher and explain the performance changes when compared to the clean air case, FC1.

4.2 Forces

As outlined in Appendix B, the maximum uncertainties in the downforce and drag coefficients were approximated as being ±0.002 and ±0.0004 respectively. Figure 4.1 presents a comparison of the downforce coefficients while varying the height of the wing in flow conditions FC1, FC2, and FC3. On initial observation, it is clear that there were successive decreases in downforce as the oncoming flow progressed from FC1 to FC3. The plots for FC1 and FC2 showed the characteristic increase in the variable to a certain point, as the ride height was reduced. Below this particular point, the downforce then began to decrease. With regard to FC1, the maximum downforce coefficient of 1.56 occurred at $h_r/c = 0.094$, while for FC2, the maximum downforce coefficient of 1.52 occurred at $h_r/c = 0.100$. Therefore, there was a 2.6% decrease in maximum downforce, with this point occurring slightly earlier in FC2. Closer scrutiny of the two plots reveals that the downforce loss in progressing from FC1 to FC2 was not consistent over the range of ride heights investigated. In general, there was a greater loss at high ride heights than there was at low ride heights. For comparison, at $h_r/c = 0.833$, there was approximately 13% loss in downforce, while at $h_r/c = 0.401$ and $h_r/c = 0.107$ there was approximately a 7.6% loss and a 3% loss, respectively.

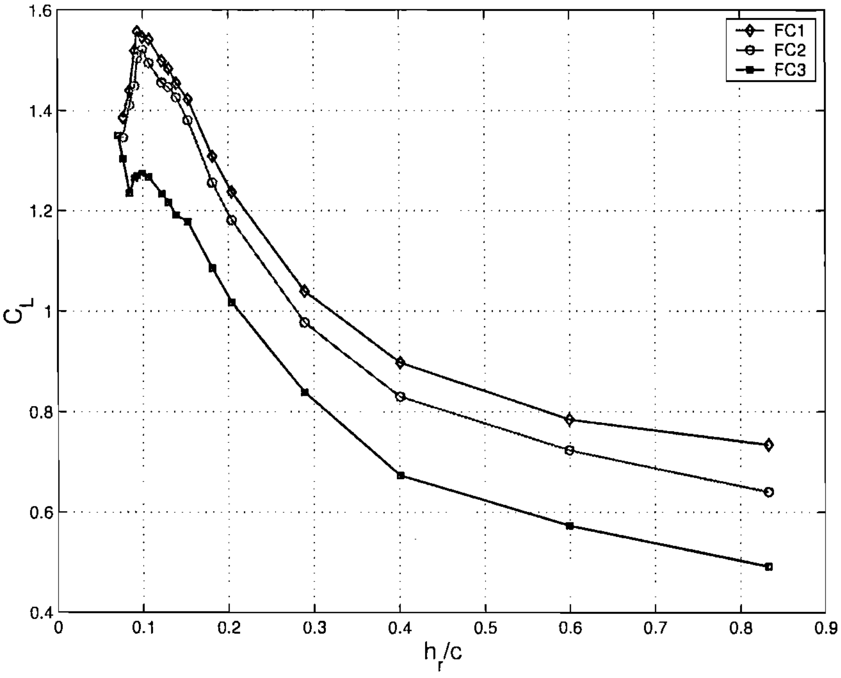

Figure 4.1: The experimental downforce coefficients in ground effect for clean air (FC1), behind the upstream wing (FC2), and behind the upstream wing and bluff body (FC3).

The plot for FC3 shows an interesting new characteristic. As in the previous plots, the downforce increased with a reduction in ride height, to a point that one would have considered as being the maximum downforce ($C_L = 1.27$ at $h_r/c = 0.100$), based on the plots of FC1 and FC2. After this "expected" point of maximum downforce, there was again the familiar decrease. However, the decrease was then halted by a second abrupt increase in downforce at very low ride heights. This second increase then produced higher force values than were recorded at the previously "expected maximum." In fact, at the lowest ride height of $h_r/c = 0.071$, there is 6% more downforce than at the previously "expected maximum," which occurred at $h_r/c = 0.100$.

In an attempt to investigate whether the new phase of the flow appeared at a higher Reynolds number in FC3, the oncoming velocity was increased to 25 m/s. A comparison of the results in the region of maximum downforce is presented in Fig. 4.2. Two things become clear immediately. Firstly, it is apparent that the new phase of flow also existed at the higher wind speed, however, the point at which it commenced now occurred at $h_r/c = 0.091$ as opposed to $h_r/c = 0.085$ at 20 m/s. This suggested that it was a Reynolds number dependent phenomenon. Secondly, less downforce was generated at 25 m/s than was the case at 20 m/s, an outcome similar to that reported by Zerihan and Zhang [35]. The authors surmised that the result may have been caused by the different sizes of the laminar separation bubble for each case.

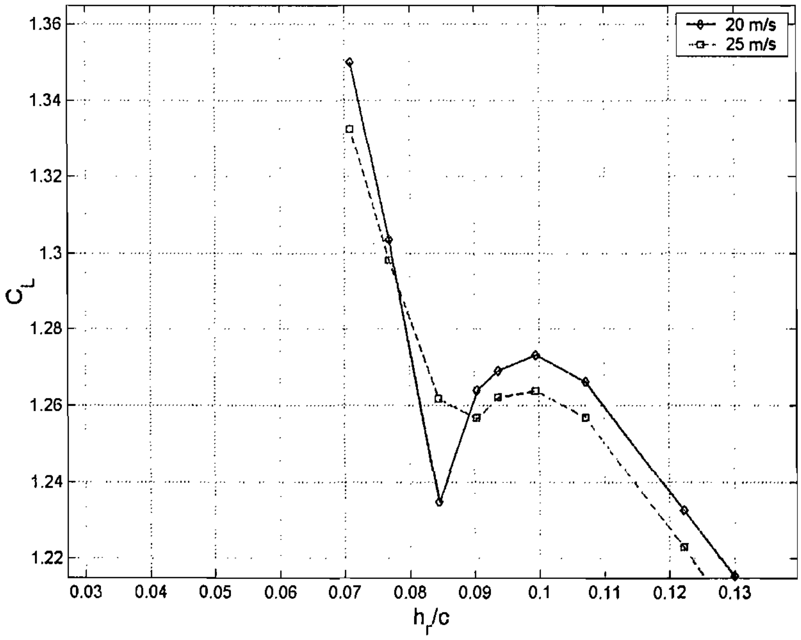

Figure 4.2: A closer view of the force reduction region in FC3, which is terminated by an increase in downforce at very low ride heights.

The variation of the drag values with ride height in the three flow conditions is presented in Fig. 4.3. Considering first the results from FC1, it can be deduced that there was the expected increase in drag with reducing ride height. The increase, however, was not monotonic. At ride heights below $h_r/c = 0.153$, fluctuations in the values became evident. In general, the results from the three curves indicated that the presence of the upstream bodies caused an increase in the drag of the downstream test wing. When compared to FC1, the curve for FC2 showed this characteristic throughout the ride height range. The curve for FC3, however, was slightly different. It commenced with the greatest drag values for ride heights from $h_r/c = 0.833$ to $h_r/c \approx 0.37$. Below this ride height, the values were less than FC2, but higher than FC1 until $h_r/c \approx 0.097$. Below $h_r/c \approx 0.097$, it crossed below the curve for FC1.

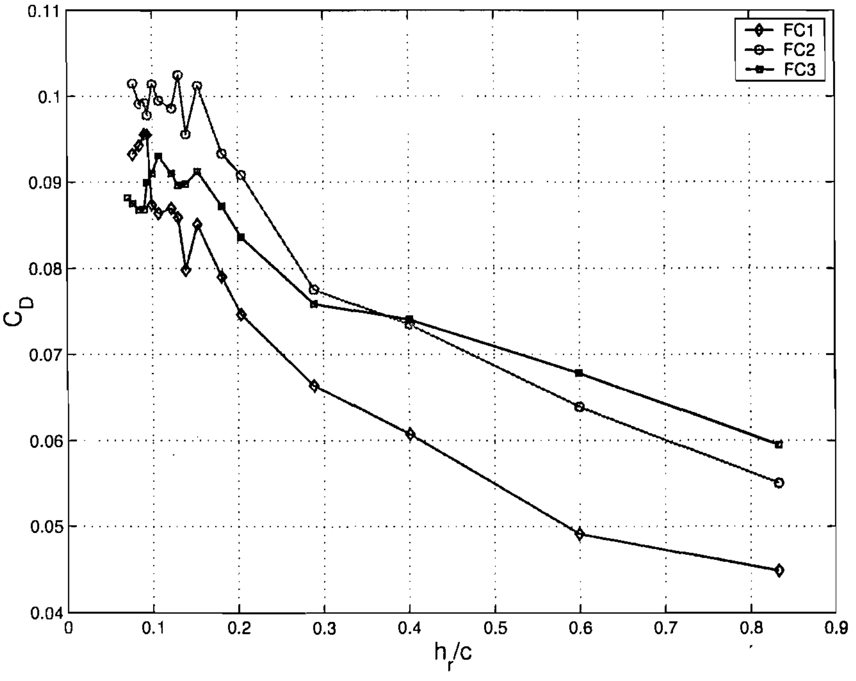

Figure 4.3: The experimental drag coefficients in ground effect in the three flow conditions in which they were measured.

Curves depicting the angle of attack variation in FC1 and FC3 at $h_r/c = 0.833$ and 0.153 are presented in Fig. 4.4. In the linear range of wing operation, it can be deduced that more lift was lost at greater ride heights than at lower ride heights. For example, at

-5 deg and $h_r/c = 0.833$, $\Delta\ C_L = 0.138$, while at $h_r/c = 0.153$, $\Delta\ C_L = 0.076$. Similarly, at 5 deg, the corresponding values of $\Delta\ C_L$ were 0.279 and 0.196 respectively. It is also clear that the trend of increasing lift curve slope with decreasing ride height also existed in FC3. Closer scrutiny of the curves for FC1 at both ride heights will highlight the fact that the wing stalled more abruptly at $h_r/c = 0.833$ than it did at $h_r/c = 0.153$. In dirty air conditions at $h_r/c = 0.833$, however, stall became more gradual.

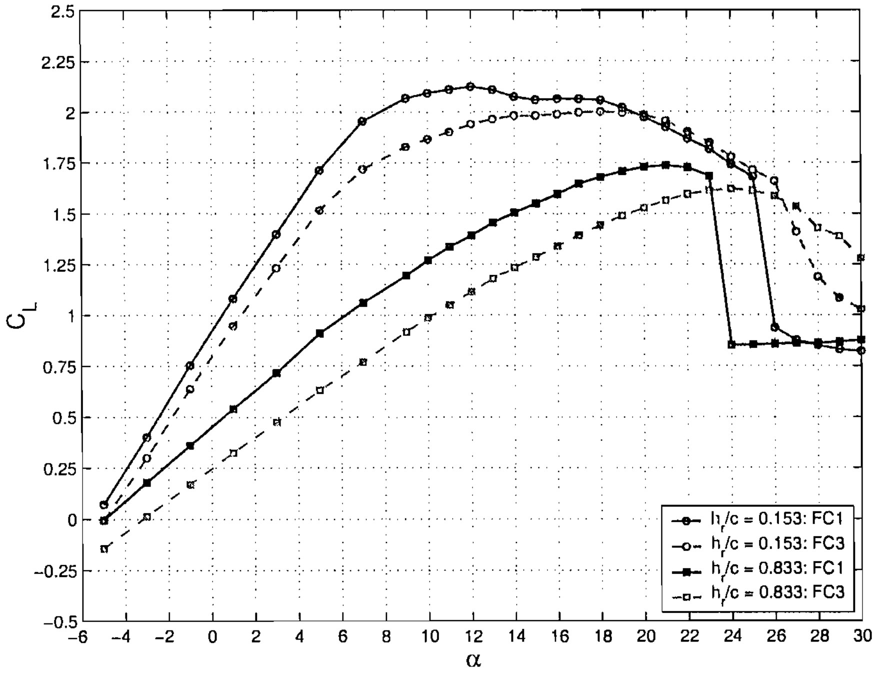

Figure 4.4: The lift curves at h_r/c = 0.153 and 0.833 with and without the presence of the diffuser bluff body.

Figure 4.5 presents data showing the variation in drag with angle of attack at the two ride heights investigated. In general, at angles above 1 deg at $h_r/c = 0.833$, there appeared to be more drag in the dirty air flow than there was in the clean air flow. Below this angle of attack, there was not a discernable difference. In contrast, at $h_r/c = 0.153$, a discernable difference in the drag from the two flow conditions appeared at approximately 8 deg. It also seemed that the drag increments were generally higher at the lower ride height.

A comparison of the lift to drag ratios is presented in Fig. 4.6. It can be seen that

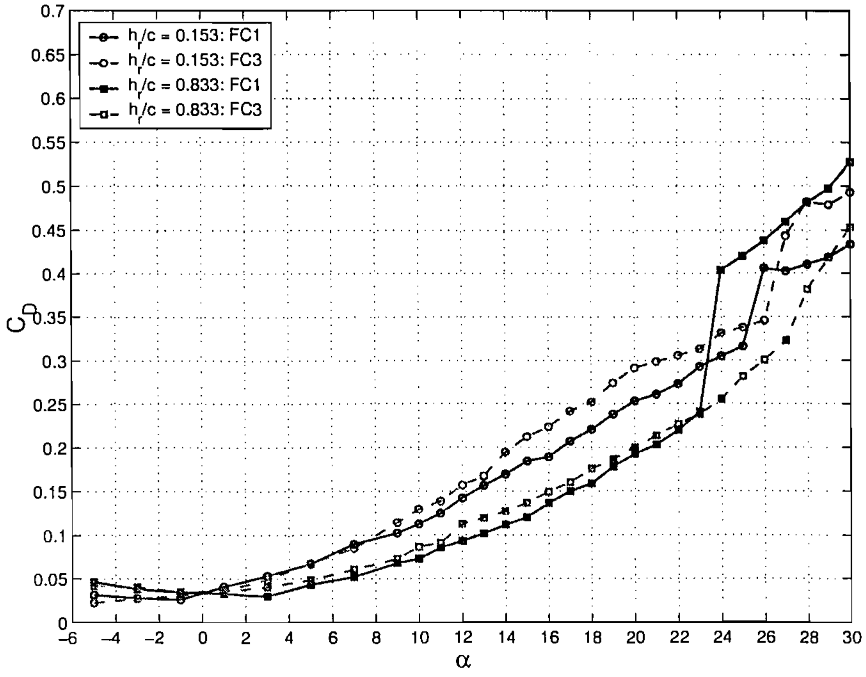

Figure 4.5: The drag curves at $h_r/c = 0.153$ and 0.833 with and without the presence of the diffuser bluff body.

in the cases of both FC1 and FC3, the lower ride height produced higher maximum L/D values than the higher ride height. Additionally, at each ride height, the angle at which the maximum L/D occurred in FC3 was greater than the angle at which the maximum L/D occurred in FC1. For example, at $h_r/c = 0.153$ in FC3, a maximum L/D of approximately 26 occurred at 1 deg, while in FC1, a maximum L/D of 29 occurred at -1 deg. Also evident from the data was the fact that there was a more gradual change in values in the region of maximum L/D at the higher ride height than there was at the lower ride height.

A series of measurements were taken while moving the diffuser bluff body laterally away (indicated by 2z/b) from its original position in front of the test wing. 2z/b is a normalised coordinate in the spanwise direction of the wing such that 2z/b = 0 at the midspan and 2z/b = 1 at the wing tips. At 2z/b = 0, the diffuser centreline coincided with the wing centreline, while at 2z/b =1, the diffuser centreline coincided with the wing tip. Figures 4.7 and 4.8 show that at both ride heights investigated, the downforce

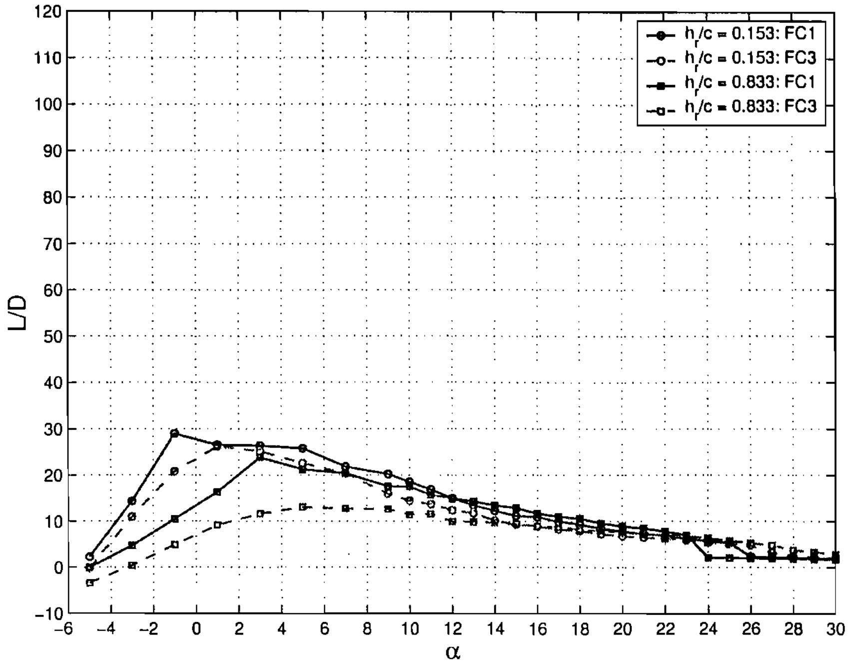

Figure 4.6: The lift to drag curves at $h_r/c = 0.153$ and 0.833 with and without the presence of the diffuser bluff body.

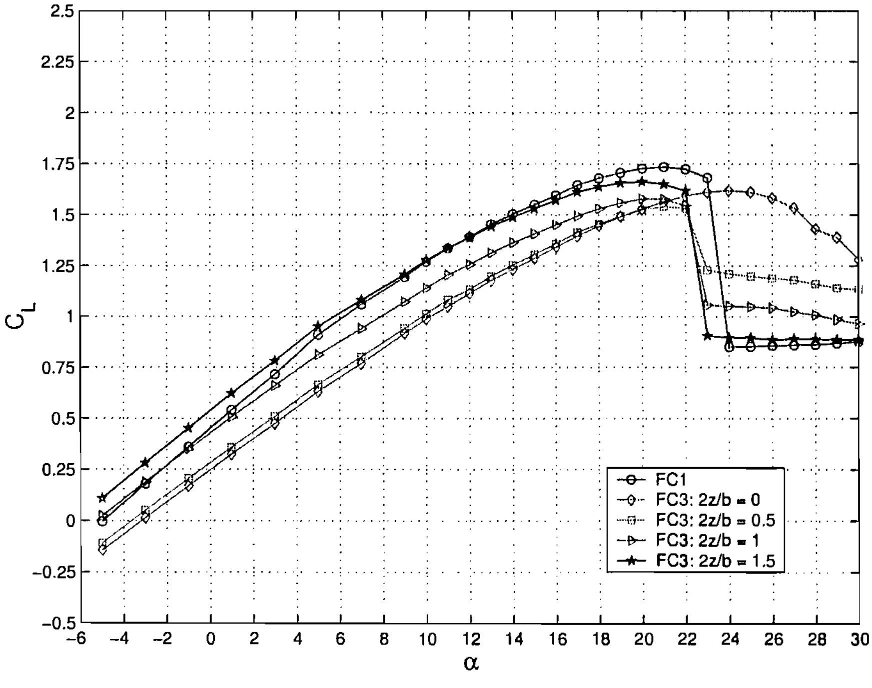

Figure 4.7: The downforce curves at $h_r/c = 0.833$, while moving the bluff body laterally away from its original position.

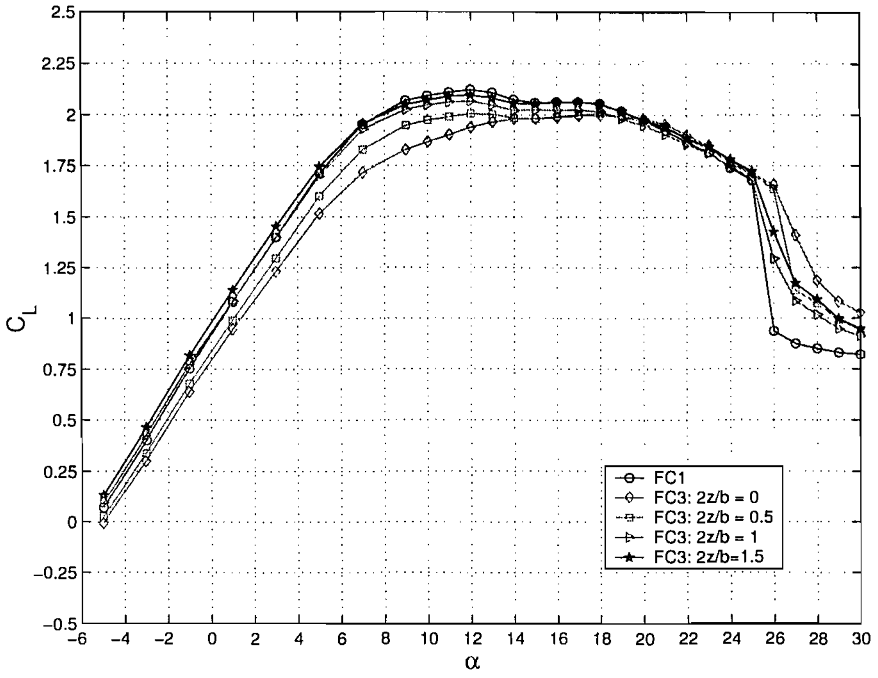

Figure 4.8: The downforce curves at $h_r/c = 0.153$, while moving the bluff body laterally away from its original position.

gradually recovered to the freestream values, and in the case of 2z/b = 1.5, surpassed them. Sharper wing stall was also evident at the greater ride height of $h_r/c = 0.833$ for all cases except for 2z/b = 0. This result suggested that the boundary layer remained attached at higher angles of attack only when the diffuser was directly in front of the wing. At the lower ride height of $h_r/c = 0.153$, stall was gradual in all cases.

The plots for drag versus increasing wing angle of attack show no particular discernable trend, Figs. 4.9 and 4.10. What is clear though, is that different values of drag arose, depending on the lateral position of the upstream bluff body, and on the height of the wing. At the ride height of $h_r/c = 0.833$, the case for $2z/b = 1.5$ showed significantly lower drag values from the remaining lateral positions, and from the FC1 values. This was most likely a result of the relative location of the diffuser trailing vortex and the downstream test wing. The wing way may now have been operating in the downwash of the vortex at this lateral position.

Given the lack of a clear trend from the drag data, the lift to drag ratios were then ex-

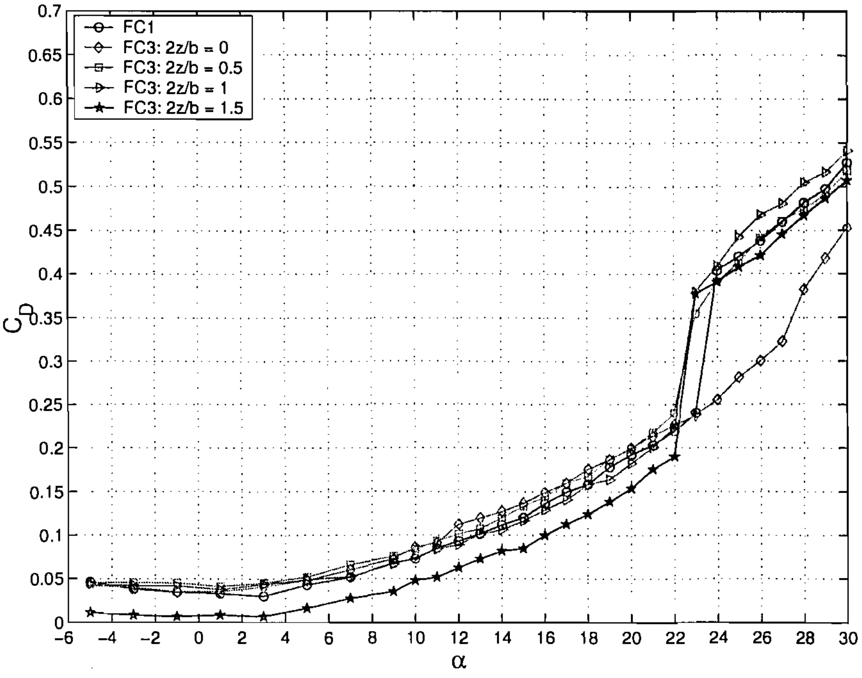

Figure 4.9: The drag curves at $h_r/c = 0.833$, while moving the bluff body laterally away from its original position.

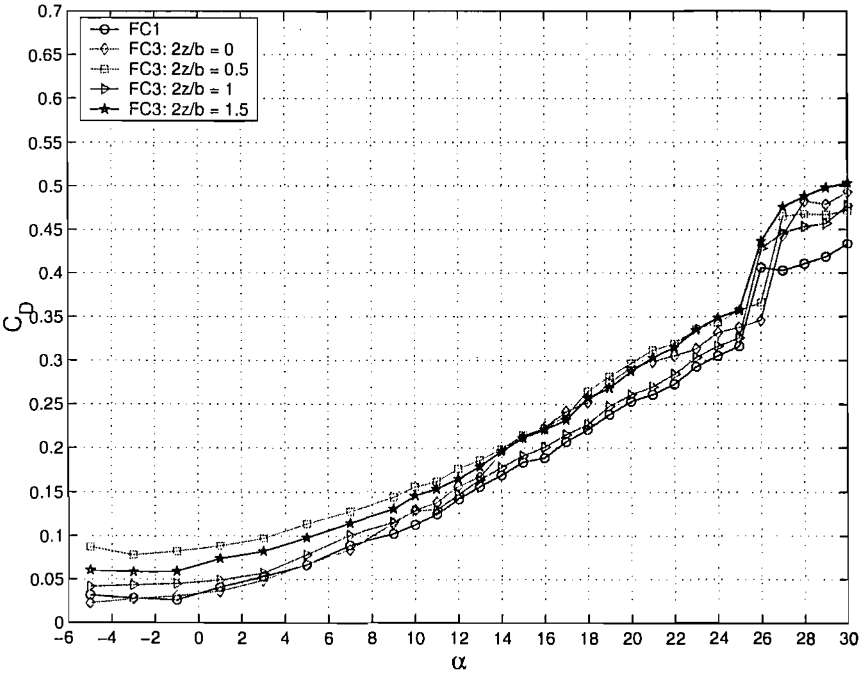

Figure 4.10: The drag curves at $h_r/c = 0.153$, while moving the bluff body laterally away from its original position.

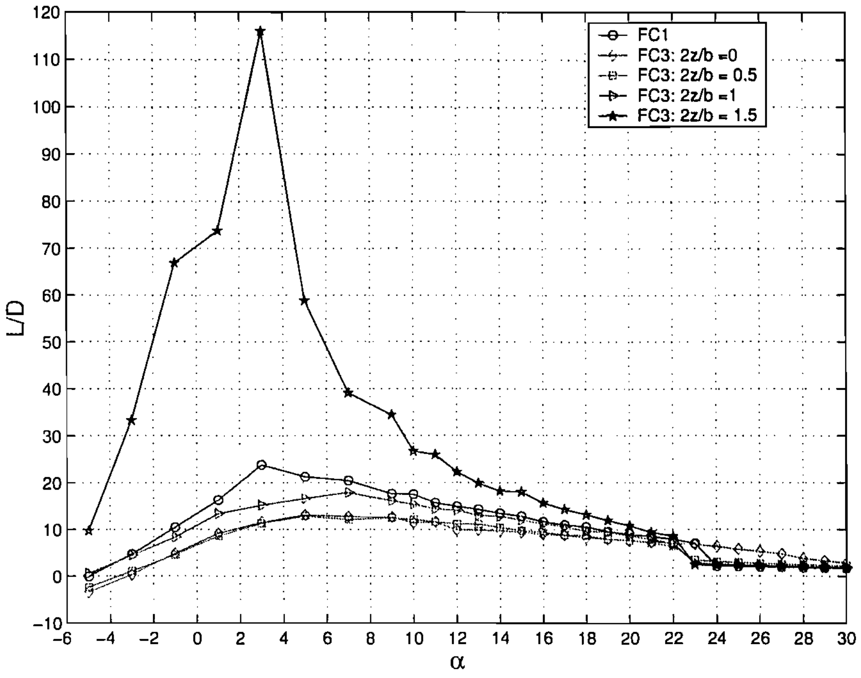

Figure 4.11: The lift to drag ratios at $h_r/c = 0.833$, while moving the bluff body laterally away from its original position.

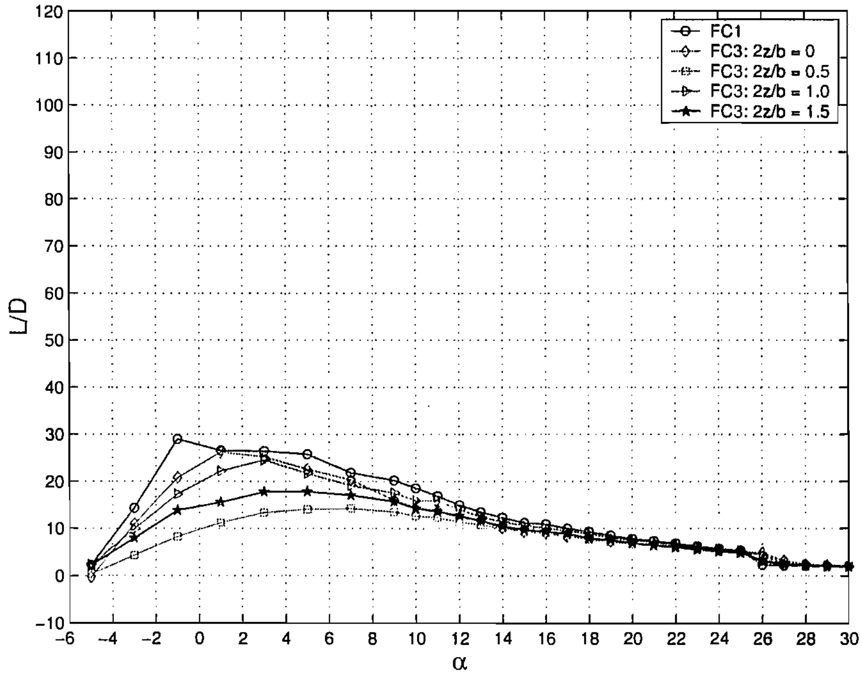

Figure 4.12: The lift to drag ratios at $h_r/c = 0.153$, while moving the bluff body laterally away from its original position.

amined. The results for $h_r/c = 0.833$ are shown in Fig. 4.11, while those for $h_r/c = 0.153$ are shown in Fig. 4.12. Again, a comparison at each specific ride height showed no discernable trend. What can be deduced from the two figures, however, is that the ratio was generally higher at $h_r/c = 0.153$, than it was at each corresponding position of the greater ride height of $h_r/c = 0.833$. The exception to this observation was the lateral position of 2z/b = 1.5. At the greater ride height of $h_r/c = 0.833$, the lift to drag ratio for this position was significantly higher than all other values, including those of FC1.

4.3 Flow Visualisation

Figure 4.13 shows the flow over the suction surface of the wing in FC1. Close observation shows that there is a laminar separation bubble across the majority of the span of the wing (a). At mid span, it can be deduced that the bubble trapped some of the flow visualisation fluid while it was drying (b), thereby causing an additional obstruction to the flow, which then went on to cause premature trailing edge separation (c). The premature separation was also aided by a blob of unmixed solution (d). Close to each endplate, at the trailing edge of the wing, a region of recirculating bubble flow can be identified (e).

In comparison, Fig. 4.14 shows the flow over the suction surface of the wing in FC3. It can be deduced that there is now a dramatic difference in the surface flow, when compared to FC1. At a considerable distance either side of midspan the laminar separation bubble has disappeared (f), as the flow is turbulent from the outset. The flow also appears to be antisymmetric, as evidenced by the comparable sizes of the regions labelled (g) and (h). It is also reflected in the slightly different shape of the separation region at (i) and (j). The recirculating bubble regions (k, l), which now have distinctly different shapes when compared to each other, are still observed at either endplate, close to the trailing edge.

Figure 4.15 shows the flow over the pressure surface of the wing in FC1. It can be deduced that there are large regions of laminar flow, with a laminar separation bubble

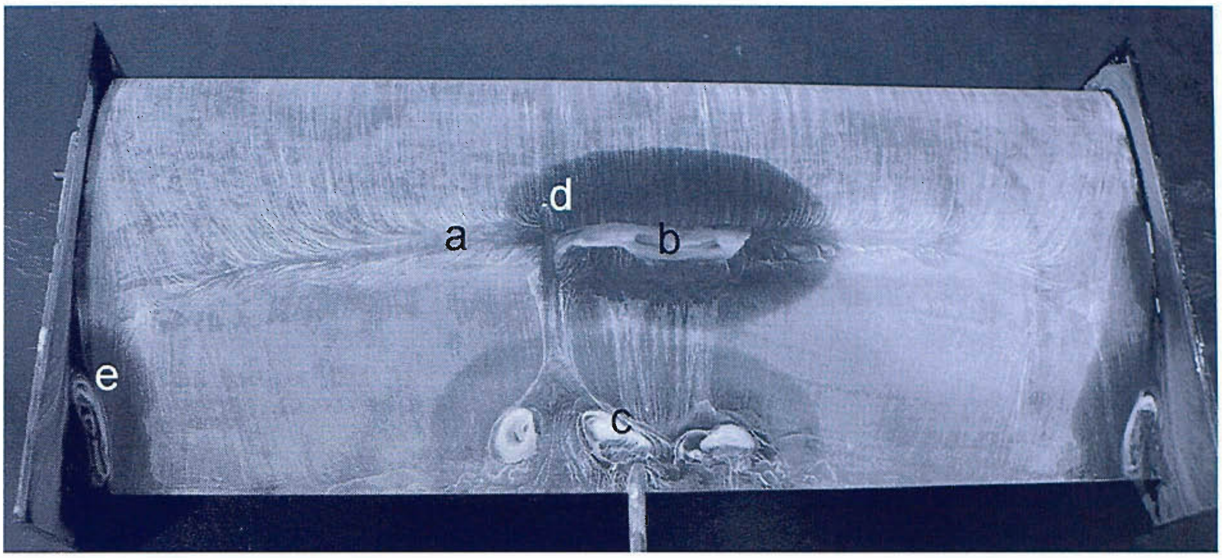

Figure 4.13: Suction surface flow for the wing in ground effect at $h_r/c = 0.153$ and 5 deg aoa.

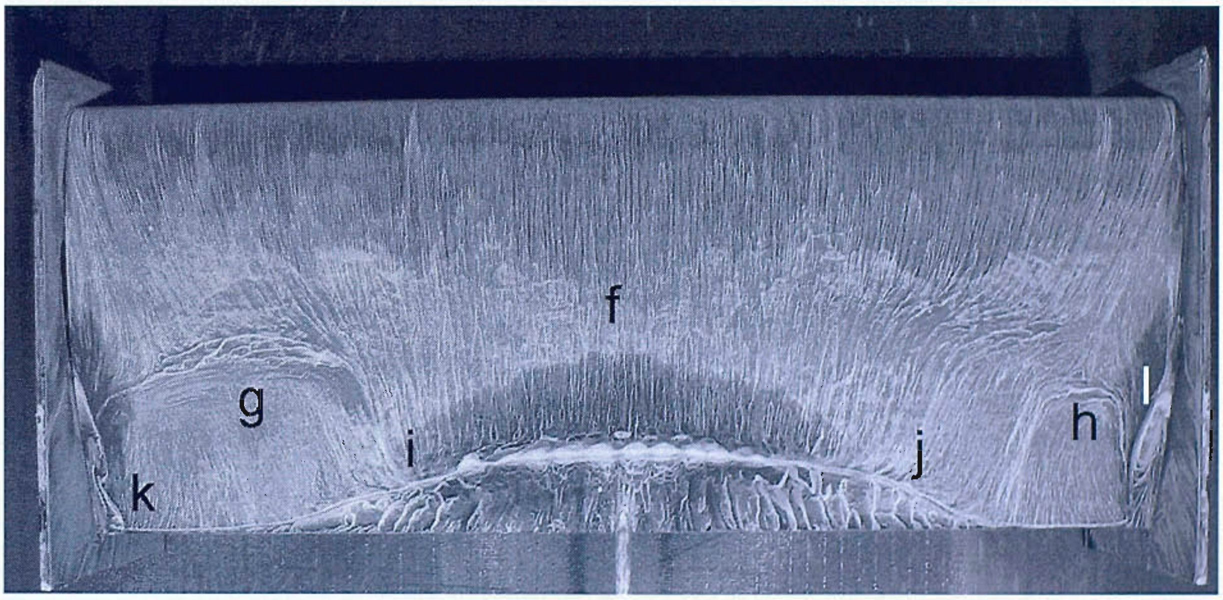

Figure 4.14: Suction surface flow for the wing in ground effect at $h_r/c = 0.153$ and 5 deg aoa, while behind the upstream wing and bluff body.

clearly visible across the span (m).

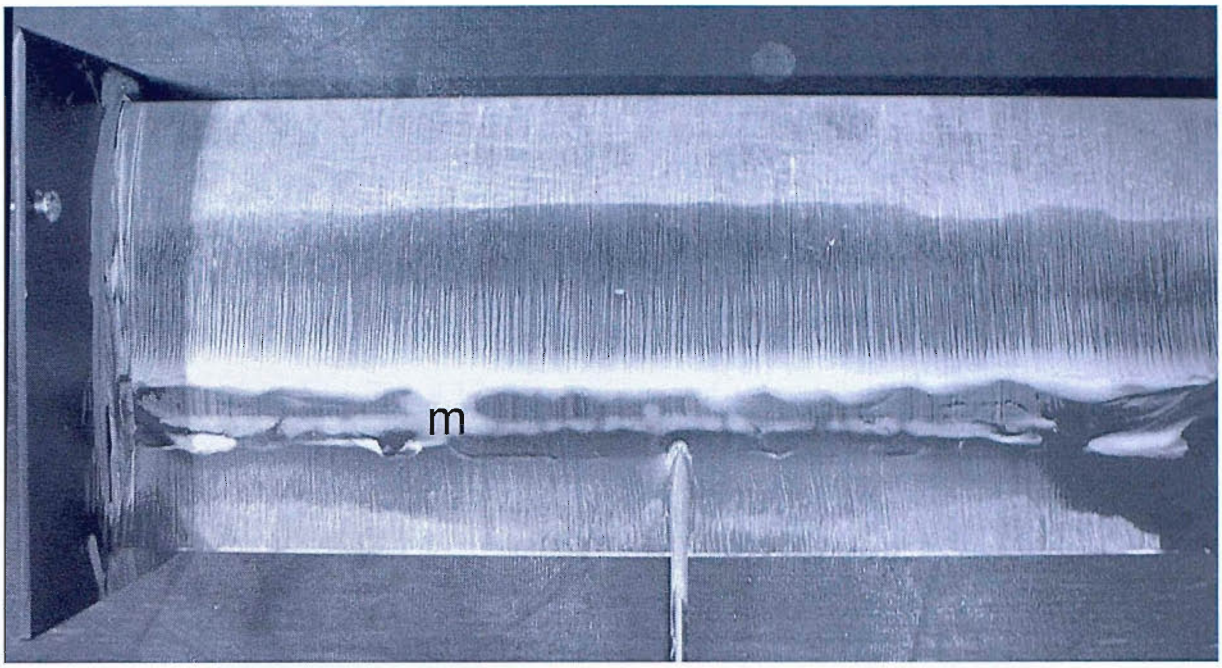

Figure 4.15: Pressure surface flow for the wing in ground effect at $h_r/c = 0.153$ and 5 deg aoa.

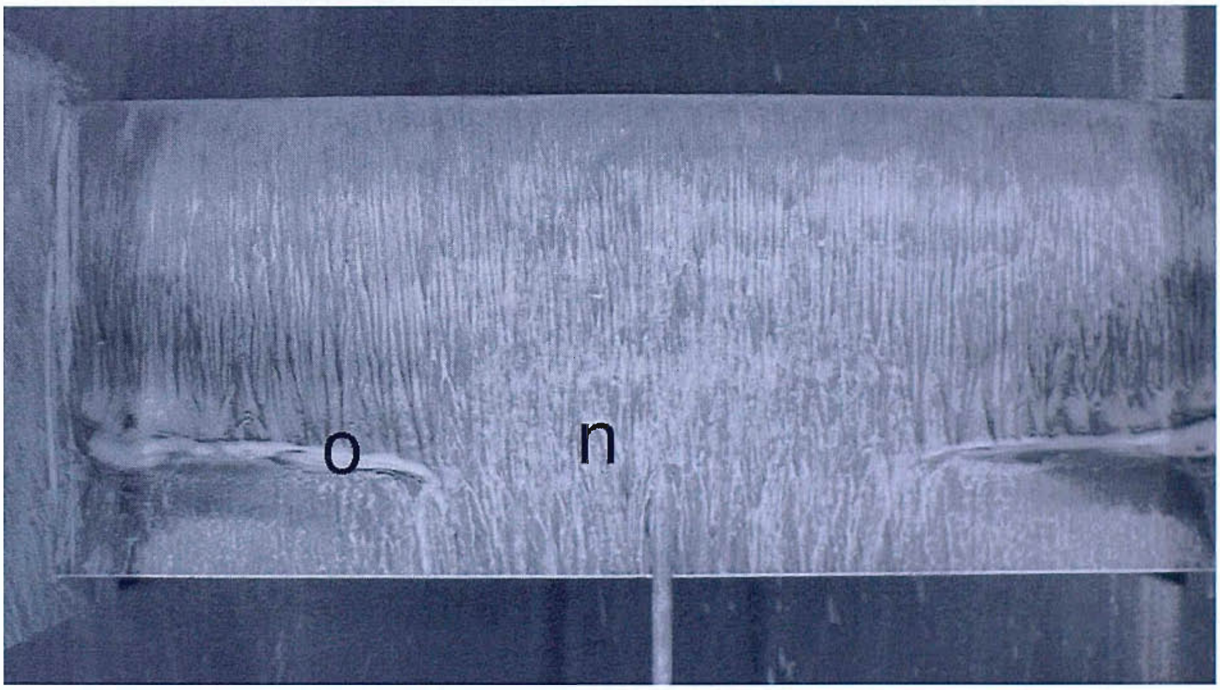

Figure 4.16: Pressure surface flow for the wing in ground effect at $h_r/c = 0.153$ and 5 deg aoa, while behind the upstream wing and bluff body.

In comparison Fig. 4.16 shows the flow over the pressure surface of the wing in FC3. There is again another striking difference when compared to FC1. The laminar separation bubble has been eliminated from a considerable distance either side of the midspan of the wing (n), but is still clearly visible towards the tips (o). In contrast to the overall flow on the suction surface, the flow on the pressure surface appears to be symmetric.

In order to ascertain the type of flow emanating from the upstream diffuser bluff body in its baseline configuration, flow visualisation was performed on the ramp and endplate region. As illustrated in Fig. 4.17, the presence of vortex flow was highlighted by the swirling lines that trailed along the edge of the ramp, close to the endplate [50]. The flow was symmetric about the bluff body centreline, Fig. 4.18, and showed the characteristics of high angle diffusers as outlined in Ref. [51].

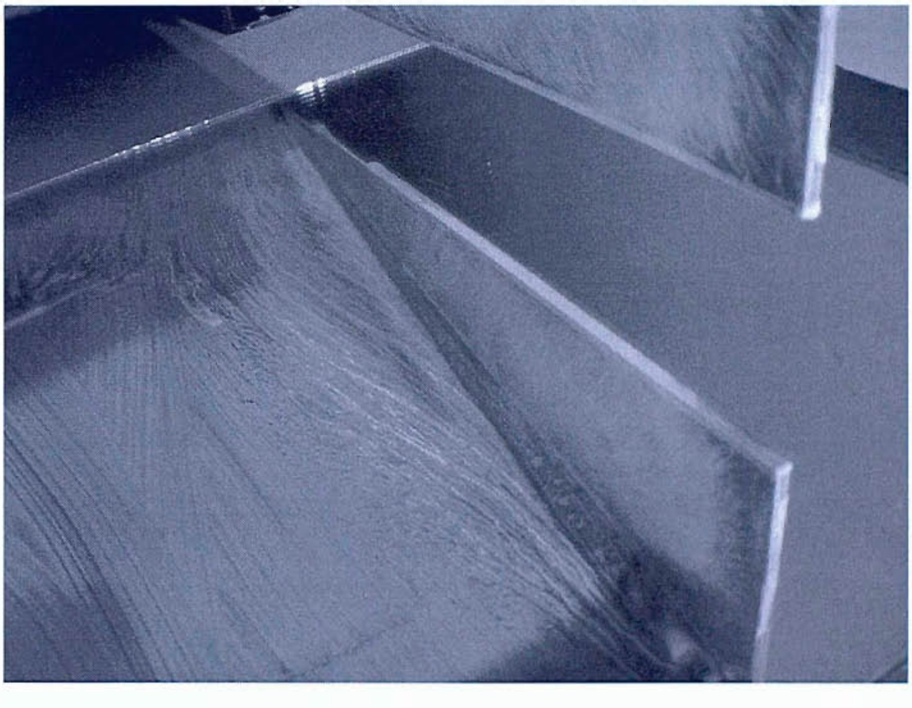

Figure 4.17: Swirling lines on the diffuser ramp, indicating the presence of vortex flow.

Figures 4.19 and 4.20 depict the flow on the suction surface of the wing in FC1 and FC3, at $h_r/c = 0.077$. This ride height is well within the force reduction region in $FC1$ and within the newly identified region of force increase in FC3. Firstly, from Fig. 4.19, it must be noted that at the time, it was not possible to apply the flow visualisation mixture to

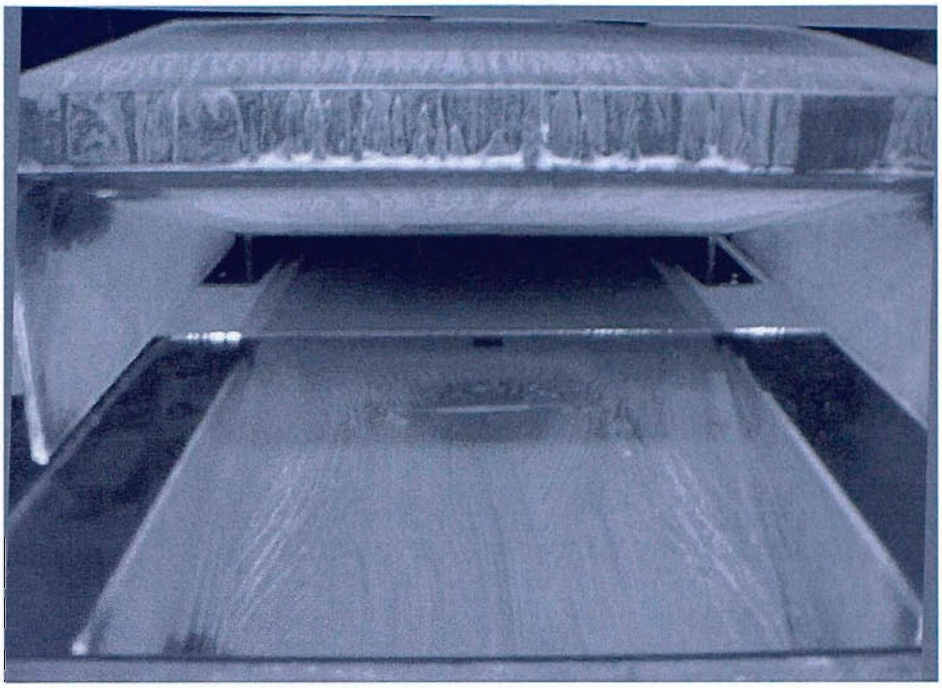

Figure 4.18: A view of the entire ramp, confirming that the flow is symmetric about the centreline.

the entire suction surface because the distance between the ground and the lowest portion of the wing was too small for the applicators that were available. Nevertheless, it can be deduced that there was widespread separation across the whole trailing edge of the wing. In addition to the large semi circular shaped separation region in the middle, there appeared to be two further triangular shaped separation regions, close to each endplate. In Fig. 4.20, the two triangular separation regions have disappeared, having been replaced instead by attached flow. The semi circular separation region centred at the middle of the trailing edge was still evident.

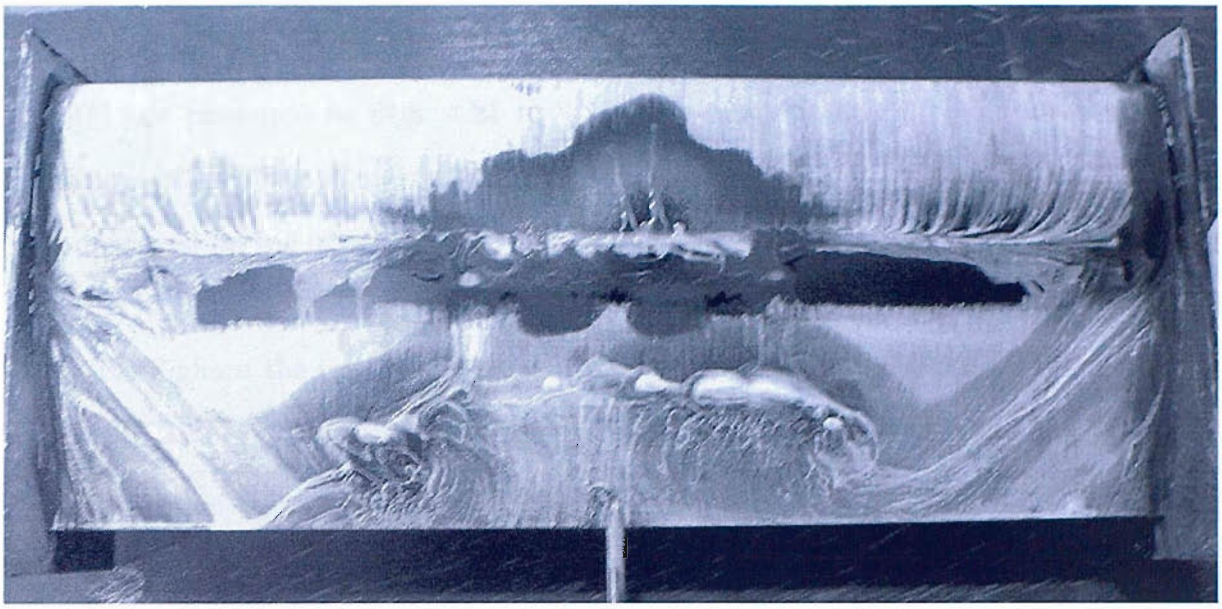

Figure 4.19: The flow on the suction surface of the wing in the force reduction region at $h_r/c = 0.077$ in FC1.

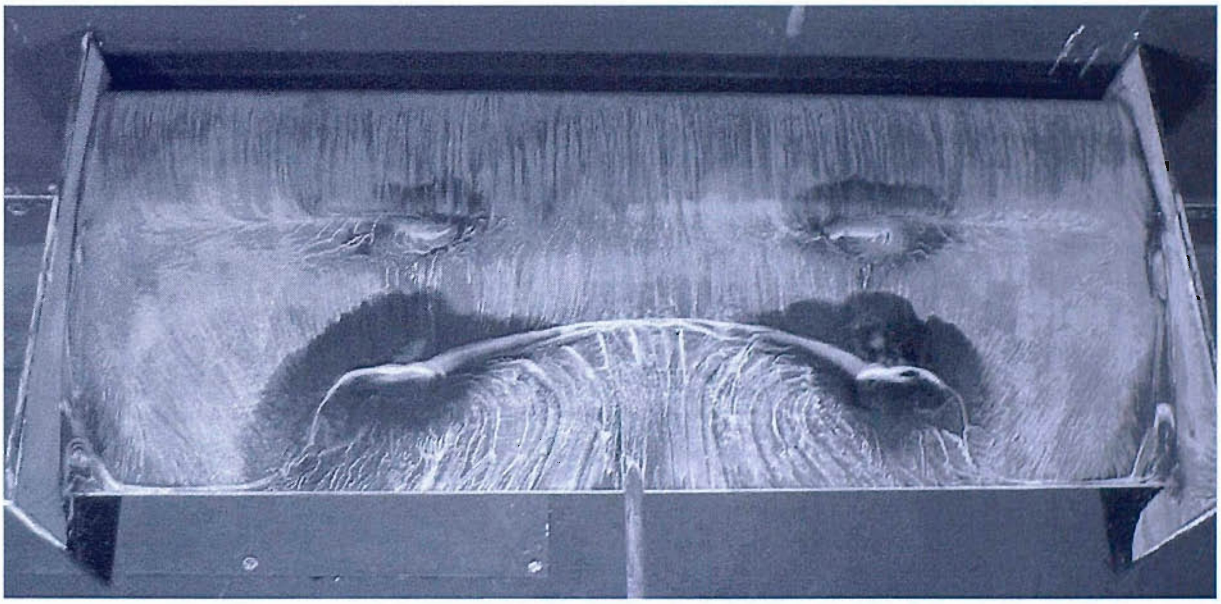

Figure 4.20: The flow on the suction surface of the wing in the force reduction region at $h_r/c = 0.077$ in FC3.

4.4 Pressures

Chordwise pressure distribution data at ride heights of h_r/c = 0.833, 0.401, 0.153 and 0.077 are presented in Figs. 4.21 to 4.24. At each ride height, plots for the spanwise stations of 2z/b = 0.09 and 0.49 are displayed on one figure, while the plot for 2z/b = 0.89 is displayed on the other. This approach was taken to avoid excessive clutter on a single figure.

Throughout the ride height range investigated, it became clear that changing the flow from FC1 to FC3 resulted in a decrement in the pressure distribution at each station investigated. The decrement appeared to be greater at stations closer to the centre of the wing, than at stations further away. Also evident was the fact that the majority of the loss occurred from the suction surface of the wing, especially at 2z/b = 0.09 and 0.49. To provide further insight, the 2-D sectional downforce coefficients were estimated for each case. The trapezium rule was used to integrate the distributions between x/c = 0 and x/c = 0.9. Owing to manufacturing constraints, no pressure tap was located beyond x/c = 0.9 on the wing pressure surface and beyond x/c = 0.95 on the suction surface. The integration was therefore not carried out for the last 10% of each section. Table 4.1 summarises the changes as the oncoming flow evolved from FC1 to FC3. It is clear that at each ride height, the most lift was lost at 2z/b = 0.09. This was followed by the section at 2z/b = 0.49, then 2z/b = 0.89. Additionally, the sections lost more lift at greater ride heights than at lower ride heights.

The pressure distribution data also shows the existence and disappearance of separation bubbles. In the case of the suction surface in FC1, the effect of the bubble became more pronounced as the ride height was reduced, especially at 2z/b = 0.09 and 0.49. A typical location of the bubble can be pinpointed by a plateau like region followed by a steep drop, both of which produce an area that does not appear to fit with the natural curvature of the plot. For example, the region bounded by x/c ≈ 0.45 and x/c ≈ 0.6 at 2z/b = 0.09 for h_r/c = 0.153 (Fig. 4.23). When the flow was changed to FC3, the region

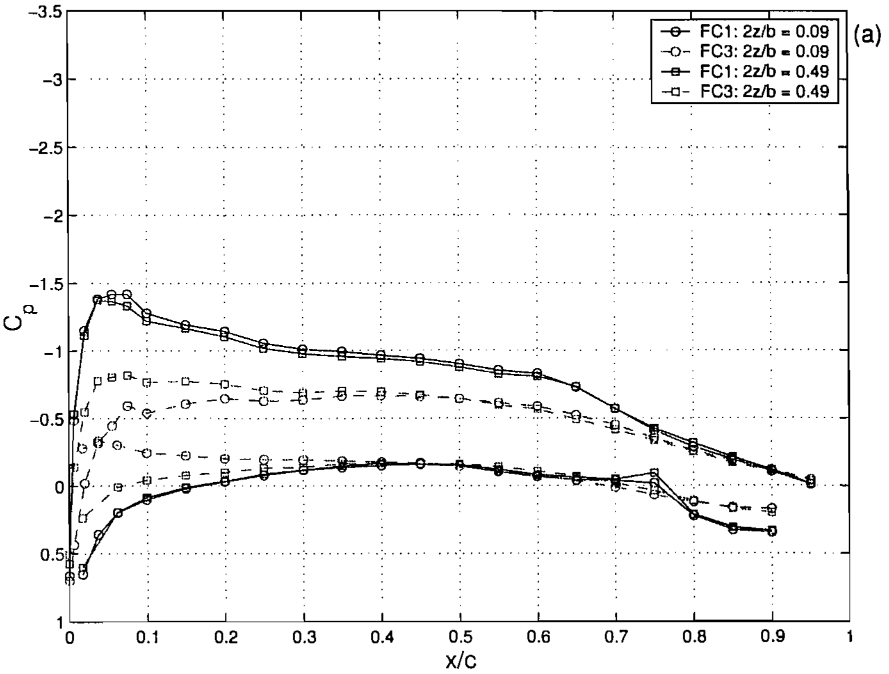

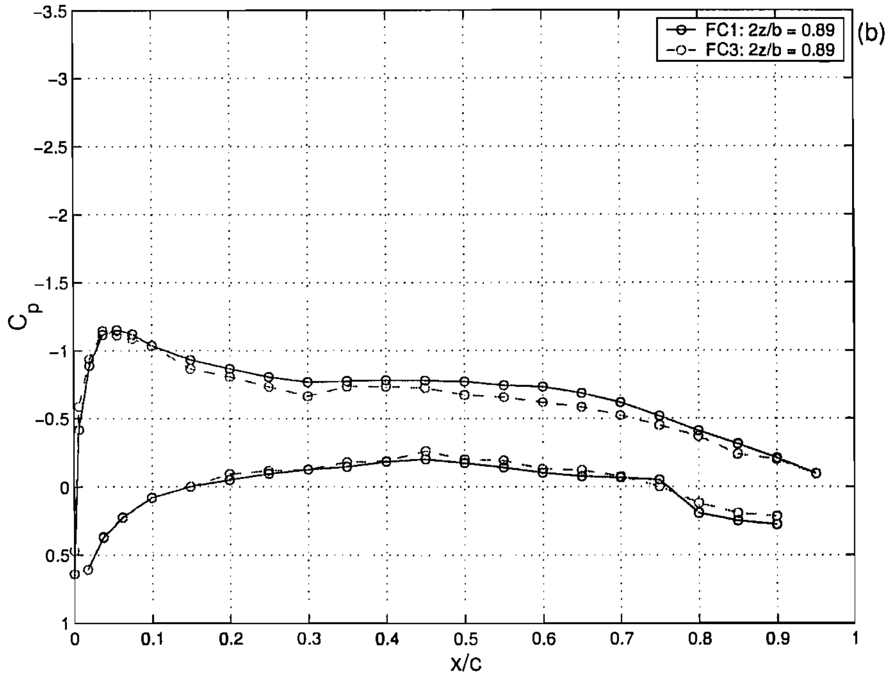

Figure 4.21: The pressure distribution at 2z/b = 0.09, 0.49 (a) and 2z/b = 0.89 (b) for $h_r/c = 0.833$, in FC1 and FC3.

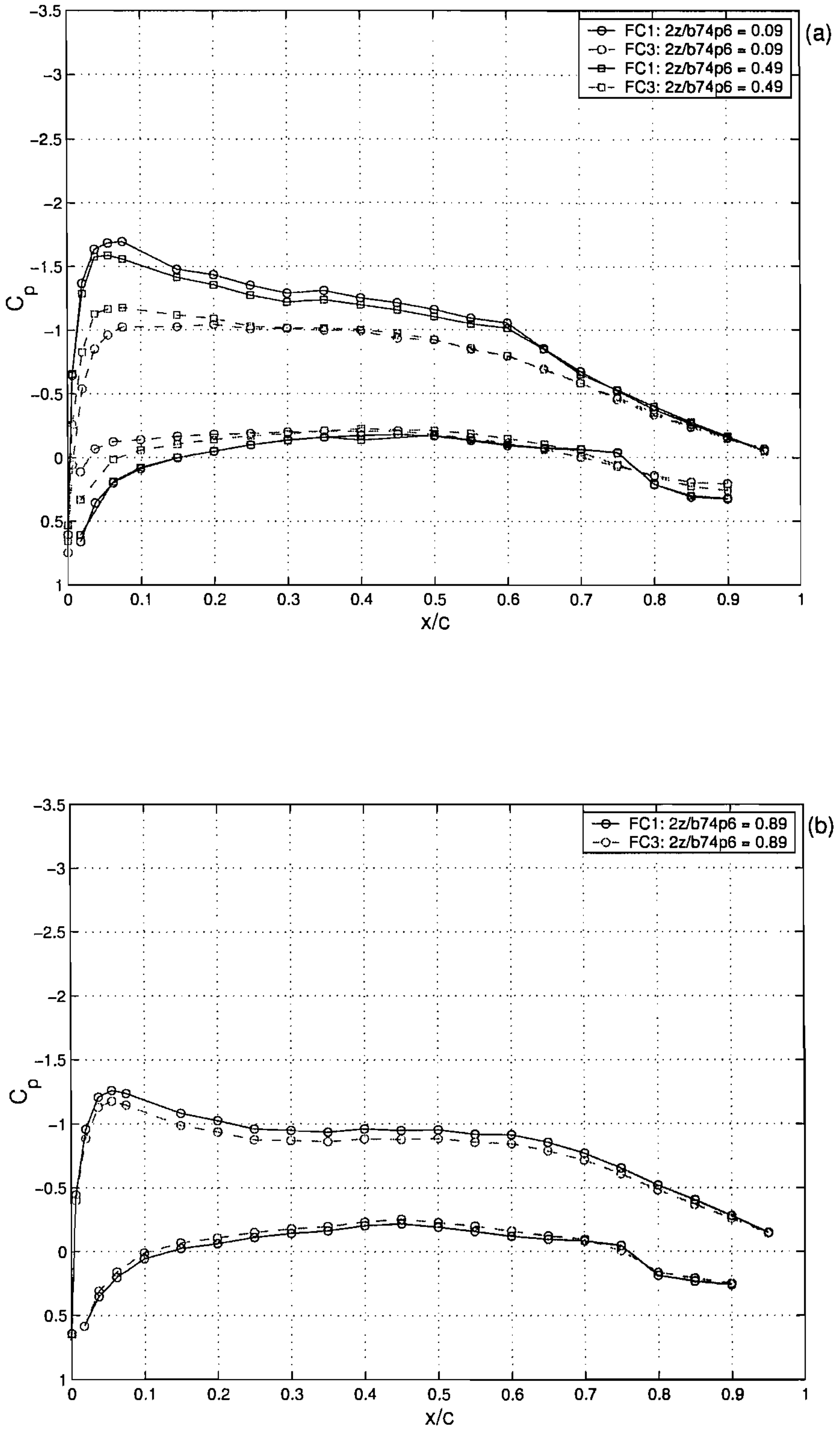

Figure 4.22: The pressure distribution at 2z/b = 0.09, 0.49 (a) and 2z/b = 0.89 (b) for $h_r/c = 0.401$, in FC1 and FC3.

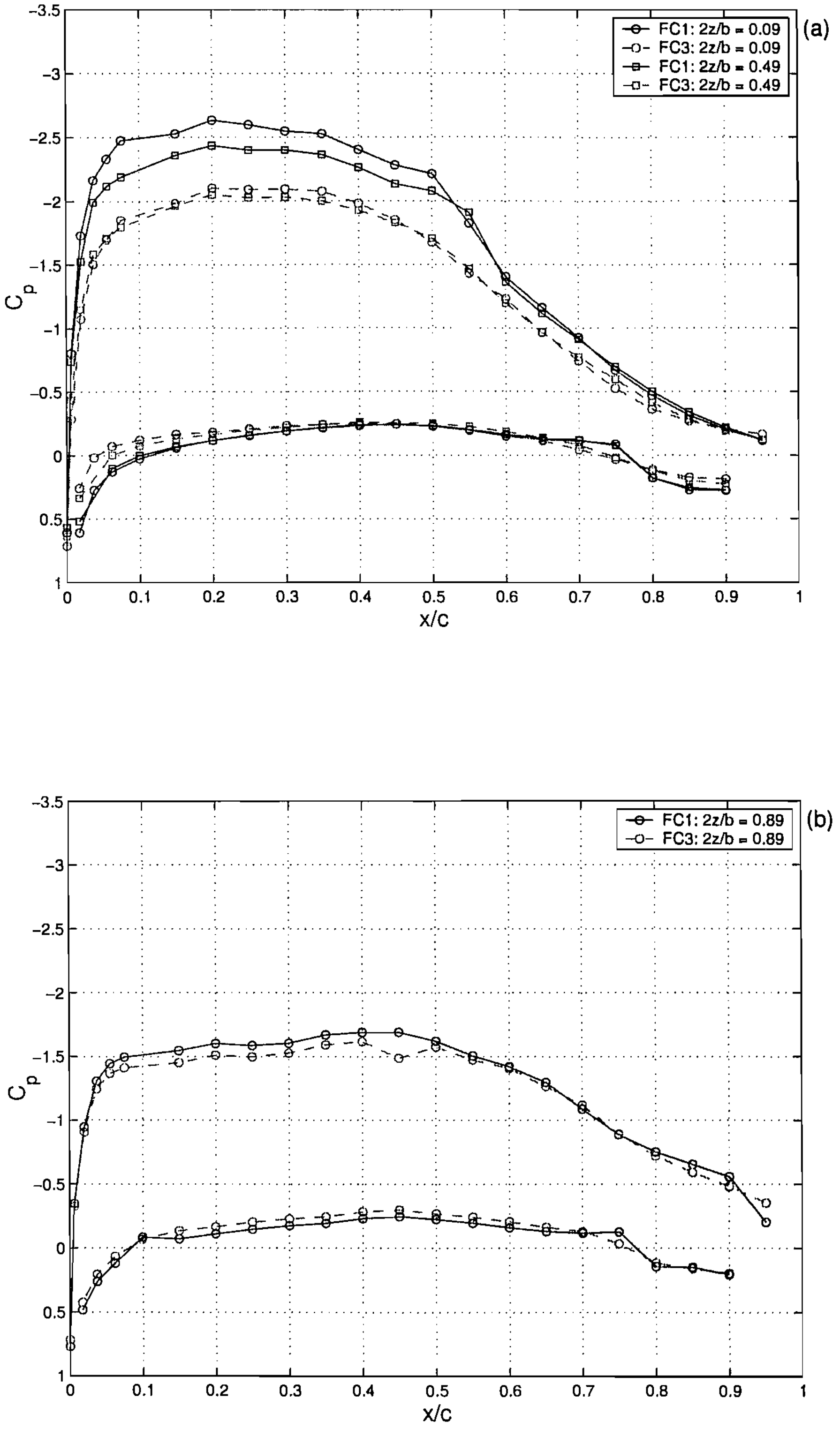

Figure 4.23: The pressure distribution at 2z/b = 0.09, 0.49 (a) and 2z/b = 0.89 (b) for $h_r/c = 0.153$, in FC1 and FC3.

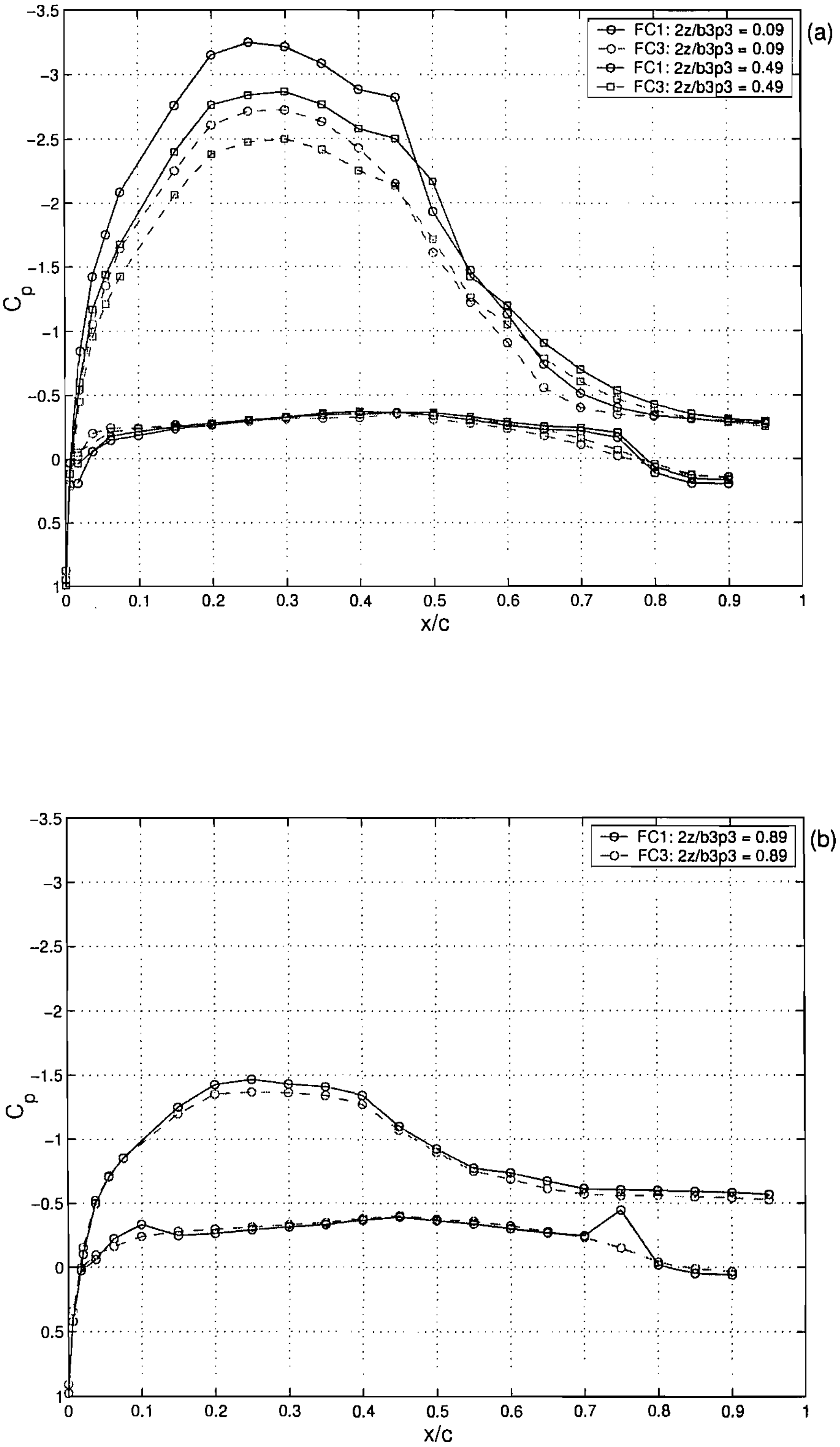

Figure 4.24: The pressure distribution at 2z/b = 0.09, 0.49 (a) and 2z/b = 0.89 (b) for $h_r/c = 0.077$, in FC1 and FC3.

$h_r/c = 0.833$			
	2z/b = 0.09	2z/b = 0.49	2z/b = 0.89
C_l: FC1	0.779	0.750	0.648
C_l: FC3	0.361	0.472	0.572
$\%\Delta C_l$	53.7	37.1	11.7
$h_r/c = 0.401$			
C_l: FC1	0.956	0.916	0.766
C_l: FC3	0.626	0.680	0.679
$\%\Delta C_l$	34.5	25.8	11.4
$h_r/c = 0.153$			
C_l: FC1	1.54	1.45	1.14
C_l: FC3	1.17	1.17	1.05
$\%\Delta C_l$	24.0	19.3	7.89
$h_r/c = 0.077$			
C_l: FC1	1.44	1.30	0.613
C_l: FC3	1.15	1.10	0.580
$\%\Delta C_l$	20.1	15.4	4.89

Table 4.1: Sectional downforce coefficient values for each of the ride heights investigated.

just described, vanished. A similar scenario existed on the pressure surface between x/c $\approx$ 0.65 and x/c $\approx$ 0.75.

A more detailed examination of the same plot can provide the reader with further insight into the aerodynamic changes experienced by the wing. The presence of a separation bubble on the suction surface in FC1 was highlighted by the portion of the curve between x/c $\approx$ 0.45 and x/c $\approx$ 0.6. This implied that the boundary layer prior to the bubble was laminar, while the boundary layer after the bubble was turbulent. Comparison with the corresponding curve for FC3 will show that in general, the greatest difference in C_p between the two plots occurred between x/c $\approx$ 0.01 and x/c $\approx$ 0.6. As the bubble had disappeared in this flow condition, it was evident that the flow prior to that point did not support its existence. That is, the boundary layer was now turbulent. One can then infer that the greatest loss in C_p on the suction surface occurred because of the elimination of an extensive region of laminar flow when progressing from FC1 to FC3. In contrast, between x/c $\approx$ 0.6 and x/c $\approx$ 0.95 the loss in C_p was not as great, suggesting that the turbulent boundary layer was not that sensitive to the change in the characteristics of the oncoming flow.

Figure 4.25 presents the spanwise pressure distribution at the quarter chord of the wing in FC1 and FC3. The data was extracted from the appropriate taps at each spanwise station. The plots for FC1 show the expected shape characteristic of sections towards the centre of the wing producing more lift than sections towards the end. In contrast, in FC3, the shape of the load distribution depended on the ride height of the wing. At $h_r/c = 0.833$ and 0.401, sections towards the middle of the wing produced less lift than sections towards the end. At $h_r/c = 0.153$ and 0.077, the opposite occurred. The phenomena just described only appeared to occur over the first 45% of the wing surface as examination of Figs. 4.21 to 4.24 will show.

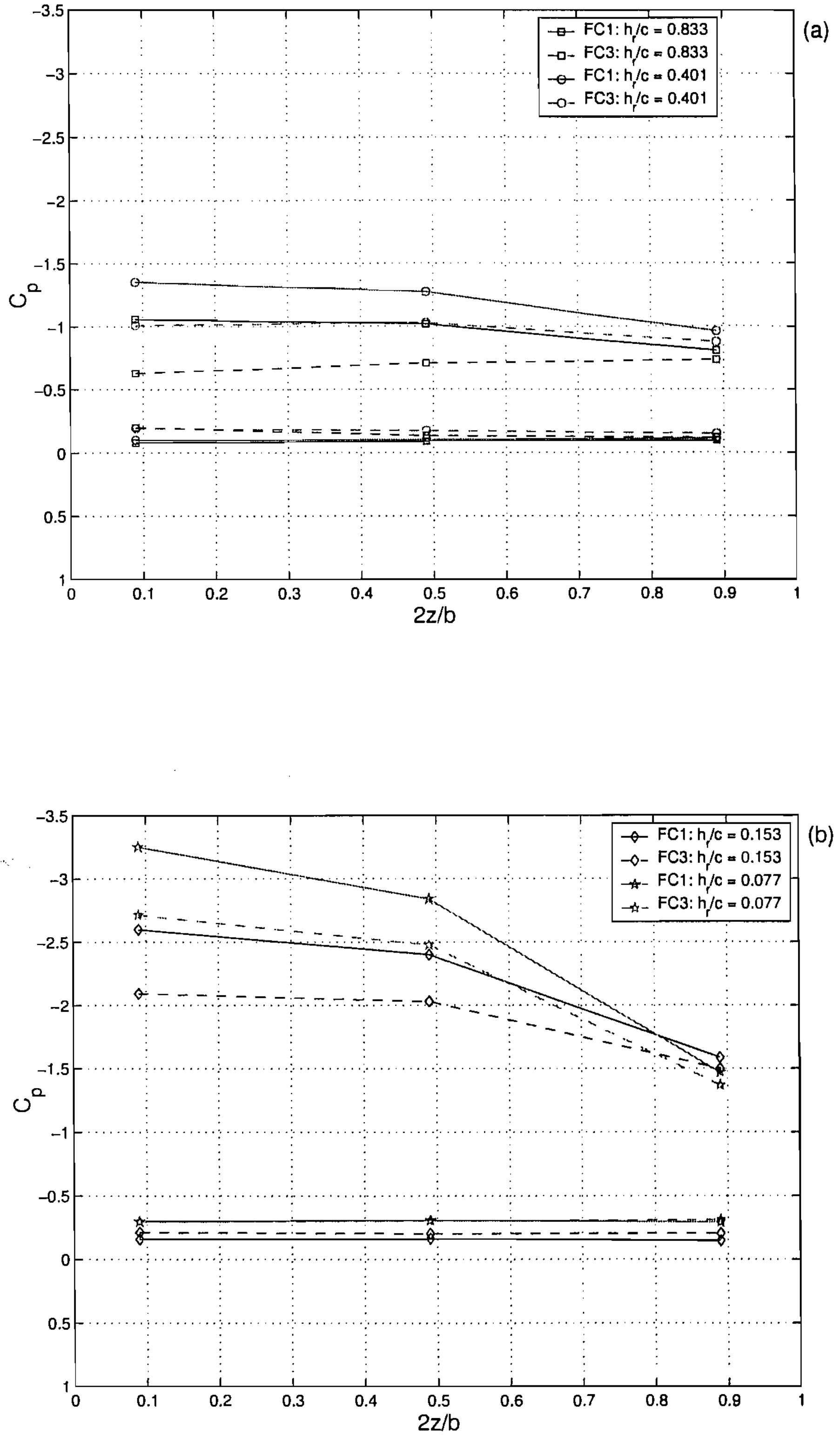

Figure 4.25: The spanwise loading at the wing quarter chord in FC1 and FC3.

4.5 Flow Field

Examination of the flow field in both FC1 and FC3 commences with Fig. 4.26. PIV images of the trailing vortex flow at x/c = 1.5 for $h_r/c = 0.153$ are depicted. The outline of the wing is also included for presentation purposes. Close observation will show that the streamwise vorticity associated with the tip vortex appeared to have been slightly more diffuse in FC3, than it was in FC1. Computations showed that the maximum vorticity decreased slightly from $\frac{\omega c}{U_\infty} = 11.86$ in FC1 to $\frac{\omega c}{U_\infty} = 11.27$ in FC3.

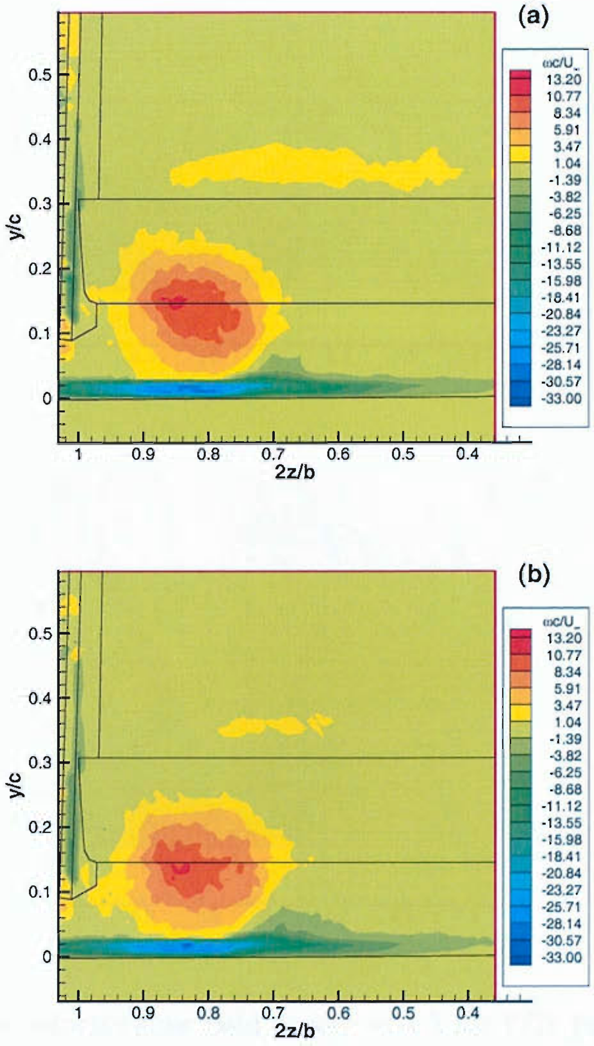

Figure 4.26: Vorticity contours at x/c = 1.5 for FC1 (a) and FC3 (b).

In order to pinpoint the location of the trailing vortex, the velocity vector flow field was extracted via PIV. Two hundred and fifty instantaneous images were averaged to produce the final vector map. Figure 4.27 shows the results for both FC1 and FC3. Examination of the images showed that there was a slight inward horizontal movement of the vortex from 2z/b = 0.82 to 2z/b = 0.81, while changing the flow from FC1 to FC3. This movement was equivalent to approximately 3 mm in physical units.

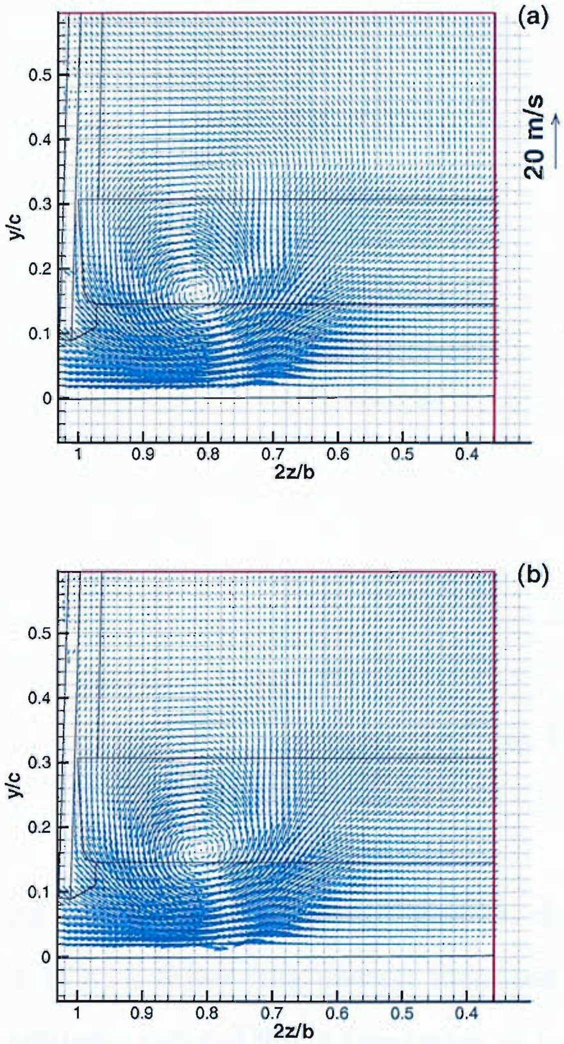

Figure 4.27: The velocity flow field at x/c = 1.5 for FC1 (a) and FC3 (b).

To supplement the previous flow field data, the flow along the tunnel centreline in FC1 and FC3 was examined without the presence of the test wing. This experiment allowed for changes induced by the diffuser bluff body to be documented. Owing to restrictions on the available tunnel time, it was only possible to gather data in the streamwise direction at the corresponding heights indicated.

Figure 4.28 shows profiles of u/U_∞. It can be seen that in FC1, the flow generally remained very close to the freestream value, deviating to a maximum of 1% at some heights. In contrast, the streamwise flow for FC3 showed a deficit of 2% at $h_r/c = 0.08$, increasing to 4% at $h_r/c \approx 0.596$.

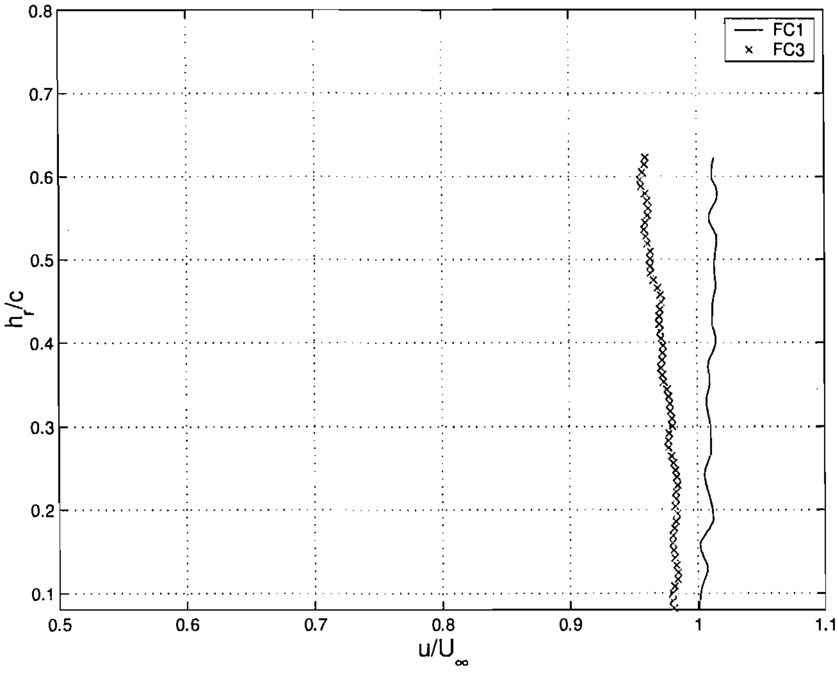

Figure 4.28: Wind tunnel centreline profiles of u/U_∞ in FC1 and FC3, without the presence of the test wing.

Examination of the corresponding upwash, Fig. 4.29, showed that the was none in existence in FC1. In FC3, however, the upwash increased as the distance above the ground increased, attaining a value of 6% of freestream at $h_r/c \approx 0.62$.

Flow field tests were carried out in the larger 3.5 m × 2.5 m facility as it was equipped with a 3-component LDA system. The objective was to provide a more detailed map of the wake of the bluff body. The measurements, which were taken $3l$ downstream of the bluff body, are presented in Figs. 4.30 to 4.33 for clarity. Two components of velocity were

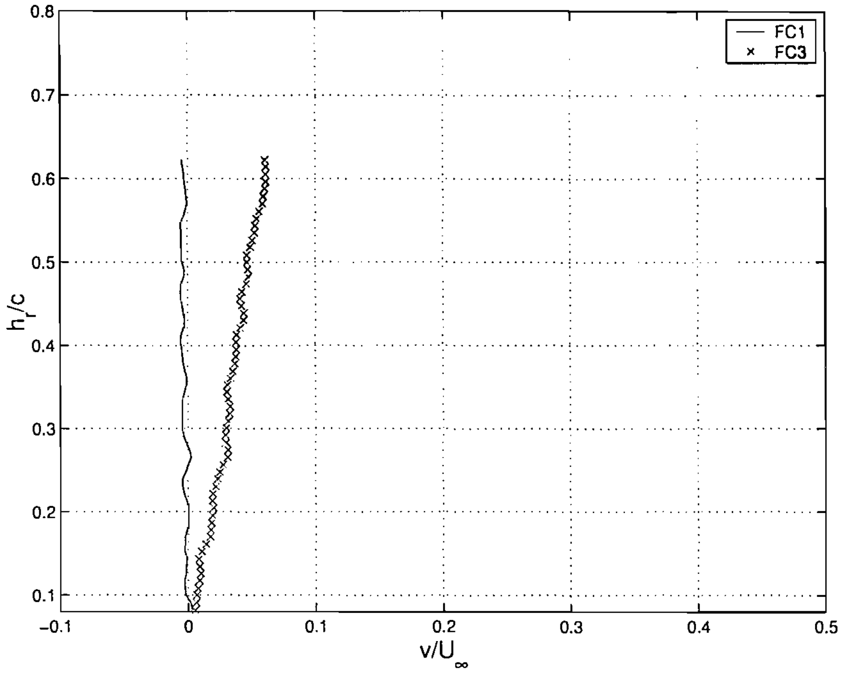

Figure 4.29: Wind tunnel centreline upwash profiles in FC1 and FC3, without the presence of the test wing.

extracted. The plots reveal a variation in the horizontal and vertical velocity components while progressing through the *yz* plane. The wake deficit – highlighted by plots of u/U_∞ – is seen to have been greater at locations closer to the centre of the tunnel (2z/b = 0), than it was at locations closer to where the tips of the wing would have been positioned (2z/b = 1). The plots for v/U_∞ highlight an upwash close to the centre of the tunnel. Away from the centreline, the upwash gradually decreased, transitioning to a downwash by the location of 2z/b = 0.80. At 2z/b = 0, the turbulence intensity was found to vary from a minimum of 4.1% to a maximum of 11%, while at 2z/b = 0.87, it was found to vary from a minimum of 1.4% to a maximum of 7.4%.

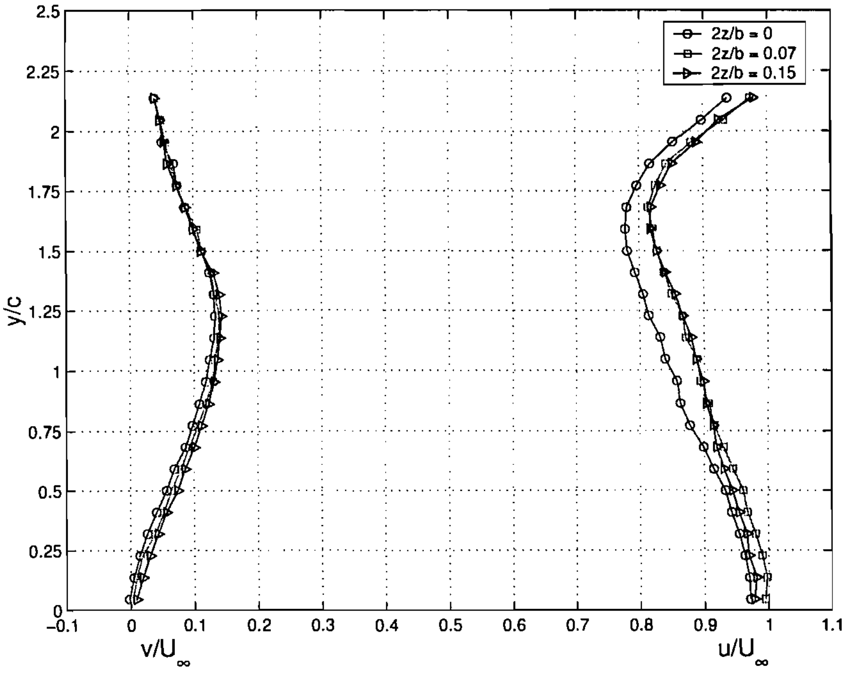

Figure 4.30: Velocity profiles $3l$ downstrem of the diffuser bluff body.

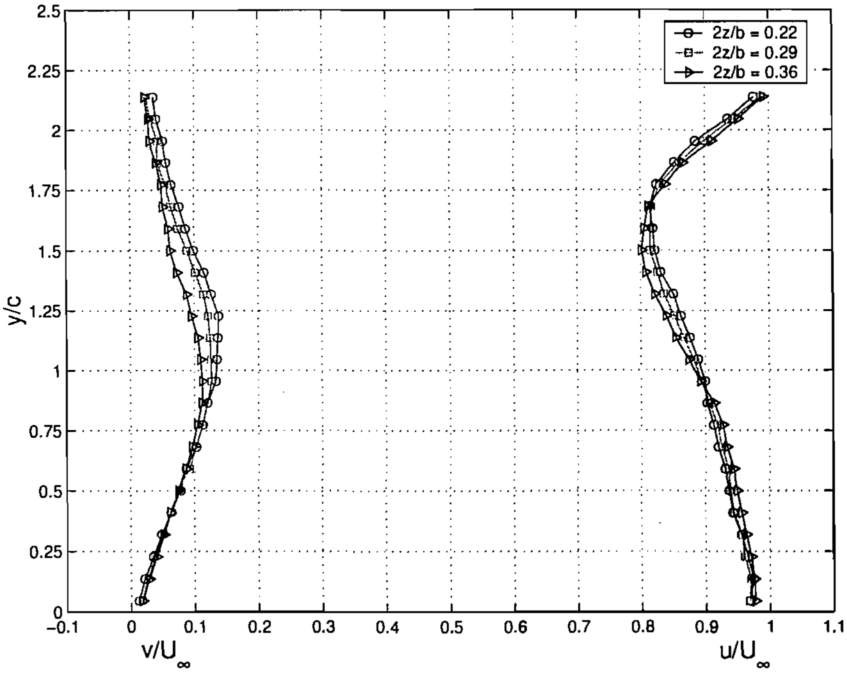

Figure 4.31: Velocity profiles $3l$ downstrem of the diffuser bluff body.

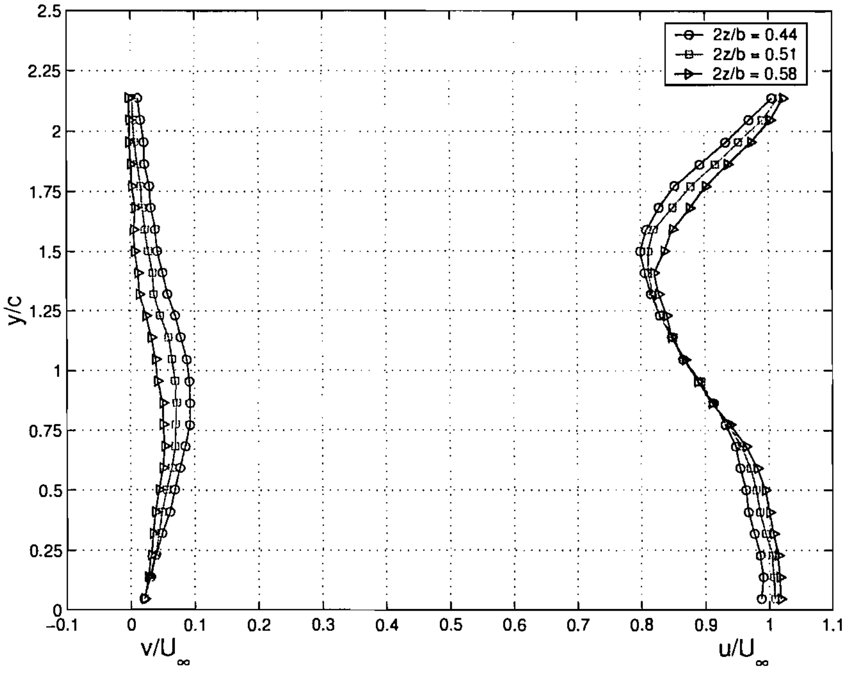

Figure 4.32: Velocity profiles 3*l* downstrem of the diffuser bluff body.

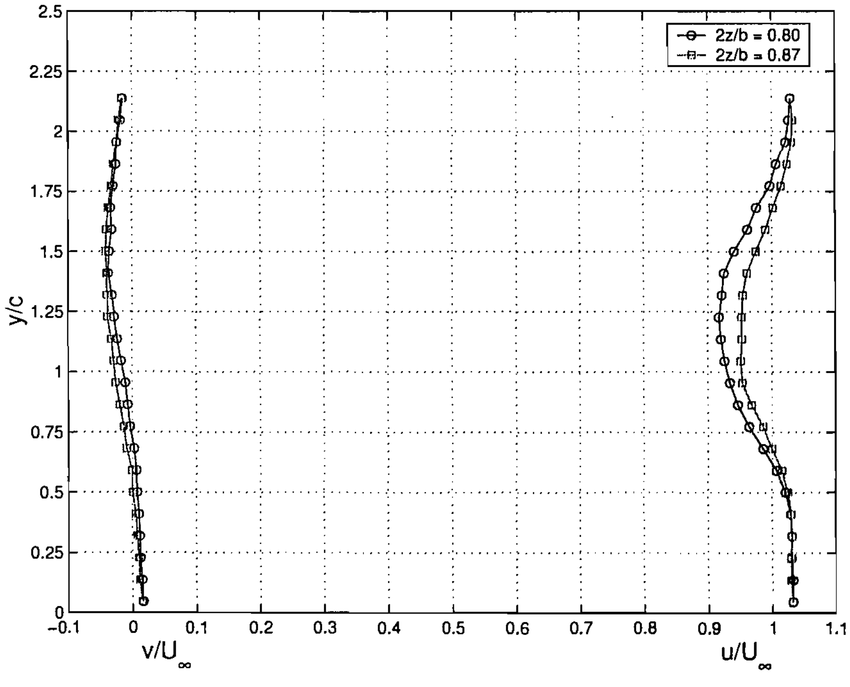

Figure 4.33: Velocity profiles 3*l* downstrem of the diffuser bluff body.

4.6 Discussion

The results of the preceding sections showed that a single element wing in ground effect experienced changes to its aerodynamic characteristics when placed behind upstream bodies that simulated a leading racing car. These changes included a reduction in downforce, an increase in drag and a change in the downstream wake of the wing. It is believed that the changes were caused by the flow that emanated from the upstream body. This flow was significantly more disturbed, when compared to the normal flow of the wind tunnel test section. It also radiated a large amount of audible noise; an indication of the generation of turbulent flow [79].

Confirmation of the physical effects that this flow had on the downstream wing was provided by surface flow visualisation images that highlighted early transition from laminar to turbulent flow in the middle portion of the span. This earlier formation of the turbulent surface flow was significant enough to cause the elimination of the separation bubble from the middle portion of both surfaces of the wing. In contrast, the undisturbed flow conditions indicated that there was laminar to turbulent transition via a laminar separation bubble, visible across the span of both upper and lower surfaces, albeit at different chordwise locations.

Flow visualisation results from the upstream bluff body highlighted the existence of two vortices that in this case, rotated in such a manner as to produce an upwash along their downstream path. Smoke trails then showed that the flow around the rear of the bluff body was sucked in towards a plane that would have coincided with the centreline of the bluff body, wing and tunnel. It was this greatly disturbed, turbulent flow, concentrated in the middle of the tunnel as it progressed downstream, that was responsible for the early transition from laminar to turbulent surface flow on the central portion of the wing only. The flow to both outer edges of the wing may also have been disturbed, however, it may not have been significant enough to promote early transition.

The reduction in downforce of the wing can be explained by the changes in the oncoming flow, which produced lower C_p values and hence lower total forces. These changes included a reduced freestream velocity, an upwash of the flow and increased turbulence. The reduced freestream velocity essentially lowered the Reynolds number at which the wing was operating, while the upwash had the effect of reducing its effective angle of attack. Both scenarios would have contributed to lower pressures. The increased turbulence in the oncoming flow promoted early laminar to turbulent boundary layer transition on the wing. Consequently, the boundary layer was much thicker from the outset, therefore having a greater decambering effect on the profile. That is, the wing effectively lost camber, which would have also resulted in lower pressures.

Also evident from the results was the fact that more downforce was lost at greater ride heights than was the case at lower ride heights. This observation can be linked to the change in upwash with increasing distance above the ground, when in the flow produced by the diffuser. As the wing ride height was increased, it operated in a region of greater upwash which continued to reduce the effective angle of attack at which it operated. At greater ride heights, there was also continued slowing of the oncoming flow, in addition to increased turbulence levels. The end result for the wing was therefore lower overall downforce values.

Comparisons at the spanwise stations at which pressure distributions were recorded indicated that more lift was lost from the midspan of the wing than was the case from the ends of the wing. The midspan was thought to have experienced a greater loss in downforce than the tips because the majority of the disturbed flow appeared to be concentrated in that region, and because that region experienced an upwash, while the tips experienced flow with a neutral to slight downward component of velocity, in addition to a slightly higher freestream velocity.

It also became evident that the force reduction region changed in character in FC3, at very low ride heights. Instead of the expected continual decrease in forces, an unexpected increase occurred after the initial period of decrease. The second region of force increase was unexpected because prior research into ground effect aerodynamics had not discovered its presence, most likely a consequence of the associated tests being carried out in FC1 conditions. Flow visualisation images at the ride heights in question showed that the suction surface experienced massive flow separation in FC1, but that the flow remained attached in FC3. Consequently, the wing was able to generate more downforce at that very low ride height. The ride heights at which the phenomenon occurred, however, may be too low to render the effect of any practical importance.

The results for the variation of the angle of attack at the heights investigated showed the expected result of an increase in the lift curve slope of the wing as the ground was approached. However, what has also now become evident is that the same holds true when the wing is directly behind the upstream bluff body that was used to simulate a leading car.

At the greater ride height of $h_r/c = 0.833$, it was observed that in general, the wing experienced an abrupt stall because of the Reynolds number at which the tests were carried out, Fig. 4.4. This pattern, however, was altered when the bluff body was directly in front of the wing. For this case, the wing experienced a gradual stall, most likely a consequence of early laminar to turbulent boundary layer transition delaying separation.

The increase in the drag of the wing can be explained by the resultant interaction of a number of factors. Firstly, flow visualisation in the disturbed conditions highlighted the fact that the laminar separation bubble was eliminated from the middle portion of both the upper and lower surfaces of the wing. This result in itself should have accounted for a decrease in the drag, however, this decrease may have seemingly been outweighed by drag increments from increased induced drag [80] and the increased extent of the turbulent boundary layer. Increased induced drag resulted from the fact that the wing operated in the upwash of the upstream diffuser bluff body. The increased extent of the turbulent boundary layer would have caused increased skin friction drag.

4.7 Conclusions

The measurements and associated analyses presented in this chapter were aimed a cataloguing the aerodynamic changes that may be experienced by a single element wing when it operated in ground effect, downstream of a leading racing car. The compilation of data from disparate experimental procedures has allowed for the following conclusions to be drawn:

1. In the flow produced by bodies used to simulate a leading racing car, a downstream single element wing in ground effect experienced a decrease in its downforce values and an increase in its drag values.

2. When varying the height of the wing in the dirty air flow, more downforce was lost at greater ride heights than was the case at lower ride heights.

3. When in the dirty air flow, more lift was lost from sections closer to the midspan of the wing than was the case for sections closer to the tip of the wing.

4. When in the dirty air flow, the shape of the spanwise load distribution altered, depending on ride height. At greater ride heights, the load distribution was lower at midspan than it was towards the wing tips. At lower ride heights, the trend reversed.

5. The downstream wing was affected by the upwash flow field of the upstream diffuser bluff body. The presence of an upwash would have resulted in an increase in the induced drag experienced by the wing.

6. The disturbed flow emanating from the upstream body had the ability to significantly alter the surface flow patterns on the downstream wing. The altered characteristics included earlier laminar to turbulent boundary layer transition, and the elimination of laminar separation bubbles.

Chapter 5

The Effect of Changes to the Diffuser Ramp Angle and Bluff Body Height

5.1 Introduction

This chapter presents the aerodynamic changes experienced by the test wing, on modification of the original configuration of the diffuser bluff body. The modifications included changes to the angle of the diffuser ramp, changes to the height of the diffuser bluff body and changes to its lateral position. Force measurements and flow field data were obtained for the series of tests outlined.

5.2 Forces

Figure 5.1 presents the downforce coefficients experienced by the test wing as the angle of the diffuser ramp was varied from 16.7 deg to 10 deg, then to 5 deg. For comparison, the results from FC1 are also shown. It can be stated that for this dataset, the effect of changing the ramp angle depended on the height at which the downstream wing was positioned. In FC3, above $h_r/c \approx 0.28$, the wing generated the most downforce behind the 5 deg ramp diffuser, while it generated the least downforce behind the 16.7 deg ramp diffuser. Below $h_r/c \approx 0.28$, the wing generated the most downforce behind the 16.7 deg ramp diffuser. Also, below this height, both the 10 and 5 deg ramp diffusers seemed to induce comparable levels of wing downforce, except in the region of $h_r/c \approx 0.1$, where the curve for the 10 deg ramp was lowest.

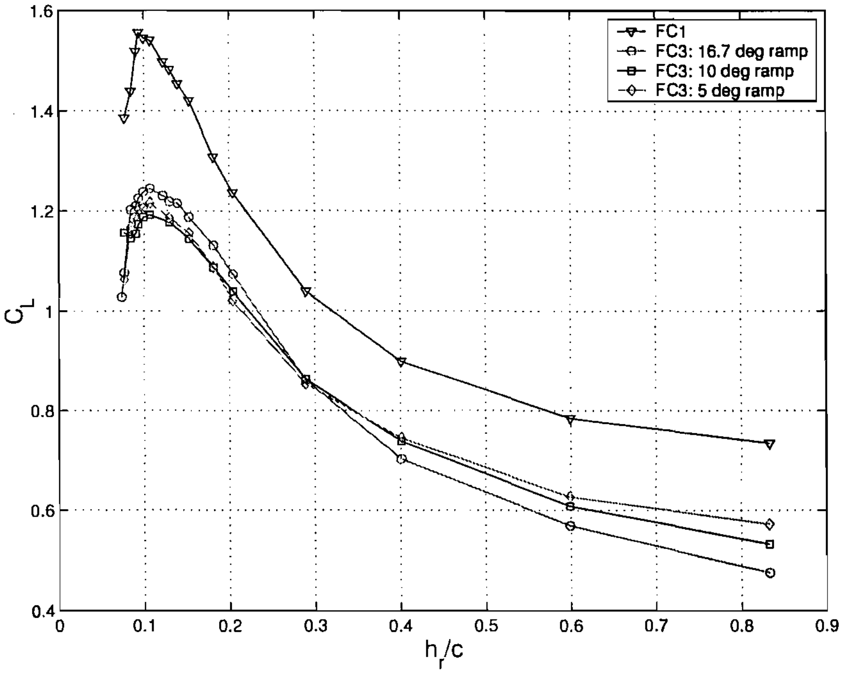

Figure 5.1: The wing downforce coefficients, for the diffuser ramp angles of 16.7, 10 and 5 deg.

The drag coefficients are presented in Fig. 5.2. In general, it can be seen that at all ramp angles, the wing experienced more drag in FC3 than it did in FC1. More specifically, the data for FC3 suggested that there was no particular trend with regard to the dependence of drag on the ramp angle. However, for the majority of ride heights investigated, the 5 deg ramp diffuser seemed to produce the lowest wing drag values.

Examination of the wing lift to drag ratios indicated a clear trend, Fig. 5.3. Between $h_r/c \approx 0.83$ and $h_r/c \approx 0.18$, decreasing the diffuser ramp angle increased the lift to drag ratio of the downstream wing. Below $h_r/c \approx 0.18$, the curves criss-crossed randomly.

Measurements were also taken as the height of the diffuser bluff body was decreased from its original position of $h_r/d = 0.3$. It must be noted, that according to Ref. [50], the diffuser was operating in the maximum downforce region of its own downforce curve. Reducing its height above the ground from $h_r/d = 0.3$ to $h_r/d = 0.2$ therefore corre-

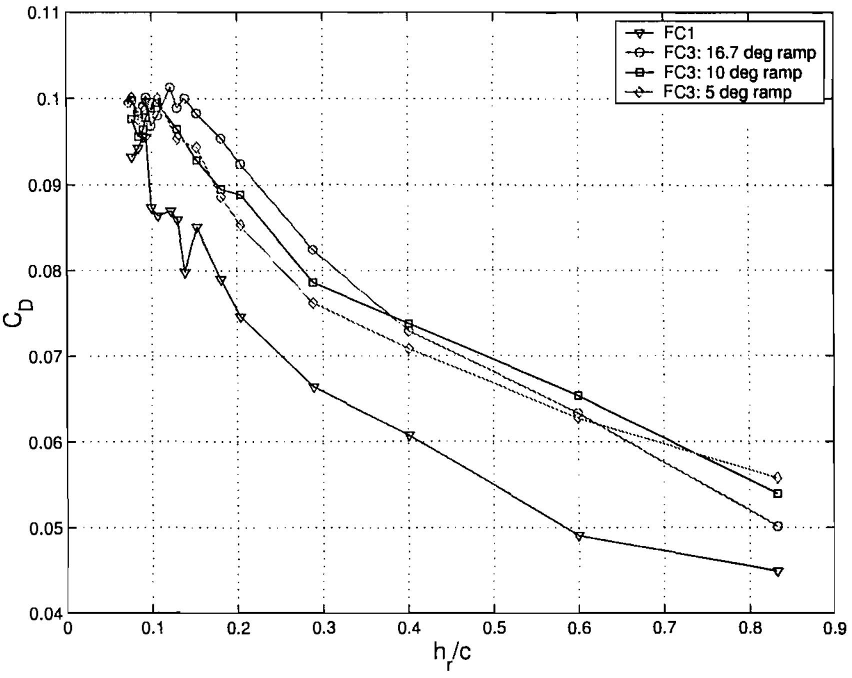

Figure 5.2: The wing drag coefficients, for the diffuser ramp angles of 16.7, 10 and 5 deg.

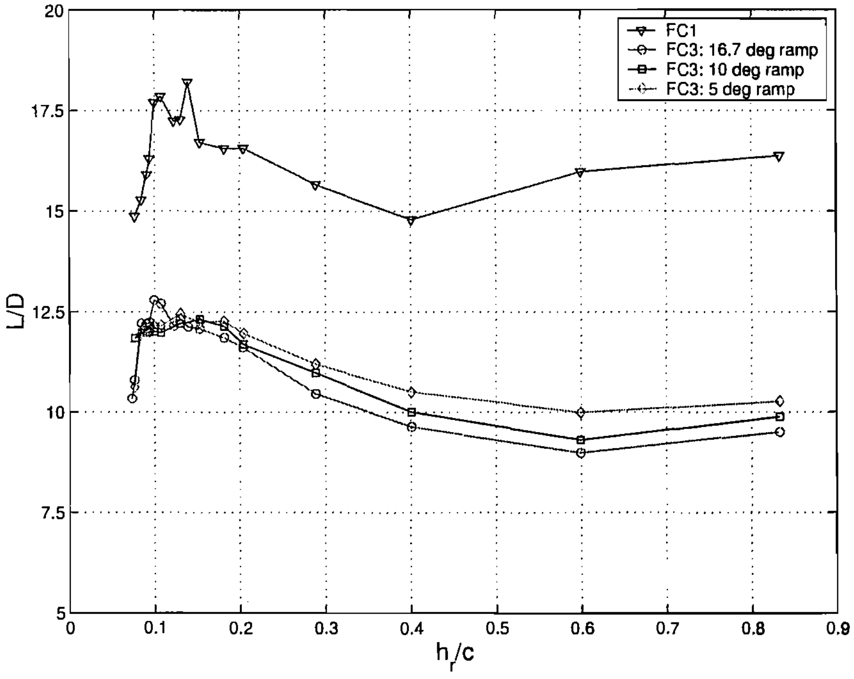

Figure 5.3: The wing lift to drag ratios, for the diffuser ramp angles of 16.7, 10 and 5 deg.

sponded to shifting its operating point from maximum downforce to the region of the force reduction phenomenon. This change implied that there may have been different flow regimes at each height extreme, and possibly some state of transition between them. The results of the height variation therefore have to be considered within these bounds.

Figure 5.4 presents the wing downforce coefficients while varying the height of the diffuser bluff body. As can be seen, the plots for the two greatest diffuser ride heights are fairly close. The plot for diffuser $h_r/d = 0.2$, however, shows significantly less downforce at lower ride heights when compared to diffuser $h_r/d = 0.25$ and diffuser $h_r/d = 0.3$. For example, there was a 2.1% decrease in the maximum downforce between diffuser $h_r/d = 0.3$ and diffuser $h_r/d = 0.25$, and a further 5.5% decrease between diffuser $h_r/d = 0.25$ and diffuser $h_r/d = 0.2$.

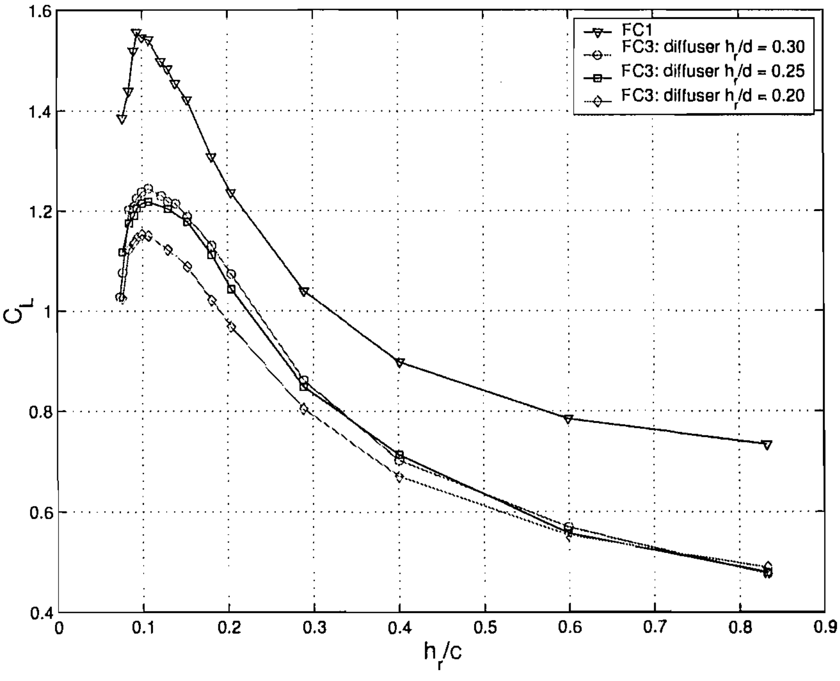

Figure 5.4: The test wing downforce coefficients, while varying the diffuser height above the ground.

The corresponding drag curves are shown in Fig. 5.5. Firstly, it must be stated that the curve for diffuser $h_r/d = 0.25$ appeared to show an apparent anomaly above $h_r/c = 0.4$. This may indicate a possible error or an unexplained flow feature. The reader should note, however, that the whole series of data was gathered at the same time, and that it was not possible to identify the hypothetical anomaly at that specific moment since post-processing entailed a very lengthy procedure. Additionally, owing to the constraints on the availability of wind tunnel time, it was not possible to perform a second test to assess this anomaly. In general, the plots in the figure show that the diffuser conditions produced more drag than FC1. A more specific comparison between diffuser $h_r/d = 0.3$ and diffuser $h_r/d = 0.2$ showed that the former produced more drag than the latter.

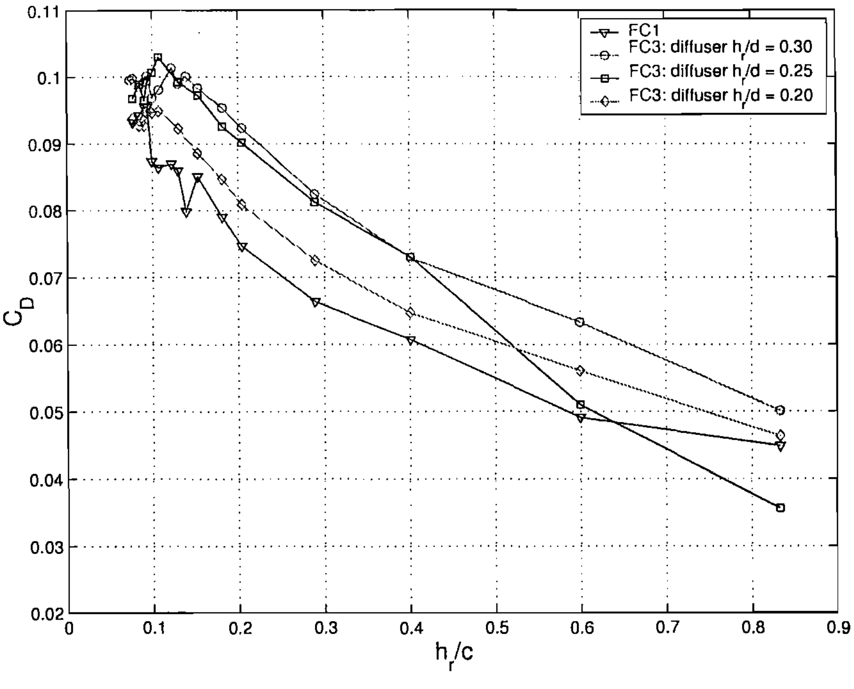

Figure 5.5: The test wing drag coefficients, while varying the diffuser height above the ground.

The lift to drag ratios are shown in Fig. 5.6. It can be seen that in the diffuser conditions, the wing experienced a deterioration in its efficiency when compared to FC1. Comparing diffuser $h_r/d = 0.3$ and diffuser $h_r/d = 0.2$ will show that the latter produced more efficient operating conditions than the former.

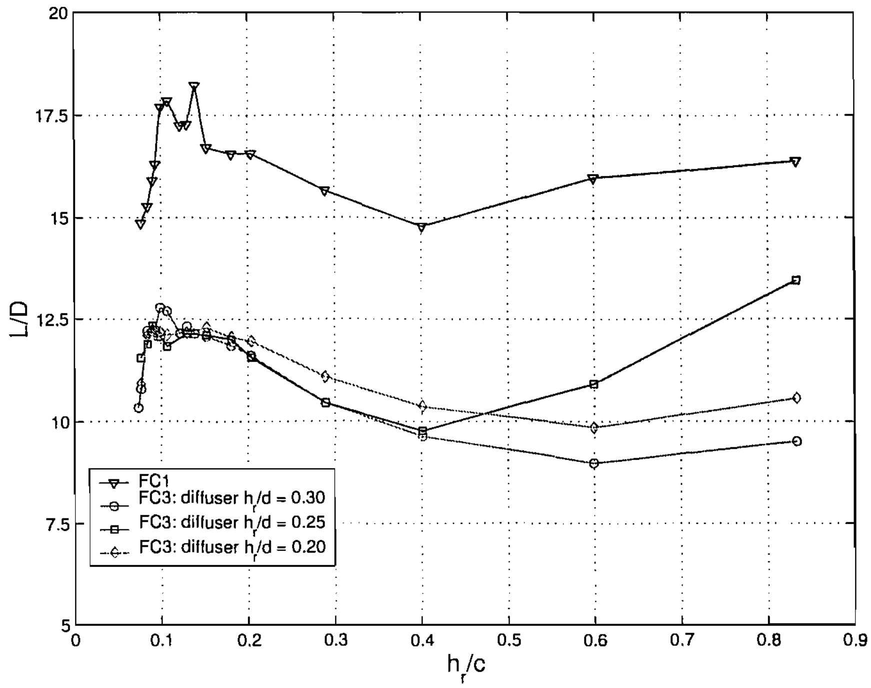

Figure 5.6: The test wing lift to drag ratios, while varying the diffuser height above the ground.

5.3 Flow Field

Images of the streamwise vorticity at x/c = 1.5 are depicted in Fig. 5.7. The 3-D outline of the wing in the background is shown for presentation purposes. Also included is the ground plane at the image location. Observation of the figure will show that when compared to FC1, there was no particular discernable difference in the size of the area that highlighted the presence of the trailing vortex. It can also be seen that there was a reduction in the band of vorticity that highlighted the presence of the wake of the wing.

The corresponding maximum vorticity values, which were extracted from the images, are outlined in Table 5.1. As the diffuser angle progressed from high to low, the maximum wing related vorticity was seen to occur in the flow emanating from the 10 deg ramp. This value, 12.36, was even greater than that associated with FC1, 11.86. Both the 16.7 deg and 5 deg ramp diffusers produced wing related vorticities that were less than FC1.

The associated velocity vector flow fields are plotted in Fig. 5.8. The vectors were

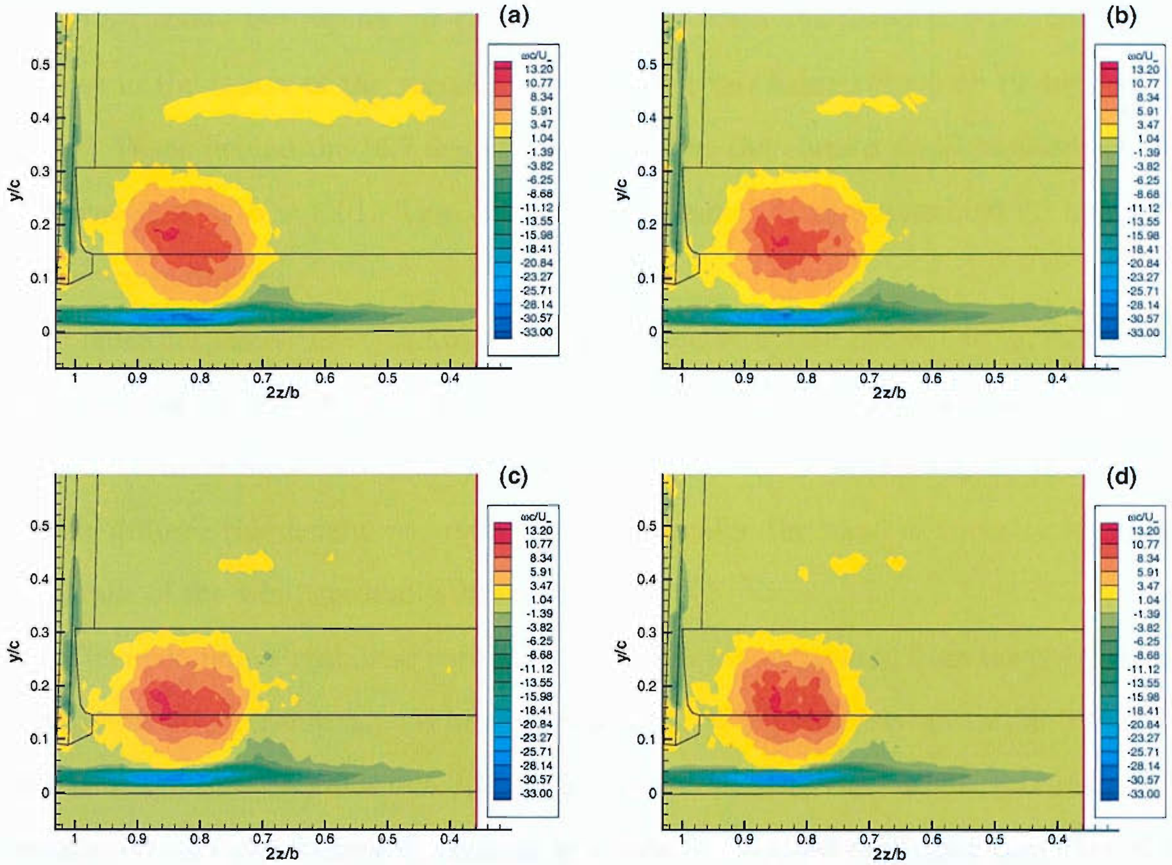

Figure 5.7: Vorticity contours at x/c = 1.5 while varying the diffuser angle of attack. FC1 (a), 16.7 deg diffuser (b), 10 deg diffuser (c), 5 deg diffuser (d).

Diffuser	$\frac{\omega c}{U_\infty}$
None	11.86
16.7 deg	11.27
10 deg	12.36
5 deg	11.68

Table 5.1: Maximum normalised streamwise vorticity values at x/c = 1.5, while varying the upstream diffuser angle.

obtained by averaging two hundred and fifty instantaneous images at the same position. After averaging, the centres of the vortices were estimated from post-processing software. Table 5.2 shows the results. It can be seen that when compared to FC1, there was no change in the centre of the vortex when the wing was behind the 5 or 10 deg ramp diffusers. When behind the 16.7 deg diffuser, however, there was a slight inboard horizontal movement of 2z/b = 0.01. This change corresponded to an approximate 3 mm shift in metric coordinates.

Figure 5.9 shows the streamwise vorticity associated with the test wing, while varying the height of the upstream diffuser. A visual comparison with FC1 will show that the region of vorticity highlighting the presence of the tip vortex became slightly more compact as the diffuser ride height was reduced. Additionally, the band of vorticity highlighting the wake of the wing gradually disappeared.

The maximum streamwise vorticity values that were extracted from the previous figure are presented in Table 5.3. When compared to FC1, there was an initial 5% decrease when in the flow of diffuser $h_r/d = 0.3$. As the diffuser ride height was reduced, the maximum vorticity increased, peaking at a value that was 11% higher that that of FC1.

The wing vector flow field associated with the changing of the diffuser height is displayed in Fig. 5.10, while the corresponding vortex centres are outlined in Table 5.4. When compared to FC1, the most significant movement of the vortex occurred when the wing was behind diffuser $h_r/d = 0.20$. There was an outward horizontal translation of 2z/b = 0.02, which equated to approximately 6 mm in metric units. There was also a downward movement of y/c = 0.01, which equated to approximately 2 mm.

Flow field data downstream of the test wing was also taken with the bluff body moved laterally to a position of 2z/b = 1. In Fig. 5.11 the streamwise vorticity contour plot obtained is compared to that of FC1. It can be seen that the wake of the wing was more clearly highlighted and that the region of vorticity highlighting the tip vortex was more compact. The maximum normalised vorticity value increased from 11.86 in FC1 to 13.10 for the offset case. Also more prominent in the latter was the vorticity generated from

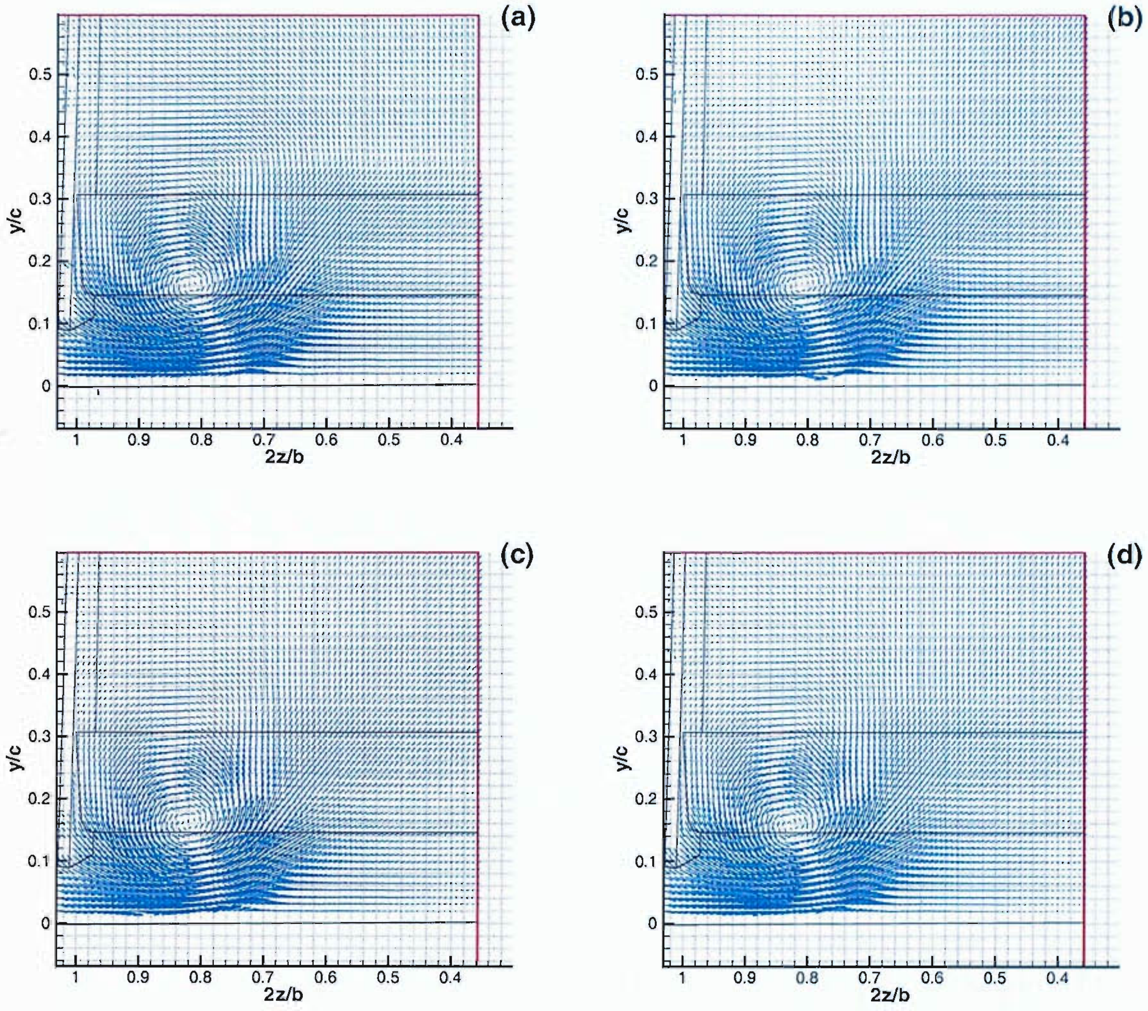

Figure 5.8: The velocity flow field at x/c = 1.5 while varying the diffuser angle of attack. FC1 (a), 16.7 deg diffuser (b), 10 deg diffuser (c), 5 deg diffuser (d).

Diffuser	2z/b	y/c
None	0.82	0.16
16.7 deg	0.81	0.16
10 deg	0.82	0.16
5 deg	0.82	0.16

Table 5.2: Approximate vortex centres at x/c = 1.5, while varying the upstream diffuser angle.

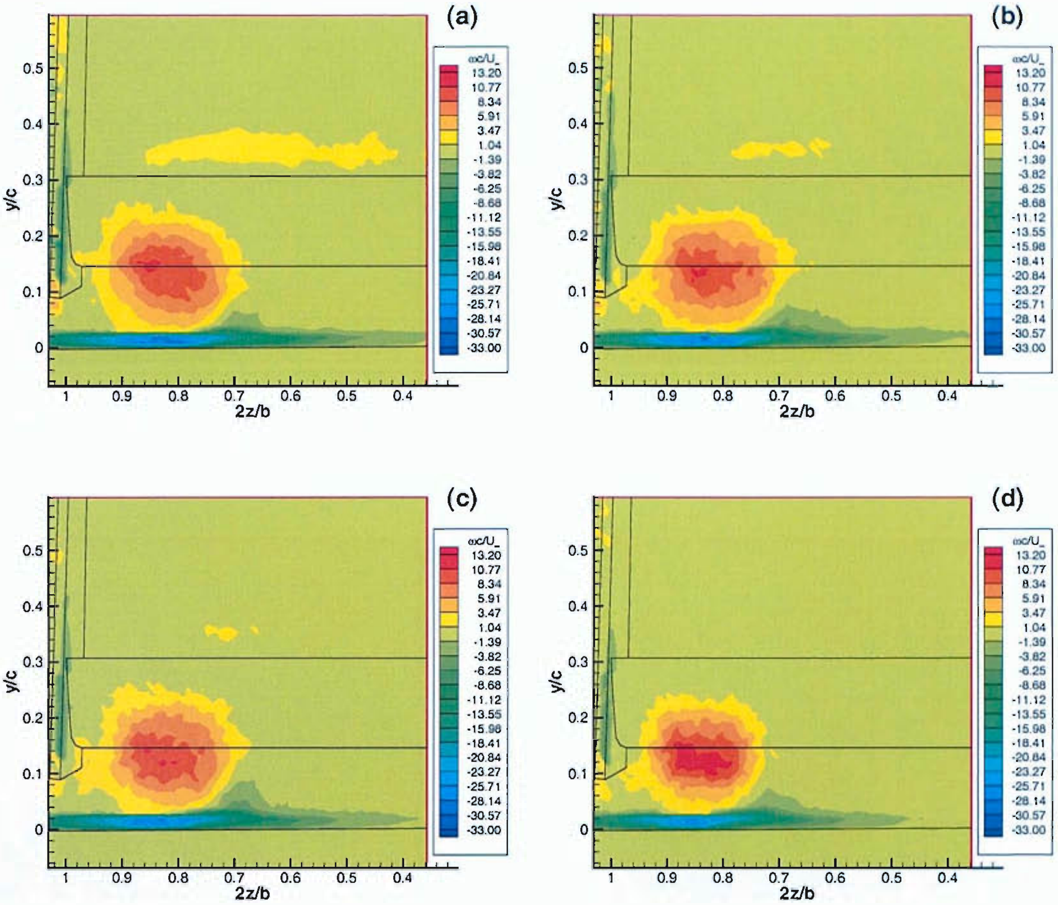

Figure 5.9: Vorticity contours at x/c = 1.5 while varying the diffuser height. FC1 (a), diffuser $h_r/d = 0.30$ (b), diffuser $h_r/d = 0.25$ (c), diffuser $h_r/d = 0.20$ (d).

Diffuser	$\frac{\omega c}{U_\infty}$
None	11.86
$h_r/d = 0.30$	11.27
$h_r/d = 0.25$	11.44
$h_r/d = 0.20$	13.21

Table 5.3: Maximum normalised streamwise vorticity values at x/c = 1.5, while varying the upstream diffuser height.

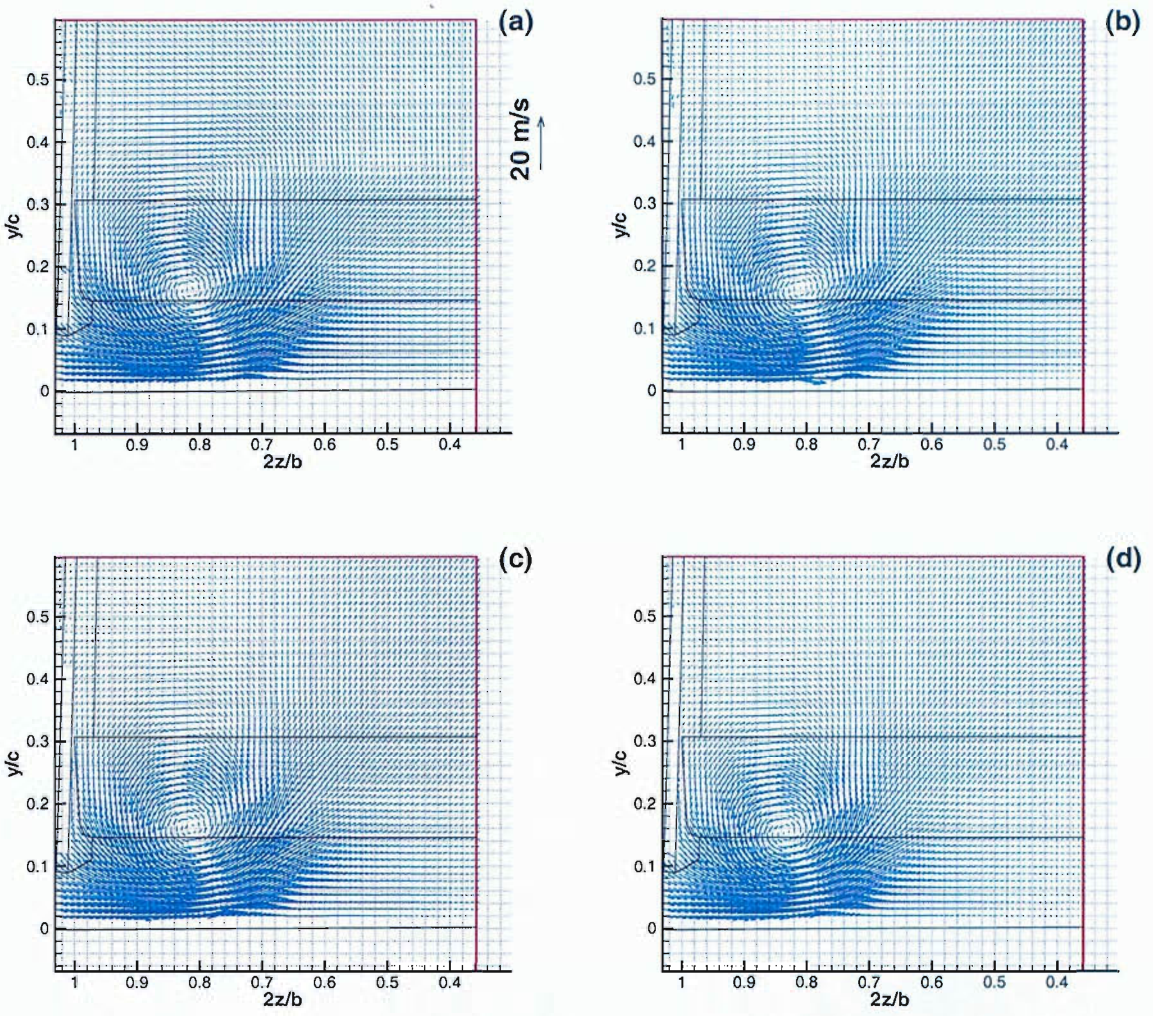

Figure 5.10: The velocity flow field at x/c = 1.5 while varying the diffuser height. FC1 (a), diffuser $h_r/d = 0.30$ (b), diffuser $h_r/d = 0.25$ (c), diffuser $h_r/d = 0.20$ (d).

Diffuser	2z/b	y/c
None	0.82	0.16
$h_r/d = 0.30$	0.81	0.16
$h_r/d = 0.25$	0.81	0.16
$h_r/d = 0.20$	0.84	0.15

Table 5.4: Approximate vortex centres at x/c = 1.5, while varying the upstream diffuser height.

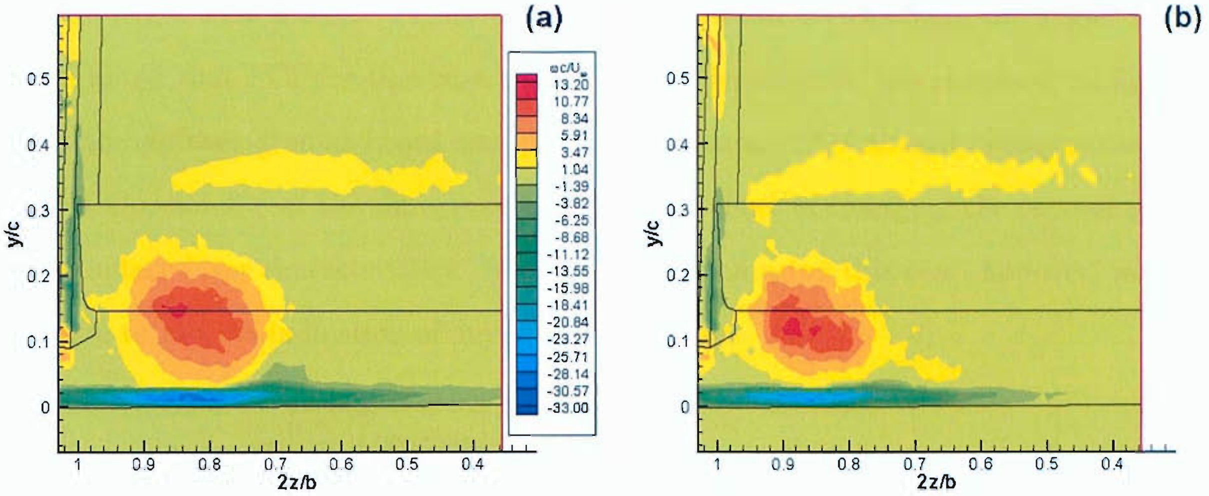

Figure 5.11: Vorticity contours at x/c = 1.5 after moving the diffuser laterally away (2z/b = 1) from the test wing. (a) FC1, (b) 2z/b = 1.

the shear in the wake of the wing. The vector flow field plots highlight a change in the centre of the vortex, Fig. 5.12. There was an outboard horizontal shift of 2z/b = 0.04, which equated to a movement of 11 mm in metric units. There was also a downward vertical movement of y/c = 0.01, which equated to approximately 2 mm in metric units.

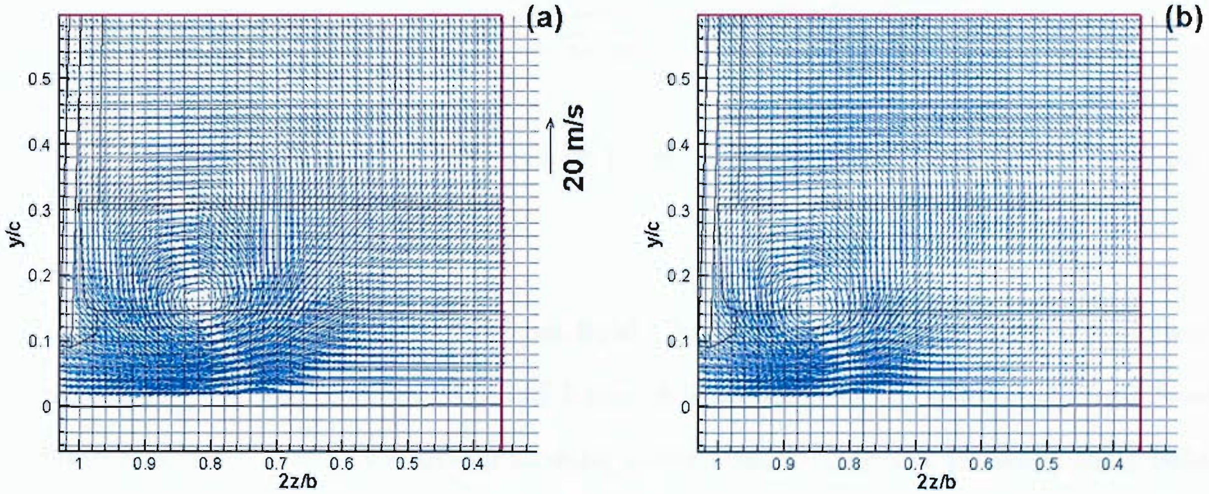

Figure 5.12: The velocity vector flow field at x/c = 1.5 after moving the diffuser laterally away (2z/b = 1) from the test wing. (a) FC1, (b) 2z/b = 1.

Velocity profiles in the wake of the wing were extracted from the PIV data. The intention was to shed light on the change in the wake properties as the diffuser angle and height were altered. Figure 5.13 shows the results for changing the angle. It should be noted that FC1 for this case was slightly different from the standard configuration, as the diffuser ground board was present upstream. This altered configuration, which was unavoidable at the time, may have had the effect of changing the oncoming ground boundary layer characteristics. A wake comparison using this case, however, would still serve to give an indication of any ensuing changes.

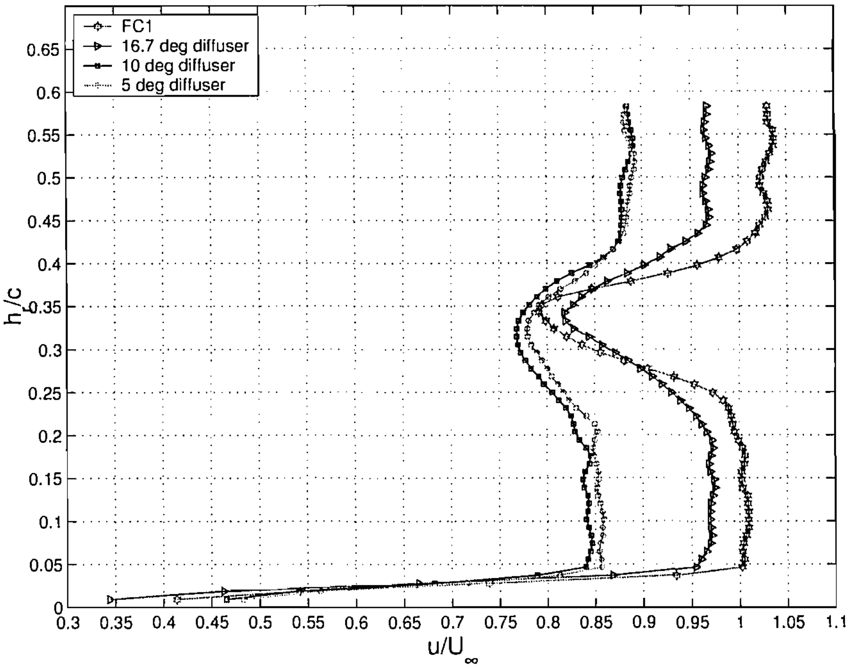

Figure 5.13: Velocity profiles at $x/c = 1.6$ in the wake of the wing, while varying the upstream diffuser ramp angle.

As can be seen in the figure, the fluid transporting the wake downstream became slower when behind the diffuser bluff body. Additionally, as the ramp angle was lowered from 16.7 deg, there was a further slowing of the flow. In fact, the 10 deg diffuser induced the slowest moving fluid in the wake. This was followed by flow from the 5 deg diffuser, then by flow from the 16.7 deg diffuser. The general shape of the wake also appeared to change as the angle of the ramp was altered. Both the 5 and 10 deg diffusers induced a U like shape at the measurement location in the wing wake, while the 16.7 deg diffuser induced a V like shape. The V like shape of the latter more closely resembled the shape of the FC1 wake measured in this dataset, albeit of different thickness and depth.

Some of the profiles showed fluctuations at the point at which the wake joined the transporting fluid. As a consequence, it was not possible to accurately identify the thickness of the wake. This discrepancy prevented a thorough comparison of wake thickness from being made, while varying the diffuser ramp angle. Closer scrutiny of the plots, however, would seem to suggest that there was a slight lowering of the height at which the top boundary of the wake joined the transporting fluid, as the flow changed from FC1 to that produced by the 16.7 deg diffuser, then to those produced by the 10 and 5 deg diffusers.

The approximate maximum wake deficits relative to the transporting fluid are summarised in Table 5.5. The values were computed by taking an average relative to the top and bottom boundaries of the wake. The data highlighted an apparent decrease in the deficit as the flow progressed from FC1 to that produced by the 16.7 deg diffuser, then to the flow produced by the 10 and 5 deg diffusers.

Diffuser	Max wing wake deficit
None	0.23
16.7 deg	0.15
10 deg	0.10
5 deg	0.10

Table 5.5: The maximum wing wake deficits relative to the transporting fluid, while varying the upstream diffuser ramp angle.

Further profiles were extracted at the same measurement location while varying the ride height of the diffuser. The dataset is presented in Fig. 5.14. Again, the gradual slowing of the wake of the wing can be seen; this time as the ride height was reduced. In general, the wake itself maintained a V like shape in all cases, despite spreading via the lower boundary. The spreading increased as the ride height was reduced. For example, the approximate wing wake thickness induced by diffuser $h_r/d = 0.3$ was 55 mm, while that induced by diffuser $h_r/d = 0.2$ was 66 mm.

The approximate maximum wake deficits for each case are listed in Table 5.6. It can

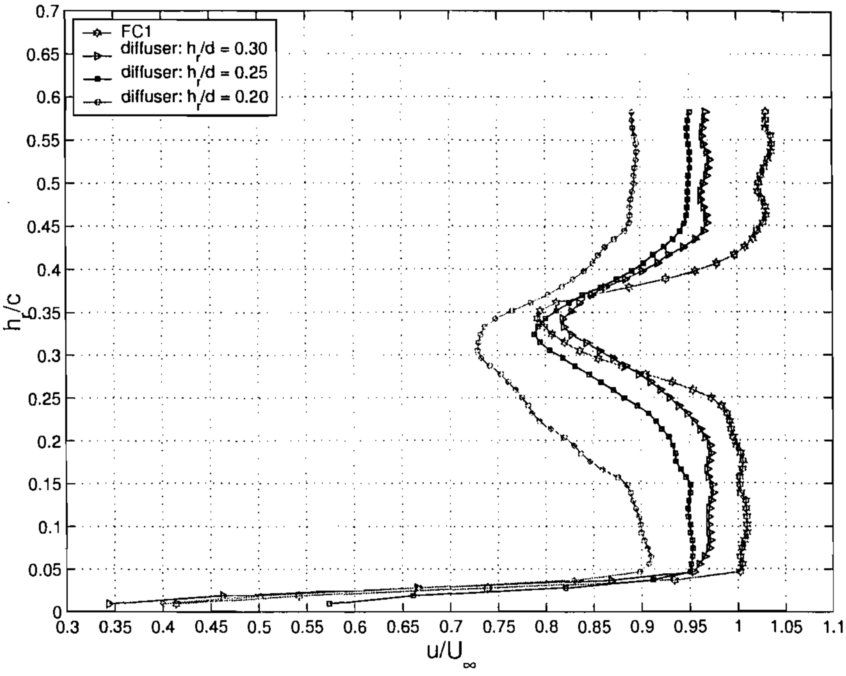

Figure 5.14: Velocity profiles at $x/c = 1.6$ in the wake of the wing, while varying the height of the diffuser.

be seen that this variable can be considered as being constant as the diffuser height was reduced. This constant value was still less than the value for the FC1 case specific to this test.

Diffuser	Max wing wake deficit
None	0.23
$h_r/d = 0.30$	0.15
$h_r/d = 0.25$	0.16
$h_r/d = 0.20$	0.16

Table 5.6: The maximum wing wake deficits relative to the transporting fluid, while varying the upstream diffuser height.

Profiles of u/U$_\infty$ while varying the diffuser angle are shown in Fig. 5.15. The wing was taken out of the tunnel for these tests as the profiles were taken where it would normally be mounted. It can be seen that the streamwise flow was slowed when behind the diffusers. The 5 and 10 deg diffusers induced the greatest deficit; approximately 6% for the 5 deg case, and 6% at $h_r/c = 0.08$ to 8% at $h_r/c = 0.62$ for the 10 deg case. The flow from the 16.7 deg diffuser was previously described in Section 4.5, page 59.

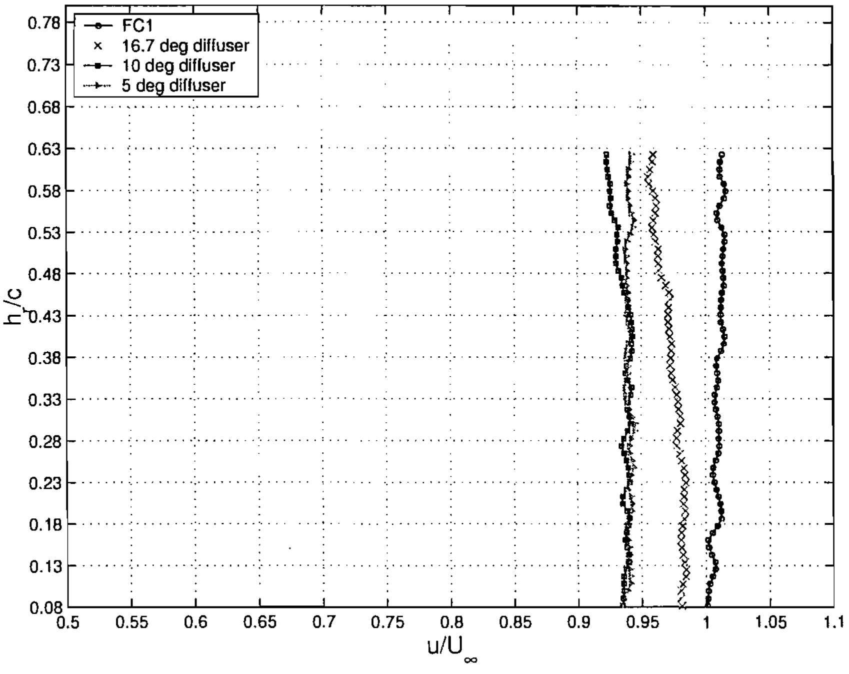

Figure 5.15: Wind tunnel centreline profiles of u/U$_\infty$ at $x/c = 0.5$, while varying the upstream diffuser angle. Test wing not present.

The corresponding upwash profiles are depicted in Fig. 5.16. The plots show that the 5 deg diffuser produced the least amount of upwash, the maximum being 3% at $h_r/c = 0.62$ for this dataset. The greatest amount of upwash was produced by the 16.7 deg diffuser (6%), with the 10 deg diffuser producing slightly less (5.7%).

Profiles of u/U$_\infty$ while varying the diffuser height are plotted in Fig. 5.17. It can be seen that there was a significant slowing of the oncoming flow in the case of diffuser $h_r/d = 0.2$. The deficit increased from 10% at $h_r/c = 0.08$ to 19% at $h_r/c = 0.62$. Diffuser $h_r/d = 0.25$ and diffuser $h_r/d = 0.3$ produced deficits ranging from 2.6% to 5.8% and 1.5% to 4.4% respectively.

Plotting upwash profiles, Fig. 5.18, showed that there was no discernable difference between this characteristic of the flow emanating from diffuser $h_r/d = 0.25$ and diffuser $h_r/d = 0.3$. The upwash for both cases increased from 0.5% at $h_r/c = 0.08$ to a maximum of 6% at $h_r/c = 0.62$. Diffuser $h_r/d = 0.2$ produced an upwash that mostly resembled the

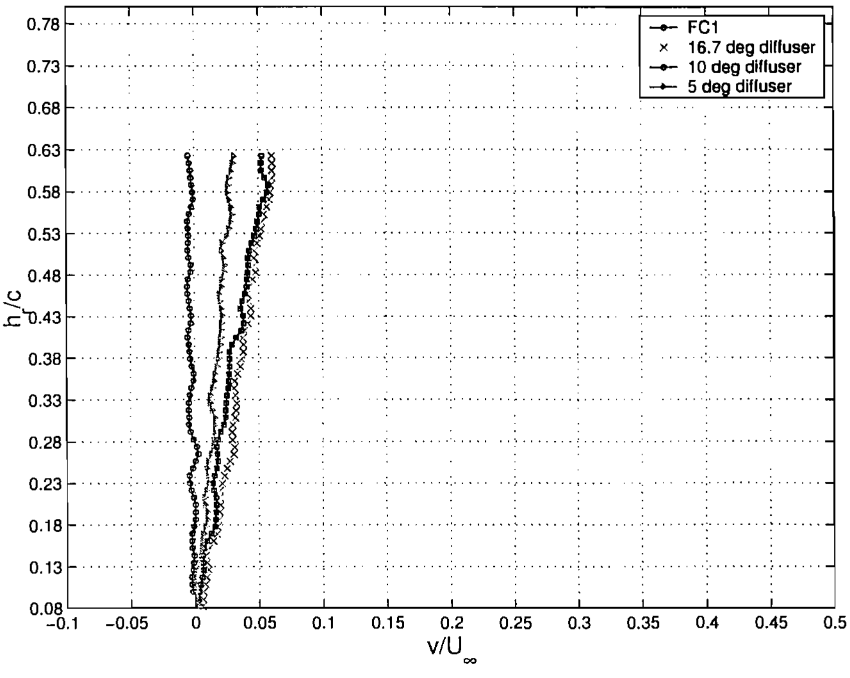

Figure 5.16: Wind tunnel centreline upwash profiles at $x/c = 0.5$, while varying the diffuser angle. Test wing not present.

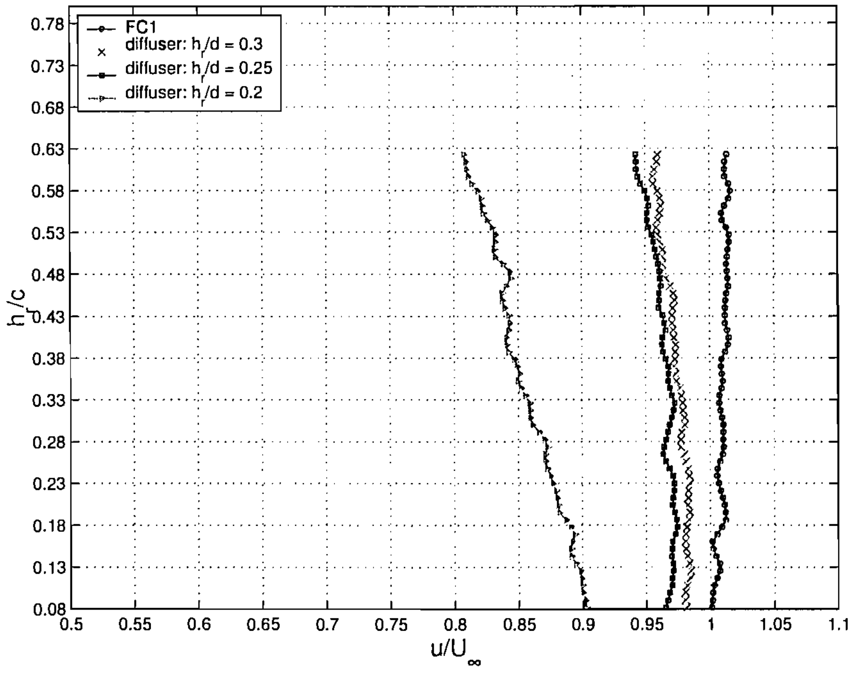

Figure 5.17: Wind tunnel centreline profiles of u/U_∞ at $x/c = 0.5$, while varying the diffuser height. Test wing not present.

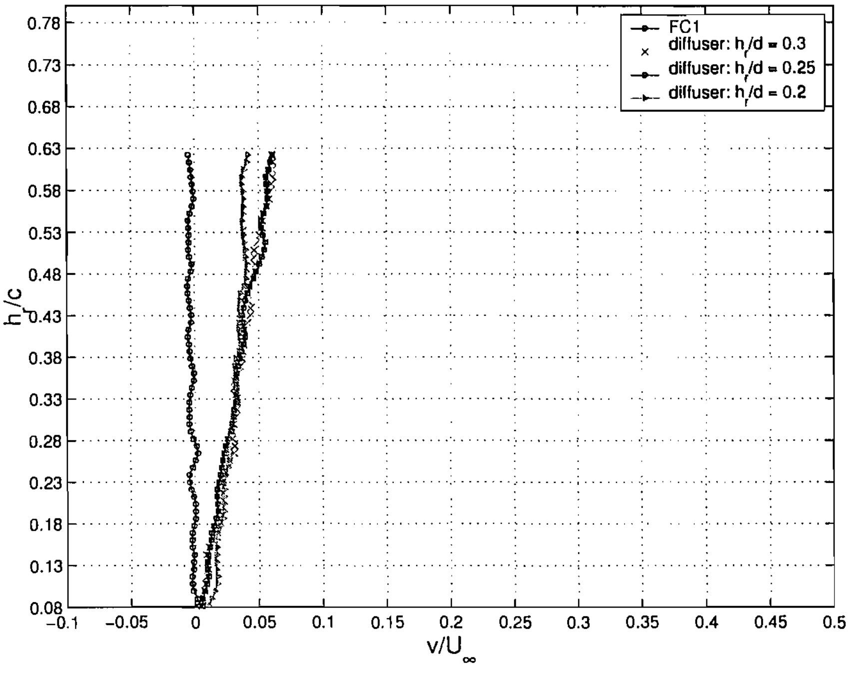

Figure 5.18: Wind tunnel centreline upwash profiles at $x/c = 0.5$, while varying the diffuser height. Test wing not present.

prior cases. The differences were slightly more upwash below $h_r/c \approx 0.2$ and less upwash above $h_r/c = 0.5$. The maximum value attained in this case was 4% at $h_r/c = 0.62$.

5.4 Discussion

An investigation of the streamwise velocity flow field generated by the diffusers showed that the 5 deg ramp diffuser produced the least amount of upwash in the vicinity of the wing, while the 16.7 deg diffuser produced the most, Fig. 5.3. It then became clear that the increase in the wing lift to drag ratio with decreasing diffuser angle was at least in part, caused by a decrease in the amount of upwash generated by diffusers with successively lower ramp angles. The decreased upwash would have contributed to a decrease in the induced drag experienced by the wing, which meant that it would have operated more efficiently at a given ride height.

Observation of the characteristics of the wake of the wing highlighted the fact that the 5 and 10 deg ramps seemed to induce similar flow characteristics, while the 16.7 deg ramp induced a different flow characteristic. This hypothesis is supported by the following evidence.

- It was shown that in the flow of the 5 and 10 deg diffusers, the wake had more of a U like shape, while in the flow of the 16.7 deg diffuser, it had more of a V like shape.
- It was shown that the fluid transporting the wake was significantly slower in the flow of the 5 and 10 deg diffusers, than it was in the flow of the 16.7 deg diffuser.
- It was shown that in the flow of the 5 and 10 deg diffusers, similar wake deficits were induced relative to the transporting fluid, while in the flow of the 16.7 deg diffuser, a larger deficit was induced.

The hypothesis gains further credence, on consideration of the results presented in Refs. [51, 52]. The authors measured the downforce curves for a series of low and high angle diffusers, including a 5, 10 and 17 deg ramp. They then divided the force curves into various regions, depending on the changes to its slope characteristics. In particular, there were regions (a), (b), (c) and (d), as shown in Fig. 5.19. Some of the regions could also be further subdivided, owing to hysteresis effects. Analysis of the diffuser configurations investigated in this research indicated that at the ride height at which the ramp study was performed, the 5 and 10 deg diffusers operated in region (a), while the 16.7 deg diffuser operated in region (b).

The authors further showed that the vortices emanating from the diffusers in region (a) were different from the vortices emanating in region (b). The vortices from region (a) were described as being stable and highly concentrated, with a high axial speed core and a high vorticity level. The turbulence level at the core was described as being low. In contrast, the vortices from region (b) were reported to have increased substantially in size, and to have a low axial speed in their cores. High levels of turbulent stress were also reported to have existed in these vortices.

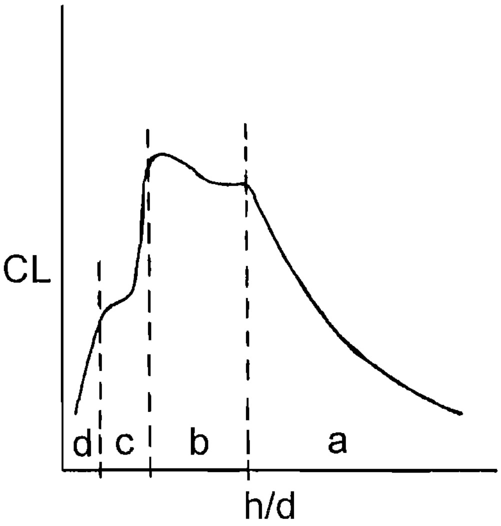

Figure 5.19: A typical downforce vs. ground clearance curve for a generic diffuser in ground effect.

It is plausible then to surmise that the downstream flow fields resulting from the flow of regions (a) and (b) were sufficiently different so as to induce different characteristics in the wake of the downstream wing. That is, the wake of the wing developed in a different manner for each case. The smaller wake deficits in the cases of the 5 and 10 deg diffusers would seem to suggest that these wakes were closer to final dissipation than was the wake associated with the 16.7 deg diffuser or with FC1 for that matter.

When placed in the flow of diffuser $h_r/d = 0.2$, the wing experienced reduced lift, decreased drag and an improved lift to drag ratio, as compared to the flow of diffuser $h_r/d = 0.3$. Examination of the downstream upwash for both cases, however, indicated that in general, the upwash for each configuration was broadly similar, below a ride height of $h_r/c \approx 0.43$. It therefore cannot be assumed that any differences to the aforementioned plots were caused solely by this variable. Further insight was gained from an examination of the streamwise velocity component. Figure 5.17 highlighted a significant slowing in the wake of diffuser $h_r/d = 0.2$. It can therefore be stated that the reduction in the drag, and in the lift of the wing, was induced mainly by the slow moving fluid in the wake of the diffuser. Essentially, the wing was operating at a significantly lower dynamic pressure. Conversely, it can be stated that the downforce of the downstream wing could be increased if it were possible to inject higher momentum streamwise fluid into the wake produced by the upstream body.

In the case of the downstream wing, when compared to FC1, there was a noticeable movement in the position of the trailing vortex, while in the flow of diffuser $h_r/d = 0.2$. This movement was approximately a 6 mm outward translation, in conjunction with an approximate 2 mm downward shift. This change may have consequences for components located downstream of the wing, as their incoming flow may be altered.

5.5 Conclusion

The results presented in this chapter were focused on investigating whether changes made to the body that was used to simulate a leading racing car would affect the aerodynamics of the downstream wing. From a combination of force and flow field measurements, the following conclusions can be drawn:

1. Varying the angle of the ramp of the diffuser had no dramatic effect on the downforce deficit experienced by the downstream wing. Similarly, there was no dramatic effect on the drag experienced by the wing.

2. As the angle of the ramp was decreased, the downstream wing experienced an increase in its lift to drag ratio. The increase in the ratio was at least in part, influenced by the decreasing amount of upwash present in the vicinity of the wing.

3. Varying the angle of the diffuser appeared to influence the development of the downstream wake of the wing. The wake showed similar characteristics when behind the 5 deg and 10 deg diffusers, and different characteristics when behind the 16.7 deg diffuser. By linking the current ramp configurations to previously published results, it was shown that the 5 deg and 10 deg diffusers produced a similar type of vortex flow, while the 16.7 deg diffuser produced a different type of vortex flow.

4. Decreasing the height of the diffuser had the effect of increasing the thickness of the wake of the downstream wing, with the wake deficit remaining approximately constant for each upstream configuration.

Chapter 6

Computational Methodology

6.1 Introduction

In this chapter, the governing equations of fluid flow will be outlined, as they relate to the computational solution of the problem in question. Next, general information on the strategies to be used in grid construction and case solution will be presented, so that the reader may become familiar with the techniques employed in latter chapters.

6.2 Governing Equations

Newtonian fluid motion is governed by the principles of conservation of mass, conservation of momentum and conservation of energy. These principles can be expressed mathematically by the continuity equation, the Navier-Stokes equations and the energy equation [70]. The continuity equation can be expressed as:

$$\frac{\partial \rho}{\partial t} + \nabla \cdot (\rho \mathrm{V}) = 0 \tag{6.1}$$

The Navier-Stokes can be expressed in component form as:

$$\begin{aligned}\frac{\partial(\rho u)}{\partial t}+\nabla\cdot(\rho u\mathrm{V}) &= -\frac{\partial p}{\partial x}+\rho f_x+\frac{\partial}{\partial x}\left(\lambda\nabla\cdot\mathrm{V}+2\mu\frac{\partial u}{\partial x}\right)\\ &+\frac{\partial}{\partial y}\left[\mu\left(\frac{\partial v}{\partial x}+\frac{\partial u}{\partial y}\right)\right]+\frac{\partial}{\partial z}\left[\mu\left(\frac{\partial u}{\partial z}+\frac{\partial w}{\partial x}\right)\right]\end{aligned} \tag{6.2}$$

$$\begin{aligned}\frac{\partial(\rho v)}{\partial t}+\nabla\cdot(\rho v\mathrm{V}) &= -\frac{\partial p}{\partial y}+\rho f_y+\frac{\partial}{\partial y}\left(\lambda\nabla\cdot\mathrm{V}+2\mu\frac{\partial v}{\partial y}\right)\\ &+\frac{\partial}{\partial x}\left[\mu\left(\frac{\partial v}{\partial x}+\frac{\partial u}{\partial y}\right)\right]+\frac{\partial}{\partial z}\left[\mu\left(\frac{\partial w}{\partial y}+\frac{\partial v}{\partial z}\right)\right]\end{aligned} \tag{6.3}$$

$$\begin{aligned}\frac{\partial(\rho w)}{\partial t}+\nabla\cdot(\rho w\mathrm{V}) &= -\frac{\partial p}{\partial z}+\rho f_z+\frac{\partial}{\partial z}\left(\lambda\nabla\cdot\mathrm{V}+2\mu\frac{\partial w}{\partial z}\right)\\ &+\frac{\partial}{\partial x}\left[\mu\left(\frac{\partial u}{\partial z}+\frac{\partial w}{\partial x}\right)\right]+\frac{\partial}{\partial y}\left[\mu\left(\frac{\partial w}{\partial y}+\frac{\partial v}{\partial z}\right)\right]\end{aligned} \tag{6.4}$$

The Energy equation can be expressed as:

$$\begin{aligned}\frac{\partial}{\partial t}\left[\rho\left(e+\frac{V^2}{2}\right)\right]+\nabla\cdot\left[\rho\left(e+\frac{V^2}{2}\right)\mathrm{V}\right] &= \rho\dot{q}+\frac{\partial}{\partial x}\left(k\frac{\partial T}{\partial x}\right)+\frac{\partial}{\partial y}\left(k\frac{\partial T}{\partial y}\right)\\ &+\frac{\partial}{\partial z}\left(k\frac{\partial T}{\partial z}\right)-\frac{\partial up}{\partial x}-\frac{\partial vp}{\partial y}-\frac{\partial wp}{\partial z}+\frac{\partial(u\tau_{xx})}{\partial x}+\frac{\partial(u\tau_{yx})}{\partial y}\\ &+\frac{\partial(u\tau_{zx})}{\partial z}+\frac{\partial(v\tau_{xy})}{\partial x}+\frac{\partial(v\tau_{yy})}{\partial y}+\frac{\partial(v\tau_{zy})}{\partial z}+\frac{\partial(w\tau_{xz})}{\partial x}\\ &+\frac{\partial(w\tau_{yz})}{\partial y}+\frac{\partial(w\tau_{zz})}{\partial z}+\rho\mathrm{f}\cdot\mathrm{V}\end{aligned} \tag{6.5}$$

6.3 Reynolds Averaged Navier-Stokes Equations

Reynolds Averaged Navier-Stokes (RANS) modelling results from performing a time average of the Navier-Stokes equations, in order to account for turbulent flow. To carry out this process, flow field variables are decomposed into a mean and a fluctuating component as depicted in the following:

$$u_i = \bar{u}_i + u_i^{'} \tag{6.6}$$

Substitution of the previous equation into the continuity, momentum and energy equations produces the RANS equations [71]. For continuity, the following is obtained:

$$\frac{\partial \bar{\rho}}{\partial t} + \frac{\partial}{\partial x_j}\left(\bar{\rho}\bar{u}_j + \overline{\rho^{'} u_j^{'}}\right) = 0 \tag{6.7}$$

For the Momentum equations, the following is obtained:

$$\begin{aligned} \frac{\partial}{\partial t}\left(\bar{\rho}\bar{u}_i + \overline{\rho^{'} u_i^{'}}\right) + \frac{\partial}{\partial x_j}\left(\bar{\rho}\bar{u}_i\bar{u}_j + \bar{u}_i\overline{\rho^{'} u_j^{'}}\right) &= -\frac{\partial \bar{p}}{\partial x_i} \\ &+ \frac{\partial}{\partial x_j}\left(\bar{\tau}_{ij} - \bar{u}_j\overline{\rho^{'} u_i^{'}} - \bar{\rho}\overline{u_i^{'}u_j^{'}} - \overline{\rho^{'} u_i^{'}u_j^{'}}\right) \end{aligned} \tag{6.8}$$

where

$$\bar{\tau}_{ij} = \mu\left[\left(\frac{\partial \bar{u}_i}{\partial x_j} + \frac{\partial \bar{u}_j}{\partial x_i}\right) - \frac{2}{3}\delta_{ij}\frac{\partial \bar{u}_k}{\partial x_k}\right] \tag{6.9}$$

For the Energy equation, the following is obtained:

$$\begin{aligned} \frac{\partial}{\partial t}\left(c_p\bar{\rho}\bar{T} + c_p\overline{\rho^{'} T^{'}}\right) + \frac{\partial}{\partial x_j}\left(\bar{\rho}c_p\overline{T}\bar{u}_j + c_p\overline{T}\,\overline{\rho^{'} u_j^{'}}\right) &= \frac{\partial \bar{p}}{\partial t} + \bar{u}_j\frac{\partial \bar{p}}{\partial x_j} + \overline{u_j^{'}\frac{\partial p^{'}}{\partial x_j}} \\ + \frac{\partial}{\partial x_j}\left(k\frac{\partial \overline{T}}{\partial x_j} - \bar{\rho}c_p\overline{T^{'} u_j^{'}} - c_p\overline{\rho^{'} T^{'} u_j^{'}} - \bar{u}_j c_p\overline{\rho^{'} T^{'}}\right) &+ \overline{\Phi} \end{aligned} \tag{6.10}$$

where

$$\overline{\Phi} = \overline{\tau_{ij}\frac{\partial u_i}{\partial x_j}} = \bar{\tau}_{ij}\frac{\partial \bar{u}_i}{\partial x_j} + \overline{\tau'_{ij}\frac{\partial u'_i}{\partial x_j}} \tag{6.11}$$

The preceding time-averaged equations give rise to additional unknowns that can be interpreted as stress gradient and heat flux quantities that are a consequence of turbulent motion. The situation now arises where there are more variables to be solved, than there are equations available. In order to provide a practical solution to this dilemma, turbulence models have been developed.

6.4 Turbulence Modelling

Turbulence models seek to relate the additional stress gradient and heat flux quantities to the mean flow variables. In particular, many modern turbulence models achieve this aim by utilizing a turbulent viscosity hypothesis that was formulated by Boussinesq [72]. The hypothesis relates the Reynolds stresses ($-\rho\overline{u'_i u'_j}$) to the mean rate of strain in the flow through a scalar quantity called the turbulent viscosity, ν_T. The assumption takes the following form:

$$-\rho\overline{u_i u_j} + \frac{2}{3}\rho k \delta_{ij} = \rho\nu_T\left(\frac{\partial \bar{u}_i}{\partial x_j} + \frac{\partial \bar{u}_j}{\partial x_i}\right) \tag{6.12}$$

where k is the turbulent kinetic energy as given in the following :

$$k = \frac{1}{2}\overline{u'_i u'_i} \tag{6.13}$$

Popular turbulence models that incorporate this hypothesis include the Spalart-Allmaras and κ–ϵ models. Other models exist that do not incorporate the Boussinesq hypothesis. Instead, separate transport equations are derived for the Reynolds stresses. This procedure, however, results in additional unknowns that also have to be accounted for. Examples of such models are the Reynolds Stress Model (RSM) and its variants.

6.5 Software and Facilities

The commercial CFD software package used to carry out the numerical investigations was Fluent 6. The software is distributed by worldwide branches of Fluent Inc., headquartered in Lebanon, NH, USA. It is a finite volume based code that allows the governing equations of fluid flow and heat transfer to be solved numerically. Upon achieving a solution, a variety of post-processing tools are then available to extract the relevant data from the problem under investigation.

Fluent has the ability to handle both structured and unstructured grids. The grids were created in Gambit, pre-processing software developed by the suppliers. Gambit allowed for the creation of edge, surface and volume meshes in the domain to be investigated.

The software was run on the university's Beowulf cluster, Iridis. During the period of research, the specifications of the system were as follows [73]:

- 404 processors of different variants in the Intel Pentium family (1GHz PIII, 1.8GHz PIV)
- 192 Gb of memory
- 8.5 Tb of local disk storage
- Fast Ethernet network
- Myrinet network (not used in this research)
- 2.8 Tb on RADIS disk array

Typically, jobs were submitted to a scheduling system that automatically allocated processors and run time depending on the inputs specified by the user. In the case of the meshes needed for the current research, at least 16 processors were needed to obtain a reasonable turn around time.

6.6 Grid Construction

The grids used in this research were usually hybrid in nature. That is to say, they consisted of a combination of rectangular and triangular cells in 2-D or a combination of hexahedral and prismatic cells in 3-D. 3-D hexahedral and prismatic cells were specifically needed (as opposed to tetrahedral cells) because the type of configurations being modelled involved extensive vortex flow that was to be convected downstream. These cell types minimised numerical diffusion, thus providing a better representation of the actual flow conditions.

Before a 3-D mesh was constructed, a sequence of computations was performed in 2-D in order to ensure that the cells to be used in the final grid were efficient enough to capture the important features of the flow. That is, an attempt was made to ensure that the mesh was neither too fine nor too coarse. A mesh that was too fine would take too long to produce a solution, therefore wasting computational resources. On the other hand, a mesh that was too coarse would be inadequate for capturing the important aspects of the flow field. The 2-D mesh was then extruded in the third dimension (spanwise) to form the final 3-D mesh.

6.6.1 Wing Boundary Layer Regions

At all times, the boundary layer regions adjacent to the surface of the wings were modelled with rectangular cells in 2-D and hexahedral cells in 3-D. This approach was taken because it allowed for the cells to be stretched in the direction tangential to the surface of the wing, while at the same time being compressed in the normal direction. As wing boundary layer flow properties vary greater in the normal direction than in the tangential, fewer cells could be used to discretise that particular region, without a loss in overall accuracy.

6.6.2 Estimation of 1^{st} Grid Point

In order to achieve specific y^+ values at wall boundaries, for example on the surface of the wing, a method was needed, for estimating the height of the first cell. Such a method was provided by the software vendor [74], and is of the following form:

$$\frac{\overline{c_f}}{2} \approx 0.0359\, Re_L^{-0.2} \tag{6.14}$$

$$u_\tau \equiv \sqrt{\frac{\tau_w}{\rho}} = U_e\sqrt{\frac{\overline{c_f}}{2}} \tag{6.15}$$

$$y_1 = \frac{\alpha\, \nu}{u_\tau} \tag{6.16}$$

where y_1 is the distance from the wall to the centre of the first cell and α gives the y^+ value that is to be approximated. For example, to achieve a y^+ value of 1, α becomes 1.

$$1^{st} \text{ grid point} = 2(y_1) \tag{6.17}$$

6.7 Solution Overview

For a typical CFD simulation the meshed domain that was created in Gambit was then imported into Fluent. A check of the grid was then carried out to ensure that there were no impending errors. Next the numerical solver to be used was selected. The segregated solver was chosen at all times because it was tuned for incompressible flows and because it allowed the solution to be obtained with minimum memory usage, as the governing equations were solved sequentially.

At this stage, the turbulence model to be used in the analysis was specified. Unless otherwise indicated, the Spalart-Allmaras (SA) model was used as it was found that it was the most efficient for the studies under consideration. For example when using SA, a typical file employing first order differencing schemes would converge in 200 to 300 iterations, while the use of the RNG $\kappa\epsilon$ or $\kappa\omega$ models required 900 to 1100 iterations to converge. Following the selection of the turbulence model, the reference values for calculation of the aerodynamic coefficients were set, and the solution was initialised to commence iterating.

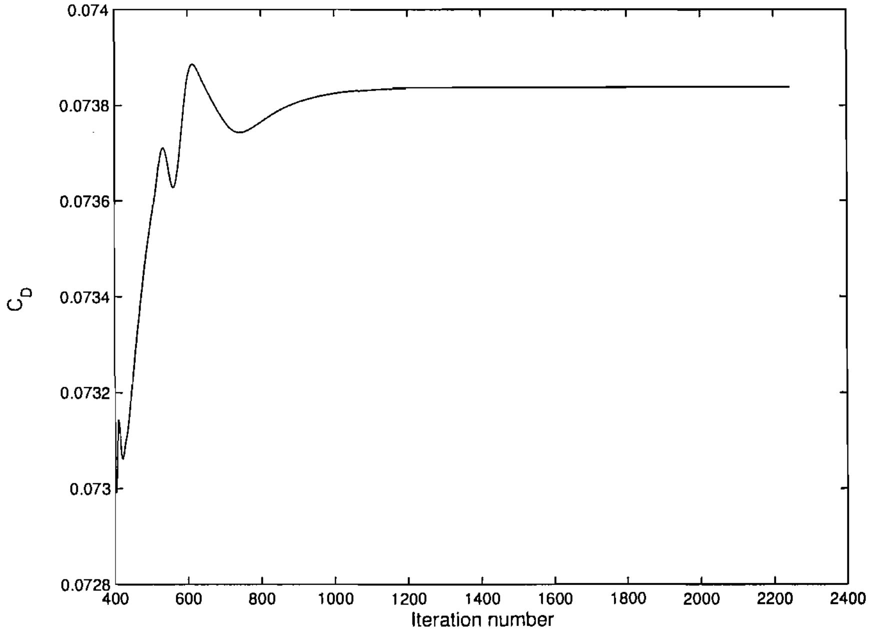

Figure 6.1: A plot showing a typical drag coefficient convergence history.

The iterative procedure commenced with the use of first order differencing schemes. After convergence of the residuals (a drop of 3 orders of magnitude), second order differencing was specified. The files were run to completion with this latter scheme. Convergence was ensured by monitoring the lift and drag coefficients generated from the surfaces under consideration. As shown in Fig. 6.1, after each iteration, the coefficient values were plotted on a graph by the software. This allowed for a plateau, which indicated a lack of change in the values, to be visually apparent. Following aerospace conventions, drag coefficients were converged to at least an order of magnitude lower than 1 drag count (0.0001). For convenience, the same criterion was also applied to the lift coefficient. Lift and drag monitoring was initiated after switching to second order differencing.

Chapter 7

Comparison to Experiment

7.1 Introduction

Fluent was used to simulate the test wing in clean air flow conditions. The purpose of the procedure was to ascertain whether it would be possible to correlate the force coefficients and pressure data from the experimental tests with those to be obtained from the computational solution. Additionally, it was felt that further insight may have been gained, regarding the modelling of wings experiencing laminar to turbulent surface flow conditions.

7.2 Grid Independence Study

A preliminary study was carried out in order to ensure that the CFD mesh was adequate enough to capture the details of the flow. Focus was centred on the boundary layer cells in the immediate vicinity of the wing, and on ensuring that an adequate balance was achieved regarding the number of cells necessary to discretise the domain. While large numbers of cells would have provided more detail of the flow, they would have approached the limits of the memory reserves of the current system and would have taken an extremely long time to provide a solution.

7.2.1 Outline of 2-D Study

The aim of the 2-D study was to ensure that there were adequate cells in the boundary layer region adjacent to the surface of the wing. The strategy taken was to obtain an estimate of the maximum boundary layer thickness from XFOIL [75]. The estimate was then used as a guide for the region in which to construct the boundary layer cells. The total number of cells filling this region was then increased to perform the study. The height of the first cell was chosen so as to produce a maximum y^+ value of 1.

Figure 7.1 shows the domain that was used for the study. The airfoil was placed above a wall boundary that was set to translate with the freestream velocity (moving ground). A velocity inlet boundary condition was constructed 23 chords ahead of the airfoil, while a pressure outlet condition was positioned 24 chords behind. The domain was closed at the top by specification of a symmetry condition at a height of 18 chords. All domain extents were chosen in accordance with guidelines provided by Fluent [76], in order to ensure that the boundary conditions did not influence the flow in the immediate vicinity of the wing.

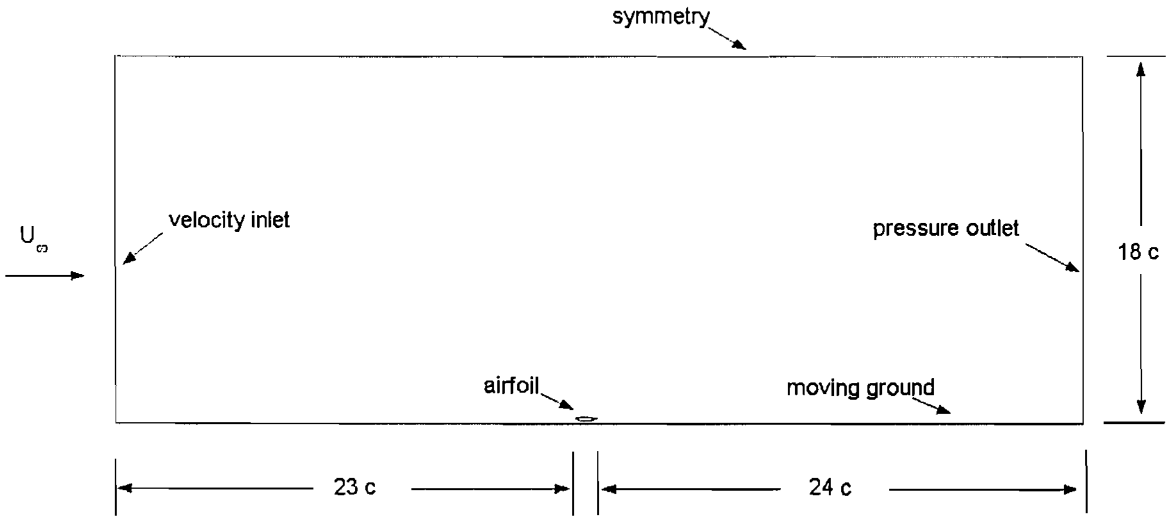

Figure 7.1: The domain used to carry out the 2-D boundary layer study.

7.2.2 Outline of 3-D Study

The aim of the 3-D study was to ensure that there were adequate boundary layer cells in the spanwise direction along the surface of the wing, and to ensure that there were sufficient cells in the domain itself, so as to be able to capture the salient flow features. Consequently, the grid was constructed in a manner that allowed these two goals to be achieved at the same time. Figure 7.2 presents a plan view of the wing in a slice of the domain. Regions *a*, *b*, *c*, *d* and *e* are grid construction sections that allow the number of spanwise cells at each station to be changed, without affecting an adjoining station. The solid lines on the left and right sides represent imposed symmetry planes.

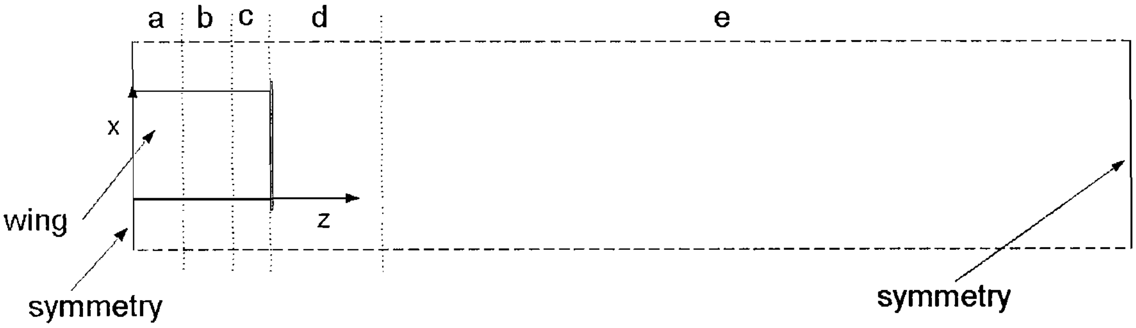

Figure 7.2: A plan view of the wing in a slice of the overall domain. The spanwise grid was altered in regions *a*, *b*, and *c*.

		No. of spanwise cells		
Region	Width (mm)	Grid 1	Grid 2	Grid 3
a	100	10	20	40
b	100	10	20	40
c	75	20 (graded)	30 (graded)	50 (graded)

Table 7.1: The number of spanwise cells used in the 3-D grid independence study. Graded cell spacing was used in the section near to the endplate.

Grid independence was performed by increasing the number of spanwise cells in regions *a*, *b* and *c* according to the values given in Table 7.1. Cells in regions *a* and *b* were evenly spaced, while those in region *c* were graded. Grading the cells (changing the cell spacing at each node point in a direction perpendicular to the sides of the endplate) allowed for the construction of tiny cells on the inner surface of the endplate, which then transitioned to the cell spacing in adjoining region *b*. Gambit contained a menu that allowed this feature to be achieved easily. The cells in regions *d* and *e* were not altered from their original values, as doing so would have increased the final mesh size beyond the practical capabilities of the hardware. Consideration of the aerodynamics of the situation being modelled, however, would highlight the fact that the main flow features would have existed in regions *a*, *b* and *c*. The total cell count for each grid is provided in Table 7.2.

Grid	Cell count
1	1 070 087
2	1 630 818
3	2 589 138

Table 7.2: The total number of cells in each grid.

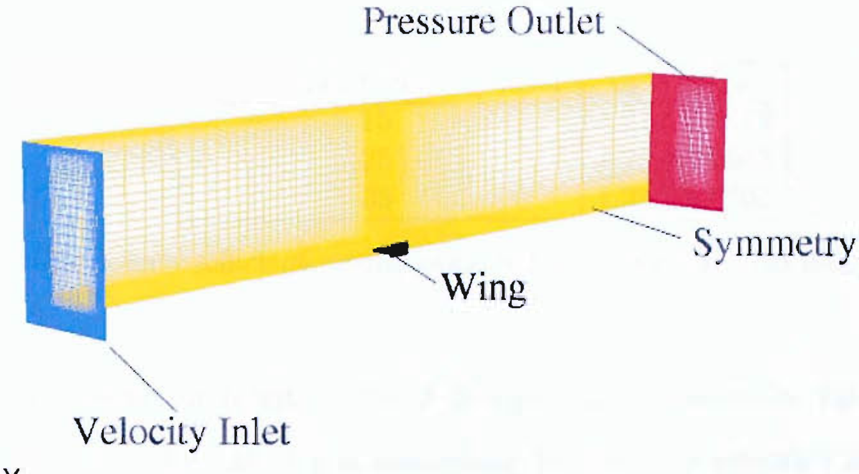

Figure 7.3: The 3-D domain used in the grid independence study.

Figure 7.3 presents a cut-away view of the whole domain that was used to carry out the 3-D study. The outer boundaries at the top, side and bottom were not shown for clarity. In this particular study, the top and side boundaries were designated to be symmetry planes, while the bottom boundary was designated to be a wall that translated with the freestream speed (moving ground). A velocity inlet boundary condition was created 20 chords ahead of the wing and endplate. This condition was used to specify a uniform inlet flow to the domain. Downstream of the wing and endplate, a pressure outlet boundary condition was created at a distance of 22 chords. The side and top boundaries were 18 chords wide and high respectively. The distances of all boundary conditions were chosen to ensure that they had minimal effect on the flow in the immediate vicinity of the wing.

7.2.3 Results

Table 7.3 presents the results of the 2-D boundary layer study. The force coefficients were recorded as the number of rows of cells in the boundary layer region was increased. It can be deduced that there was a 1.6% increase in the downforce coefficient, and a corresponding 2.5% decrease in the drag coefficient as the rows added changed from 15 to 38, the latter row count being the maximum amount that would fit in the specified region of height, 8 mm.

No. rows in boundary layer	C_l	C_d
15	1.27	0.0679
25	1.29	0.0663
38	1.29	0.0662

Table 7.3: The force coefficient results obtained from the 2-D grid independence study.

The force coefficient results of the 3-D study are presented in Table 7.4. For this study, the 2-D boundary layer grid comprising 15 rows was extruded in the z direction according to the method outlined in the previous section. This decision was taken in an effort to minimise the total cell count in the 3-D domain. The tabulated coefficients show that spanwise grid independence was essentially achieved with the cell spacing that was used on grid 2. Grid 1, however, was not far from producing the final standard; the lift and drag coefficients being 0.9% and 0.3% higher, respectively.

Grid	C_L	C_D
1	1.07	0.0935
2	1.06	0.0932
3	1.06	0.0932

Table 7.4: The force coefficient results obtained from the 3-D grid independence study.

7.3 FC1 Comparison

7.3.1 Domain

As the majority of the data collected for FC1 was obtained in the 2.1 m × 1.5 m wind tunnel, a computational model of the test section of this facility was created for comparison purposes. During the mesh construction process, however, it was found that it was necessary to slightly modify the cross sectional shape of the tunnel. The modification was required in order to construct boundary layer cells on the tunnel walls, while concurrently allowing the domain to be filled with hexahedral and prismatic cells. As previously indicated, hexahedral and prismatic cells had the advantage of minimising numerical diffusion effects in flows dominated by vortices.

Figure 7.4 provides a view of the computational cross section, along with that of the actual tunnel. Essentially, the octagonal shape was replaced with a rectangular shape of the same maximum dimensions. Note that only half of the domain was modelled, as there was an opportunity to take advantage of symmetry. The square cross section also allowed for the extrusion of a 2-D mesh to fill the 3-D domain.

The entire domain used for the wind tunnel simulation was similar in shape to that shown in Fig. 7.3. A velocity inlet boundary condition was created 18 chords ahead of the wing and endplate. This condition was used to specify a uniform inlet flow to the test section. In reality, the physical tunnel test section commenced 7 chord lengths ahead of the model, however, for the CFD simulation, a symmetry boundary condition was inserted from 7 to 18 chord lengths ahead of the wing. This modification was carried in order to ensure that the velocity inlet condition did not influence the flow in the

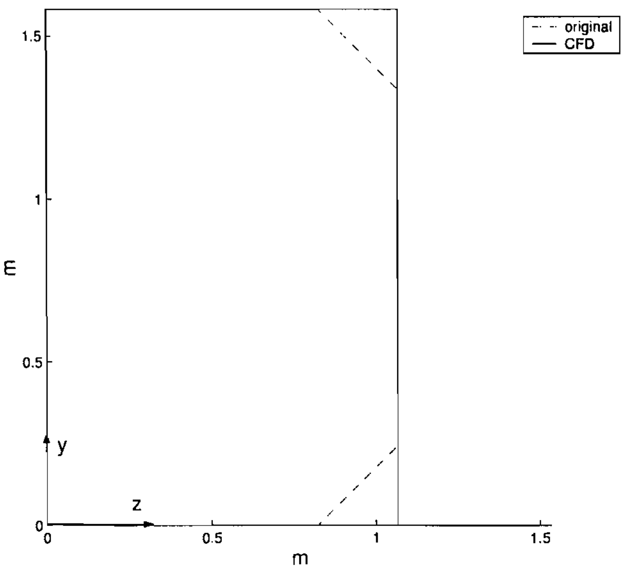

Figure 7.4: An outline of the original wind tunnel cross section, and the modified CFD cross section. The geometries are symmetric about the y-axis.

immediate vicinity of the wing.

Downstream of the wing and endplate, a pressure outlet boundary condition was created at a distance of 22 chords. Again, this distance was greater than the actual distance between the model and the end of the test section. In this case, however, the extra distance was treated as an extension of the test section confines. The tunnel walls therefore extended from 7 chords ahead of the wing to the end of the domain in the x-direction. Domain symmetry was exploited by creating a symmetry boundary condition on the tunnel centreline.

The wing boundary layer region was modelled by extruding the 2-D grid comprising of 38 rows, Fig. 7.5, along the spanwise direction. The number of spanwise cells used corresponded to the statistics given for grid 1 in Table 7.1. As regions *a*, *b* and *c* among others, existed throughout the length of the entire domain, and as boundary layer cells were constructed on the walls of the tunnel, it was imperative that the mesh be created with as few cells as possible. The final cell count was 2 635 494 cells.

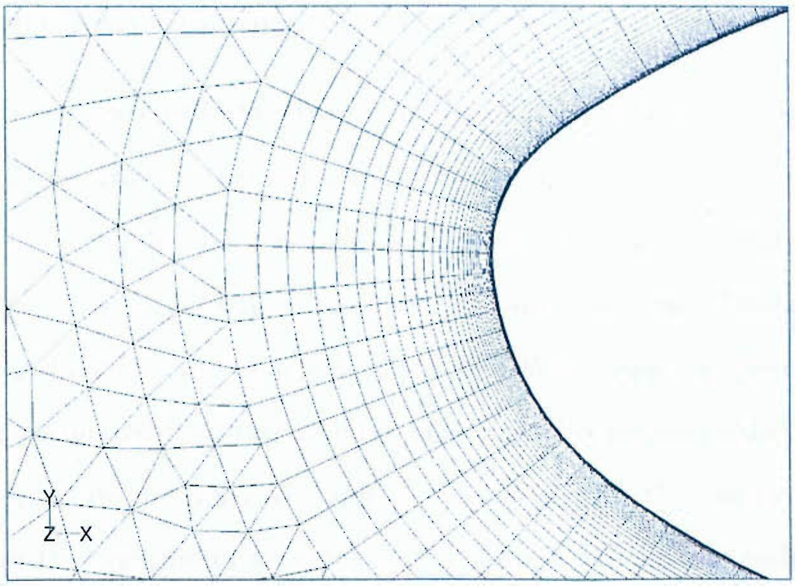

Figure 7.5: A view of the grid in the immediate vicinity of the wing leading edge.

7.3.2 Transition

In FC1 conditions, the wing experienced laminar to turbulent boundary layer transition on both its suction and pressure surfaces, as previously displayed in Section 4.3. In order to model these regimes in CFD, measurements taken from the flow visualisation tests were transferred to the computational model. Specifically, the midspan points at which turbulent flow commenced on the wind tunnel model were used as the demarcation points between laminar and turbulent zones in CFD. The locations of the transition points on both surfaces of the wing are given in Table 7.5.

Surface	x/c transition
suction	0.51
pressure	0.76

Table 7.5: The location of the points of transition, obtained from experimental flow visualisation tests.

7.3.3 Results and Discussion

A comparison of the force coefficients from experiment and CFD is presented in Table 7.6. The CFD simulations were carried out using both the Spalart-Allmaras and the RNG $\kappa\epsilon$ turbulence models. It can be seen that the experimental downforce coefficient was underestimated in both cases. The SA model predicted a value that was 6.34% lower, while the RNG $\kappa\epsilon$ model predicted a value that was 17.6% less. With regard to the drag coefficient, both models overestimated the experimental value. The SA model predicted a value that was 13.9% higher, while the RNG $\kappa\epsilon$ model predicted a value that was 8.81% higher. It was thought that the creation of an extremely fine mesh around the endplate may have helped to further reduce the drag values, however, it was not possible to investigate this scenario, owing to the amount of cells that would have been required to fill the entire domain.

	C_L	C_D
Experiment	1.42	0.0851
CFD: SA	1.33	0.0969
CFD: RNG $\kappa\epsilon$	1.17	0.0926

Table 7.6: The force coefficients obtained from experiment and CFD at $h_r/c = 0.153$.

A comparison of the pressure distribution data at the spanwise locations of 2z/b = 0.09, 0.49 and 0.89 provided further detailed insight. Figure 7.6 shows the results at the first station. Immediately, it can be seen that on the suction surface, both computational values for the region of laminar flow underestimated the experimental values between x/c ≈ 0.03 to x/c ≈ 0.51, with the RNG $\kappa\epsilon$ model being the least accurate. The region between x/c ≈ 0.51 and x/c = 0.60 was also underestimated. Beyond x/c ≈ 0.6, both the computational and the experimental data showed relatively good agreement.

On the pressure surface, different trends are visible. There was relatively good agreement between both sets of computational data and the experimental data, up to x/c ≈ 0.62. Beyond this point, the computational pressure distributions showed wiggles in their profiles. These wiggles appeared to oscillate about the experimental data for

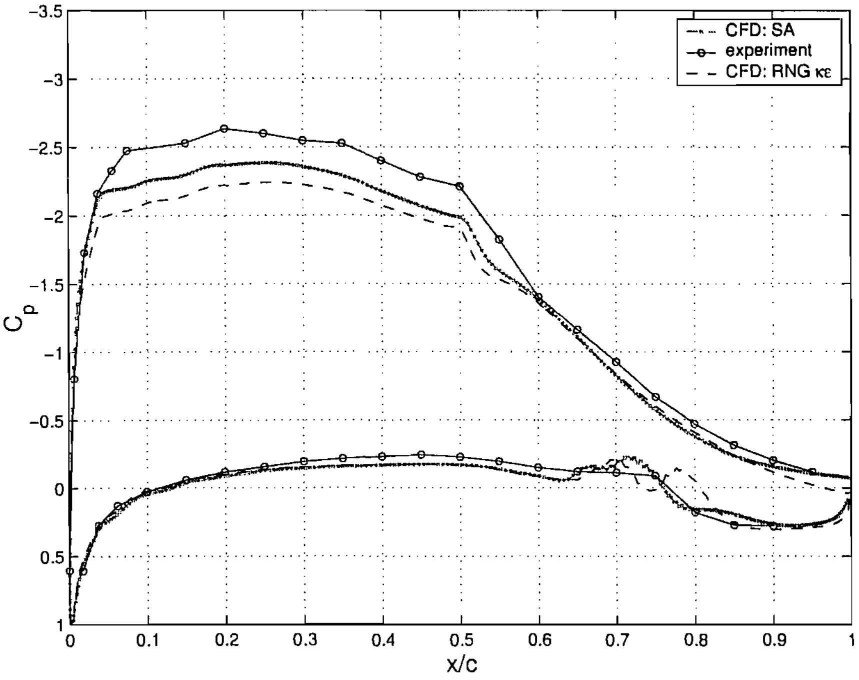

Figure 7.6: A comparison between CFD and experimental pressure distributions at 2z/b = 0.09.

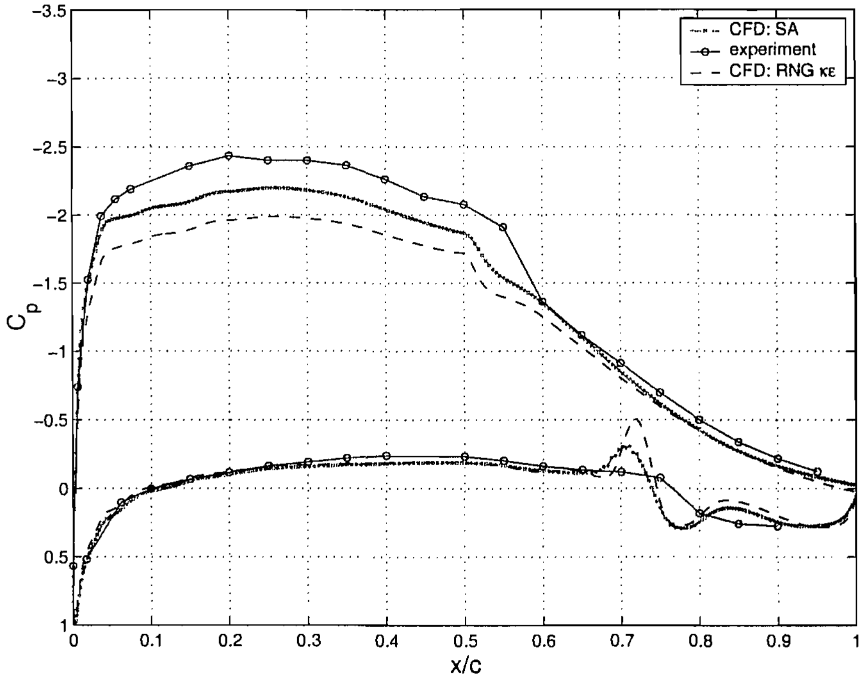

Figure 7.7: A comparison between CFD and experimental pressure distributions at 2z/b = 0.49.

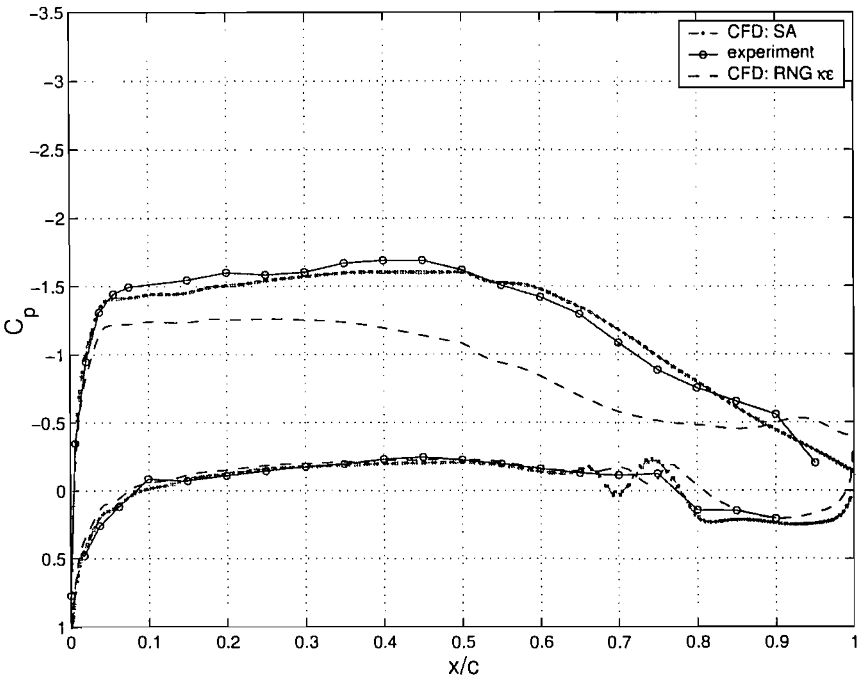

Figure 7.8: A comparison between CFD and experimental pressure distributions at 2z/b = 0.89.

that region.

At the second spanwise station, 2z/b =0.49, Fig. 7.7, similar trends to the first station were repeated. The laminar region was again underestimated on the suction surface, while the wiggles in the computational solution were again apparent beyond x/c ≈ 0.65 on the pressure surface. All other areas showed relatively good agreement.

At the spanwise station of 2z/b = 0.89, Fig. 7.8, a slightly different picture emerged. The SA turbulence model produced relatively good agreement with the experimental values from both the laminar and the turbulent flow regions on the suction surface. In contrast, the RNG $\kappa\epsilon$ turbulence model greatly underestimated the experimental values along the entire surface. On the pressure surface, both turbulence models produced excellent agreement with the experimental data, up to x/c ≈ 0.65. Beyond this point, the wiggles in the computational distribution again appeared.

In order to provide an explanation for the wiggles in the computational solution on the pressure surface, the x-wall shear stress was extracted at each location. The data is presented in Fig. 7.9 for the SA model. It can be seen that at the three spanwise stations, the x-wall shear stress values changed from positive to negative between x/c $\approx$ 0.57 to x/c $\approx$ 0.59. There were then intermittent oscillations of the values, above and below zero. The x-wall shear stress is defined as:

$$\tau_w = \mu \frac{\partial u}{\partial y} \tag{7.1}$$

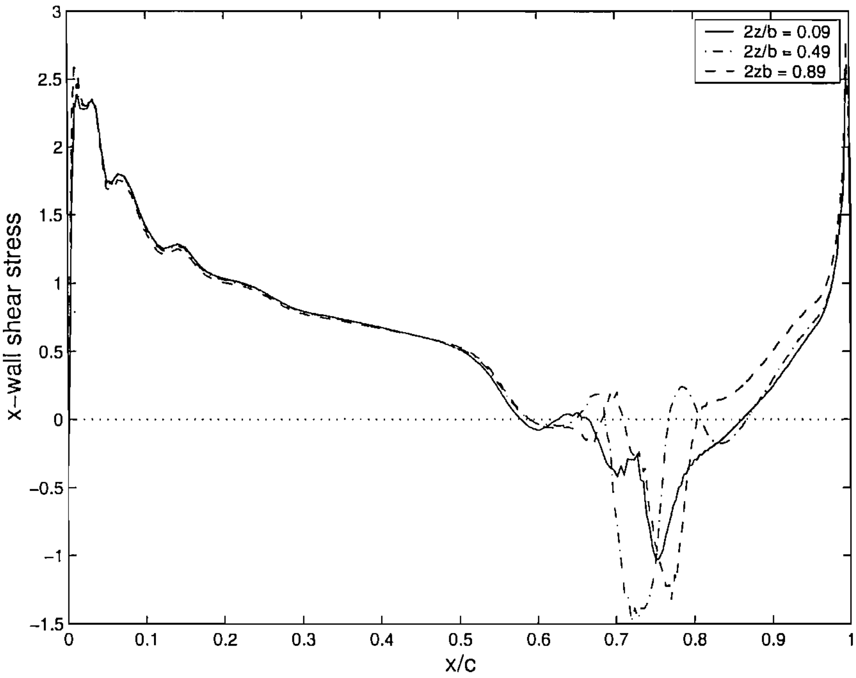

Figure 7.9: The computational x-wall shear stress on the wing pressue surface, corresponding to the previous pressure distribution locations.

Hence a negative value is indicative of flow separation. Essentially, in the computational solution, laminar flow separation on the pressure surface occurred at a much earlier point than was the case in the experimental tests (x/c $\approx$ 0.58 for CFD vs. x/c = 0.76 for experiment). The wiggles were therefore the product of early separation, and of the flow intermittently reattaching and detaching from the surface in some cases.

To provide a comparison with the experimental flow visualisation images, oil-flow lines were plotted from the CFD simulation. Figure 7.10 shows the suction surface results for the SA model. The surface flow can be compared to the experimental equivalent in

Fig. 4.13. It can be seen that the computational flow features are broadly similar to the experimental outcome. There was a difference in the shape of the line of transition, owing to the fact that it was specified at a constant x/c location for the CFD computations. Observation of the junction region of the wing and endplate shows that recirculating regions were also predicted in the computational solution.

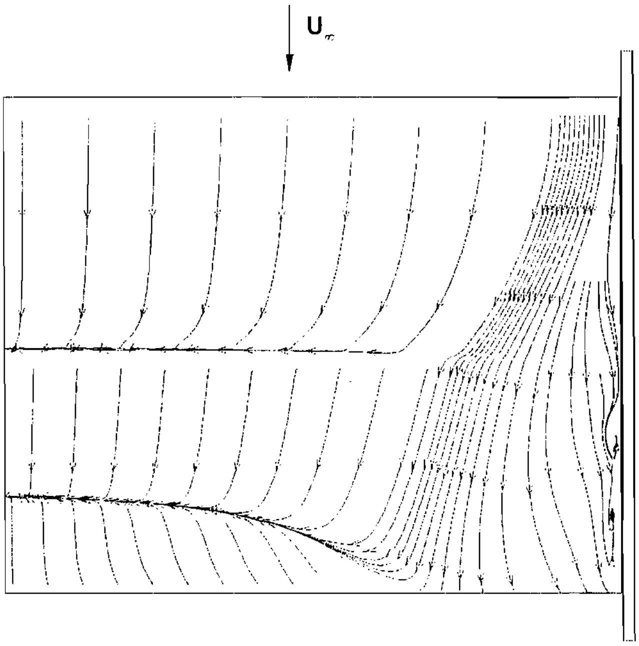

Figure 7.10: The suciton surface oil-flow lines obtained from the CFD solution while using the Spalart–Allmaras turbulence model.

The suction surface result for the RNG $\kappa\epsilon$ model is displayed in Fig. 7.11. It can be seen that no recirculation regions were predicted, and that the area of trailing edge separation was greatly reduced, as compared to the SA surface flow. Additionally, the lack of swirl in the region close to the endplate is evident.

The pressure surface oil-flow lines for the SA model are presented in Fig. 7.12. A comparison can be made with the experimental outcome that was shown in Fig. 4.15. Up to the point of premature laminar separation, the computational lines predicted a similar outcome to the experiments. Beyond the point of separation, however, there was no clear direction in the lines, a consequence of the failure of CFD to accurately model

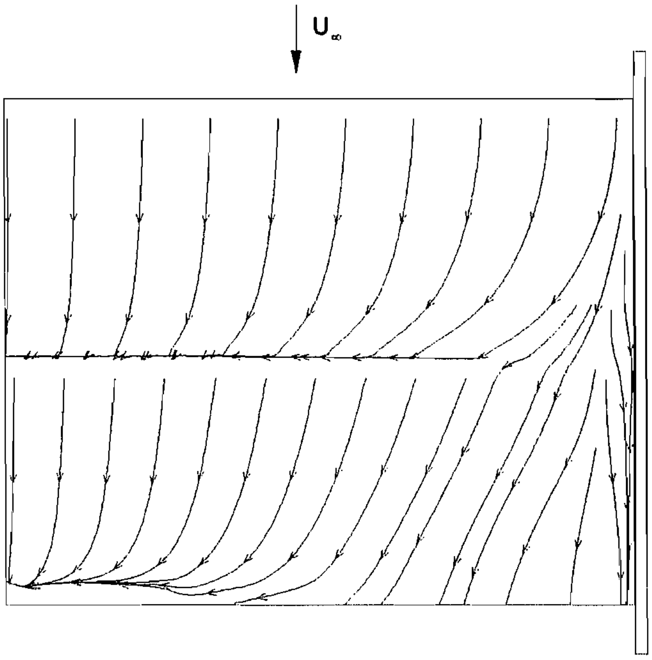

Figure 7.11: The suciton surface oil-flow lines obtained from the CFD solution while using the RNG $\kappa\epsilon$ turbulence model.

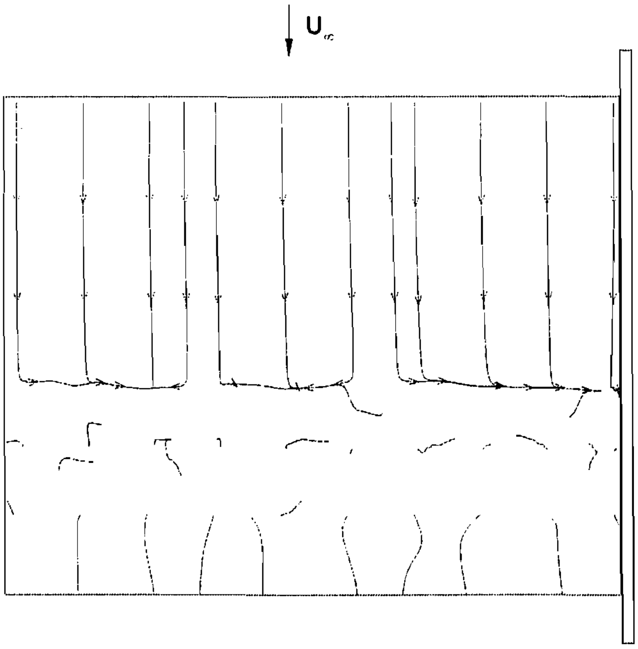

Figure 7.12: The pressure surface oil-flow lines obtained from the CFD solution while using the Spalart–Allmaras turbulence model.

this portion of the flow. The corresponding flow visualisation image for the RNG $\kappa\epsilon$ model is not shown, since it was essentially the same as that as that for the SA model. After the point of premature separation, there was no coherent structure to the surface flow lines. Before the point of premature separation, the lines were straight.

In an effort to gauge the effect of early laminar separation on the computational solution, the point of transition on the pressure surface was modified. By using the data that was plotted in Fig. 7.9, the SA CFD model was updated to specify transition at x/c = 0.56. The force coefficients obtained after the modification are compared to experiment in Table 7.7. It can be seen that the downforce coefficient improved to within 4.2% of the experimental value, while the drag coefficient deteriorated, increasing to a value that was 16.2% greater than that of experiment.

	C_L	C_D
Experiment	1.42	0.0851
CFD (modified transition)	1.36	0.0989

Table 7.7: The force coefficients obtained from experiment and CFD with modified pressure surface transition at $h_r/c = 0.153$.

The pressure distribution comparisons are presented in Figs. 7.13 to 7.15. In general, at the stations of 2z/b = 0.09 and 2z/b = 0.49 the suction surface values have increased, becoming closer to the experimental values than was the case in the original simulation, Figs. 7.6 to 7.8. The pressure surface data, however, showed distinct signs of the change in the transition location. At x/c = 0.56, there was a departure from the experimental trend, with higher C_p being produced where the laminar bubble would have existed. Beyond x/c = 0.8, the computational prediction again followed the experimental outcome. At 2z/b = 0.89, Fig. 7.15 the suction surface data hardly experienced any change, while the data on the pressure surface was broadly similar to that described for the previous spanwise stations.

The oil-flow lines on both surfaces of the wing are shown in Figs. 7.16 and 7.17. It can be seen that the suction surface flow is similar to that presented in Fig. 7.10. The

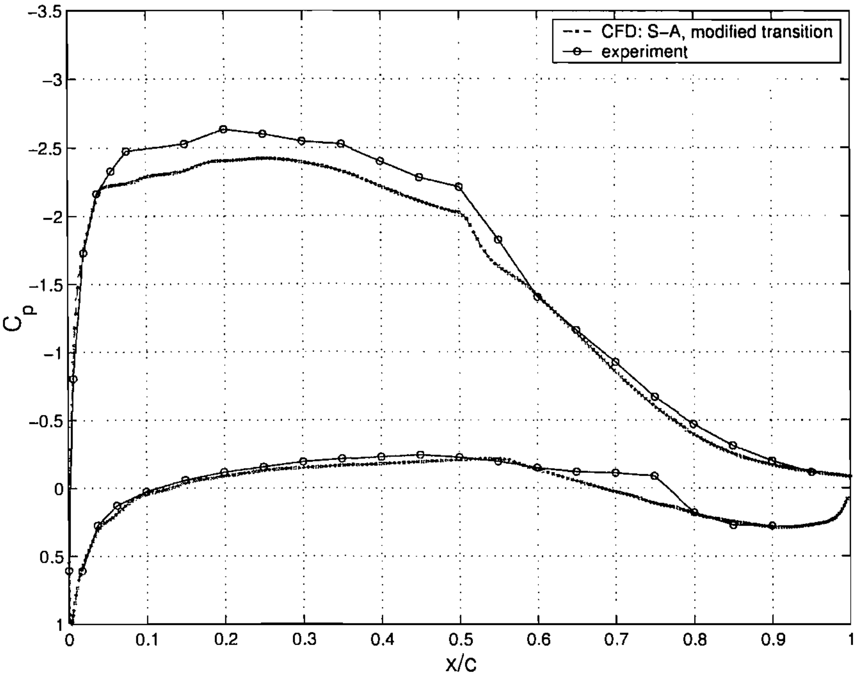

Figure 7.13: A comparison between CFD and experimental pressure distributions at 2z/b = 0.09.

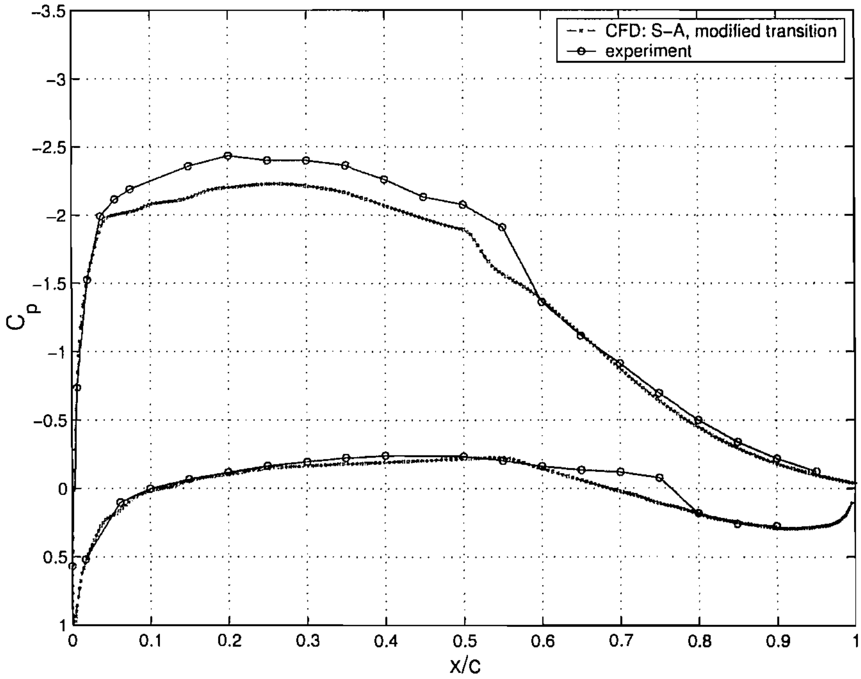

Figure 7.14: A comparison between CFD and experimental pressure distributions at 2z/b = 0.49.

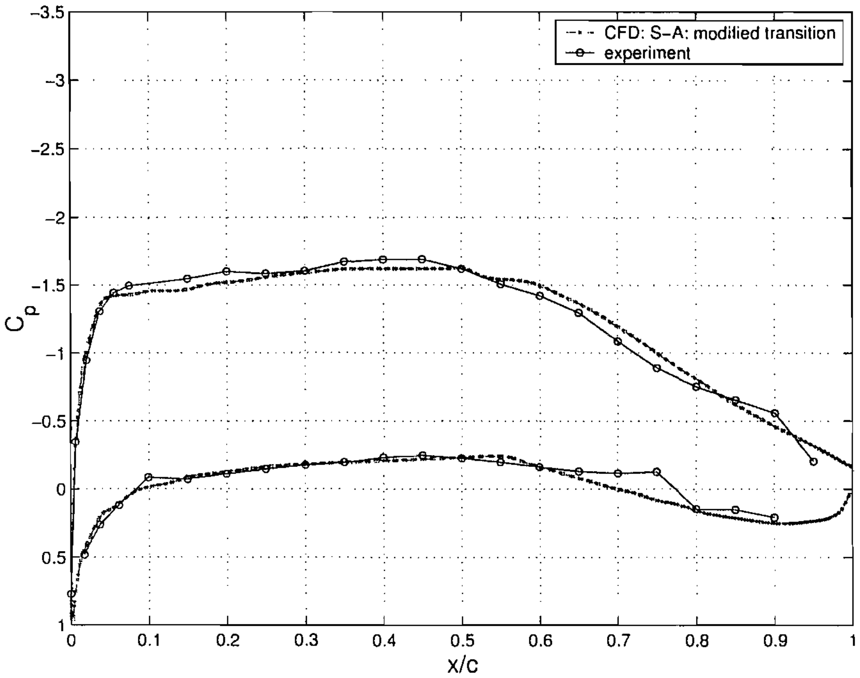

Figure 7.15: A comparison between CFD and experimental pressure distributions at 2z/b = 0.89.

recirculation regions close to the endplate were still evident, as was the region of trailing edge flow separation. The pressure surface flow, however, had changed significantly. Owing to the fact that premature separation was eliminated, the flow remained attached along the entire surface, as evidenced by the continuous lines. No other flow features were present.

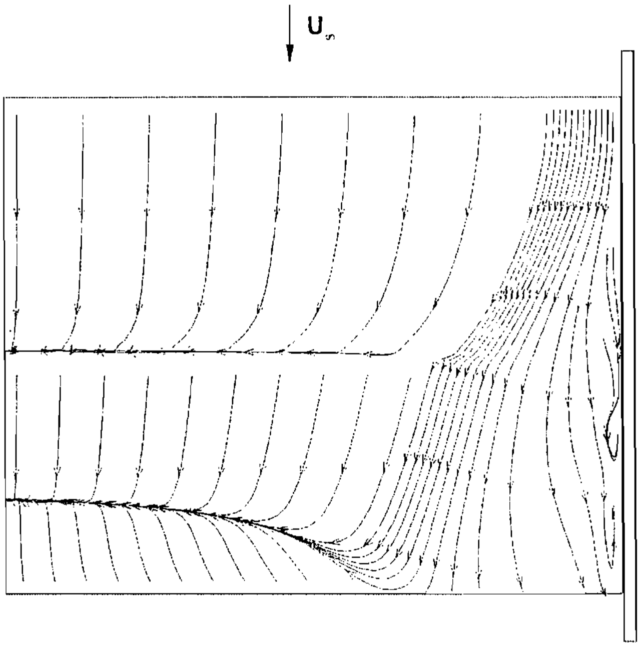

Figure 7.16: The suction surface oilflow lines obtained from the CFD solution while using the Spalart–Allmaras turbulence model, with modified pressure surface transition.

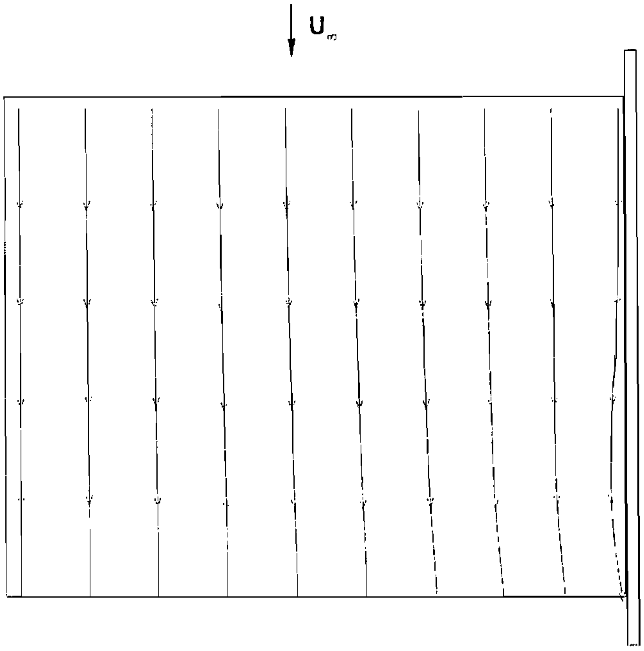

Figure 7.17: The suction surface oilflow lines obtained from the CFD solution while using the Spalart–Allmaras turbulence model, with modified pressure surface transition.

7.4 Conclusion

The comparisons between experiment and CFD that were presented in this chapter have allowed for the following conclusions to be put forward.

1. The pressure distributions from laminar flow regions at 2z/b = 0.09 and 0.49 were underestimated by both the SA and the RNG $\kappa\epsilon$ turbulence models, with the latter producing poorer results than the former.

2. CFD was not able to entirely match the experimental surface flow conditions on the pressure surface of the wing, owing to premature laminar boundary layer separation.

3. The Spalart–Allmaras turbulence model provided a better match of the experimental pressure distribution from the tip of the wing, than it did for the pressure distributions originating from sections closer to the centre of the wing.

4. Changing the point of transition on the pressure surface of the wing affected the pressure distribution values on the suction surface of the wing. Therefore, the inability of CFD to correctly model the pressure surface flow in this case, may have been partly responsible for the underestimation of some of the experimental suction surface values.

Chapter 8

CFD Investigations

8.1 Introduction

This chapter presents the results of the computational simulations that were carried out to ascertain whether the trends uncovered experimentally could be predicted with CFD. Flow conditions FC1 and FC3 were modelled, as they represented the situations of greatest practical interest. All of the computational simulations were run as fully turbulent cases using the SA model. No regions of laminar flow were constructed.

8.2 Domain

8.2.1 Discretisation

The computational domain that was used to perform this series of CFD investigations was based on the domain previously described in Section 7.2.2. The advantage gained from using this configuration was that it allowed for the minimum amount of cells to be used in grid construction, as boundary layer regions did not have to be created on the outer confines. Furthermore, with regard to the modelling of flow condition FC3, the cells that would have been used to model the boundary layer were instead used to fill the large downstream distance between the bluff body and the wing.

To further minimise the cell count while modelling FC3, the upstream bluff body and the downstream wing were created in two separate domains that were based on the same coordinate system. Essentially, the entire streamwise distance to be modelled was divided into two separate sections that contained a common overlapping x-coordinate plane. The overlapping plane was necessary to ensure that the solution generated in the upstream domain could be transferred to the downstream domain. Figure 8.1 presents a 2-D representation of the domains just described.

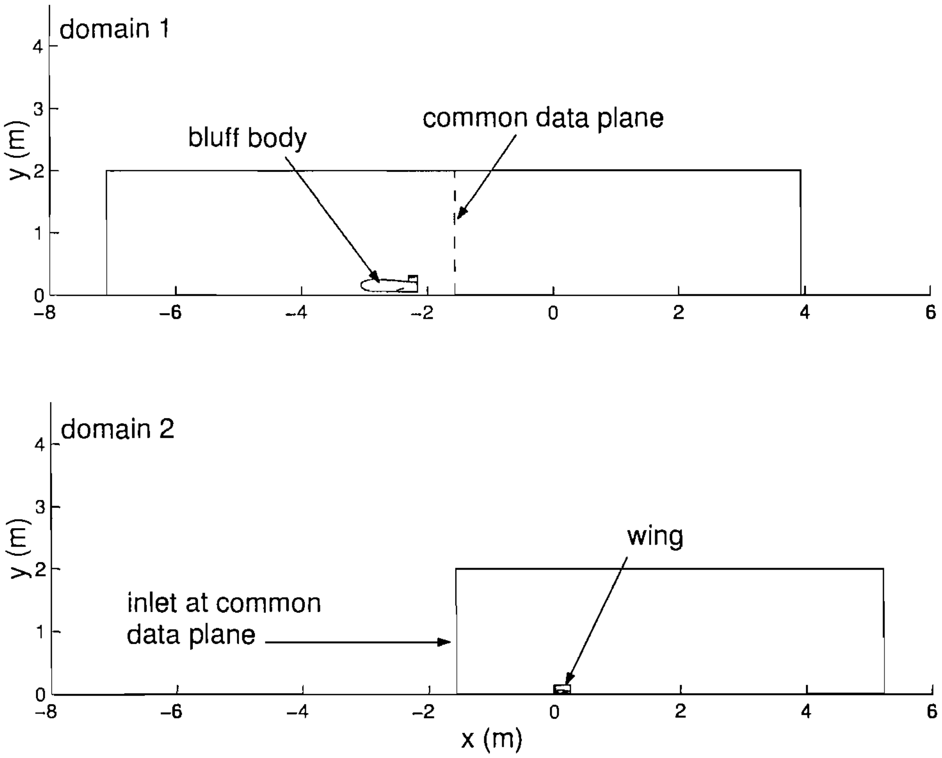

Figure 8.1: A 2-D view of the domain strategy used to model FC3.

8.2.2 Solution Strategy

The solution procedure for the computational domains was carried out in a sequential manner. Firstly, the bluff body was solved in domain 1 to develop the flow field associated with FC3. After convergence had been achieved, the 3-D velocity profiles were extracted from the common data plane shown in Fig. 8.1. The extracted profiles were then used as the velocity inlet condition for the solution of domain 2. Further information on this type of solution strategy is provided in the Fluent documentation [76].

8.3 Bluff Body Flow Field

The flow field generated by the upstream bluff body configurations will be presented in order to provide a more detailed insight into the actual flow conditions experienced by the downstream wing and endplate. The cases simulated included the 16.7 deg ramp diffuser, with and without a moving ground, and the 5 deg ramp diffuser with a moving ground.

8.3.1 Bluff Body with 16.7 Degree Ramp

Stages of the velocity flow field downstream of the bluff body are presented in Figs. 8.2 to 8.6. The data planes are located at $0.18l$, $0.73l$, $1.29l$, $1.84l$ and $2.4l$ behind the bluff body, where l is the length of the bluff body. At $0.18l$, Fig. 8.2, two vortices are present, one very much larger than the other. The large vortex can be seen to emanate from the diffuser region, while the smaller can be seen to emanate from the junction between the rear wing and endplate. At $0.73l$, the diffuser vortex has progressed inwards and upwards, while the wing vortex has moved slightly downwards and outwards. At $1.29l$, the diffuser vortex continues to move inwards and upwards, while the wing vortex has almost dissipated. At $1.84l$ and $2.4l$, only the diffuser vortex dominated the flow field, as it continued to show significant upward movement.

This particular ramp angle was used to evaluate an additional scenario that was related to the research investigation. Presented in Fig. 8.7 is a comparison of the approximate downstream vortex centres that were obtained from changing the height of the diffuser. The plots show that by the location of $2.4l$ downstream of the bluff body (the position of the leading edge of the wing), the vortex from diffuser $h_r/d = 0.6$ was positioned lower to the ground than the vortex from diffuser $h_r/d = 0.3$. At all points, the vortex from diffuser $h_r/d = 0.6$ was also further from the plane of symmetry at $2z/b = 0$,

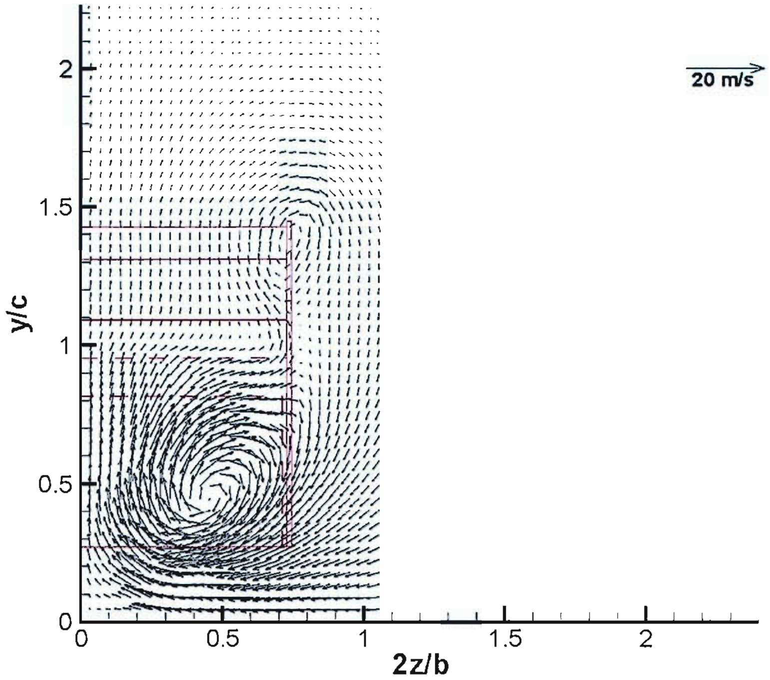

Figure 8.2: The velocity flow field at 0.18l behind the 16.7 deg ramp bluff body.

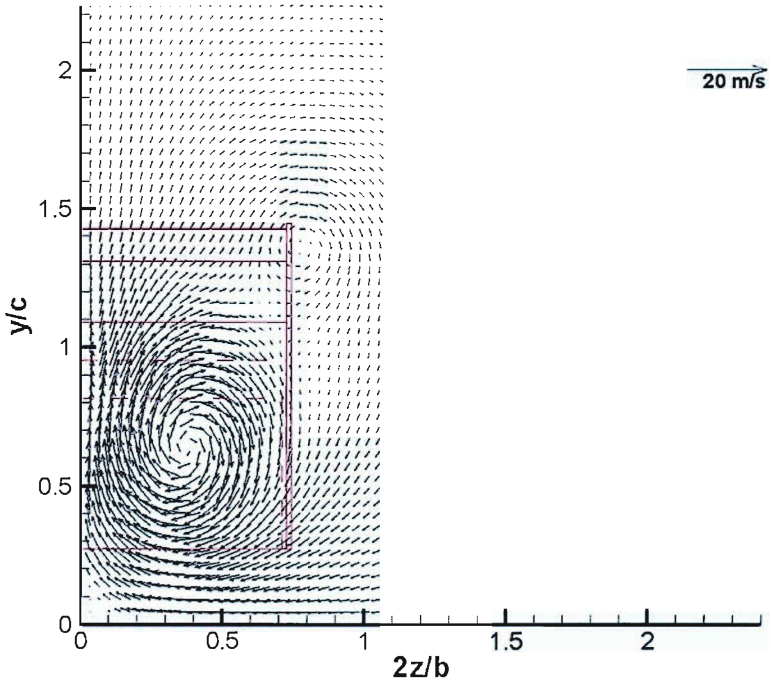

Figure 8.3: The velocity flow field at 0.73l behind the 16.7 deg ramp bluff body.

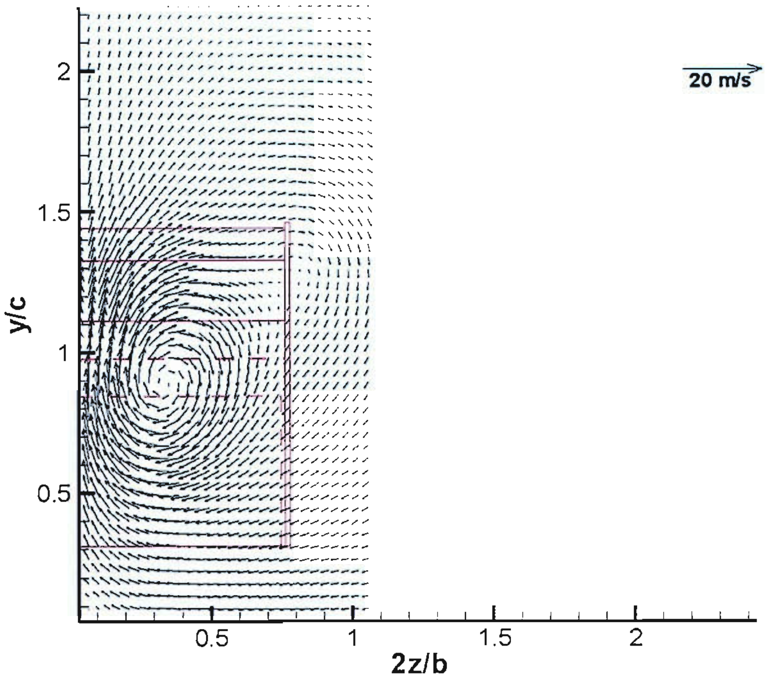

Figure 8.4: The velocity flow field at 1.29l behind the 16.7 deg ramp bluff body.

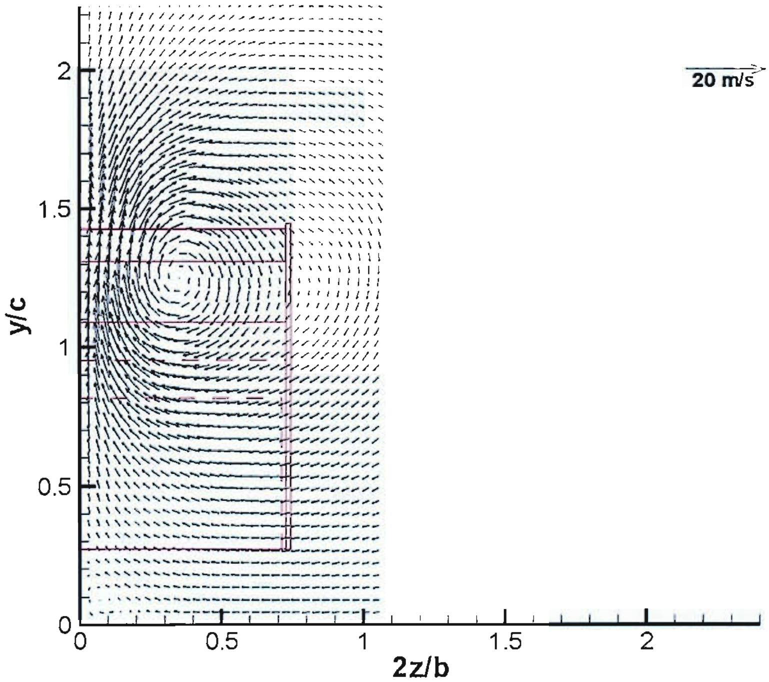

Figure 8.5: The velocity flow field at 1.84l behind the 16.7 deg ramp bluff body.

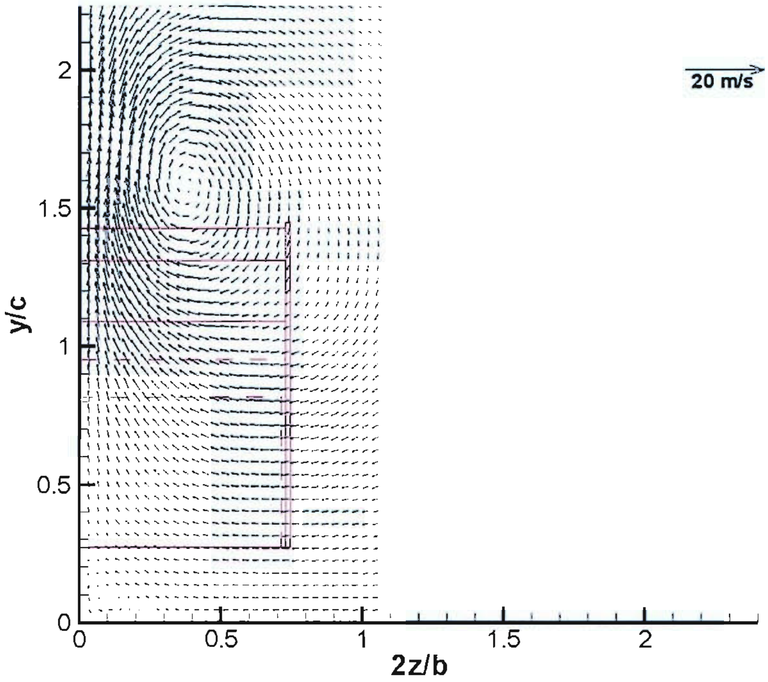

Figure 8.6: The velocity flow field at 2.40l behind the 16.7 deg ramp bluff body.

than was the vortex from diffuser $h_r/d = 0.3$.

Velocity profiles at 2z/b = 0 and 2z/b = 0.87 were also plotted 2.4l downstream of the bluff body for the two ride heights, Figs. 8.8 and 8.9. In terms of the vertical component of velocity, the plots highlighted a region of downwash below y/c ≈ 0.25. This feature was found to be the result of a secondary vortex that was formed further upstream when the main diffuser vortex induced a shear on the flow above the ground. The observation was previously reported by Harvey and Perry [77]. Above y/c = 0.25, an upwash was present for both cases, with diffuser $h_r/d = 0.3$ producing a maximum value of approximately 0.45 v/U_∞ at y/c ≈ 1.6. In comparison, diffuser $h_r/d = 0.6$ produced a maximum value of approximately 0.34 v/U_∞ at y/c ≈ 1.5. At 2z/b = 0.87, a slight downwash was evident throughout the ride height range, for both configurations. In terms of the horizontal component of velocity, the lower diffuser appeared to cause a greater slowing of the transporting fluid.

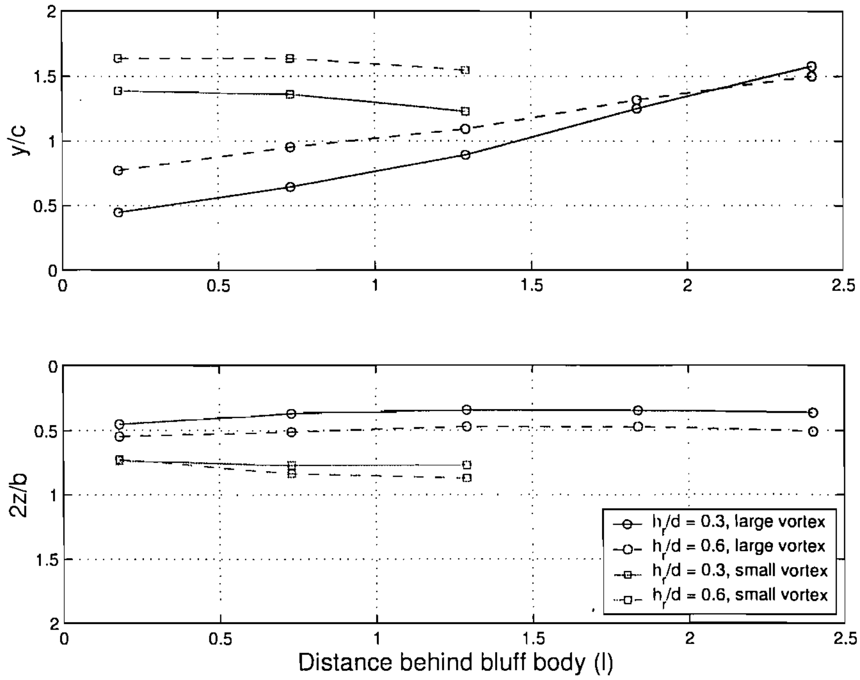

Figure 8.7: The approximate vortex centres downstream of the bluff body for two diffuser ride heights.

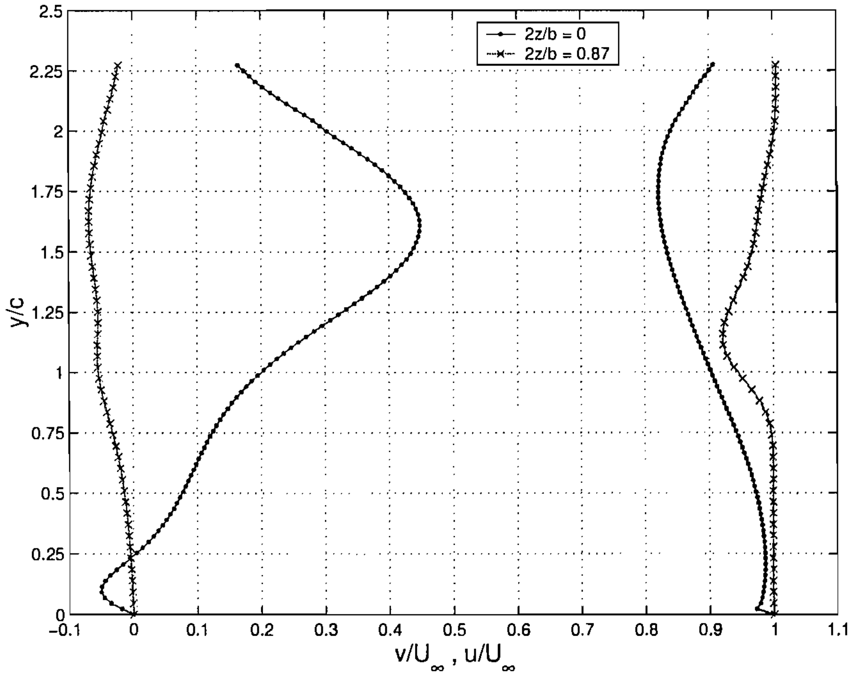

Figure 8.8: Centreline velocity components at $2.4l$ downstream of the bluff body when it was positioned at the ride height $h_r/d = 0.3$.

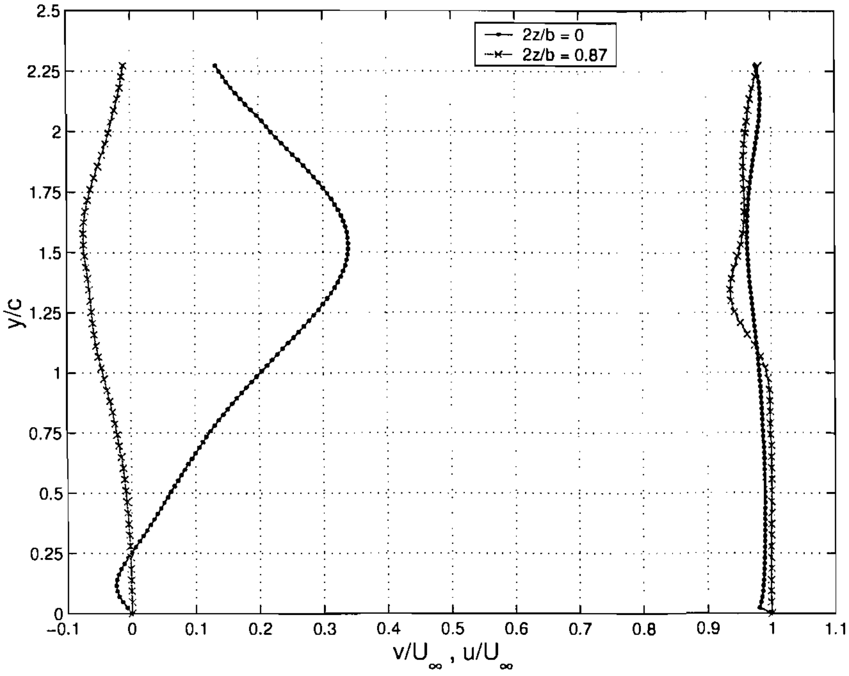

Figure 8.9: Centreline velocity components at $2.4l$ downstream of the bluff body when it was positioned at the ride height $h_r/d = 0.6$.

8.3.2 Bluff Body with 5 Degree Ramp

Images of the velocity flow field downstream of the bluff body incorporating the 5 deg ramp are displayed in Figs. 8.10 to 8.14. It can be seen that there was a significant difference in the flow structure when compared to the results from the bluff body incorporating the 16.7 deg ramp. At $0.18l$, in the region immediately behind the base of the diffuser, two counter-rotating vortices were present, while a third smaller region of rotating flow appeared to be present behind the junction of the wing and endplate. A more detailed analysis of the region between the base of the bluff body and the current plane has shown that the counter-rotating vortex closest to 2z/b = 0 was formed from a complex interaction between the slow moving fluid behind the base and the faster moving fluid exiting above and below the base. The area examined was seen to undergo stages where both counter-rotating and co-rotating vortices were intermittently present. The data at $0.18l$ merely depicts one of these flow states.

At $0.73l$, Fig. 8.11, the upper vortex from the wing and endplate junction has clearly

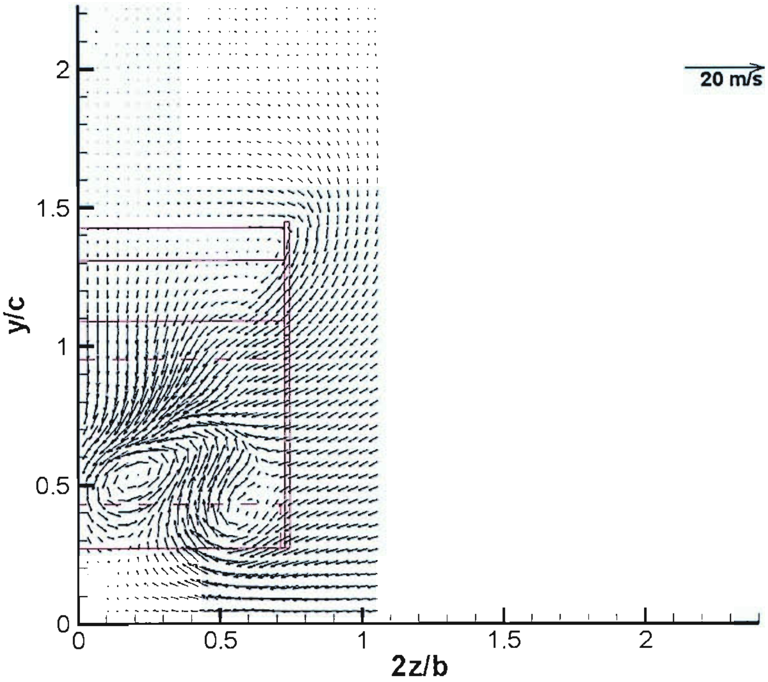

Figure 8.10: The velocity flow field at 0.18l behind the 5 deg ramp bluff body.

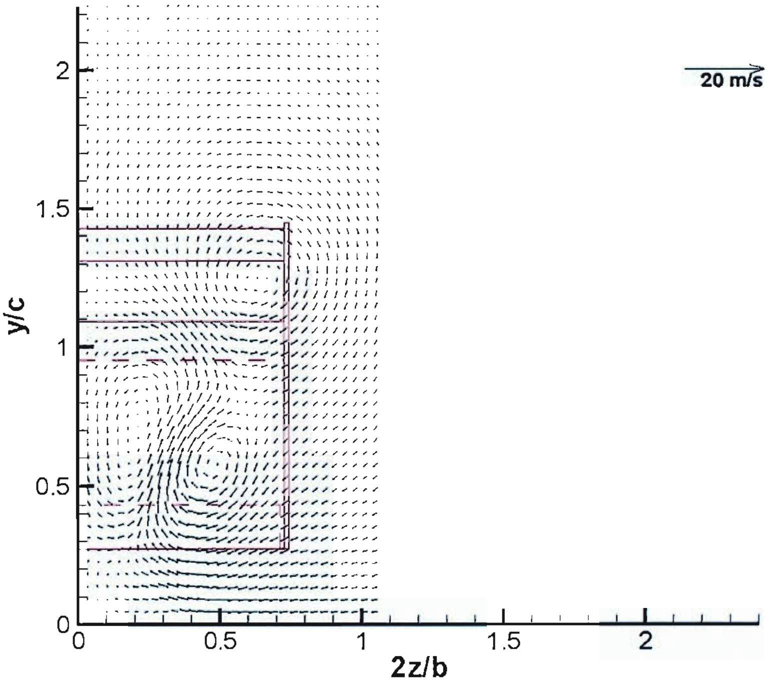

Figure 8.11: The velocity flow field at 0.73l behind the 5 deg ramp bluff body.

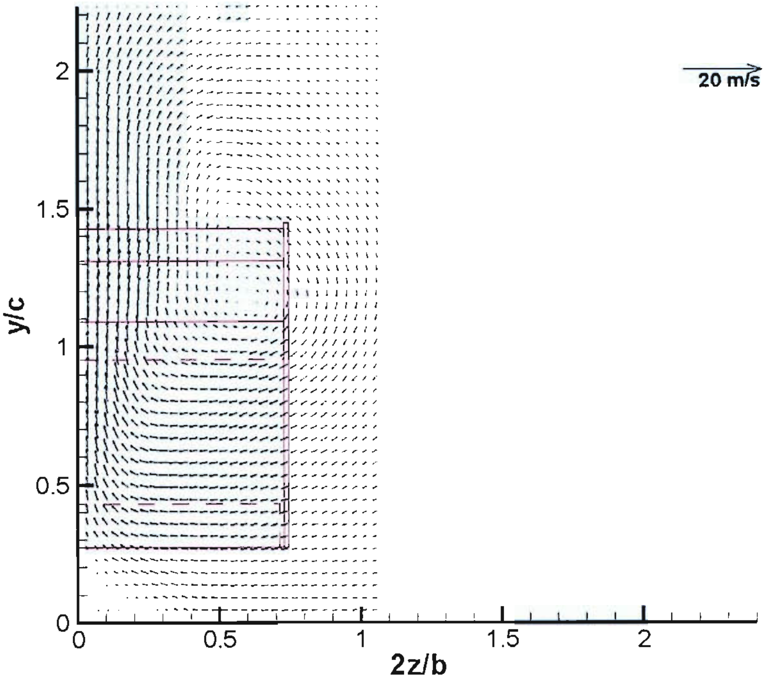

Figure 8.12: The velocity flow field at $1.29l$ behind the 5 deg ramp bluff body.

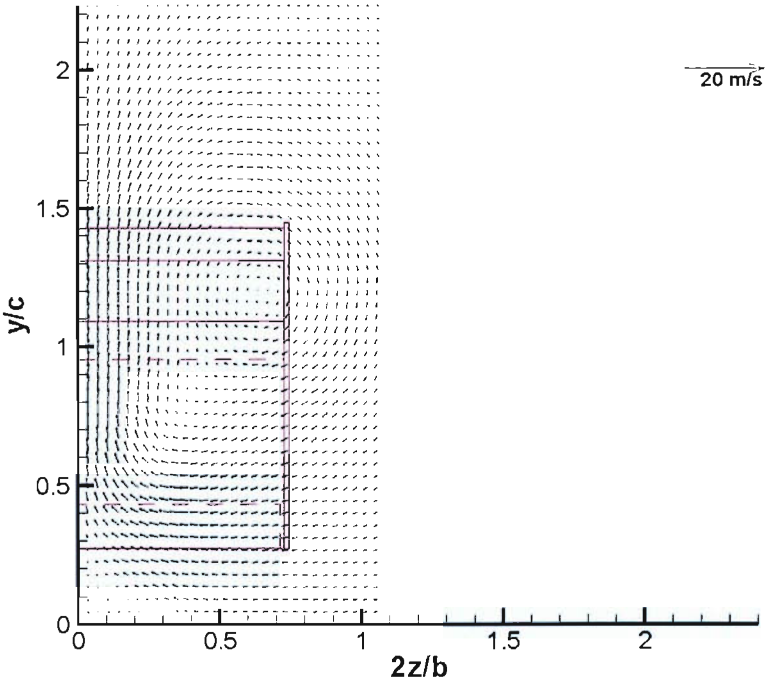

Figure 8.13: The velocity flow field at $1.84l$ behind the 5 deg ramp bluff body.

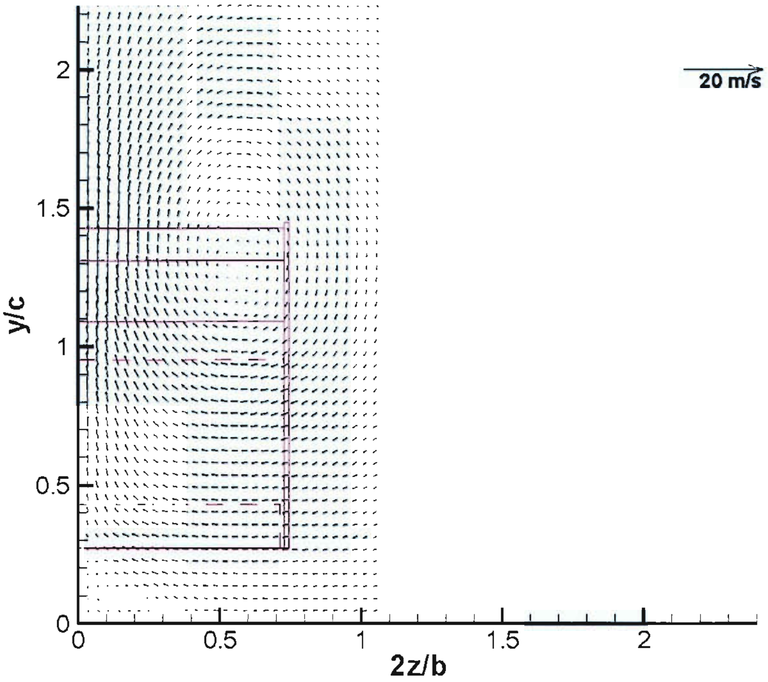

Figure 8.14: The velocity flow field at 2.40l behind the 5 deg ramp bluff body.

formed. The two lower counter-rotating vortices are still present, with the one closest to 2z/b = 0 appearing to be much more diffused. At 1.29l, Fig. 8.12, only the upper vortex appeared to be present, while at 1.84l, Fig. 8.13, a diffused second vortex seemed to have appeared, only to seemingly disappear at 2.4l, Fig. 8.14.

Again, more detailed flow visualisation has shown that the vortices that emanated from the diffuser endplate and diffuser base region switched between counter-rotating, co-rotating and merged states as they progressed downstream. The final merged state of these vortices then formed a co-rotating system with the upper vortex. This new co-rotating system then merged to form a single vortex (in the region of 2.4l), which then further progressed downstream while dissipating. For reference, the approximate downstream vortex centres are plotted in Fig. 8.15 for the vortex that was most noticeably present in all data planes.

Velocity profiles at 2z/b = 0 and 2z/b = 0.87 were also plotted at 2.4l downstream of the bluff body, Fig. 8.16. Again, considering the vertical component of velocity, a region of downwash was predicted below y/c = 0.25. Above his height, gradually more

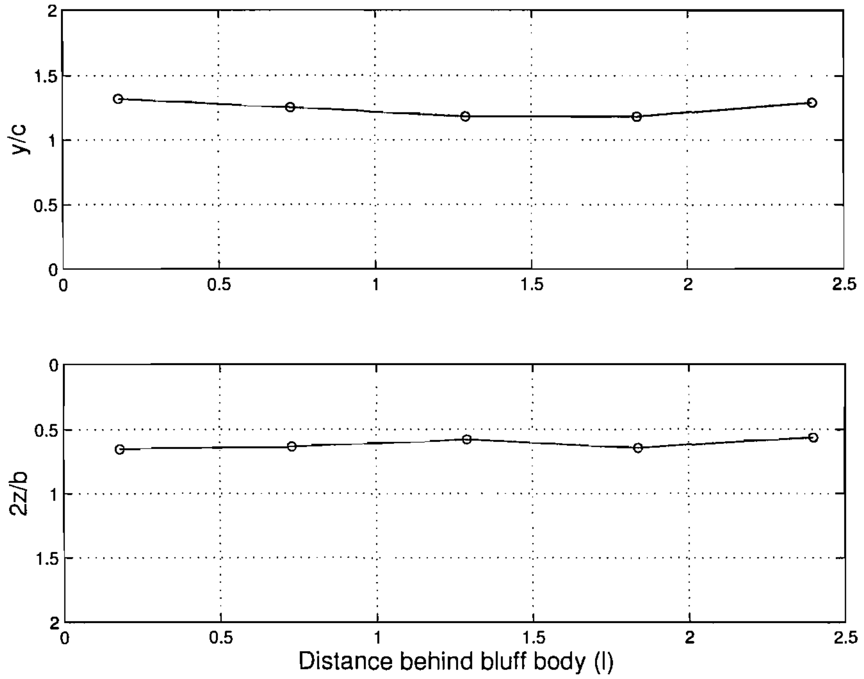

Figure 8.15: The approximate vortex centres downstream of the bluff body.

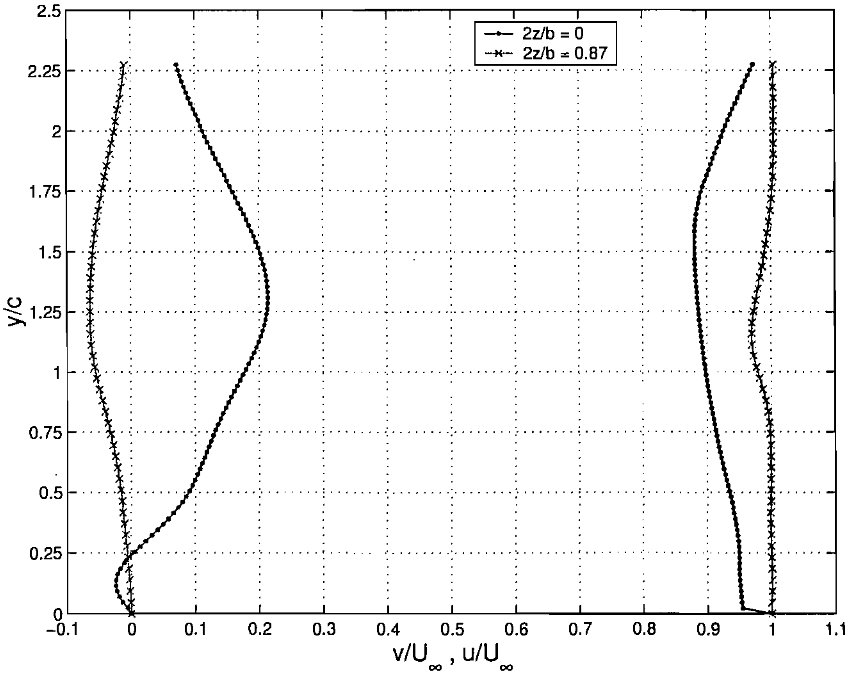

Figure 8.16: Centreline velocity components at $2.4l$ downstream of the 5 deg ramp bluff body when it was positioned at the ride height $h_r/d = 0.3$.

upwash was present, reaching a maximum value of approximately 0.21 at y/c ≈ 0.31. At 2z/b = 0.87, a slight region of downwash was present. The horizontal component of velocity highlighted a slowing of the oncoming fluid.

8.4 The Effect of an Upstream Bluff Body

This section will present computational results highlighting the effect of an upstream bluff body on the downstream wing. The bluff body configuration represented the baseline case of the 16.7 deg ramp with the height above ground being $h_r/d = 0.3$. The leading edge of the downstream wing was positioned at $2.40l$ behind the bluff body. This position corresponded to the downstream distance at which the experimental tests were carried out in the 2.1 m × 1.5 m wind tunnel.

8.4.1 Forces

The downforce coefficients in ground effect are presented in Fig. 8.17. In general, it can be seen that the computations have shown similar results to the experimental trends previously presented in Fig. 4.1. A decrease in downforce was predicted, as the oncoming flow progressed from FC1 to FC3. The computational curves also showed the fundamental characteristic of an increase in downforce to a certain ride height, after which the values then began to decrease. It can also be seen that with FC1 as the baseline, more downforce was lost at greater ride heights than was the case at lower ride heights. For example, at $h_r/c = 0.833$, there was a 39.1% decrease, while at $h_r/c = 0.401$ and $h_r/c = 0.153$, there were 21.5% and 4.63% decreases, respectively.

The computational drag coefficients in ground effect are shown in Fig. 8.18. Both curves confirm the expected result of an increase in drag with reducing ride height. It is also clear that the wing experienced more drag in FC3 than it did in FC1, except at the ride height of $h_r/c = 0.833$. At the lowest ride height for the curve representing FC3, there was a decrease in the value of the drag coefficient when compared to the previous

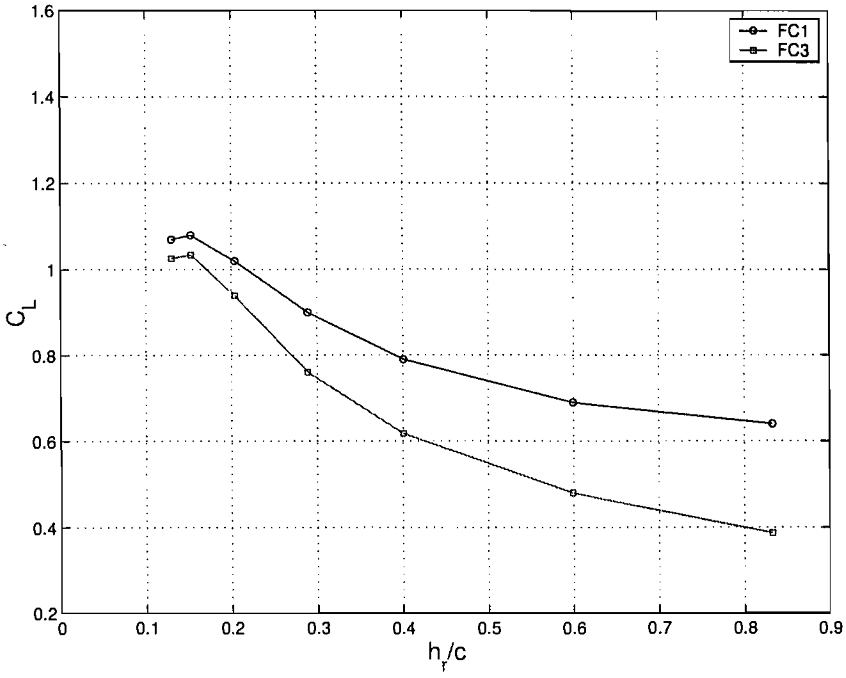

Figure 8.17: The computational downforce coefficients in ground effect for clean air (FC1) and dirty air (FC3) conditions.

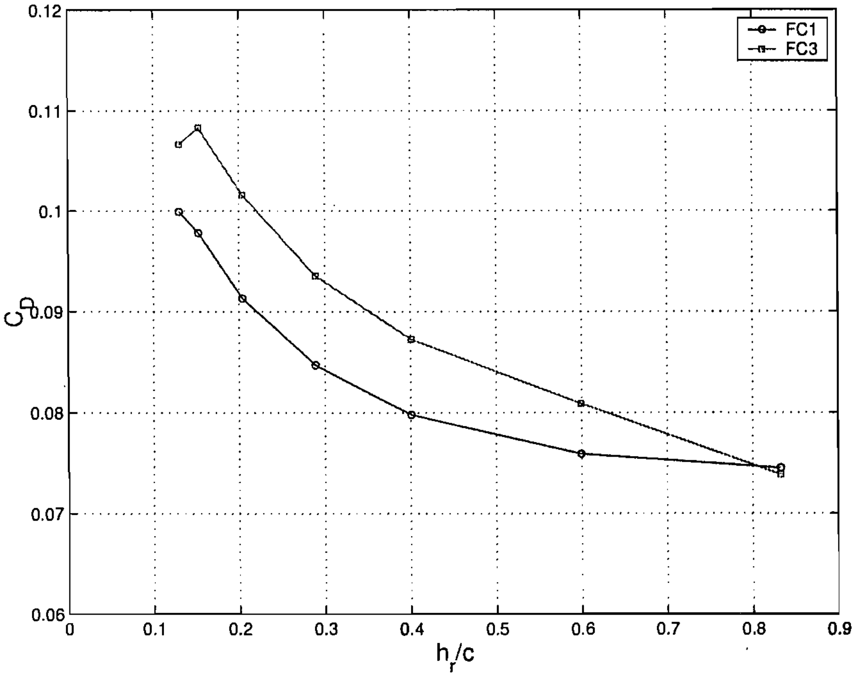

Figure 8.18: The computational drag coefficients in ground effect for clean air (FC1) and dirty air (FC3) conditions.

ride height.

The lift to drag ratios, which are plotted in Fig. 8.19, show that there is a deterioration in this variable when in dirty air. The curves also show that the ratio increased at lower ride heights, and then levelled off, before beginning to decrease for the case of FC1.

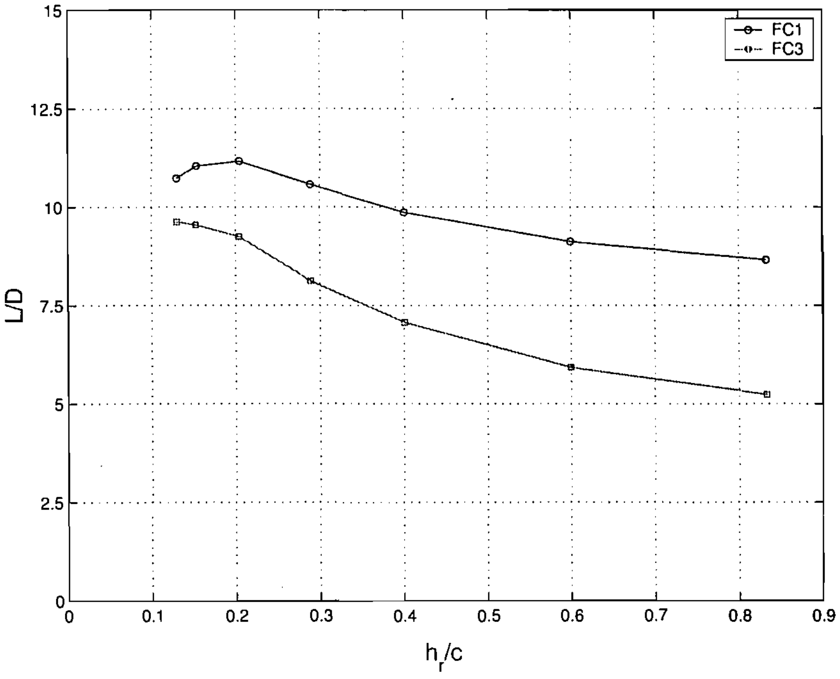

Figure 8.19: The computational lift to drag ratios in ground effect for clean air (FC1) and dirty air (FC3) conditions.

Lift curves for both the clean air and dirty air flow conditions are plotted in Fig. 8.20. Again, the trends predicted were similar to the experimental results. For the angles investigated, the wing essentially generated less downforce in FC3 than it did in FC1.

The corresponding drag curves are shown in Fig. 8.21. As with experiment, there was more drag produced in FC3 than there was in FC1, with the difference between the values increasing slightly as the angle of attack was increased. The lift to drag ratios confirmed the experimental trend of lower values at all angles of attack in FC3, Fig. 8.22. For the data plotted, the highest lift to drag ratio in FC1 occurred at 2.5 deg, while the highest in FC3 occurred at 5 deg. Although more data points need to be added, this result seems to suggest that as with experiment, the angle at which the maximum value occurred in

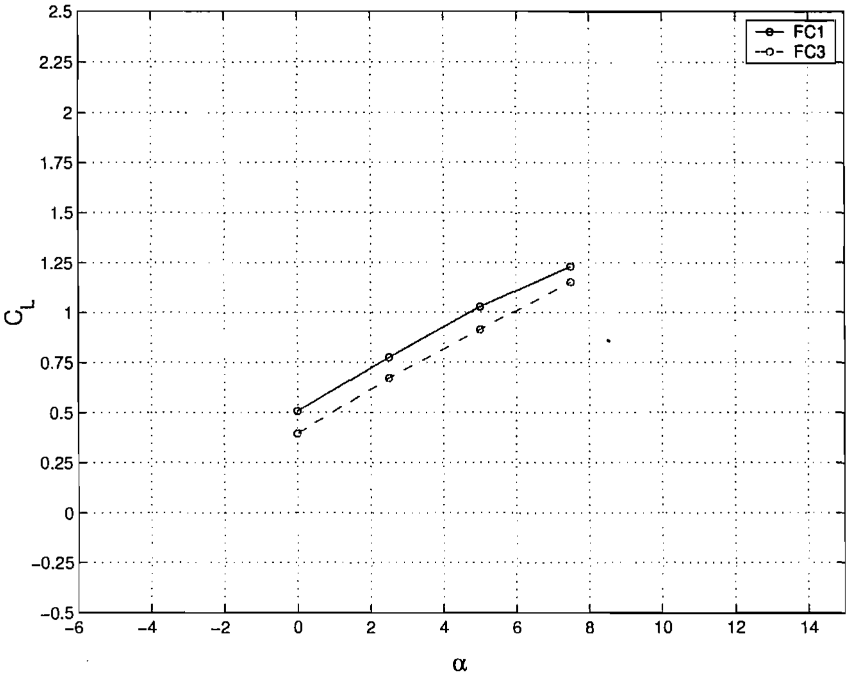

Figure 8.20: Lift curves at $h_r/c = 0.204$ for clean air (FC1) and dirty air (FC3) conditions.

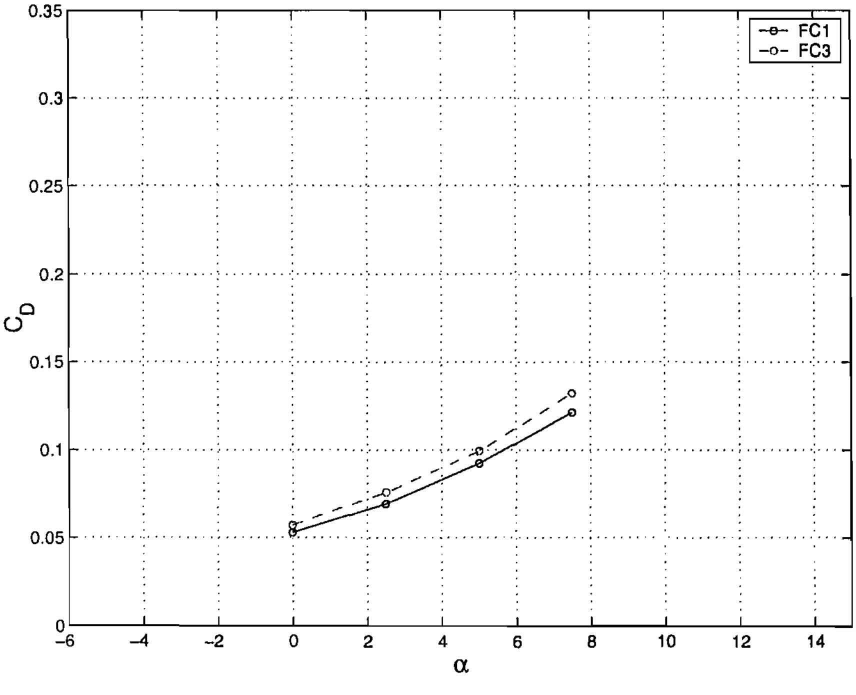

Figure 8.21: Drag curves at $h_r/c = 0.204$ for clean air (FC1) and dirty air (FC3) conditions.

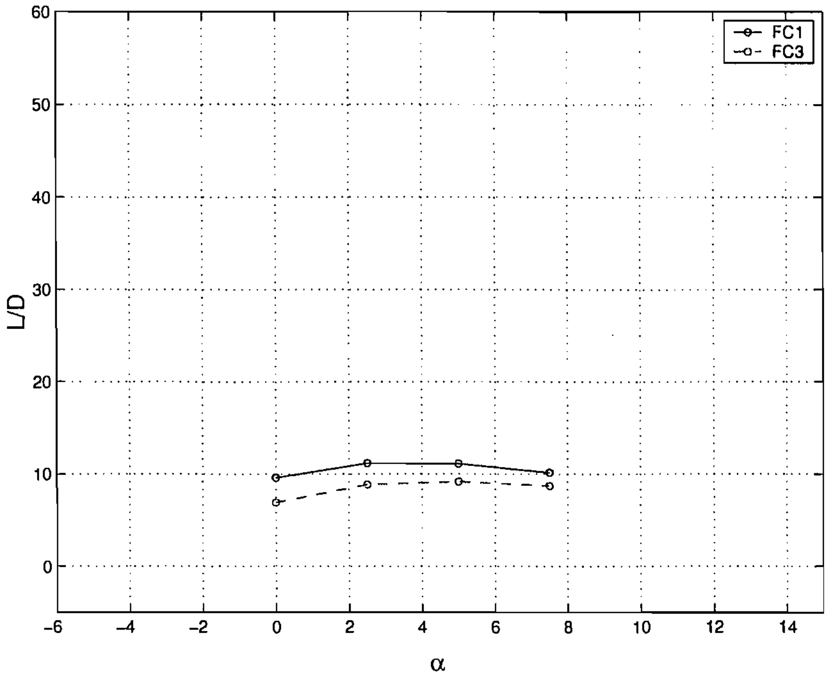

Figure 8.22: Lift to drag curves at $h_r/c = 0.204$ for clean air (FC1) and dirty air (FC3) conditions.

FC3 was greater than the angle at which it occurred in FC1.

8.4.2 Flow Visualisation

Suction surface flow visualisation images at the ride heights of $h_r/c = 0.833$, 0.401 and 0.204 are displayed in Figs. 8.23 to 8.25. Analysis of the data showed that the effect of placing the wing in FC3 was to delay trailing edge flow separation. At $h_r/c = 0.833$, separation has not explicitly commenced, but the delaying of the phenomenon is evidenced by the presence of straighter streamlines, closer to the midspan of the wing. The figures also highlighted the fact that trailing edge separation increased as the wing ride height was reduced, as was found experimentally by different authors [32, 35].

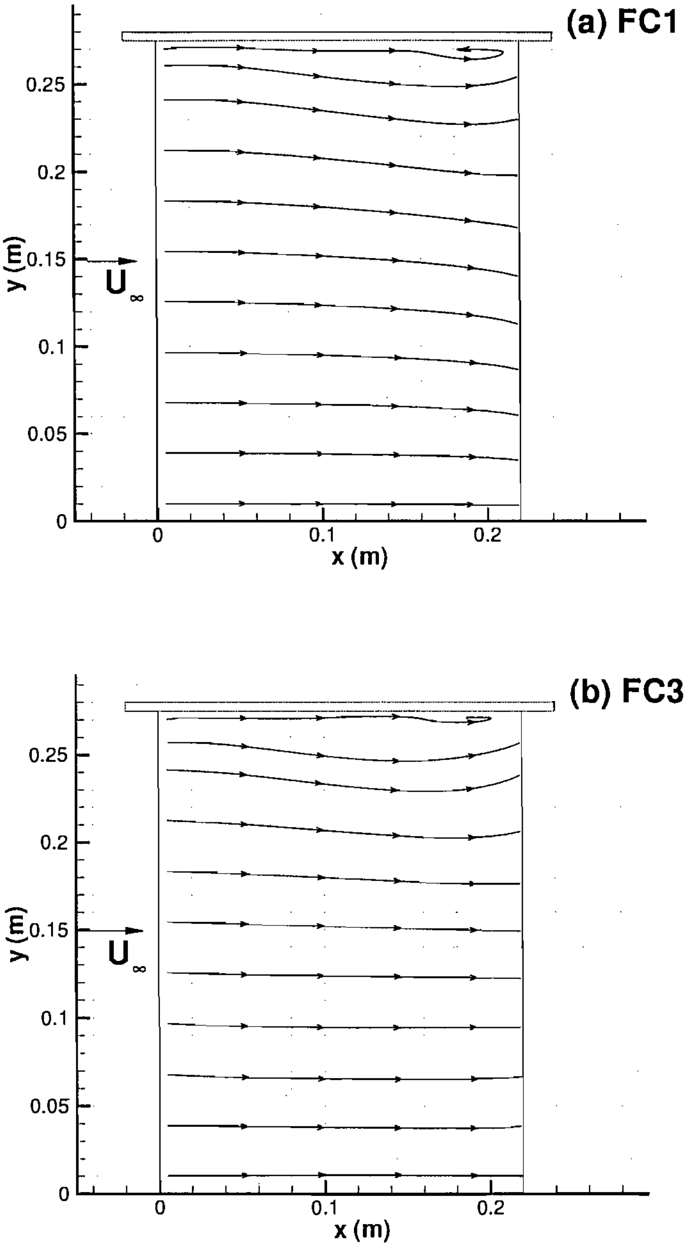

Figure 8.23: Suction surface streamlines at $h_r/c = 0.833$ in (a) FC1 and (b) FC3.

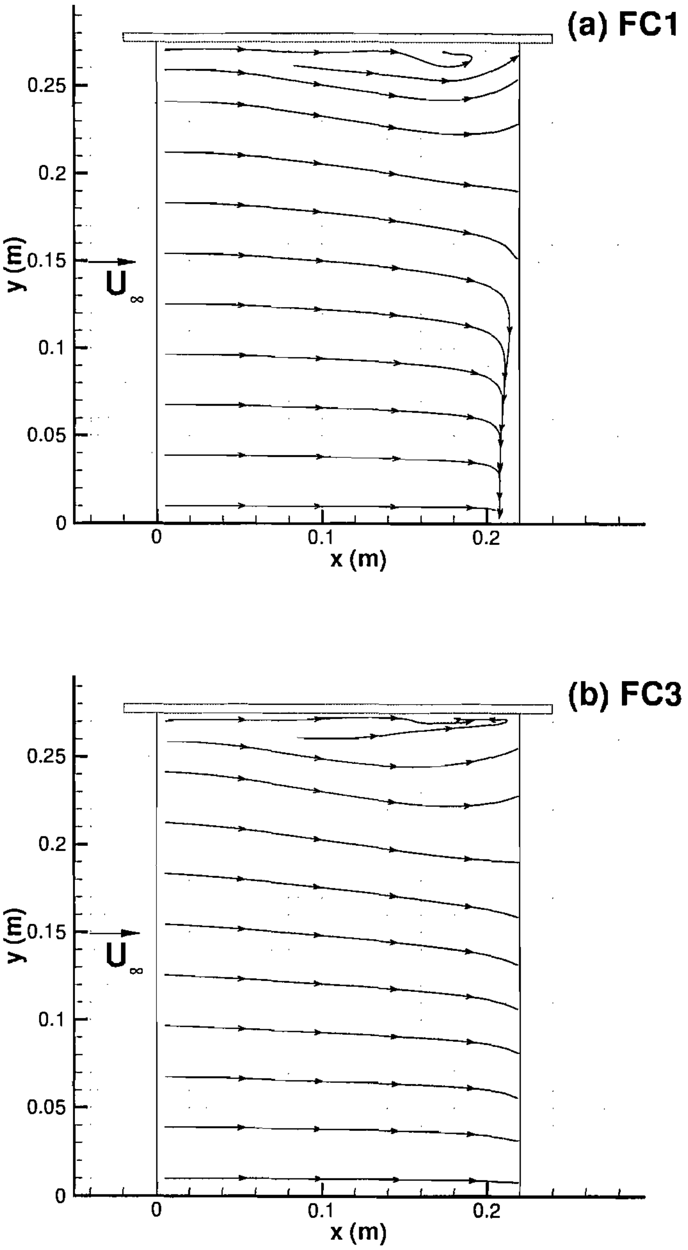

Figure 8.24: Suction surface streamlines at $h_r/c = 0.401$ in (a) FC1 and (b) FC3.

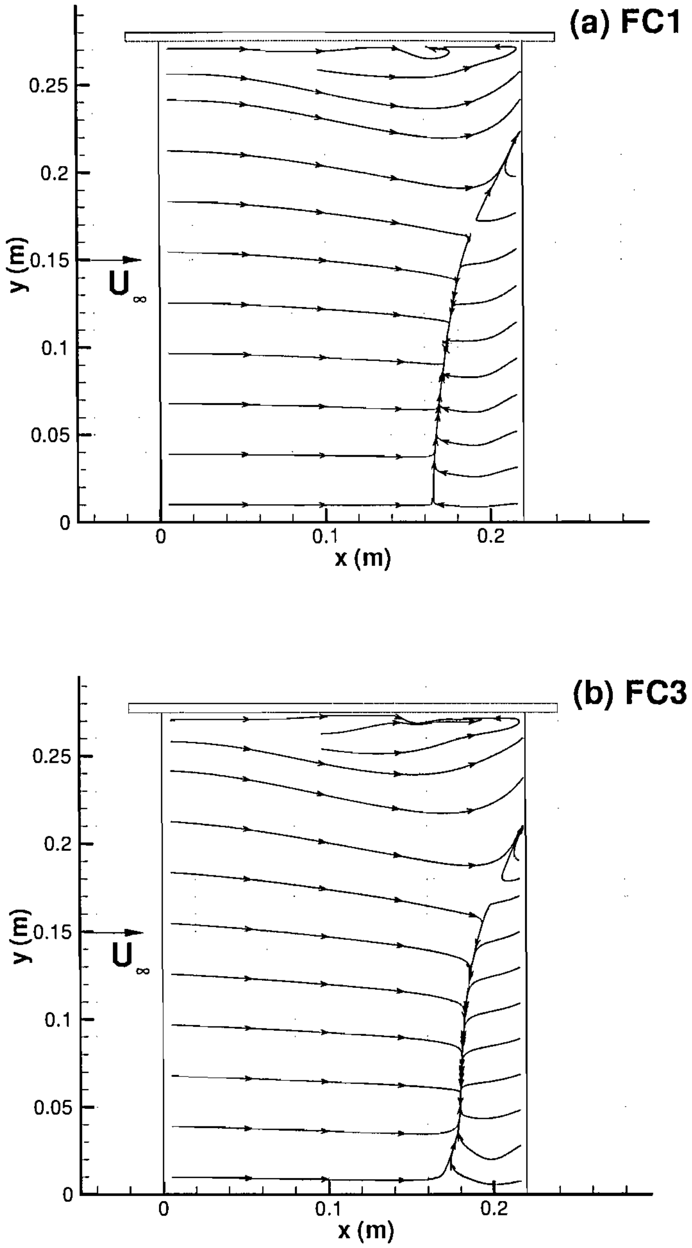

Figure 8.25: Suction surface streamlines at $h_r/c = 0.204$ in (a) FC1 and (b) FC3.

8.4.3 Pressures

Computational pressure distribution data at ride heights of h_r/c = 0.833, 0.401 and 0.204 are presented in Figs. 8.26 to 8.28. At each ride height, plots are displayed for 2z/b = 0.09, 0.49 and 0.89, and x/c = 0.25. As with the experimental results, changing the flow from FC1 to FC3 produced a decrement in the pressure distribution for both surfaces of the wing, at each station investigated.

At the ride height of h_r/c = 0.833, the data shows quite explicitly, the dramatic loss in loading from sections close to the centre of the wing. Similar to experiment, at this ride height, the outer portions of the wing generated more downforce than sections close to the semi-span. At h_r/c = 0.401 and 0.204, the load generated by the wing continued to increase in both flow conditions. In FC3, however, the load deficit in the region of the wing semi span was not as great as was the case at h_r/c = 0.833. This deficiency decreased with decreasing ride height.

As with the experimental investigation, the 2-D sectional downforce coefficients were computed for each of the spanwise stations. The results are presented in Table 8.1. It can be seen that for the cases investigated, the amount of downforce lost decreased with increasing spanwise distance at a given ride height. Additionally, the change in downforce at a given station decreased as the ride height was reduced. The trends obtained from examination of the computational pressures were similar to those obtained from experiment.

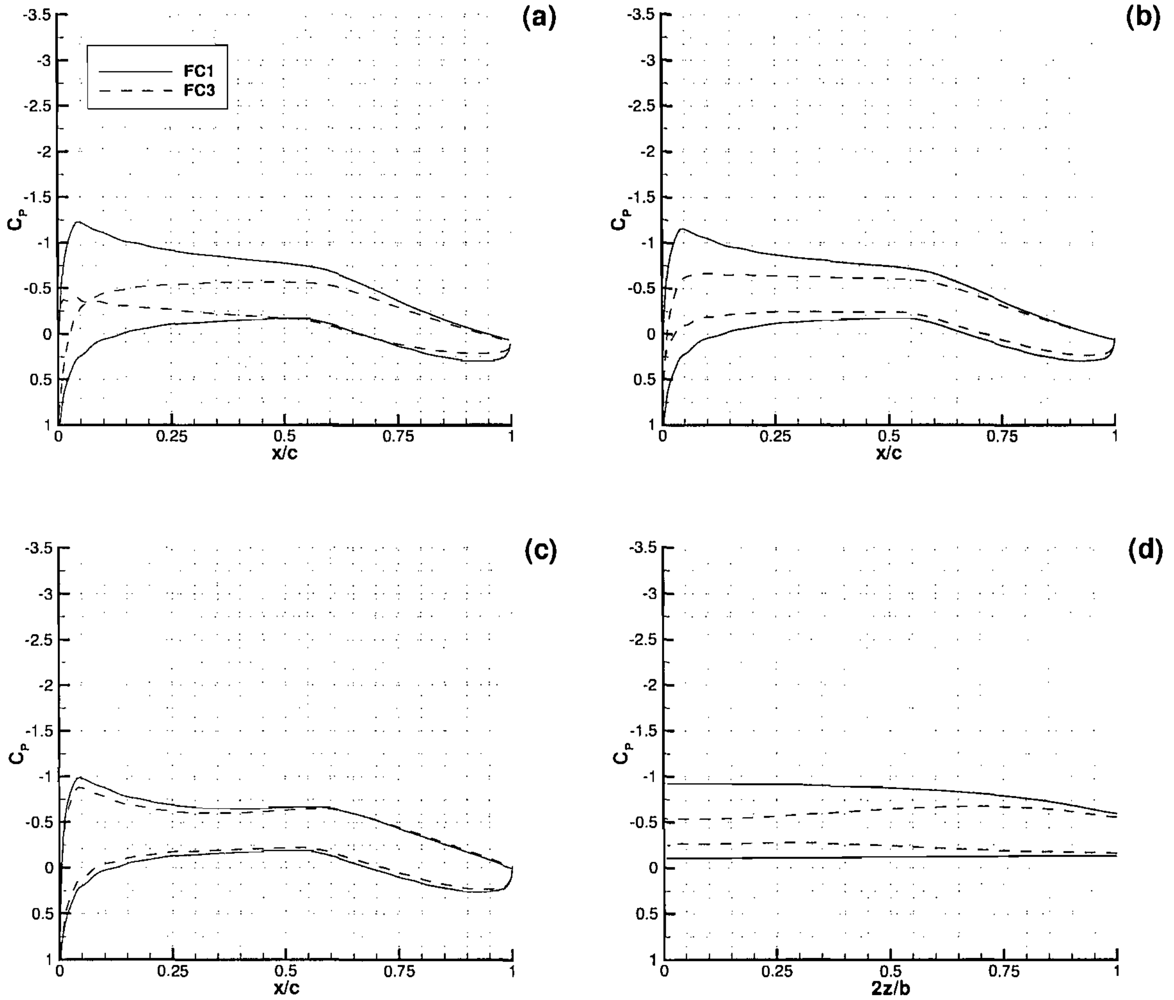

Figure 8.26: The pressure distributions at $h_r/c = 0.833$ in FC1 and FC3, at 2z/b = 0.09 (a), 0.49 (b), 0.89(c) and x/c = 0.25 (d).

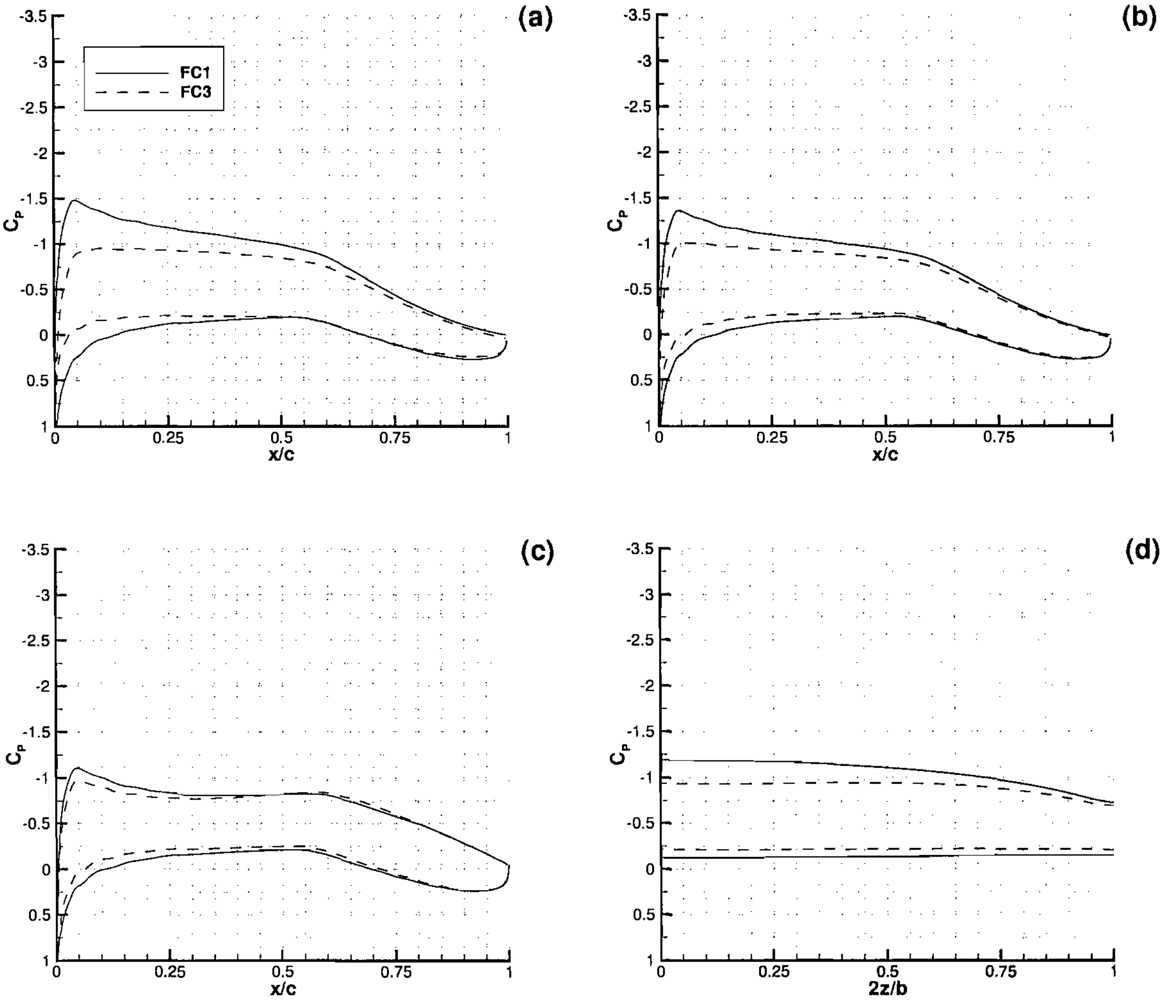

Figure 8.27: The pressure distributions at $h_r/c = 0.401$ in FC1 and FC3, at 2z/b = 0.09 (a), 0.49 (b) and 0.89(c) and x/c = 0.25.

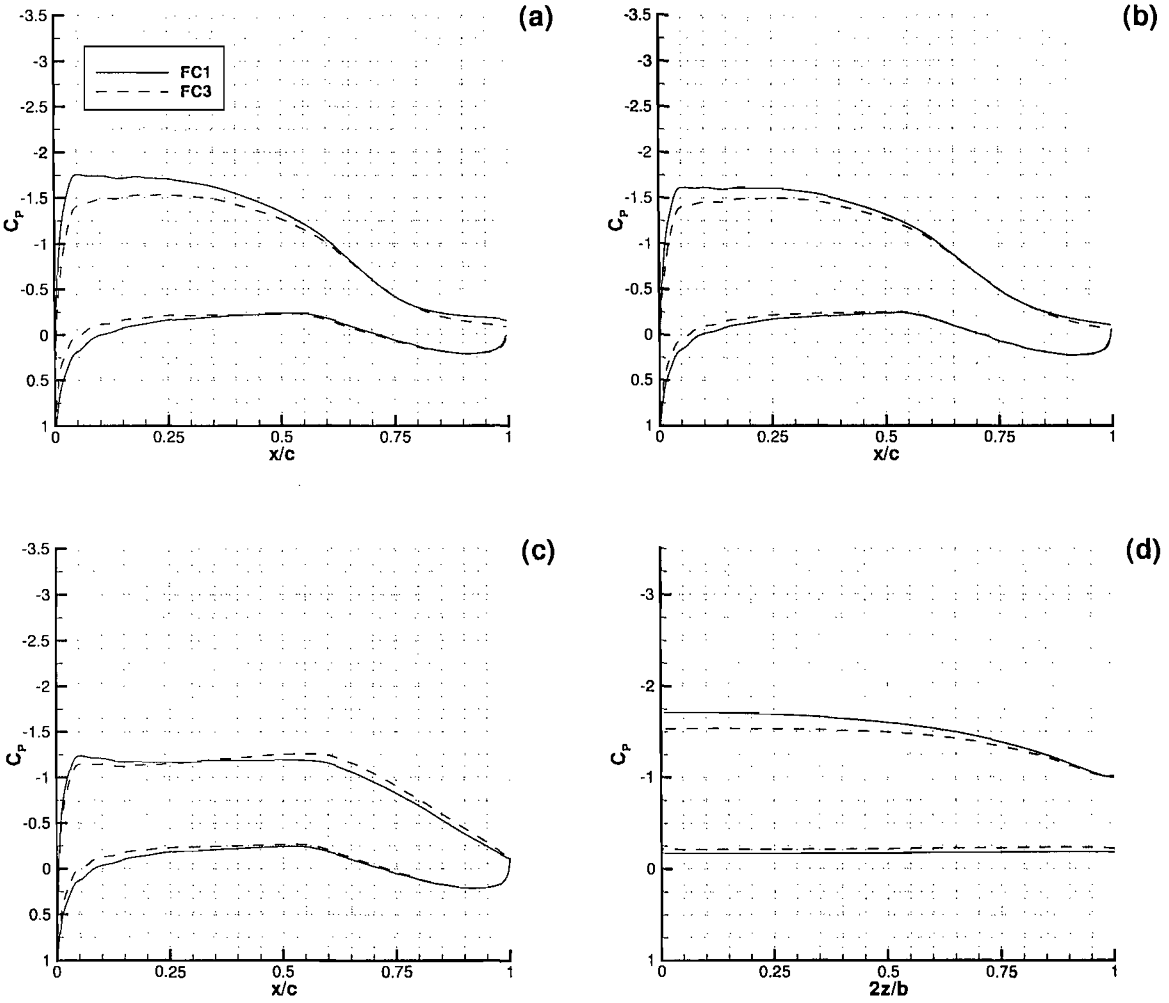

Figure 8.28: The pressure distributions at $h_r/c = 0.204$ in FC1 and FC3, at 2z/b = 0.09 (a), 0.49 (b) and 0.89(c) and x/c = 0.25.

$h_r/c = 0.833$			
	2z/b = 0.09	2z/b = 0.49	2z/b = 0.89
C_l: FC1	0.684	0.646	0.566
C_l: FC3	0.268	0.368	0.490
$\%\Delta C_l$	60.8	43.0	13.4
$h_r/c = 0.401$			
C_l: FC1	0.843	0.788	0.684
C_l: FC3	0.585	0.605	0.609
$\%\Delta C_l$	30.6	23.2	11.0
$h_r/c = 0.204$			
C_l: FC1	1.06	1.02	0.907
C_l: FC3	0.918	0.920	0.896
$\%\Delta C_l$	13.4	9.80	1.21

Table 8.1: Sectional downforce coefficient values for each of the ride heights investigated in CFD.

8.4.4 Flow Field

The flow field downstream of the wing was examined by producing contours of vorticity at x/c = 1.5, and contours of total pressure at x/c = 1.5, 2.25 and 3, for the ride heights of $h_r/c = 0.833$ and 0.204. These specific heights were chosen because they represented cases from the upper and lower regions of the ride height range investigated. Observation of the vorticity contours, Fig. 8.29, will show that there were no significant differences to be noted. The maximum vorticity decreased slightly from $\frac{\omega c}{U_\infty} = 12.15$ in FC1 to $\frac{\omega c}{U_\infty} = 11.85$ in FC3.

Using total pressure contours, at x/c = 1.5 for $h_r/c = 0.833$, Fig. 8.30, the wake of the wing in clean air is highlighted in FC1, while the wake of the wing and the vortex of the upstream diffuser are highlighted in FC3. Sole consideration of the wake of the wing in both flow conditions showed that there were some important differences to be noted. Firstly, the upper endplate vortex that was present in FC1 [33] seemed to have disappeared or to have been significantly reduced in FC3. This was also the case at x/c = 2.25, Fig. 8.31, and x/c = 3, Fig. 8.32. Secondly at all downstream positions, the area occupied by the wing's wake seemed to be larger in FC3 than it was in FC1. Lastly, in FC3, the wake of the wing appeared to be distorted by the close proximity of the diffuser

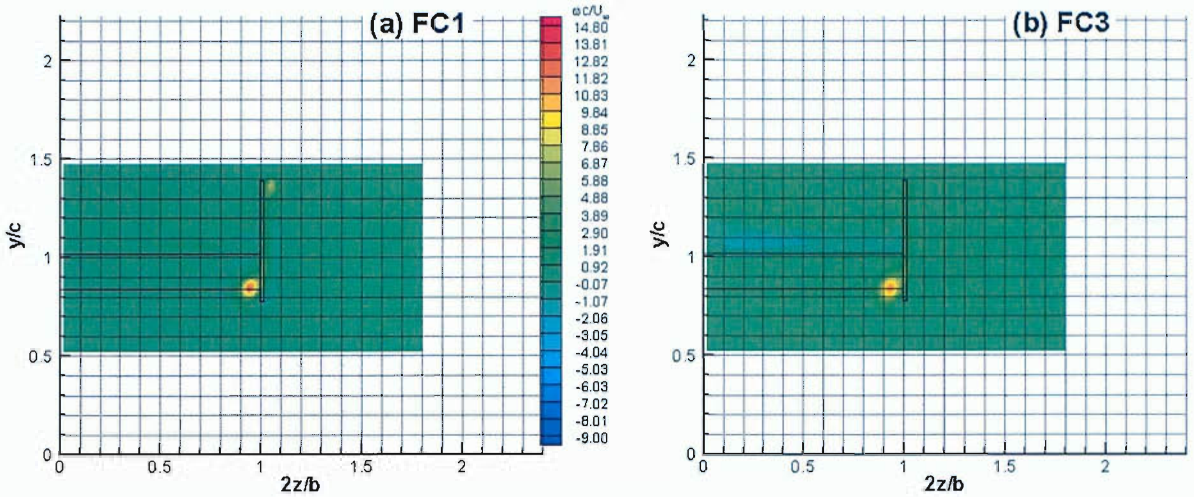

Figure 8.29: Contours of streamwise vorticity at x/c = 1.5 for the ride height of $h_r/c = 0.833$.

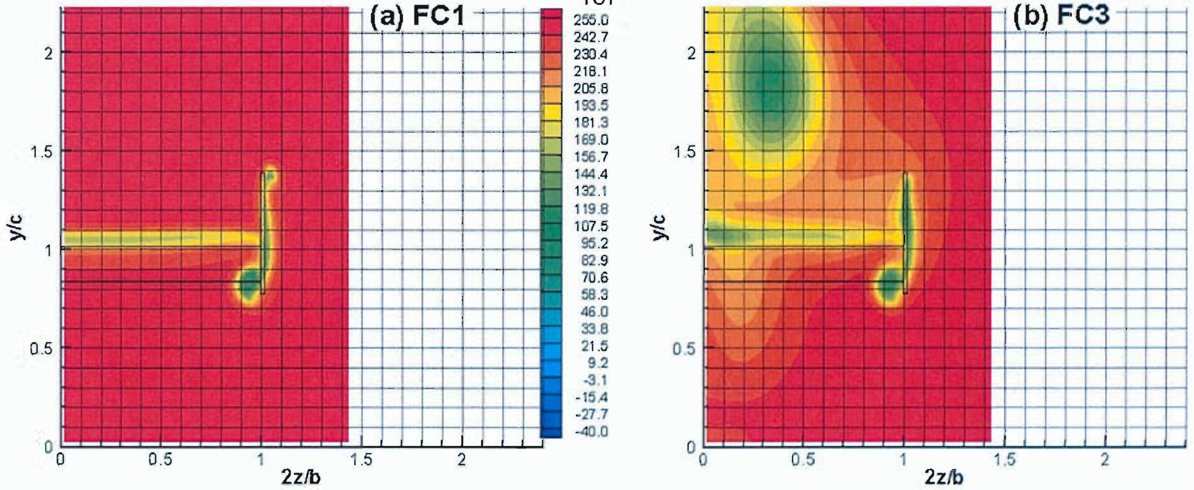

Figure 8.30: Contours of total pressure highlighting the wing's wake at x/c = 1.5 for the ride height of $h_r/c = 0.833$.

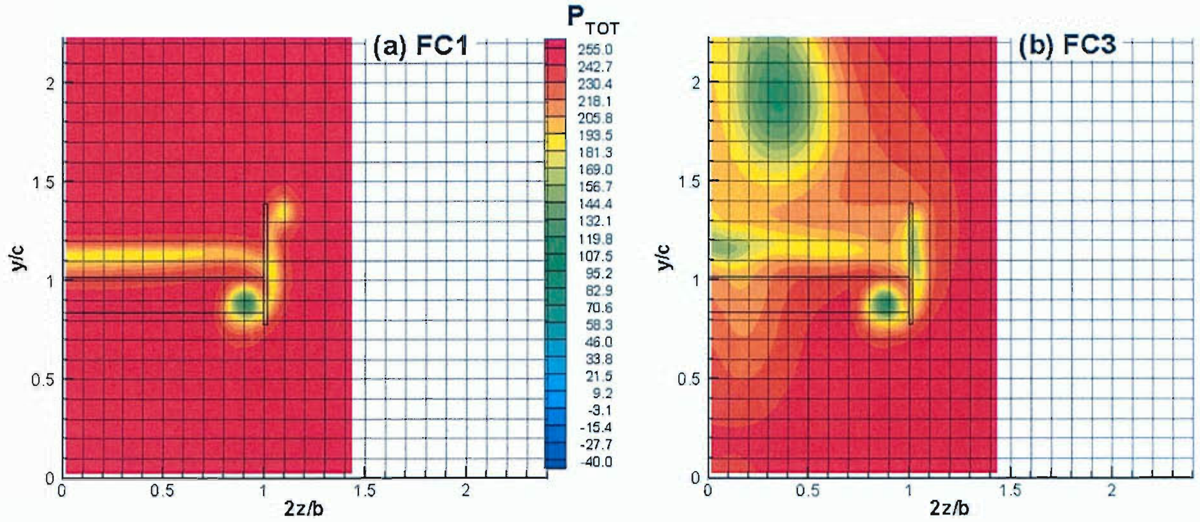

Figure 8.31: Contours of total pressure highlighting the wing's wake at x/c = 2.25 for the ride height of $h_r/c = 0.833$.

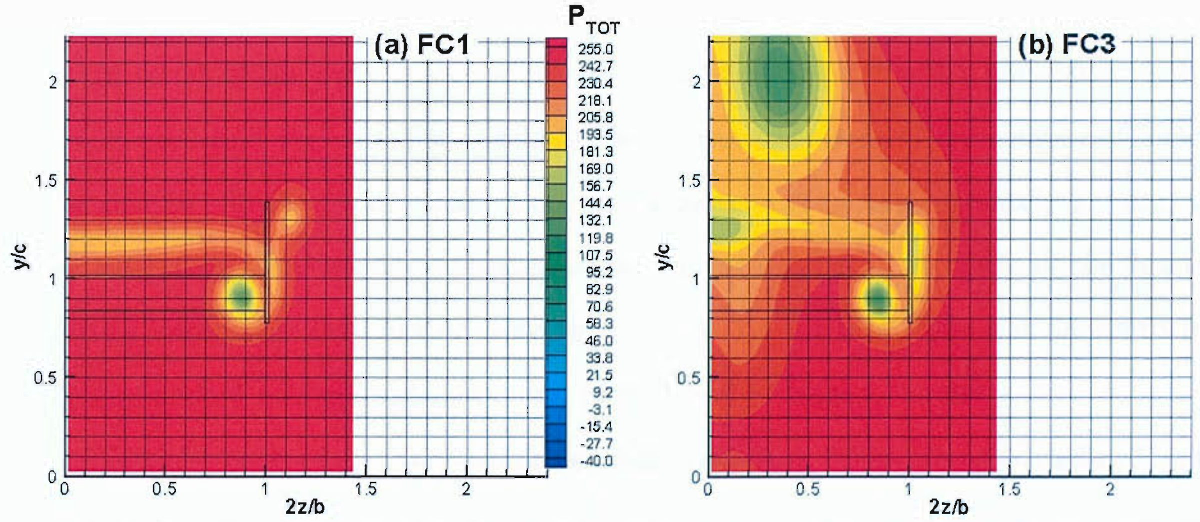

Figure 8.32: Contours of total pressure highlighting the wing's wake at x/c = 3 for the ride height of $h_r/c = 0.833$.

vortex.

The approximate centres of the main vortex in each flow condition were extracted from velocity vector data at each plane. The values are presented in Table 8.2. An analysis of the data showed that in general, the vortex of the wing tended to be displaced more towards 2z/b = 0 when it was behind the upstream diffuser bluff body. More specifically, at x/c = 1.5, there was an inward movement equivalent to 5.5 mm in metric units, when the flow changed from FC1 to FC3. At x/c = 2.25 and x/c = 3, the corresponding movements were 8.3 mm and 11 mm respectively.

FC1: $h_r/c = 0.833$		
x/c	2z/b	y/c
1.5	0.95	0.86
2.25	0.92	0.90
3	0.89	0.92
FC3: $h_r/c = 0.833$		
x/c	2z/b	y/c
1.5	0.93	0.86
2.25	0.89	0.89
3	0.85	0.91

Table 8.2: The approximate downstream vortex centres at $h_r/c = 0.833$, in FC1 and FC3.

In terms of the overall horizontal movement between x/c = 1.5 and x/c = 3, it can be deduced that the vortex travelled further towards the root of the wing in FC3 than it did in FC1. In the former case, there was a movement of approximately 22 mm, while for the latter, there was a corresponding movement of 17 mm. Analysis of the figures for vertical movement showed that between x/c = 1 and x/c = 3, there was an approximate 17 mm and 14 mm upward movement in FC1 and FC3 respectively.

Vorticity contours for the lower ride height of $h_r/c = 0.204$ are presented in Fig. 8.33. The only differences that could be noted are that the area highlighting the main vortex appeared to be slightly bigger in FC3 than it was in FC1, and that the small area of positive vorticity that was present at the top, outer edge of the endplate in FC1, was non existent in FC3. For this case, the maximum vorticity increased slightly from $\frac{\omega c}{U_\infty} = 14.64$

in FC1 to $\frac{\omega c}{U_\infty} = 14.73$ in FC3.

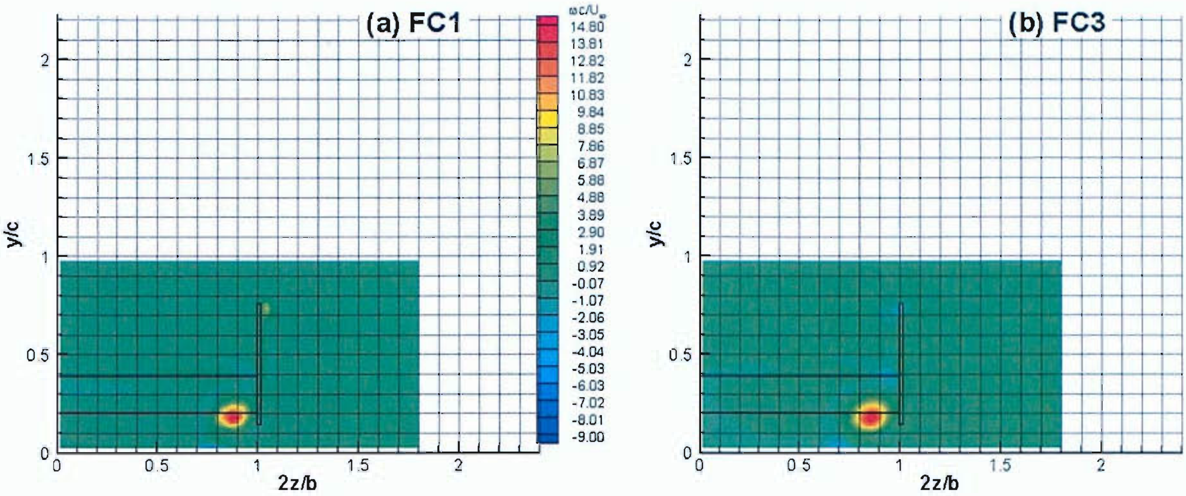

Figure 8.33: Contours of streamwise vorticity at x/c = 1.5 for the ride height of $h_r/c = 0.204$.

The total pressure contours for this ride heitht are presented in Figs. 8.34 to 8.36. Again, the disappearance of the upper endplate vortex was evident in FC3, as was the apparent increase in the thickness of the wing's wake. At this ride height, the wake also seemed to be less distorted by the presence of the diffuser vortex.

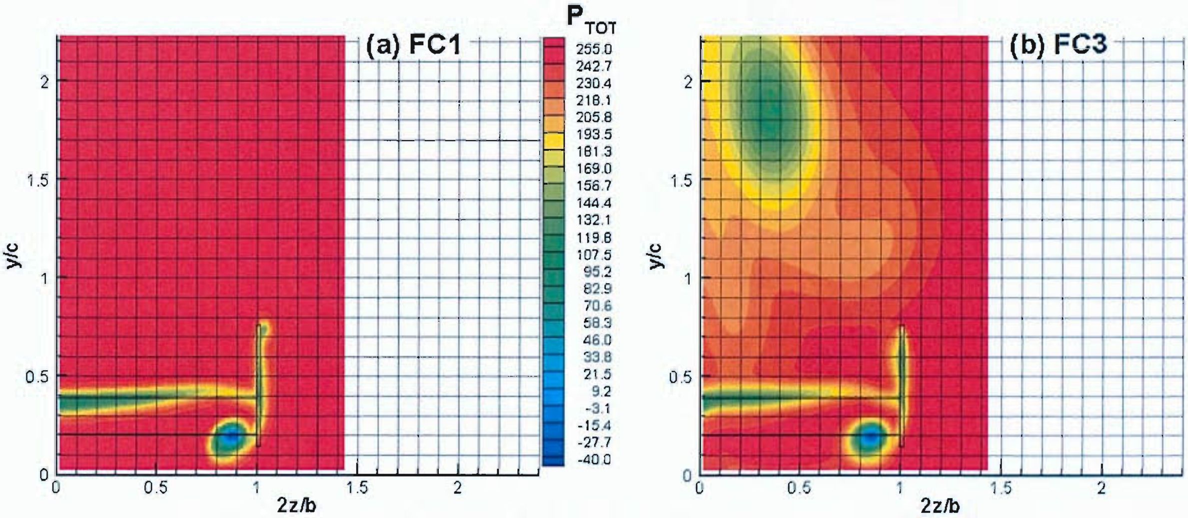

Figure 8.34: Contours of total pressure highlighting the wing's wake at x/c = 1.5 for the ride height of $h_r/c = 0.204$.

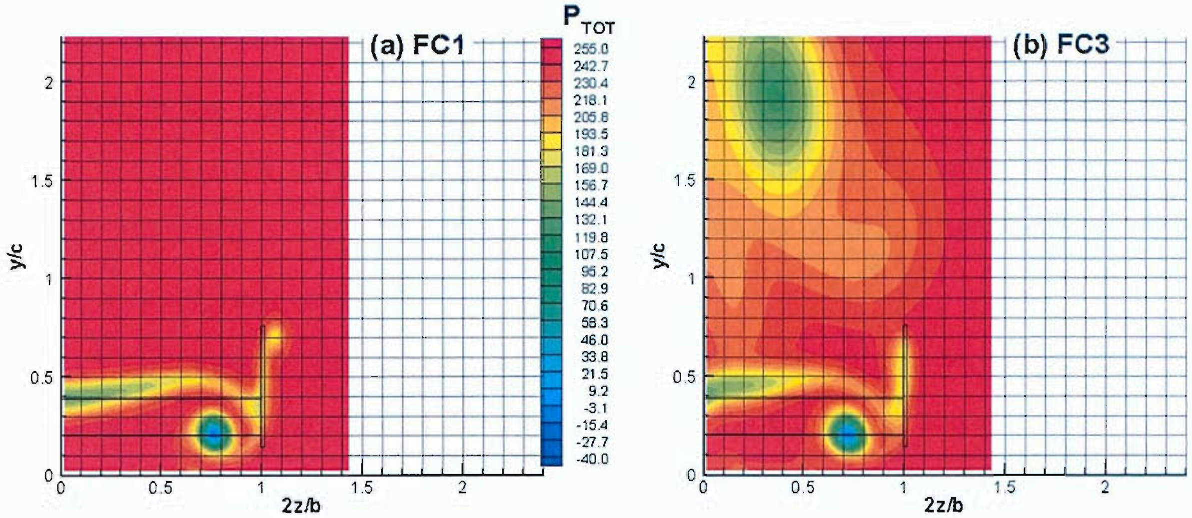

Figure 8.35: Contours of total pressure highlighting the wing's wake at x/c = 2.25 for the ride height of $h_r/c = 0.204$.

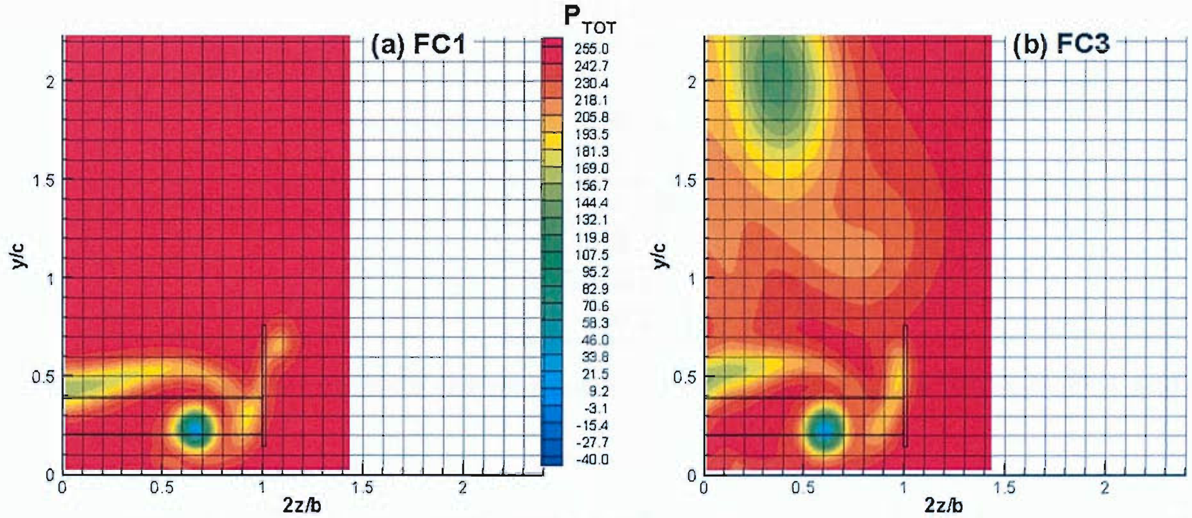

Figure 8.36: Contours of total pressure highlighting the wing's wake at x/c = 3 for the ride height of $h_r/c = 0.204$.

The approximate centres of the vortex at this lower ride height (obtained from the velocity vectors on each data plane) are outlined in Table 8.3. Again, there was a movement of the vortex towards the root of the wing, as the flow changed from FC1 to FC3. At x/c = 1.5, there was a metric equivalent, inward translation of 8.3 mm, while at x/c = 2.25 and x/c = 3, the corresponding translations were 14 mm in each case. Vertically, there was a metric equivalent, upward movement of 11 mm between x/c = 1.5 and x/c = 3, for both cases.

A comparison of the data relating to the overall vortex movement at both ride heights led to the observation that there was greater lateral movement at the lower ride height, than there was at the higher. For example, in FC1 at $h_r/c = 0.833$, there was an approximate overall 17 mm inward movement, while at $h_r/c = 0.204$, the corresponding movement was approximately 61 mm. It was also confirmed that the vertical movement of the vortex was slightly less at the lower ride height than it was at the higher. There was an approximate vertical movement of 13 mm and 9 mm at $h_r/c = 0.833$ and $h_r/c = 0.204$ respectively.

FC1: $h_r/c = 0.204$		
x/c	2z/b	y/c
1.5	0.88	0.21
2.25	0.76	0.23
3	0.66	0.25
FC3: $h_r/c = 0.204$		
x/c	2z/b	y/c
1.5	0.85	0.21
2.25	0.71	0.23
3	0.61	0.25

Table 8.3: The approximate downstream vortex centres at $h_r/c = 0.204$, in FC1 and FC3.

Comparisons of the centreline wake profiles downstream of the wing are presented in Figs. 8.37 to 8.39. The data is plotted for the ride heights of $h_r/c = 0.833$, 0.401 and 0.204. In general it can be concluded that the development of the wake was influenced by the presence of the flow generated by the upstream body. There was a slowing of the transporting fluid in FC3, with the slowing gradually reducing as the ride height of the wing was reduced. A thicker wake was also evident in FC3, with growth appearing to occur mainly via the upper boundary.

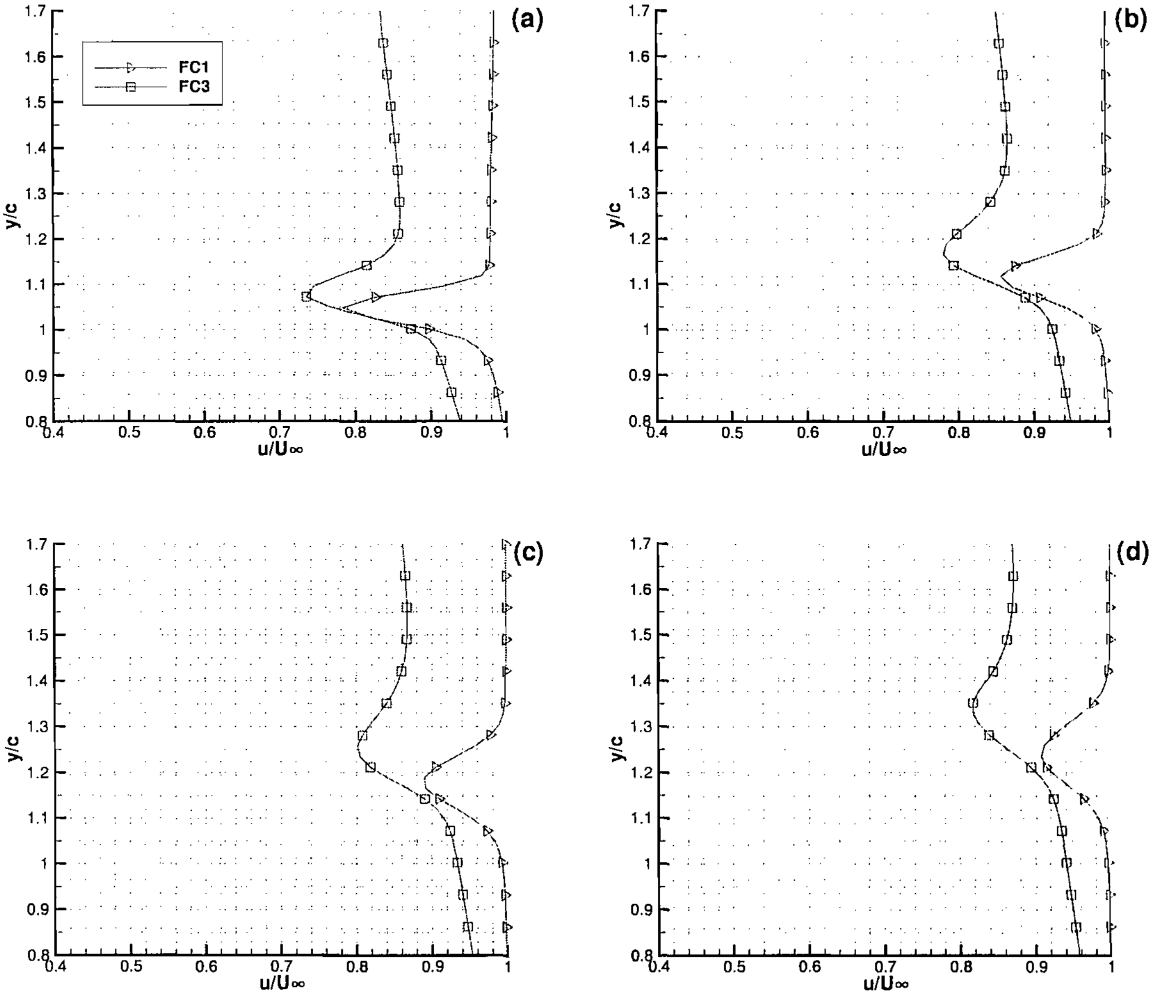

Figure 8.37: A comparison of centreline wake profiles for $h_r/c = 0.833$ at x/c = 1.5 (a), x/c = 2.25 (b), x/c = 3 (c) and x/c = 3.75 (d), for FC1 and FC3.

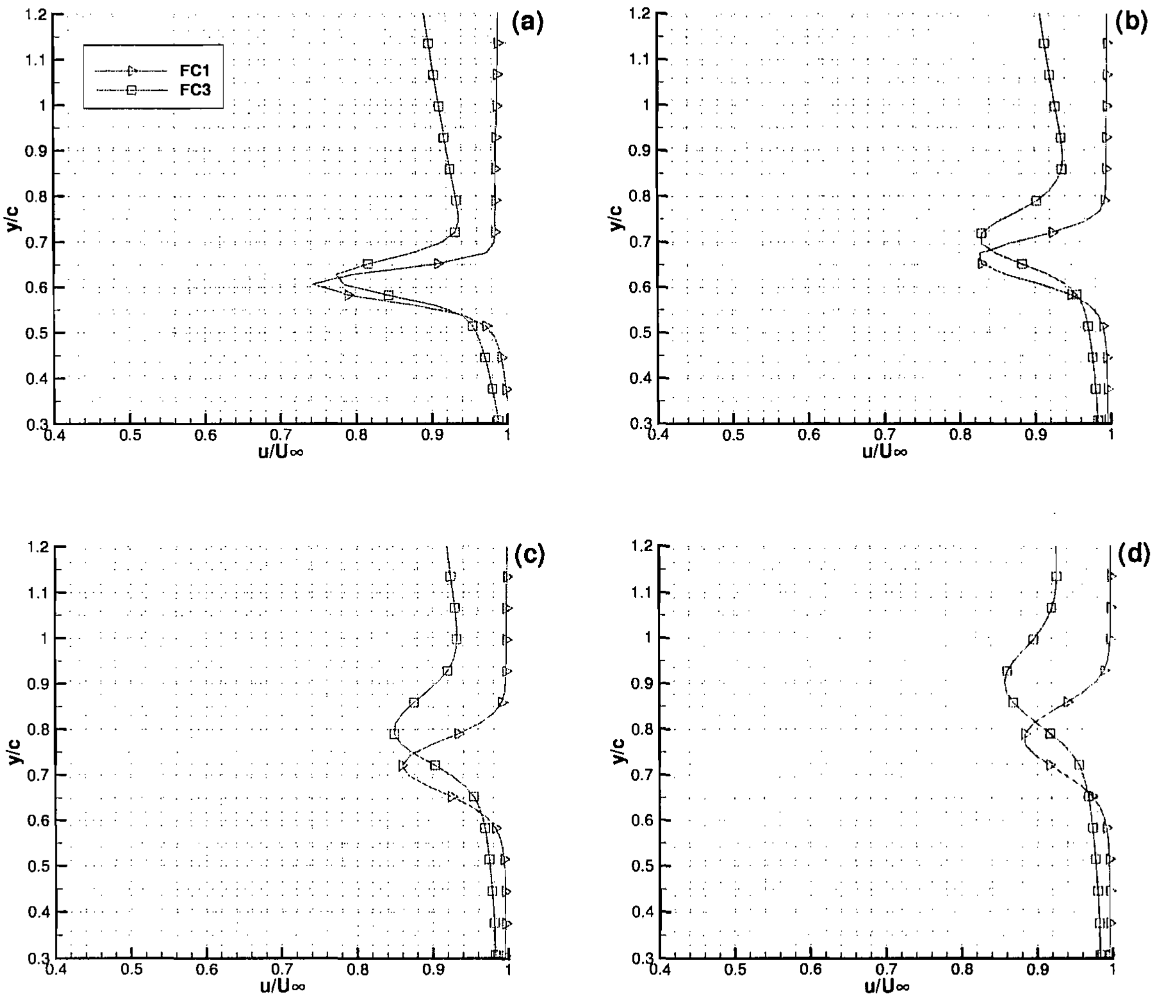

Figure 8.38: A comparison of centreline wake profiles for $h_r/c = 0.401$ at x/c = 1.5 (a), x/c = 2.25 (b), x/c = 3 (c) and x/c = 3.75 (d), for FC1 and FC3.

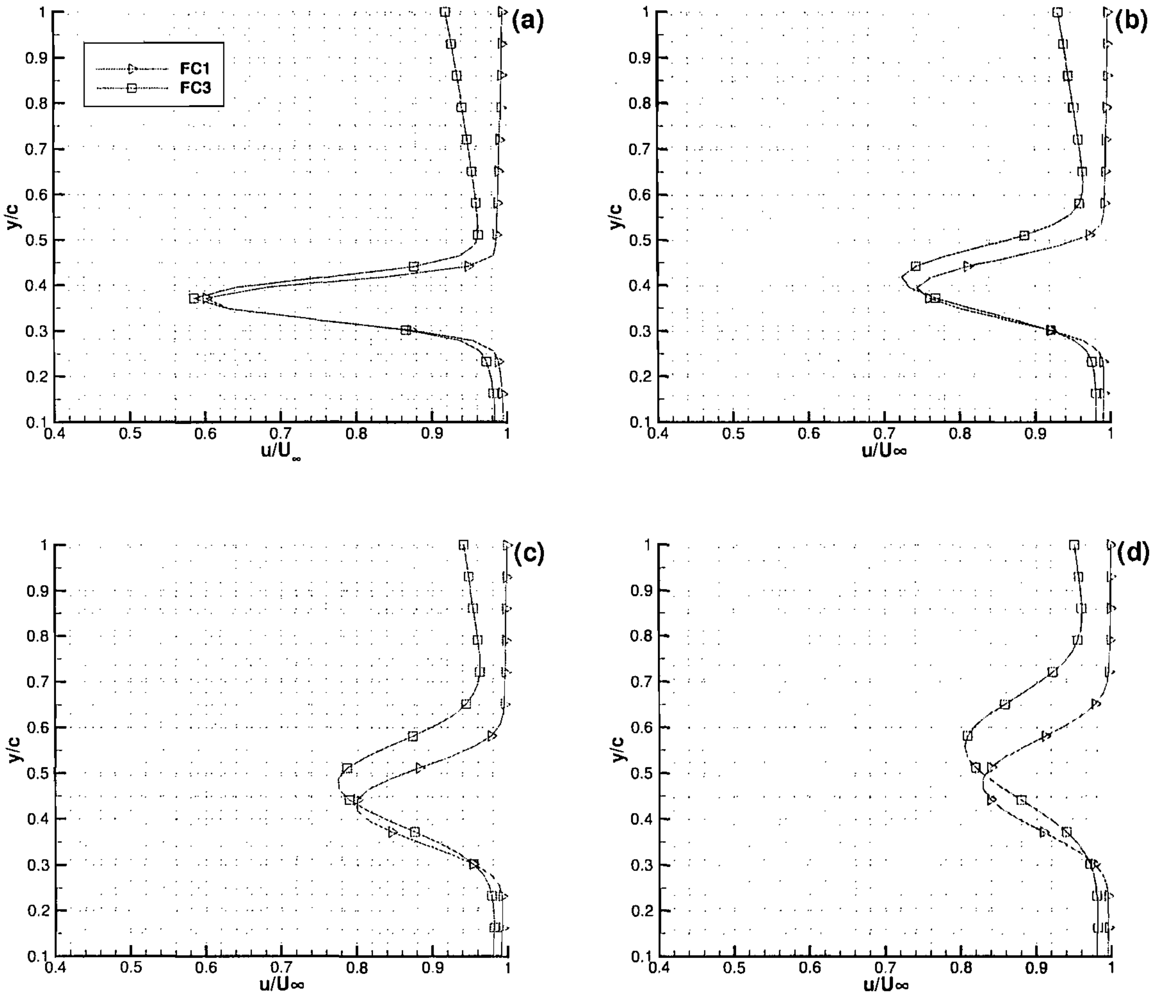

Figure 8.39: A comparison of centreline wake profiles for $h_r/c = 0.204$ at x/c = 1.5 (a), x/c = 2.25 (b), x/c = 3 (c) and x/c = 3.75 (d), for FC1 and FC3.

8.5 The Effect of a Change in the Upstream Diffuser Ramp Angle

This section will present computational results that highlight the aerodynamic changes experienced by the downstream wing when the angle of the upstream diffuser ramp was changed. The ramp angles investigated were the baseline configuration of 16.7 deg, and the 5 deg configuration. These values represented the upper and lower limits of the diffuser angles investigated in the experimental test program.

8.5.1 Forces

The downforce coefficients experienced by the wing when behind the two configurations are plotted in Fig. 8.40. It can be seen that for the majority of ride heights, more downforce was produced behind the diffuser with the 5 deg ramp, than was the case with the 16.7 deg ramp. For the range $h_r/c = 0.204$ to $h_r/c = 0.153$ both curves converge, indicating similar values of downforce. The convergence of the curves was quite similar to the trend found in the experimental tests, Fig. 5.1, except for the fact that it occurred at a lower ride height with the computations. It was not possible to investigate whether the curves would have completely crossed each other as the CFD files experienced large oscillations in the forces being computed at very low ride heights, owing to greatly increased flow separation. It was felt that an unsteady analysis would have been needed at this point.

The corresponding drag coefficients are plotted in Fig. 8.41. The curves show that at all ride heights, slightly more drag was produced behind the 16.7 deg ramp diffuser. Additionally, the incremental change in the coefficient was greater above $h_r/c = 0.4$, than it was below it. The lift to drag ratios were then examined, and are plotted in Fig. 8.42. The resulting computational trend confirmed the experimental outcome, in that the downstream wing was more efficient when in the flow produced by the 5 deg ramp diffuser. The efficiency of the wing also improved gradually as its ride height was

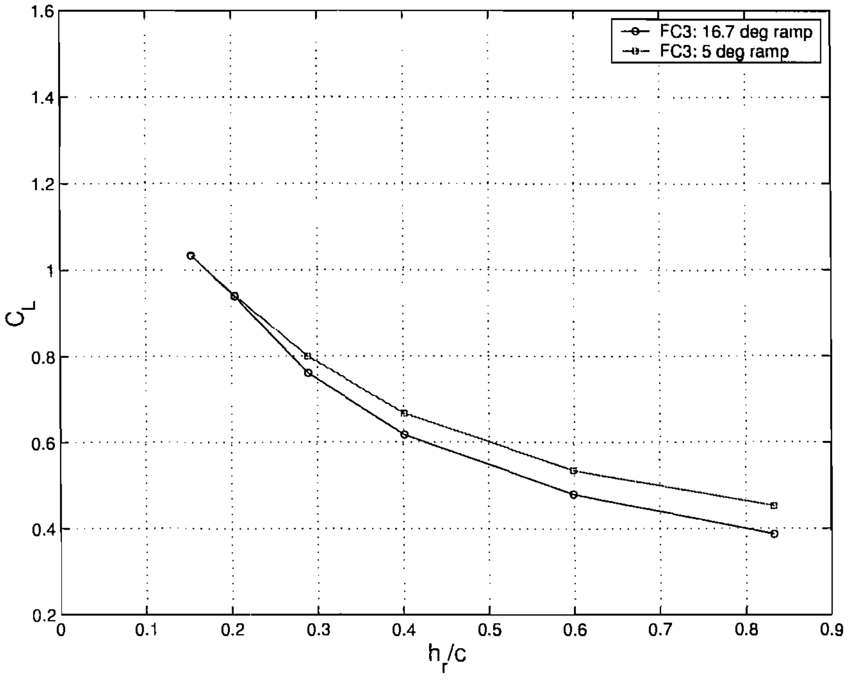

Figure 8.40: Downforce coefficients while varying the diffuser ramp angle.

reduced.

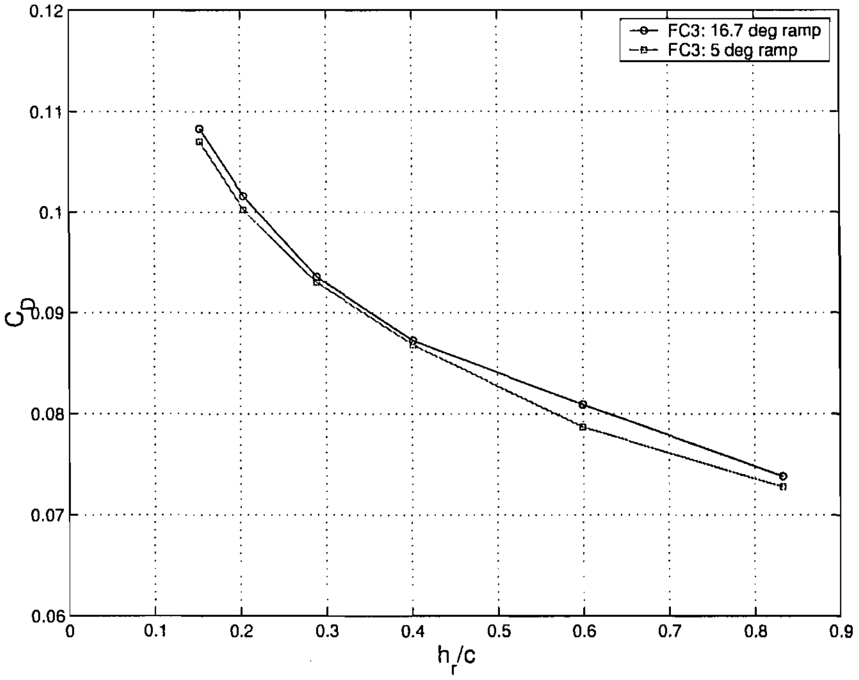

Figure 8.41: Drag coefficients while varying the diffuser ramp angle.

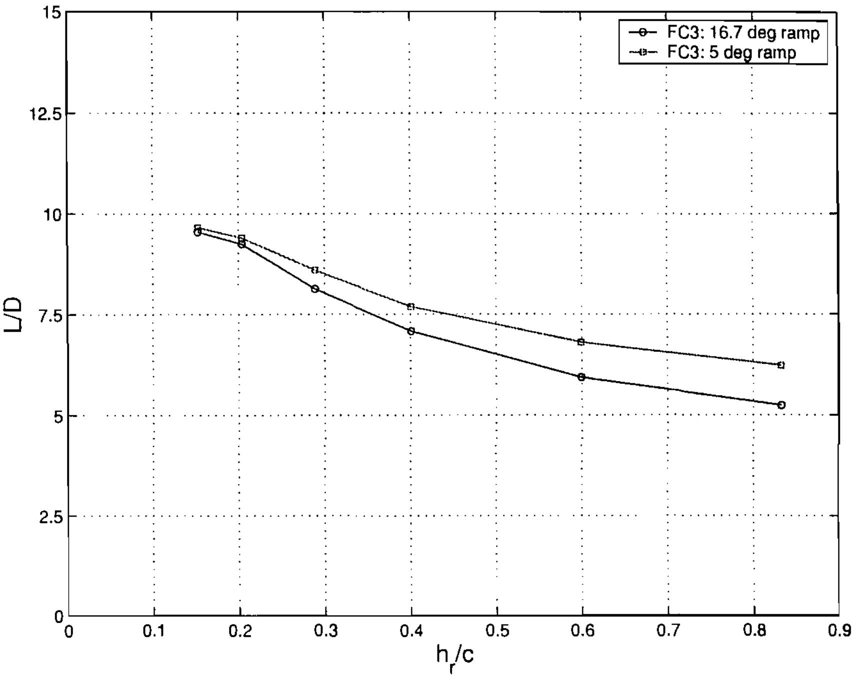

Figure 8.42: Lift to drag ratios while varying the diffuser ramp angle.

8.5.2 Flow Visualisation

Suction surface flow visualisation images from the wing downstream of the two diffuser configurations are presented in Figs. 8.43 to 8.45. The ride heights investigated were $h_r/c = 0.833$, 0.401 and 0.204. At the greatest ride height, the only discernable difference appeared to be that the streamlines between the wing quarter span and mid span showed outward movement of the surface flow when behind the diffuser with the 5 deg ramp. In contrast, the streamlines between the quarter span and the endplate appeared to be similar for both cases. At the lower ride height of $h_r/c = 0.401$, Fig. 8.44, both sets of streamlines also appeared to be similar.

At $h_r/c = 0.204$, Fig. 8.45, trailing edge separation has clearly been established, and can clearly be identified for both cases. The regions of separation, however, show distinct differences. With the wing downstream of the 5 deg ramp, a node point was present close to the mid span. The node was similar to experimental flow features reported by Winkelmann [78] for separated flow over rectangular wings at high angles of attack. The node was non-existent when the wing was placed in the flow emanating from the 16.7 deg diffuser, although a slight curling of the streamlines was evident in the same vacinity.

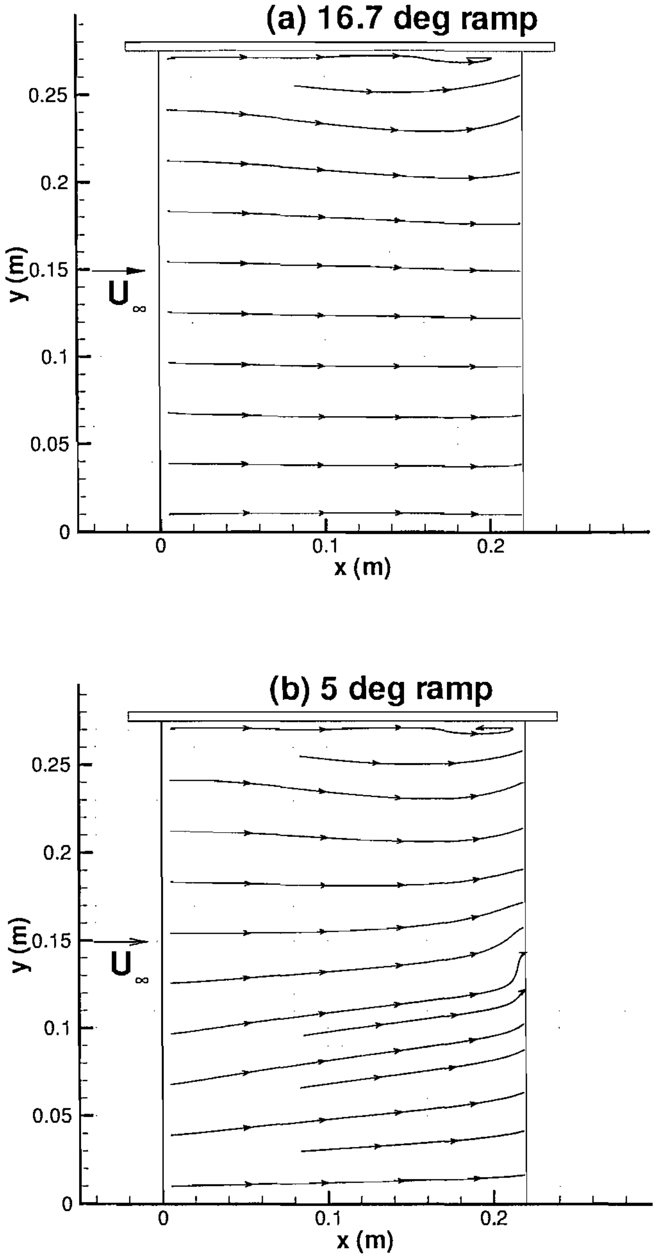

Figure 8.43: Suction surface streamlines at $h_r/c = 0.833$, for the wing downstream of the (a) 16.7 deg and (b) 5 deg diffusers.

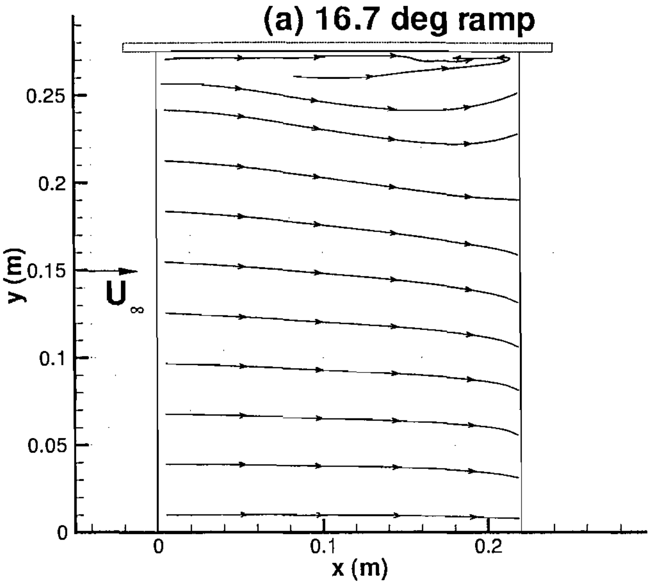
(a) 16.7 deg ramp

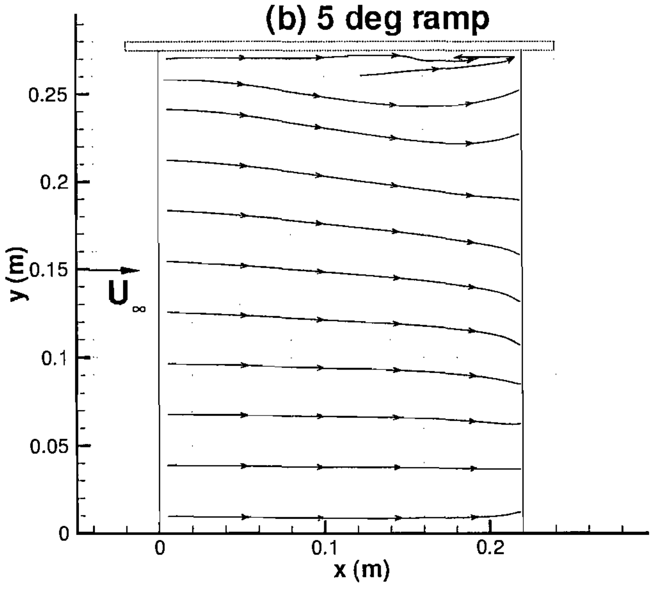
(b) 5 deg ramp

Figure 8.44: Suction surface streamlines at $h_r/c = 0.401$, for the wing downstream of the (a) 16.7 deg and (b) 5 deg diffusers.

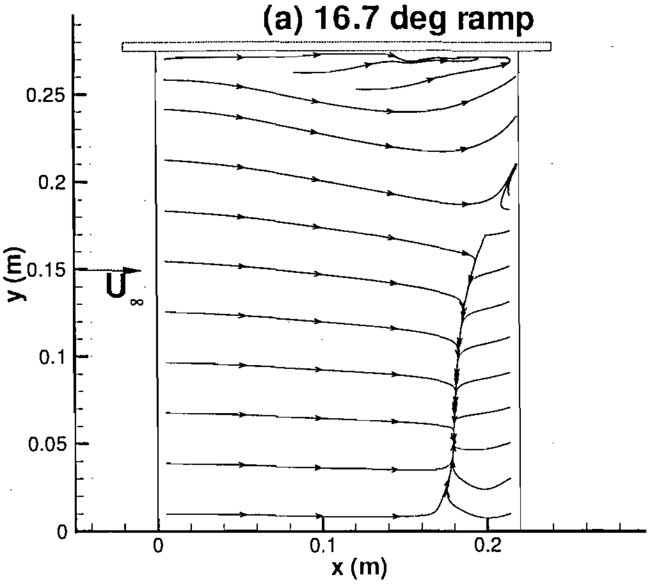

(a) 16.7 deg ramp

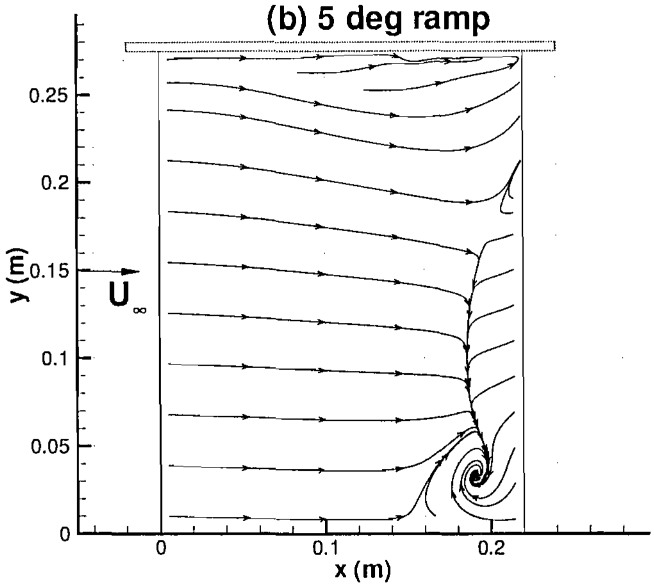

(b) 5 deg ramp

Figure 8.45: Suction surface streamlines at $h_r/c = 0.204$, for the wing downstream of the (a) 16.7 deg and (b) 5 deg diffusers.

8.5.3 Pressures

The surface pressure distributions experienced by the wing while downstream of the two diffuser configurations are presented in the plots outlined in Figs. 8.46 to 8.48. For each ride height investigated, chordwise pressures are shown for 2z/b = 0.09, 0.49 and 0.89, while spanwise pressures are shown at x/c =0.25.

At $h_r/c = 0.833$, it can clearly be seen that the wing experienced greater loads when behind the 5 deg ramp diffuser. The majority of the increase over the 16.7 deg ramp case appeared to originate from the section between 2z/b = 0 and 2z/b = 0.6. At $h_r/c = 0.401$, there seemed to be less of a difference in the pressure distributions, when compared to the previous ride height. The majority of the gains for the 5 deg ramp configuration now appeared to occur between 2z/b ≈ 0.25 and 2z/b ≈ 0.8. At $h_r/c = 0.204$, the spanwise plot showed that the load distribution was quite similar for both cases. For each ramp configuration, load losses experienced at one portion of the span appeared to be regained at another.

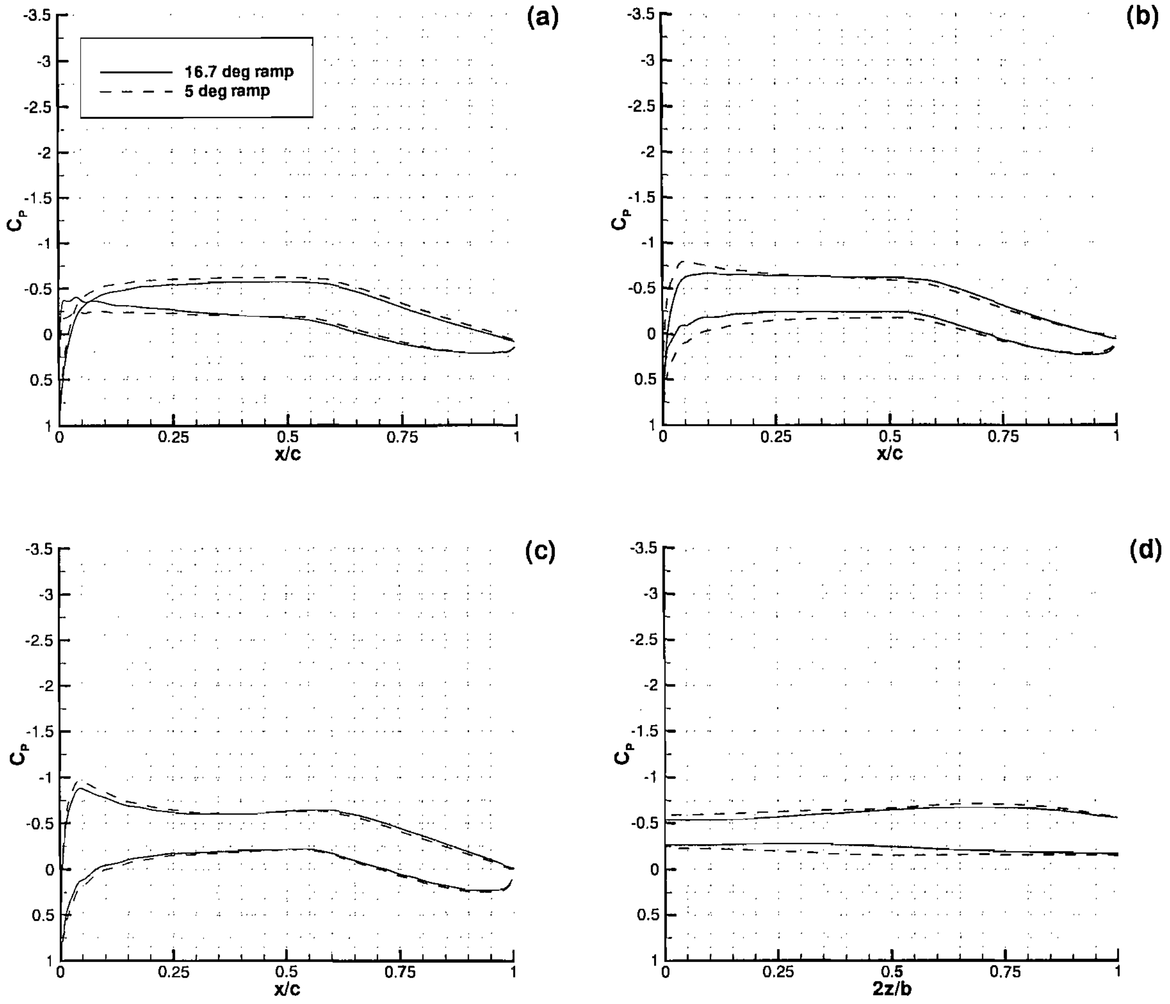

Figure 8.46: The pressure distributions at h_r/c = 0.833, for 2z/b = 0.09 (a), 0.49 (b), 0.89 (c) and x/c = 0.25 (d).

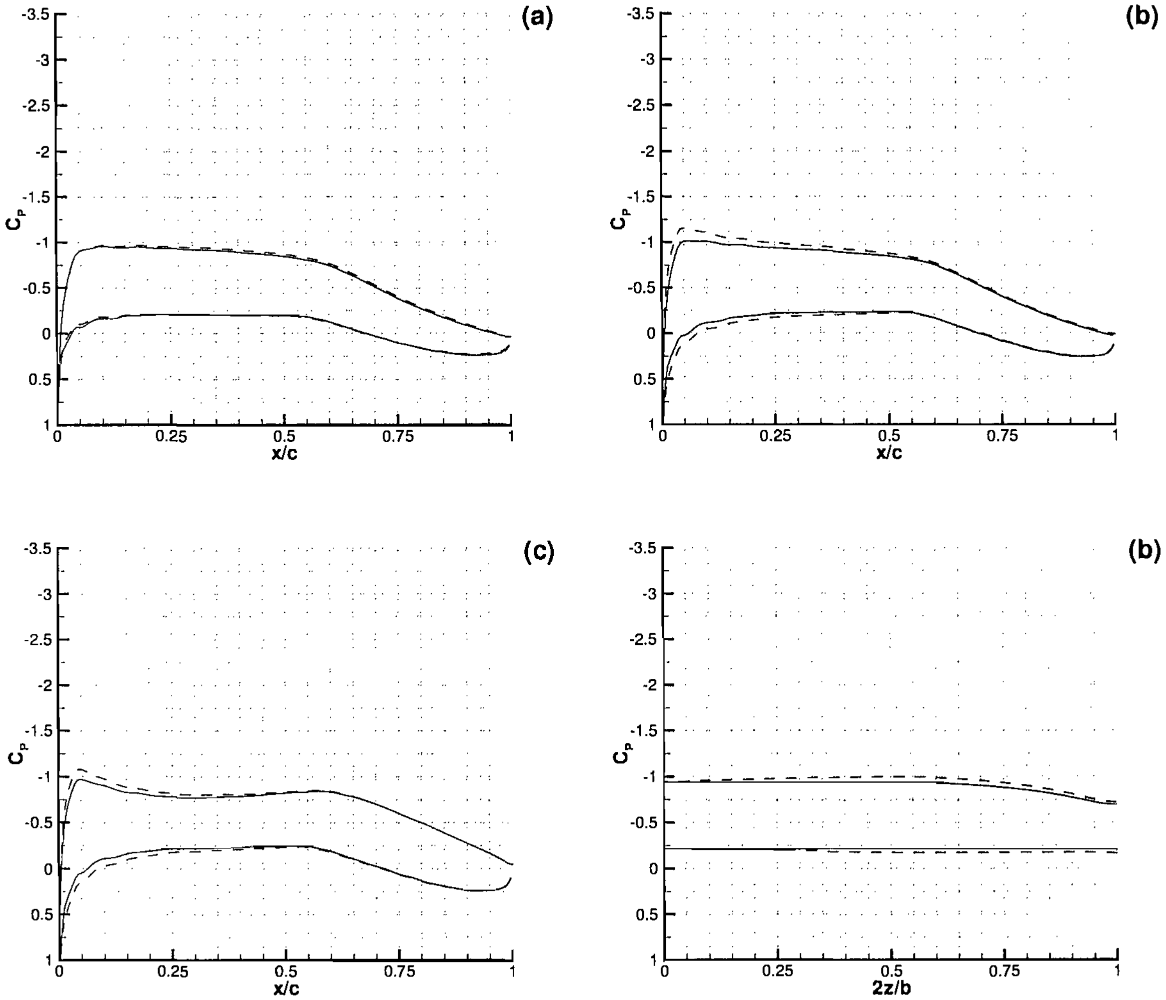

Figure 8.47: The pressure distributions at $h_r/c = 0.401$, for 2z/b = 0.09 (a), 0.49 (b), 0.89 (c) and x/c = 0.25 (d).

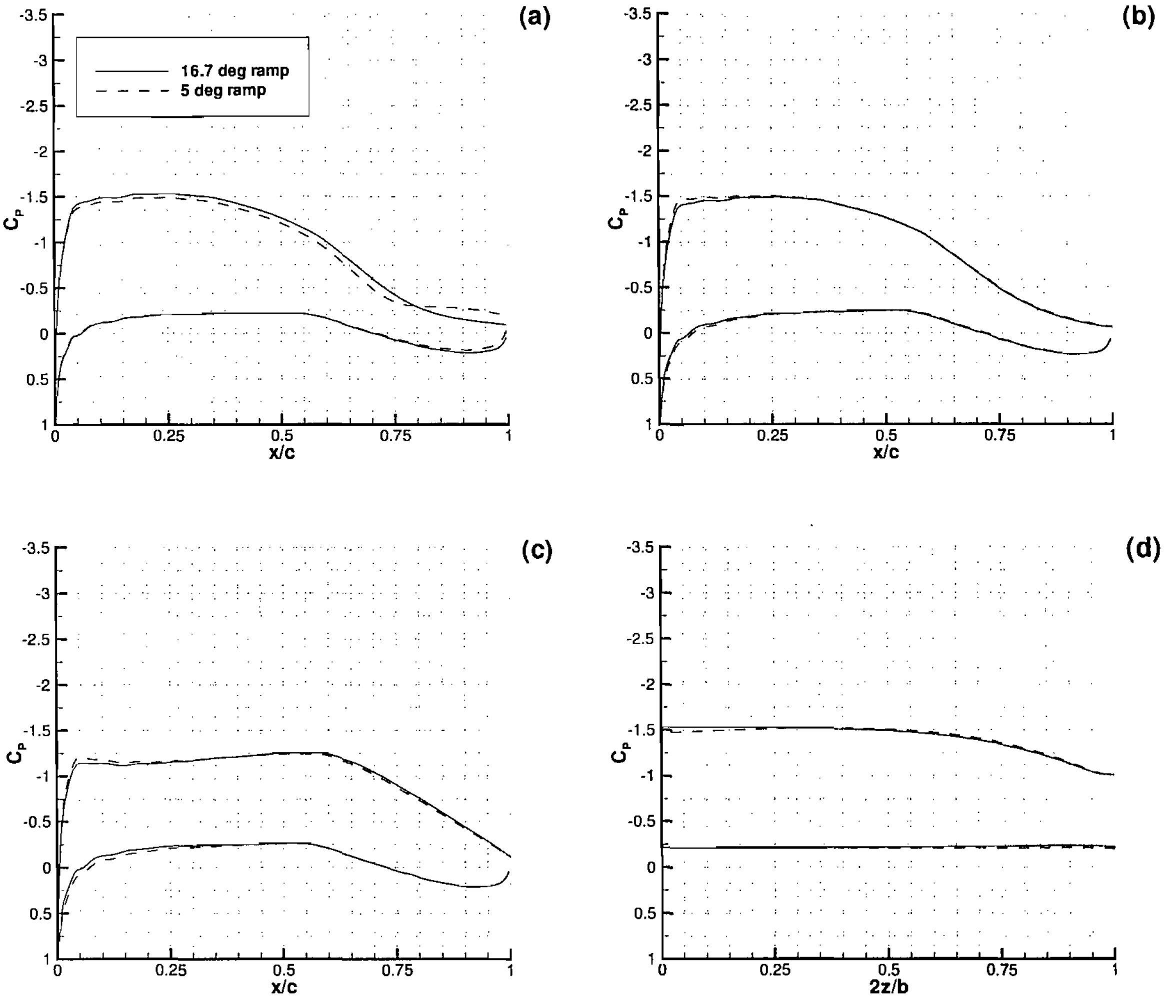

Figure 8.48: The pressure distributions at $h_r/c = 0.204$, for 2z/b = 0.09 (a), 0.49 (b), 0.89 (c) and x/c = 0.25 (d).

8.5.4 Flow Field

The flow field downstream of the wing was examined by producing contours of streamwise vorticity at x/c = 1.5, and contours of total pressure at x/c = 1.5, 2.25 and 3. Again, the ride heights investigated were $h_r/c = 0.833$ and $h_r/c = 0.204$, as they represented cases from extremities of the height variation considered.

The streamwise vorticity contours are presented in Fig. 8.49. There were no significant differences to be discussed. As the diffuser ramp angle was decreased from 16.7 deg to 5 deg, the maximum vorticity decreased slightly from $\frac{\omega c}{U_\infty} = 11.85$ to $\frac{\omega c}{U_\infty} = 11.46$.

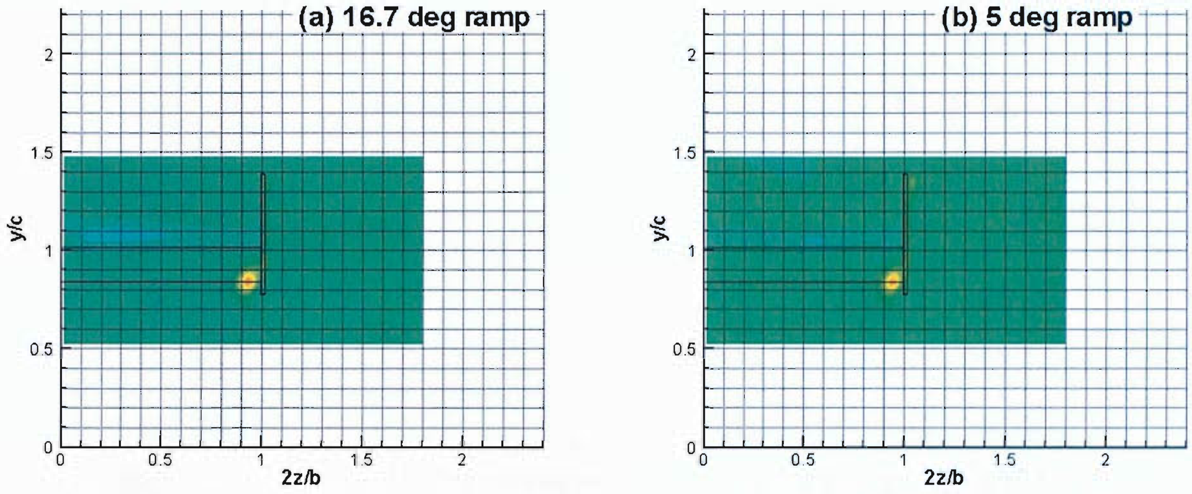

Figure 8.49: Contours of streamwise vorticity at x/c = 1.5 for the ride height of $h_r/c = 0.833$.

At x/c = 1.5 for $h_r/c = 0.833$, Fig. 8.50, the contours of total pressure highlighted different spatial positions of the vortex wake that emanated from the two upstream ramp configurations. The wake of the 16.7 deg diffuser passed over the wake of the wing, while the wake of the 5 deg diffuser appeared to pass straight through it. Consequently, in the latter case, the wake of the wing was distorted around its quarter span. Observation of the top, minor endplate vortex will show that it was somewhat structurally coherent while behind the 5 deg ramp diffuser, as opposed to being non-existent behind the 16.7 deg ramp diffuser. These general observations also held for x/c = 2.25, Fig. 8.51, and

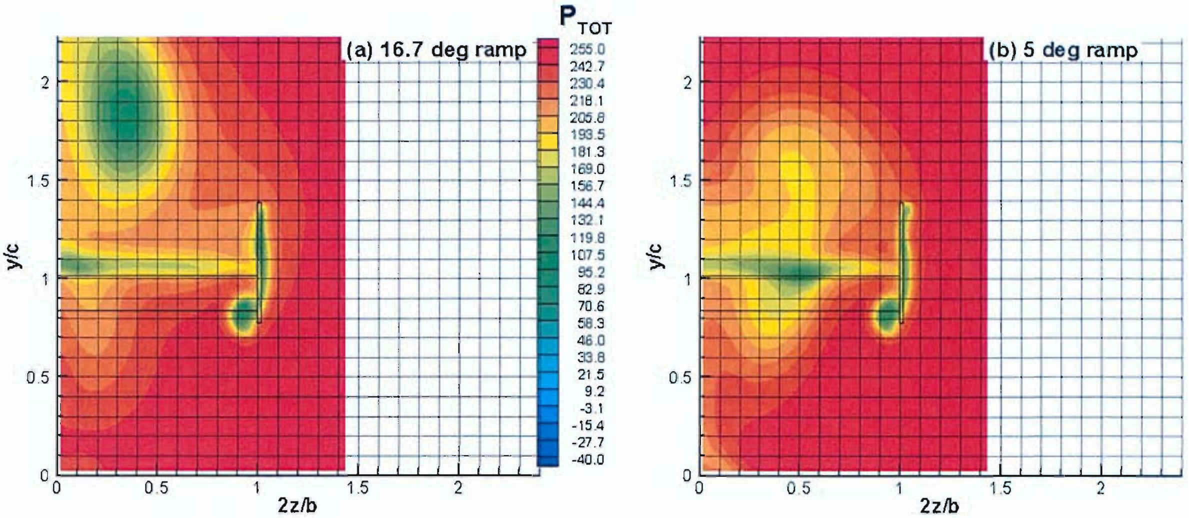

Figure 8.50: Contours of total pressure highlighting the wing's wake at x/c = 1.5 for the ride height of $h_r/c = 0.833$.

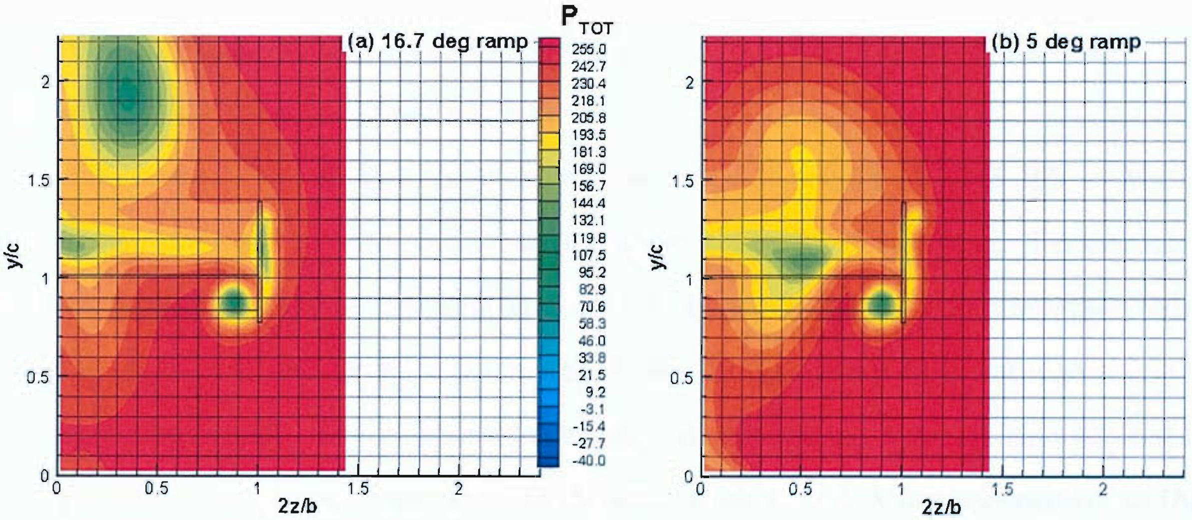

Figure 8.51: Contours of total pressure highlighting the wing's wake at x/c = 2.25 for the ride height of $h_r/c = 0.833$.

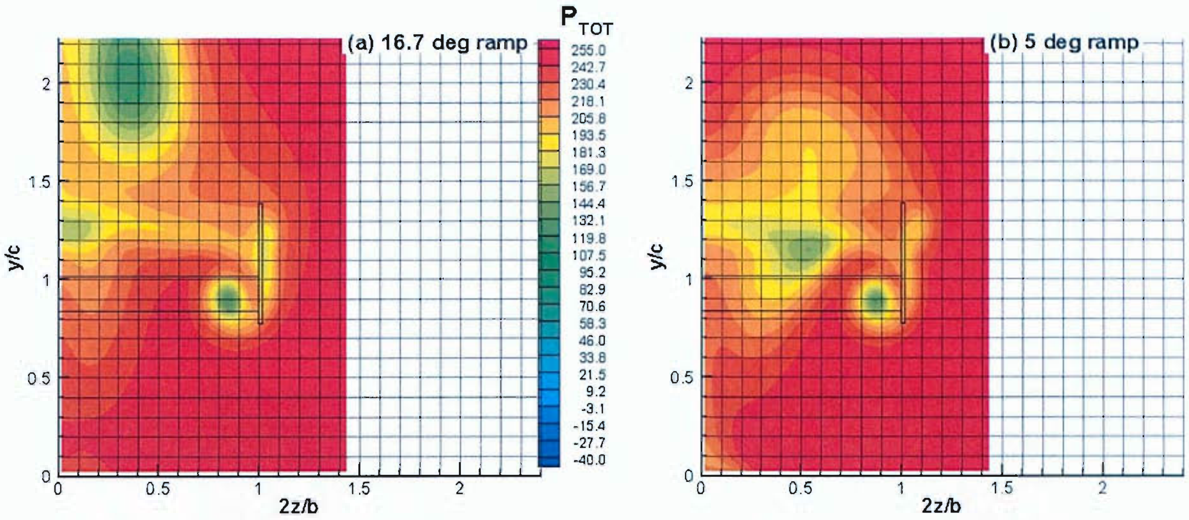

Figure 8.52: Contours of total pressure highlighting the wing's wake at x/c = 3 for the ride height of $h_r/c = 0.833$.

x/c = 3, Fig. 8.52. An analysis of the path of the main wing vortex showed that its overall horizontal movement was 22 mm in the 16.7 deg ramp flow and 19 mm in the 5 deg ramp flow. The overall upward movement was 11 mm for both cases.

Vorticity contours at the lower ride height of $h_r/c = 0.204$, Fig. 8.53, also highlighted no significant differences to be discussed. For this case, the maximum vorticity remained relatively constant, having a value of $\frac{\omega c}{U_\infty} = 14.73$ for the high diffuser angle flow, and $\frac{\omega c}{U_\infty} = 14.72$ for the low diffuser angle flow.

From an examination of the contours of total pressure, Fig. 8.54, both diffuser vortex wakes were observed to pass some distance above the wake of the wing. Furthermore, in both flows, the wake of the wing appeared to be similar, except for the lower bulge between 2z/b = 0 and 2z/b = 0.1 in the 5 deg diffuser ramp flow. Analysis of the corresponding velocity vectors showed that the bulge contained a vortex that rotated in the opposite sense (counter-clockwise) to the main wing vortex. More information on this flow feature will be given in the discussion. The top endplate vortex did not appear to be present at this ride height in any of the ramp flows. The observations just mentioned also appeared to hold further downstream at x/c = 2.25, Fig. 8.55, and x/c = 3, Fig. 8.56, with the wake of the wing getting thicker in the process. At this ride height, the vortex

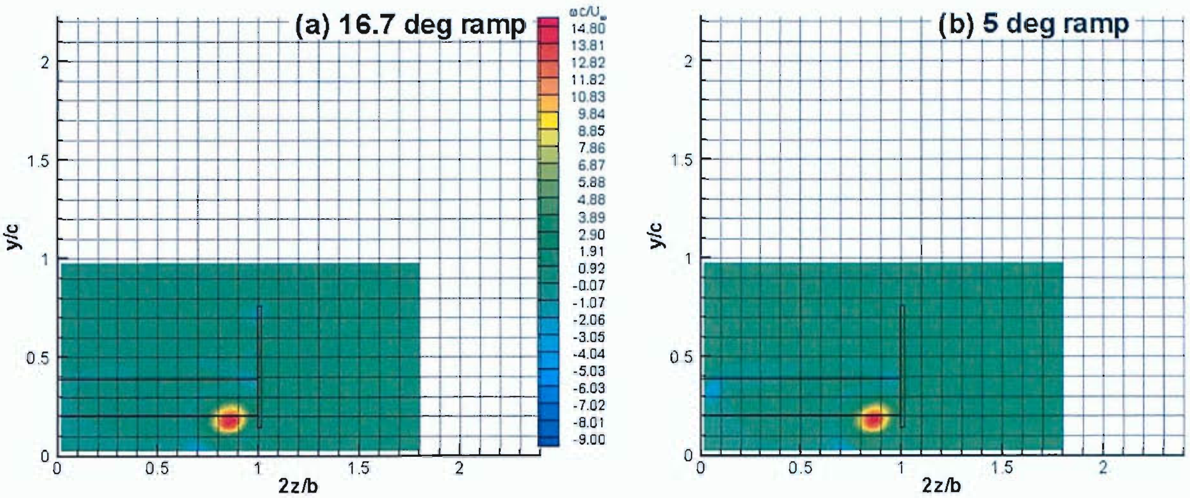

Figure 8.53: Contours of streamwise vorticity at x/c = 1.5 for the ride height of $h_r/c = 0.204$.

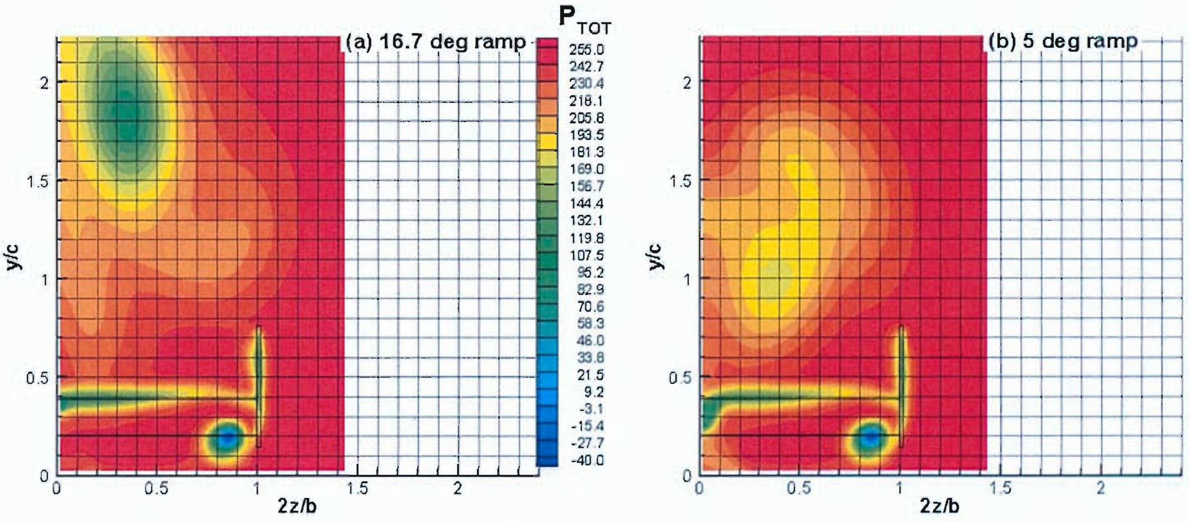

Figure 8.54: Contours of total pressure highlighting the wing's wake at x/c = 1.5 for the ride height of $h_r/c = 0.204$.

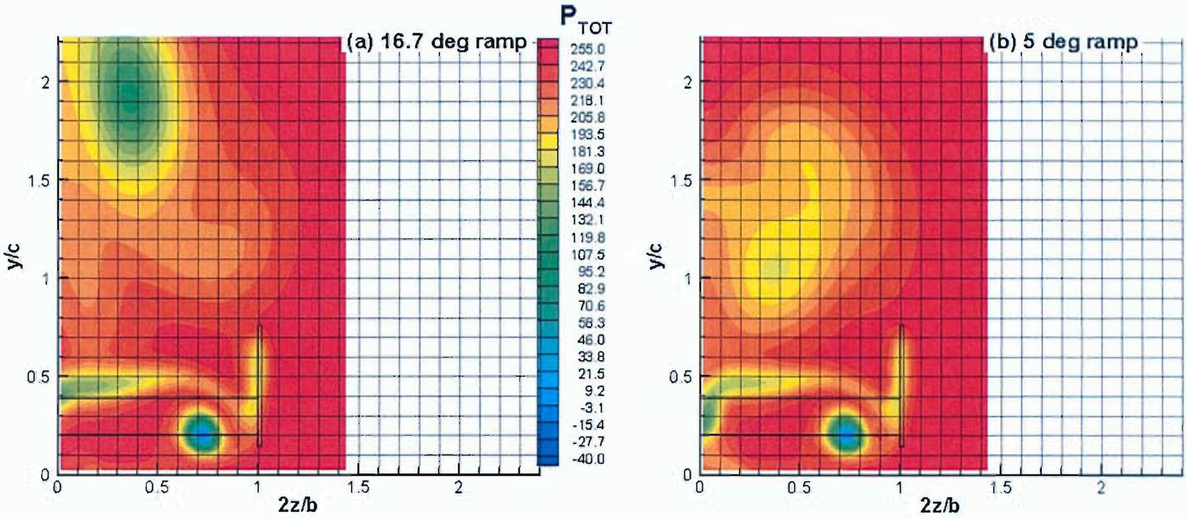

Figure 8.55: Contours of total pressure highlighting the wing's wake at x/c = 2.25 for the ride height of $h_r/c = 0.204$.

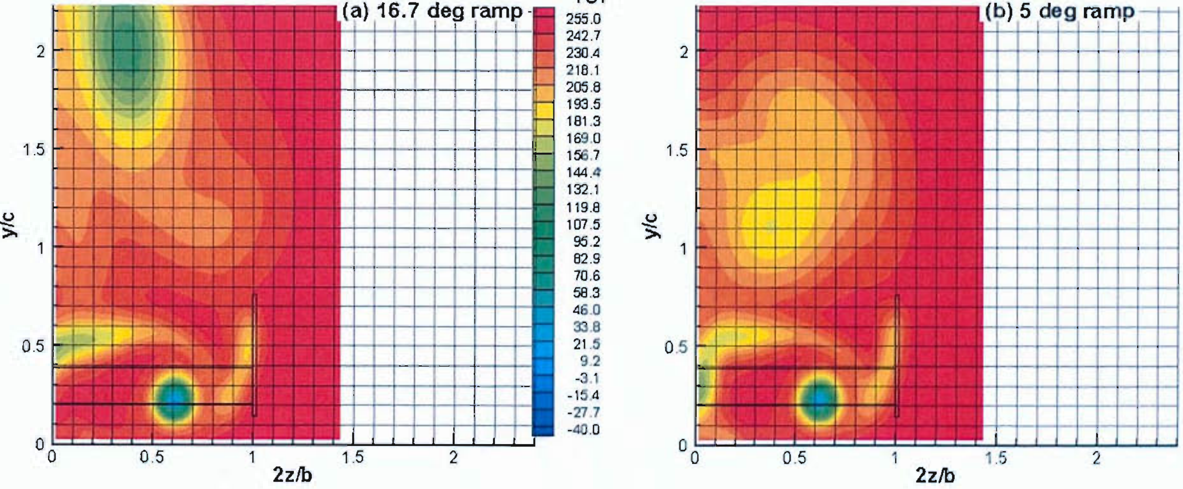

Figure 8.56: Contours of total pressure highlighting the wing's wake at x/c = 3 for the ride height of $h_r/c = 0.204$.

was found to move horizontally by 66 mm in the 16.7 deg ramp flow and 63 mm in the 5 deg ramp flow.

The centreline wake profiles downstream of the wing are plotted in Figs. 8.57 to 8.59 for the ride heights of $h_r/c = 0.833$, 0.401 and 0.204. At $h_r/c = 0.833$ and 0.401, the wake appeared to have a similar shape in both flow conditions. The main difference appeared to be the slowing of the surrounding fluid. At the greater ride height, the 16.7 deg ramp diffuser induced a slower moving wing wake, while at the lower ride height, the 5 deg ramp diffuser produced the same effect.

At $h_r/c = 0.201$, clear differences in the profiles were evident. In the 5 deg ramp flow the wake was at all points, located at lower y/c values than was the case in the 16.7 deg ramp flow. The wake was also noticeably wider in the 5 deg ramp flow.

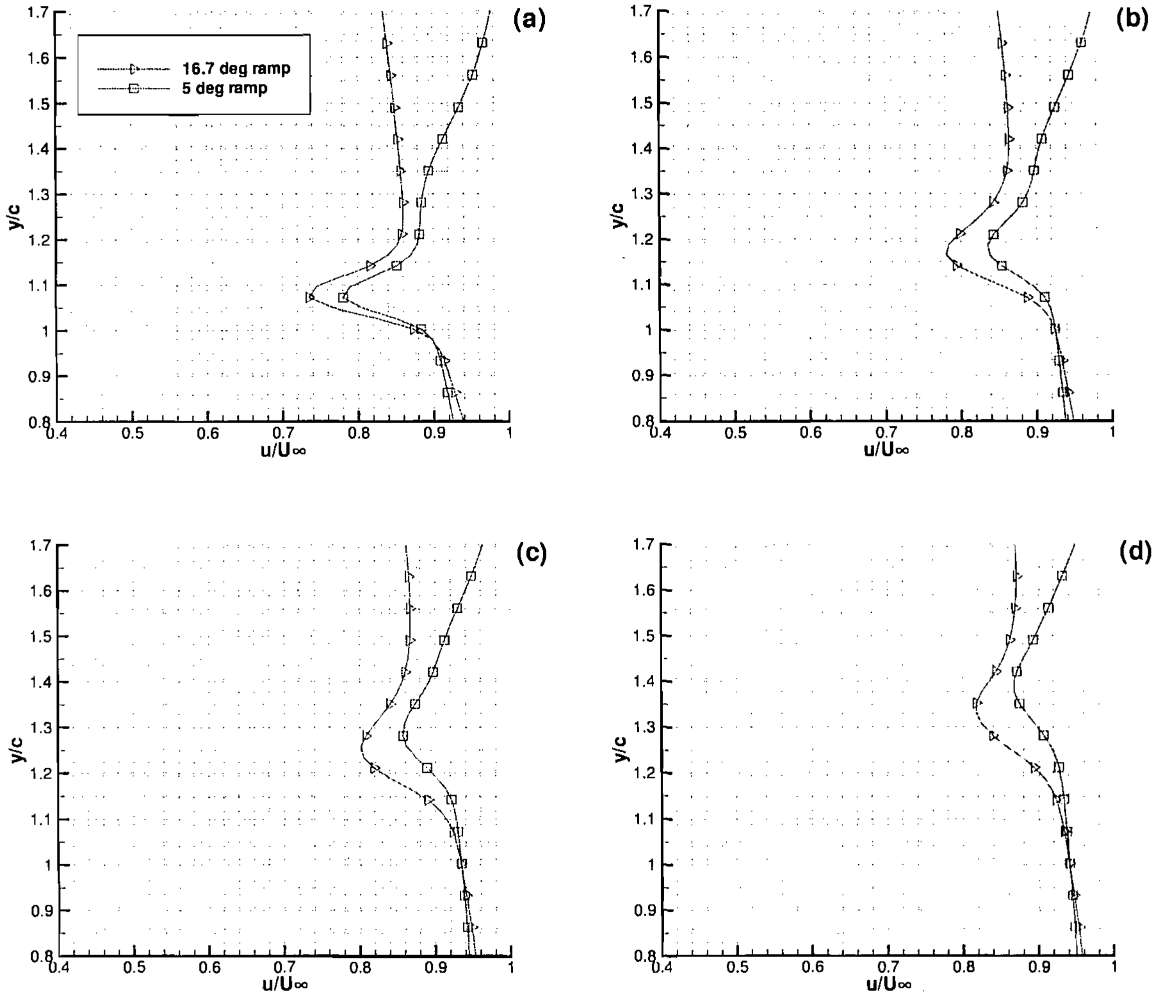

Figure 8.57: A comparison of centreline wing wake profiles for $h_r/c = 0.833$ at x/c = 1.5 (a), x/c = 2.25 (b), x/c = 3 (c) and x/c = 3.75 (d), for two diffuser ramp angles.

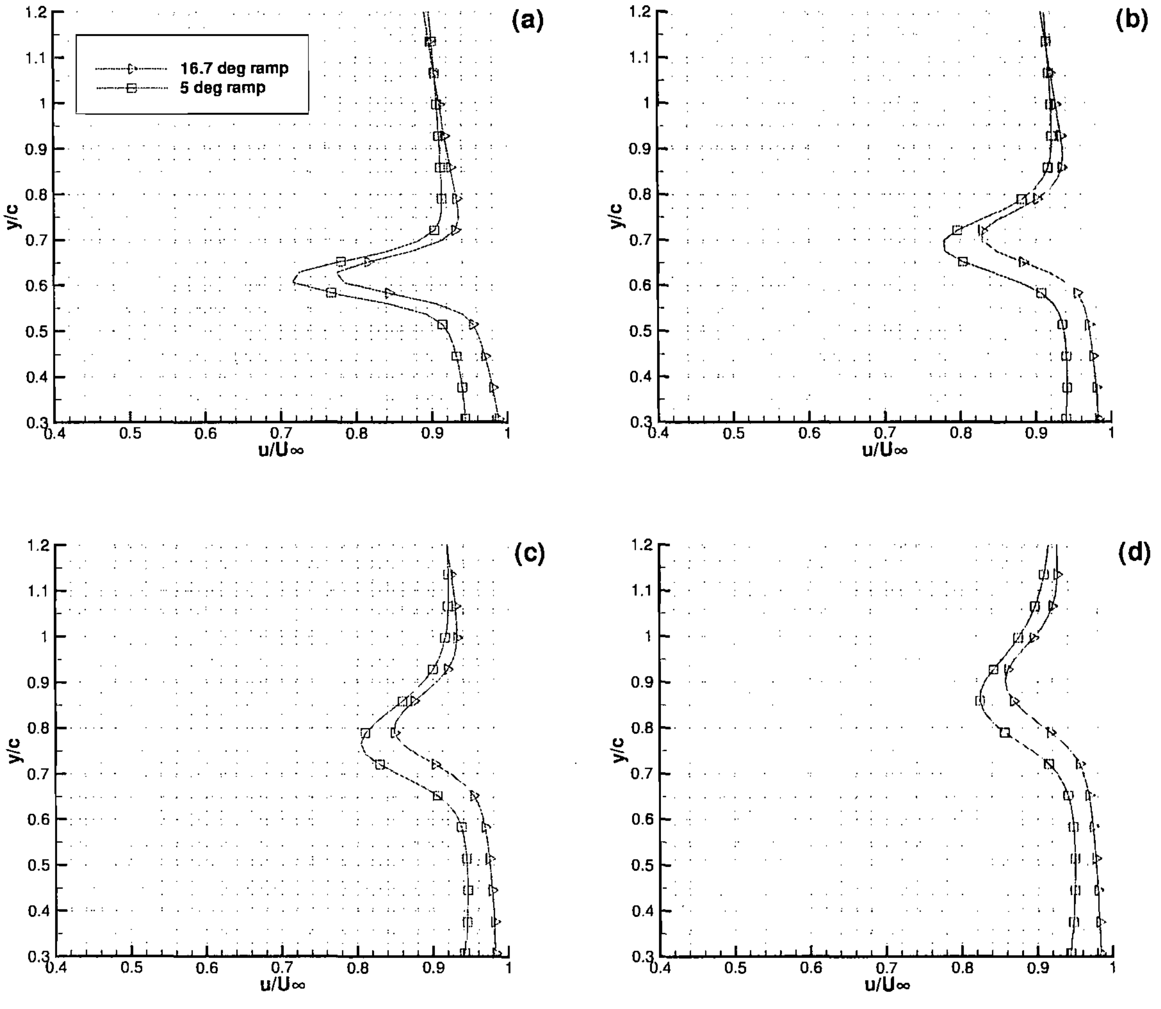

Figure 8.58: A comparison of centreline wing wake profiles for $h_r/c = 0.401$ at x/c = 1.5 (a), x/c = 2.25 (b), x/c = 3 (c) and x/c = 3.75 (d), for two diffuser ramp angles.

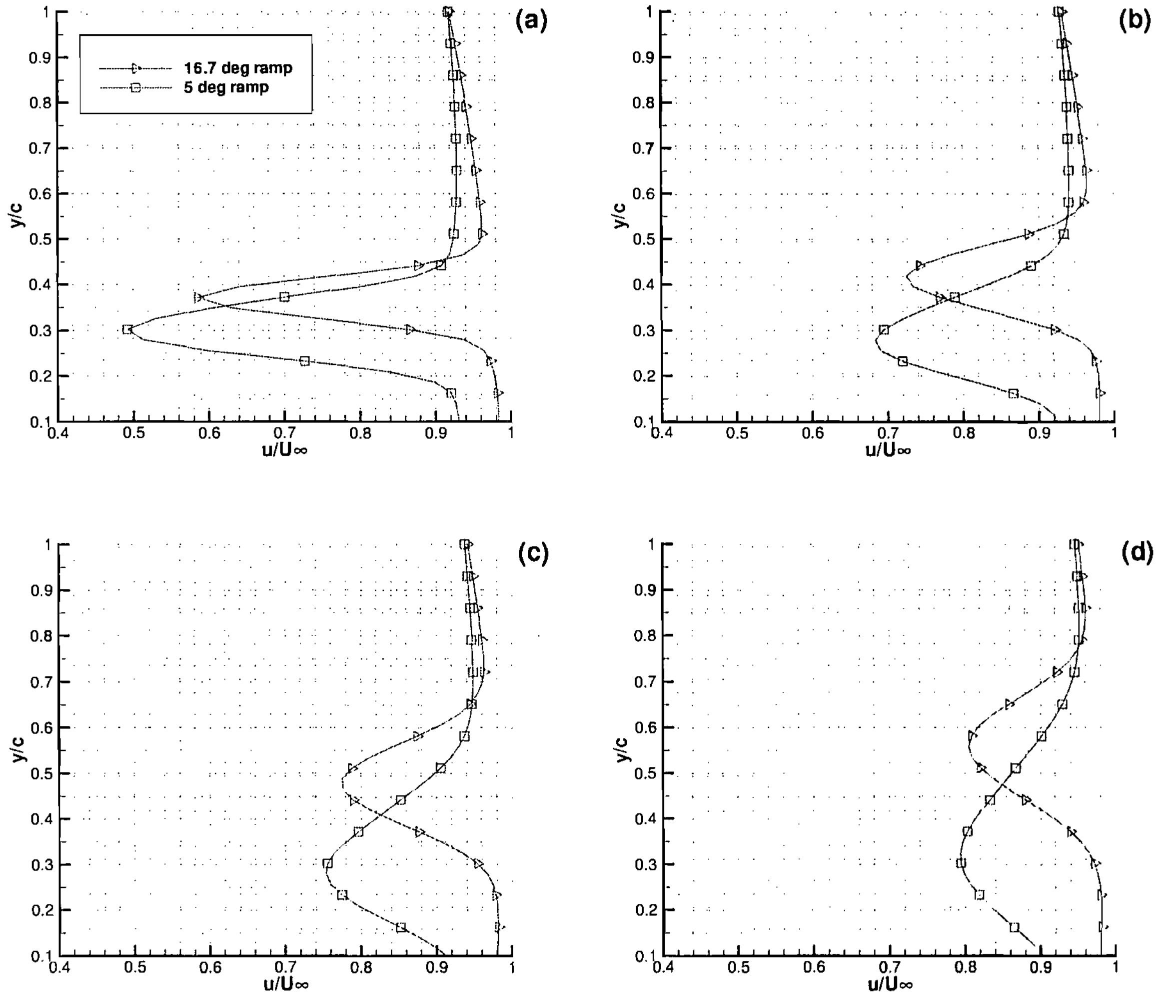

Figure 8.59: A comparison of centreline wing wake profiles for $h_r/c = 0.204$ at x/c = 1.5 (a), x/c = 2.25 (b), x/c = 3 (c) and x/c = 3.75 (d), for two diffuser ramp angles.

8.6 The Effect of a Change in the Height of the Upstream Diffuser

This section will present computational results that highlight the aerodynamic changes experienced by the downstream wing when the height of the upstream diffuser bluff body was changed. The diffuser heights investigated were $h_r/d = 0.30$ and $h_r/d = 0.60$. As a reminder, the extremities of the diffuser heights investigated experimentally were $h_r/d = 0.20$ and $h_r/d = 0.30$. At the lower height, there was a possibility of the existence of unsteady flow. Consequently, this height was not simulated computationally, but was replaced by $h_r/d = 0.60$, which was well within the reported symmetrical flow region of a diffuser with a 16.7 deg ramp angle [50].

8.6.1 Forces

The downforce coefficients that were obtained from the wing are presented in Fig. 8.60. It can be seen that there was negligible difference in the plots over the ride height range investigated. That is, altering the ride height of the diffuser from $h_r/d = 0.30$ to $h_r/d = 0.60$ induced no significant force change on the downstream wing. The corresponding drag coefficients are shown in Fig. 8.61. The plots indicate that the drag increased monotonically as the ride height was reduced, with diffuser $h_r/d = 0.60$ inducing slightly higher values between $h_r/c = 0.401$ and $h_r/c = 0.833$. Examination of the lift to drag ratios showed that there was no significant difference between the two configurations, Fig. 8.62.

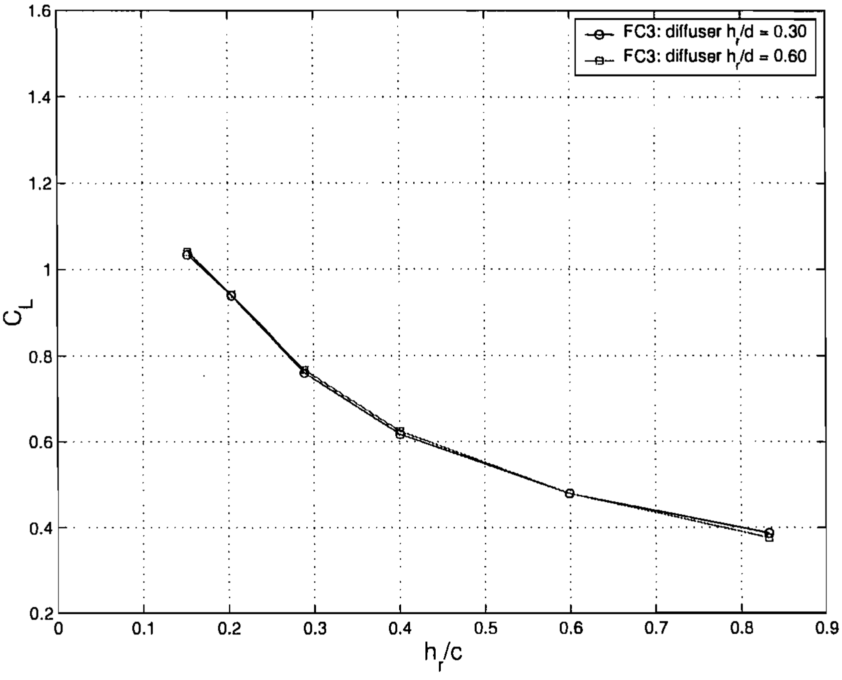

Figure 8.60: Downforce coefficients while varying the height of the upstream diffuser.

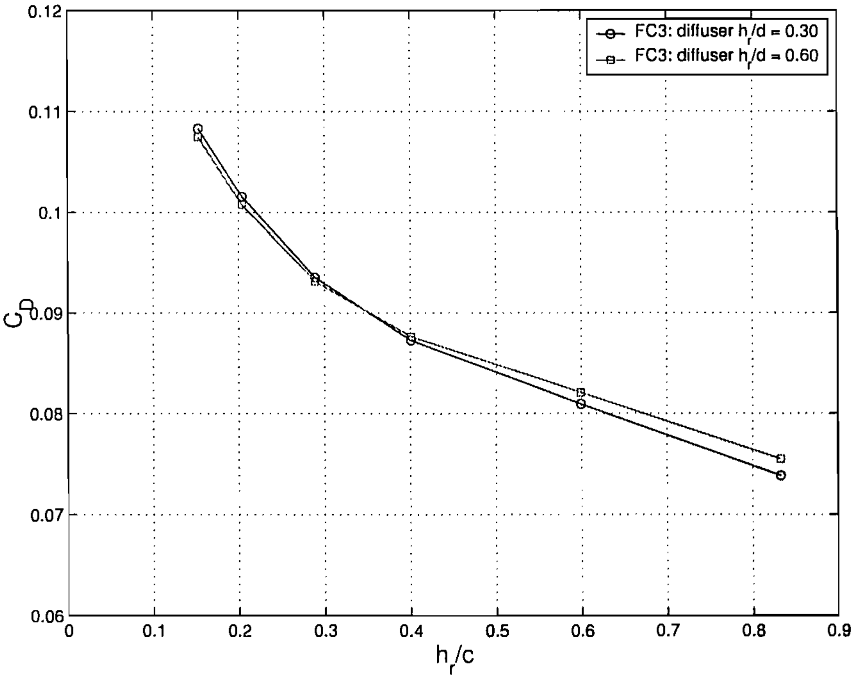

Figure 8.61: Drag coefficients while varying the height of the upstream diffuser.

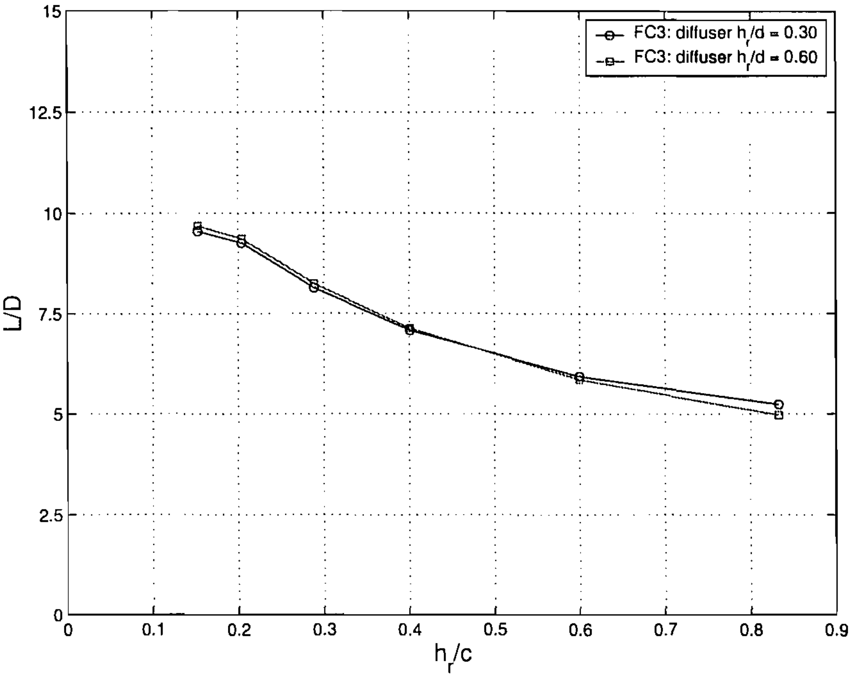

Figure 8.62: Lift to drag ratios while varying the height of the upstream diffuser.

8.6.2 Flow Visualisation

Suction surface flow visualisation for the wing downstream of both configurations are presented in Figs. 8.63 to 8.65. At each ride height, both plots look similar. There were no significant differences to be described.

(a) diffuser h_r/d = 0.30

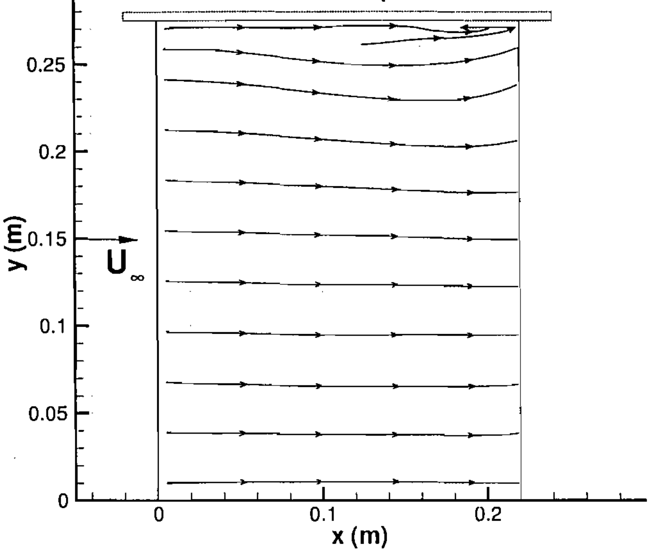

(b) diffuser h_r/d = 0.60

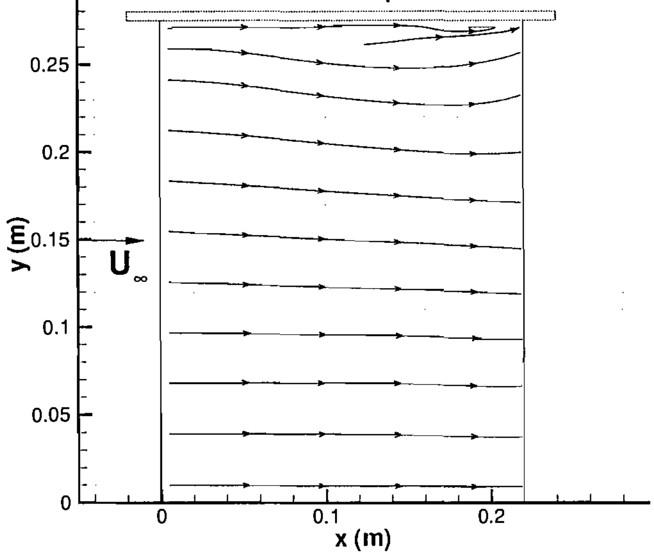

Figure 8.63: Suction surface streamlines at $h_r/c = 0.833$, for the wing downstream of (a) diffuser $h_r/d = 0.30$ and (b) diffuser $h_r/d = 0.60$.

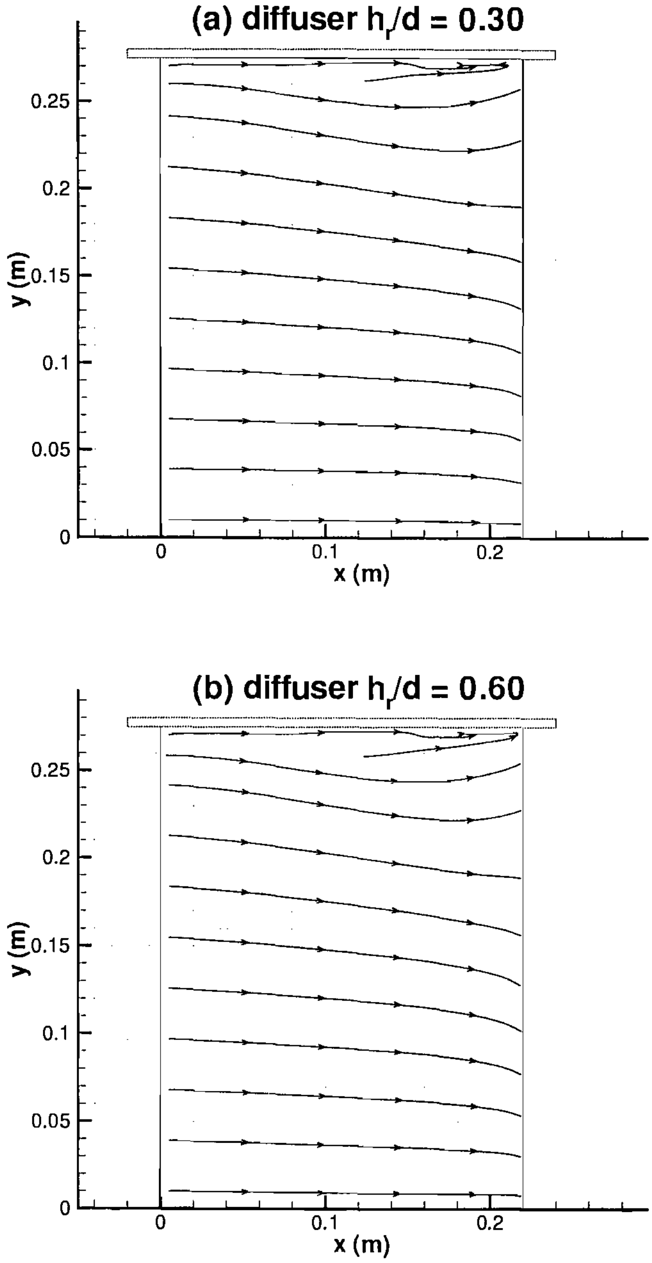

Figure 8.64: Suction surface streamlines at $h_r/c = 0.401$, for the wing downstream of (a) diffuser $h_r/d = 0.30$ and (b) diffuser $h_r/d = 0.60$.

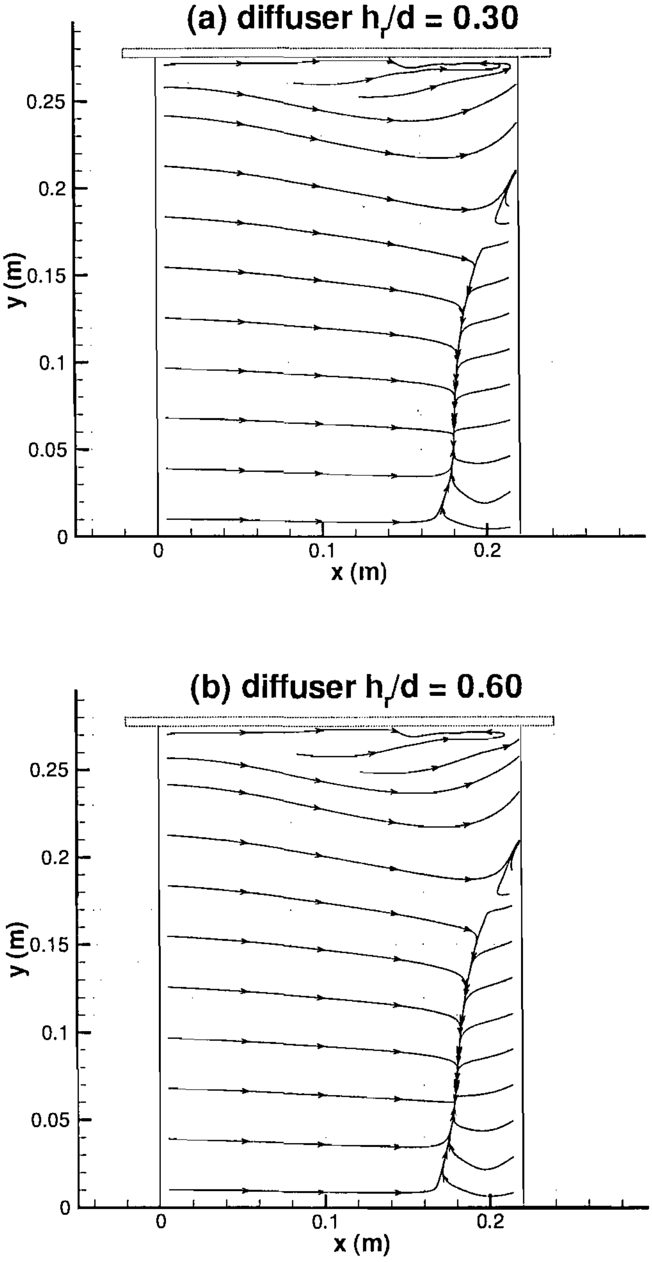

Figure 8.65: Suction surface streamlines at $h_r/c = 0.204$, for the wing downstream of (a) diffuser $h_r/d = 0.30$ and (b) diffuser $h_r/d = 0.60$.

8.6.3 Pressures

The pressure distributions at the ride heights of $h_r/c = 0.833$, 0.401 and 0.204, which are presented in Figs. 8.66 to 8.68, support the findings obtained from the force coefficients and the flow visualisation. The majority of the stations did not undergo any significant change in loading in the flow conditions simulated. If there was a slight deficiency at one part of the span, it was usually regained at another.

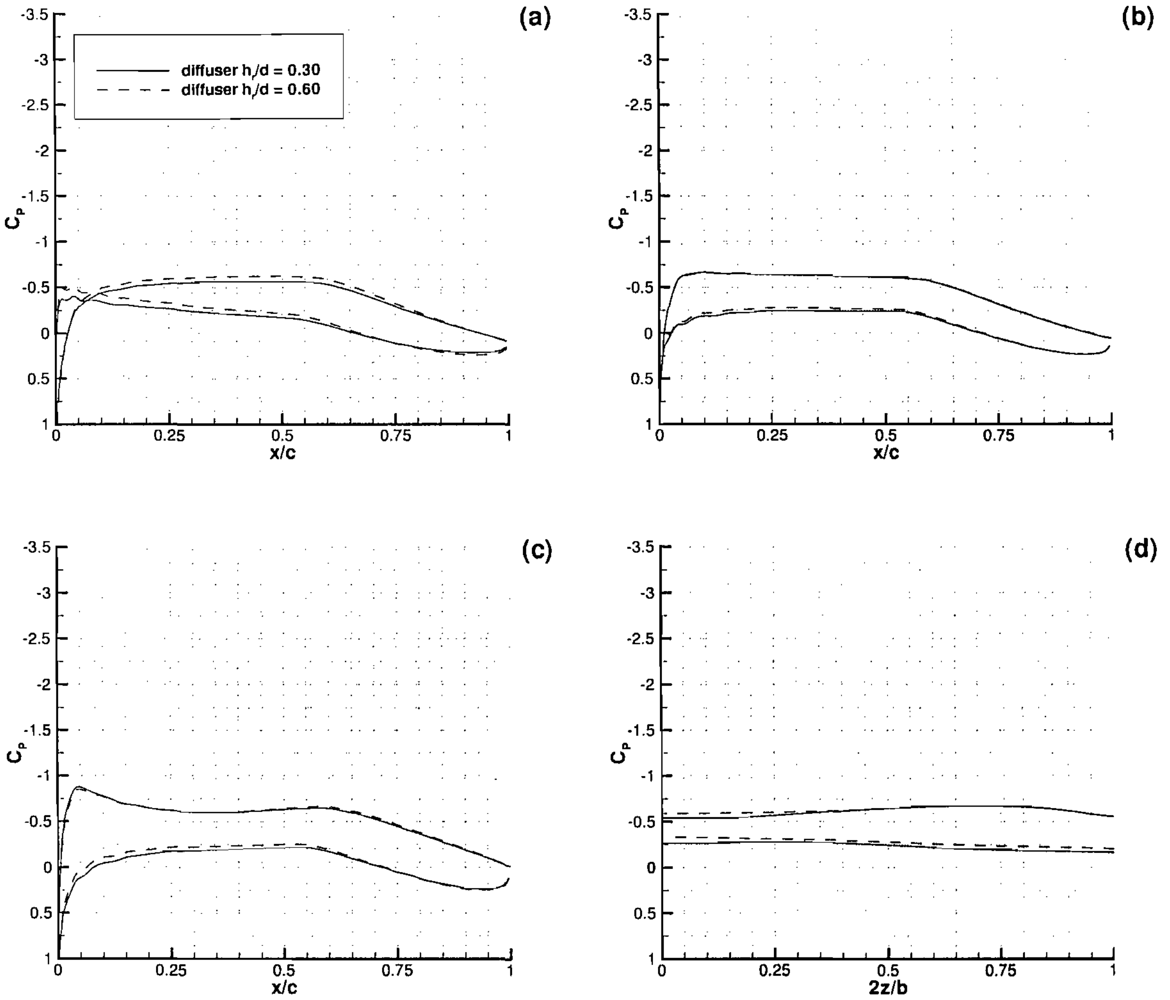

Figure 8.66: The pressure distributions at $h_r/c = 0.833$, for 2z/b = 0.09 (a), 0.49 (b), 0.89(c) and x/c = 0.25 (d).

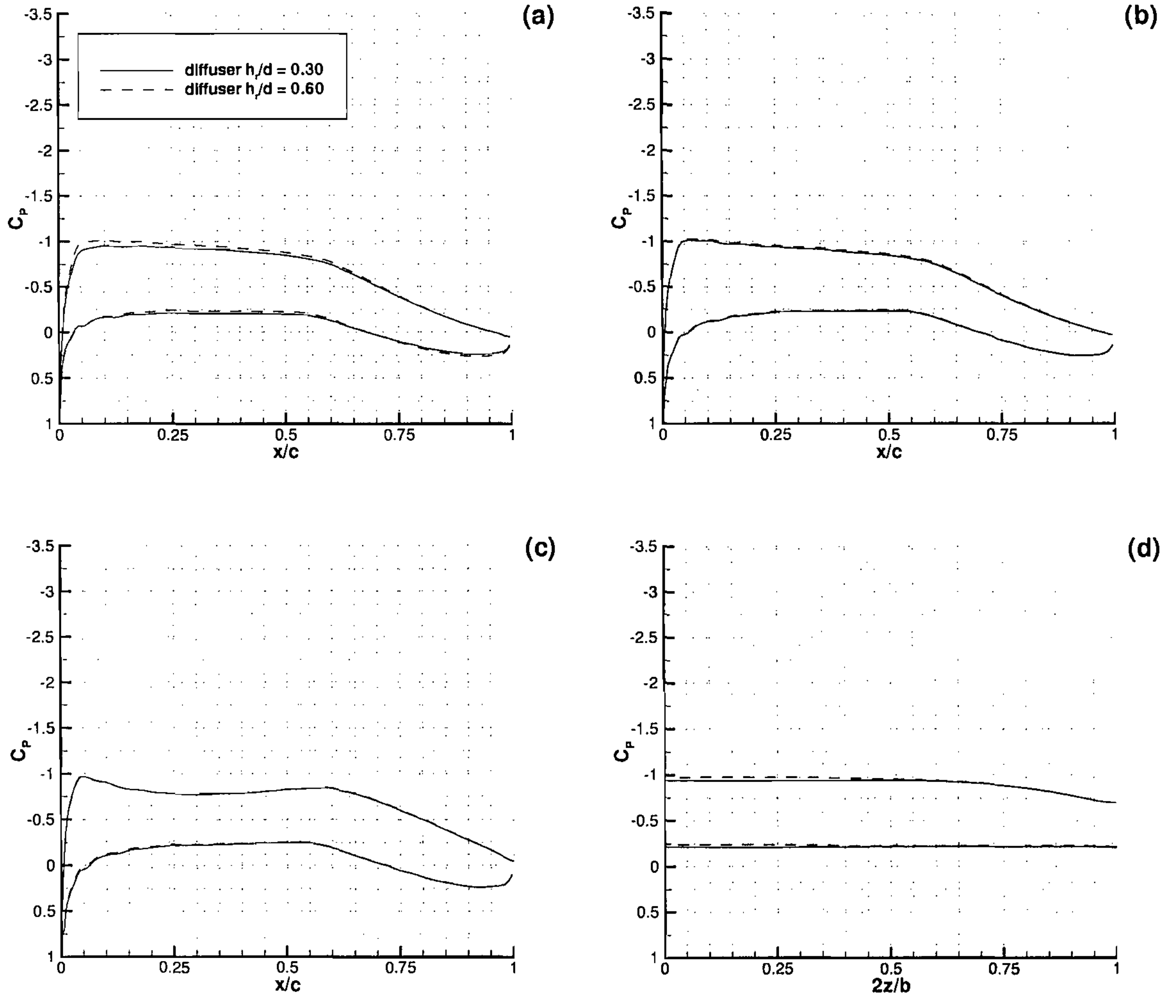

Figure 8.67: The pressure distributions at $h_r/c = 0.401$, for 2z/b = 0.09 (a), 0.49 (b), 0.89(c) and x/c = 0.25 (d).

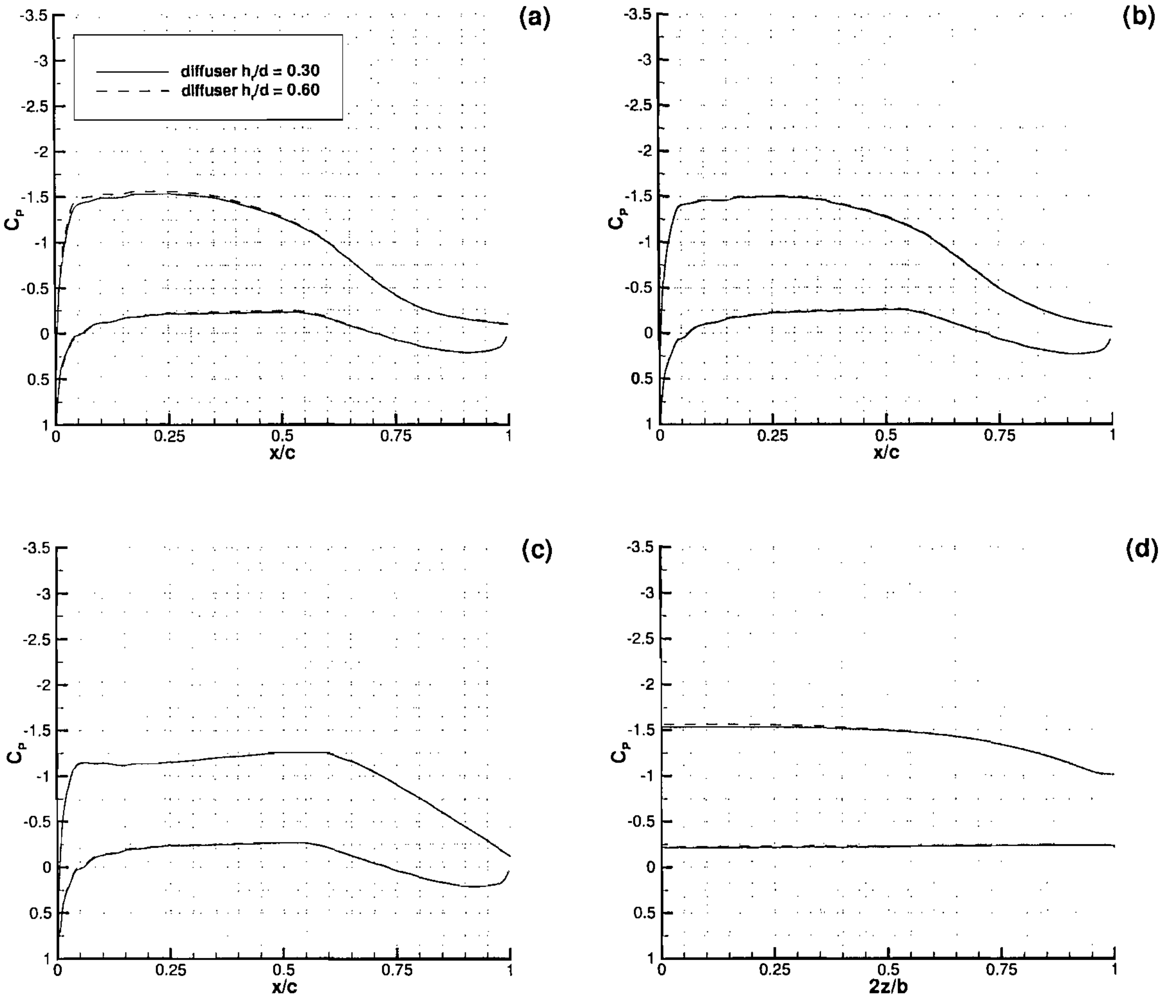

Figure 8.68: The pressure distributions at h_r/c = 0.204, for 2z/b = 0.09 (a), 0.49 (b), 0.89(c) and x/c = 0.25 (d).

8.6.4 Flow Field

The streamwise vorticity plots at x/c = 1.5 are shown in Fig. 8.69. Both images are similar. The maximum vorticity was found to increase from $\frac{\omega c}{U_\infty} = 11.85$ to $\frac{\omega c}{U_\infty} = 12.17$, as the diffuser ride height was increased.

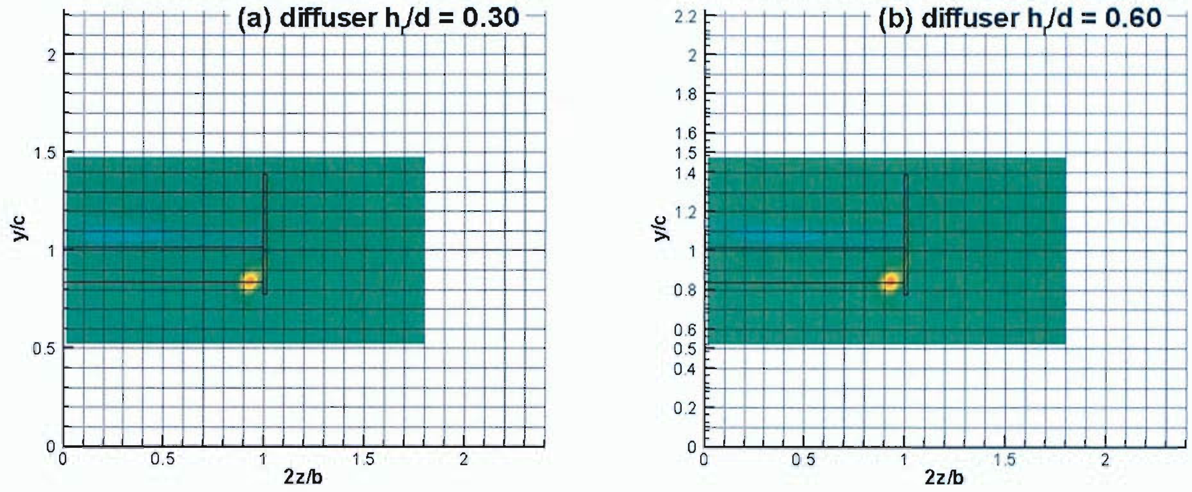

Figure 8.69: Contours of streamwise vorticity at x/c = 1.5 for the ride height of $h_r/c = 0.833$.

Comparisons of the pressure contours highlighting the development of the wake of the wing at $h_r/c = 0.833$ are shown in Figs. 8.70 to 8.72. At x/c = 1.5, Fig. 8.70, it can be observed that the vortex wakes for the two diffuser configurations occupy slightly different spatial positions in the data plane. That of diffuser $h_r/d = 0.60$ appeared to be lower, more compact, and further to the right than the corresponding vortex wake of diffuser $h_r/d = 0.30$. Despite these differences, the wake of the wing did not appear to differ significantly in either flow field. At x/c = 2.25 and x/c = 3, the wing's wake appeared to dissipate more quickly behind diffuser $h_r/d = 0.60$. In both flow fields, the top endplate vortex appeared to be non-existent.

At the lower ride height of $h_r/c = 0.204$, the vorticity contours were again similar, as shown in Fig. 8.73. The maximum vorticity was found to increase from $\frac{\omega c}{U_\infty} = 14.73$ to $\frac{\omega c}{U_\infty} = 14.77$, as the diffuser ride height was increased. The contours of total pressure are

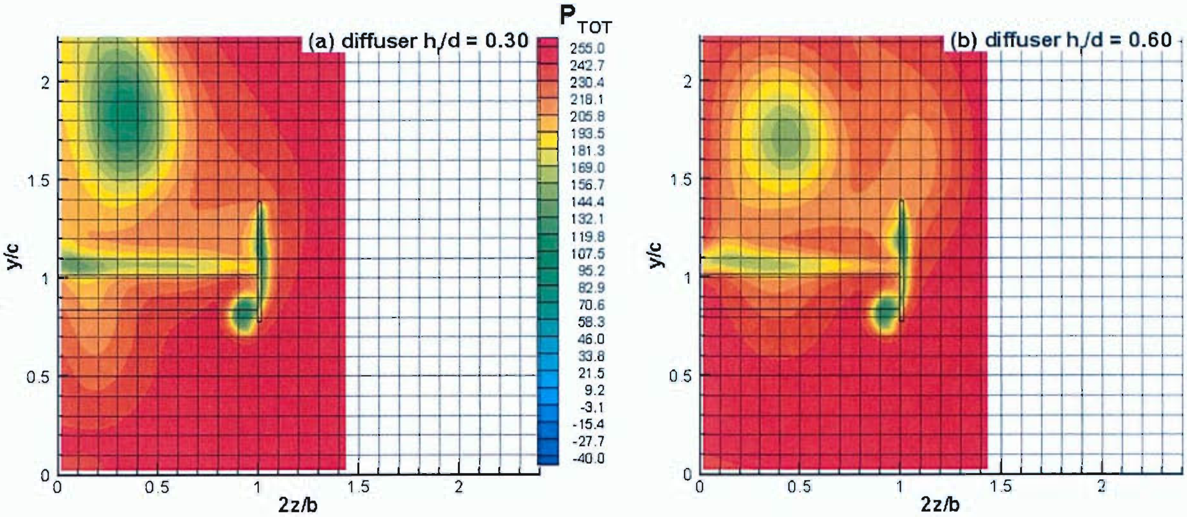

Figure 8.70: Contours of total pressure highlighting the wing's wake at x/c = 1.5 for the ride height of $h_r/c = 0.833$.

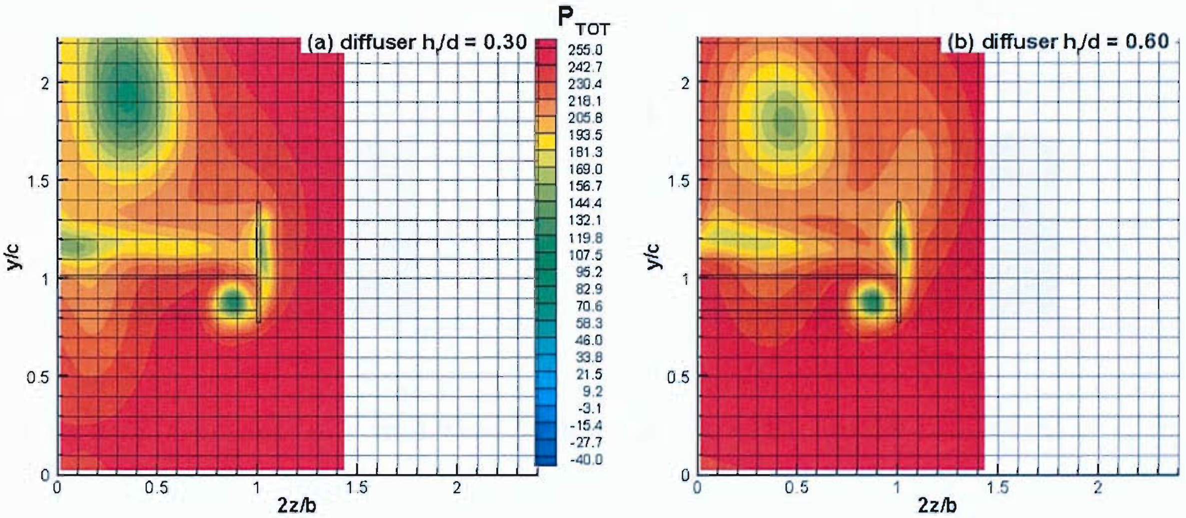

Figure 8.71: Contours of total pressure highlighting the wing's wake at x/c = 2.25 for the ride height of $h_r/c = 0.833$.

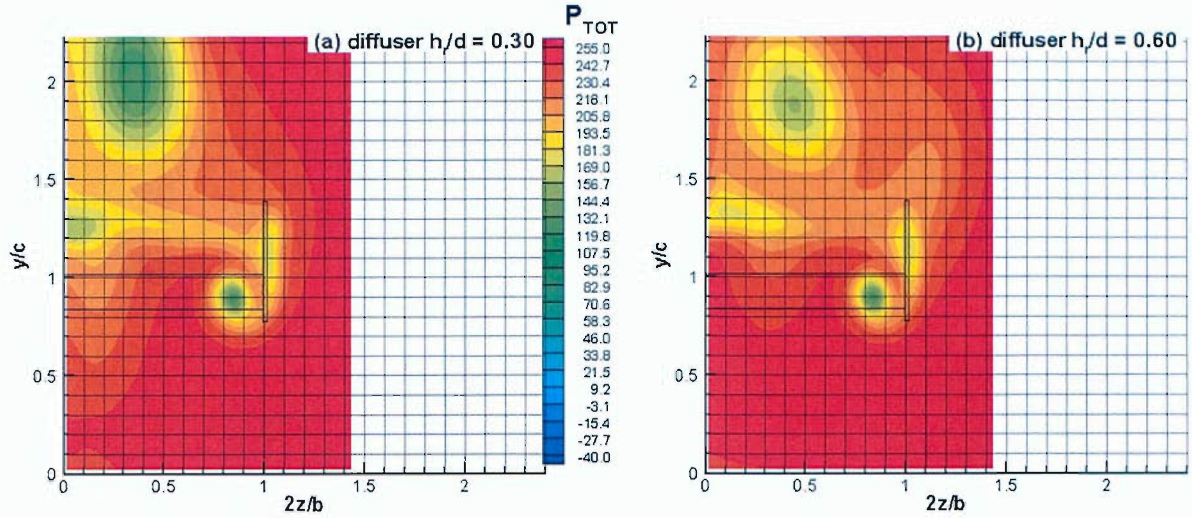

Figure 8.72: Contours of total pressure highlighting the wing's wake at x/c = 3 for the ride height of $h_r/c = 0.833$.

presented in Figs. 8.74 to 8.76. The wake of the wing appeared to develop in a similar manner in both of the surrounding flow fields.

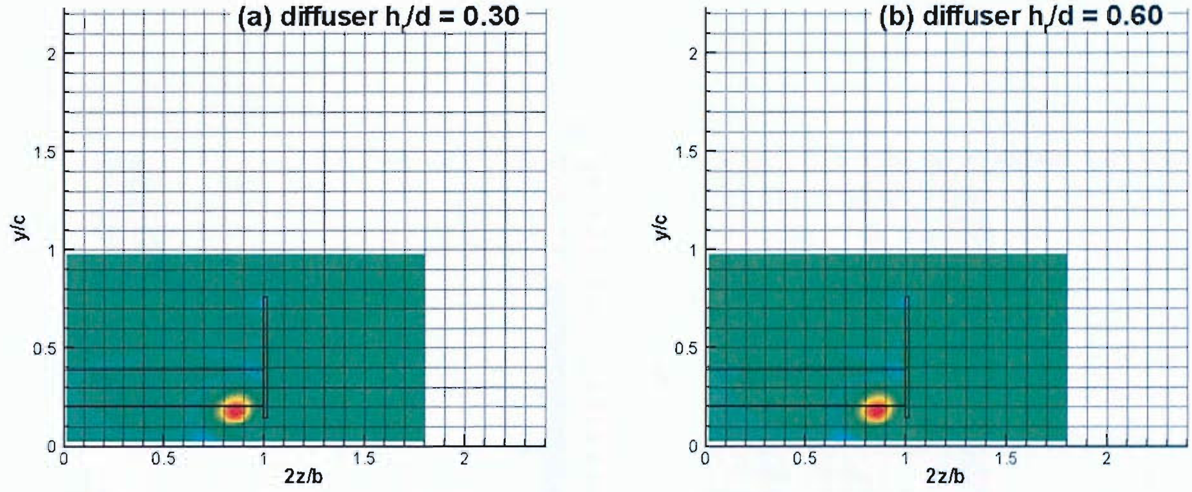

Figure 8.73: Contours of streamwise vorticity at x/c = 1.5 for the ride height of $h_r/c = 0.204$.

Comparisons of the centreline wake profiles downstream of the wing are shown in Figs. 8.77 to 8.79. Overall, the plots show that the wake development was very similar for both upstream configurations. At $h_r/c = 0.833$, both above and below the wake, the

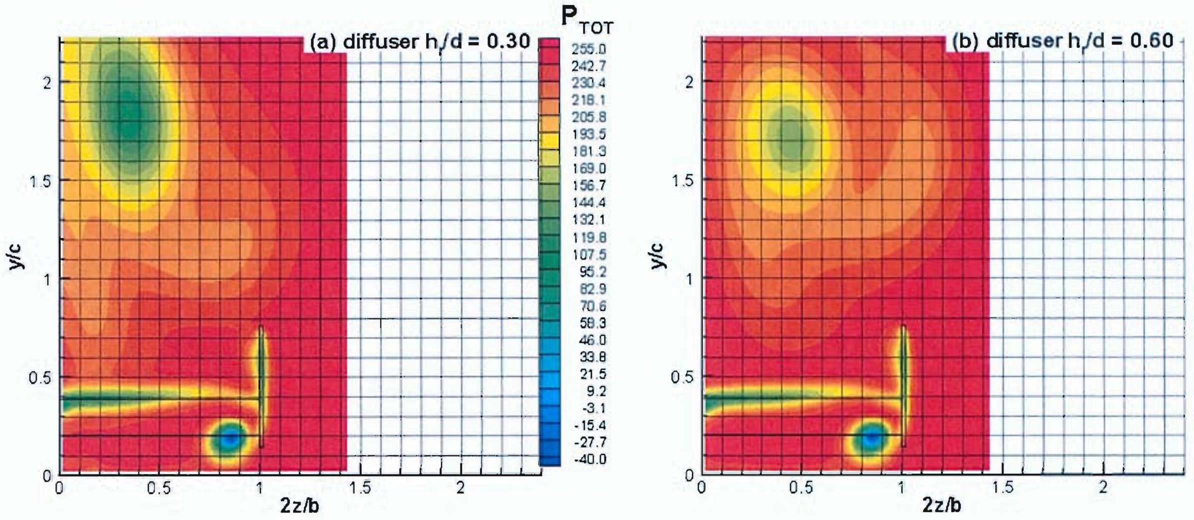

Figure 8.74: Contours of total pressure highlighting the wing's wake at x/c = 1.5 for the ride height of $h_r/c = 0.204$.

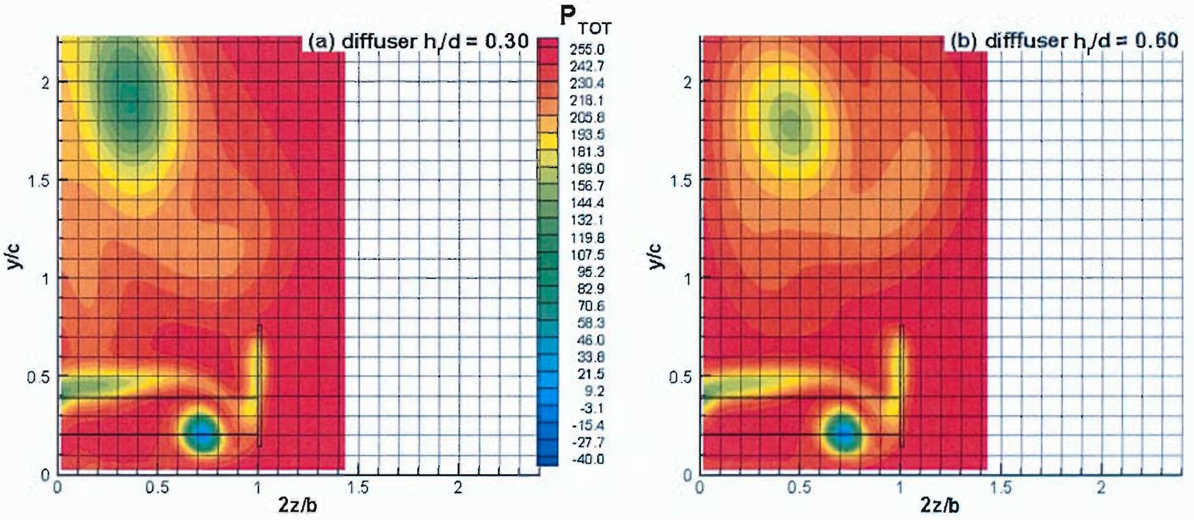

Figure 8.75: Contours of total pressure highlighting the wing's wake at x/c = 2.25 for the ride height of $h_r/c = 0.204$.

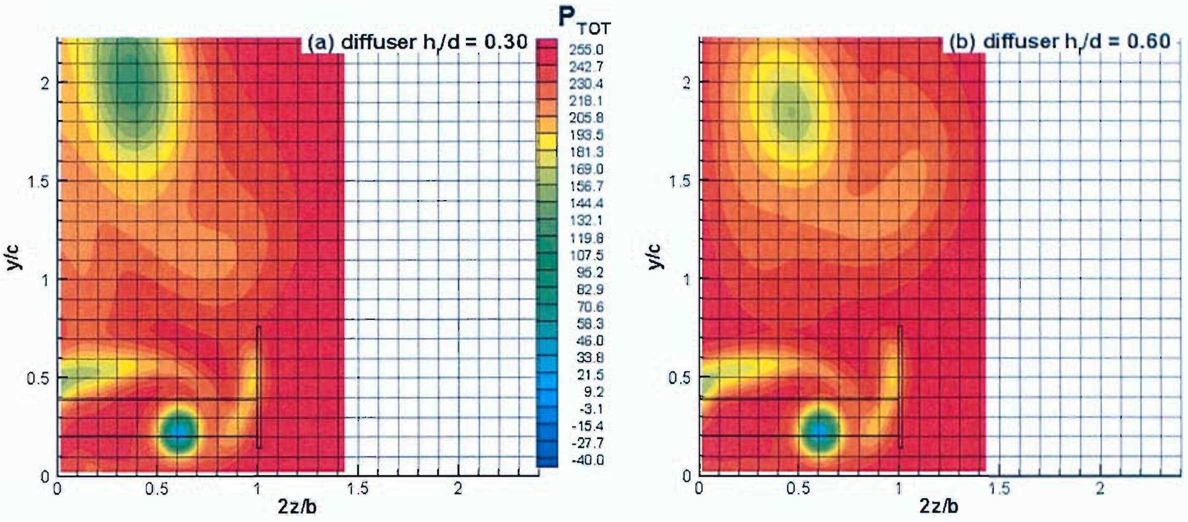

Figure 8.76: Contours of total pressure highlighting the wing's wake at x/c = 3 for the ride height of $h_r/c = 0.204$.

transporting fluid was noticeably quicker for diffuser $h_r/d = 0.60$. As the ride height of the wing was reduced, however, the transporting fluid below the wake converged to the same speed, while that above the wake was still noticeably offset as mentioned previously.

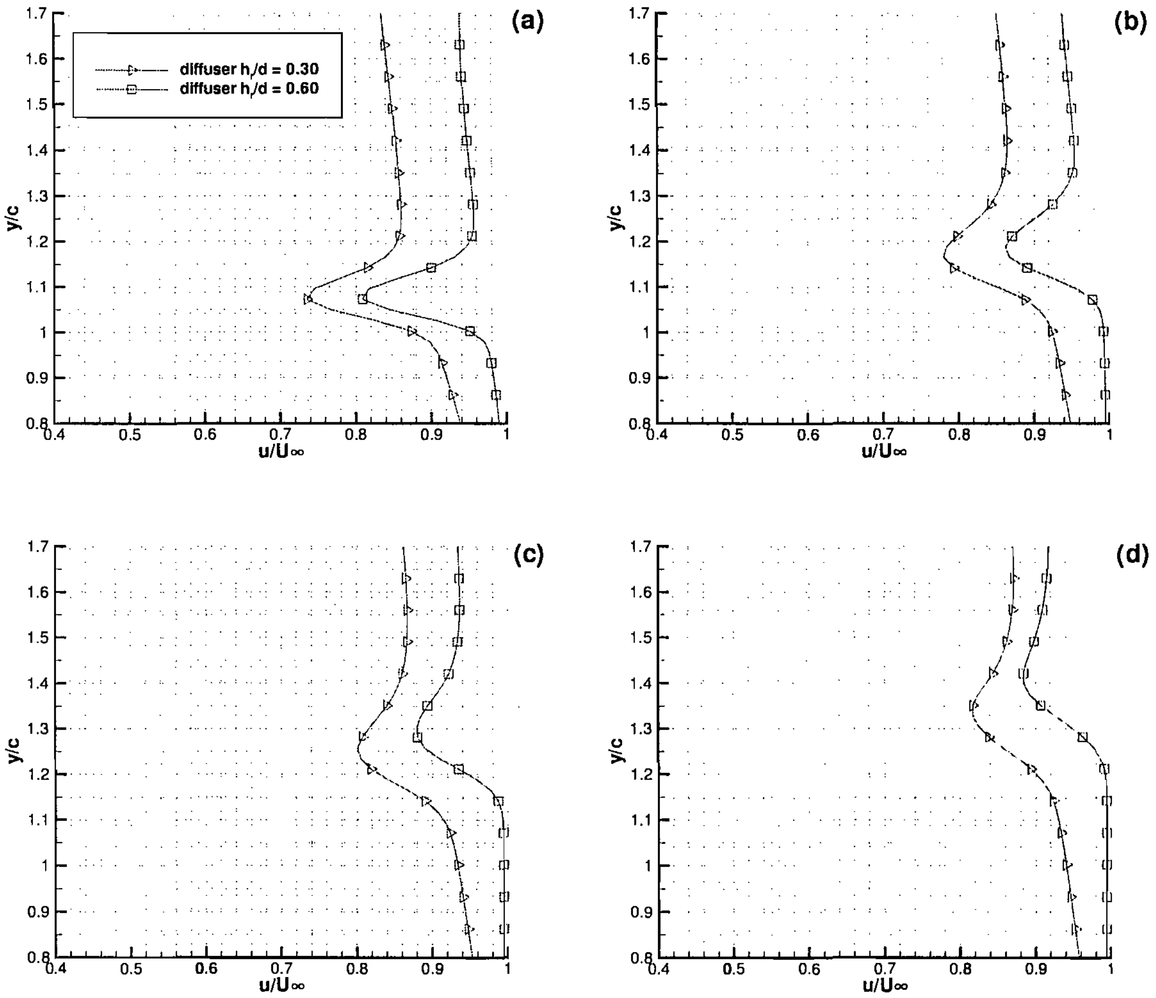

Figure 8.77: A comparison of centreline wing wake profiles for $h_r/c = 0.833$ at x/c = 1.5 (a), x/c = 2.25 (b), x/c = 3 (c) and x/c = 3.75 (d), for two diffuser heights.

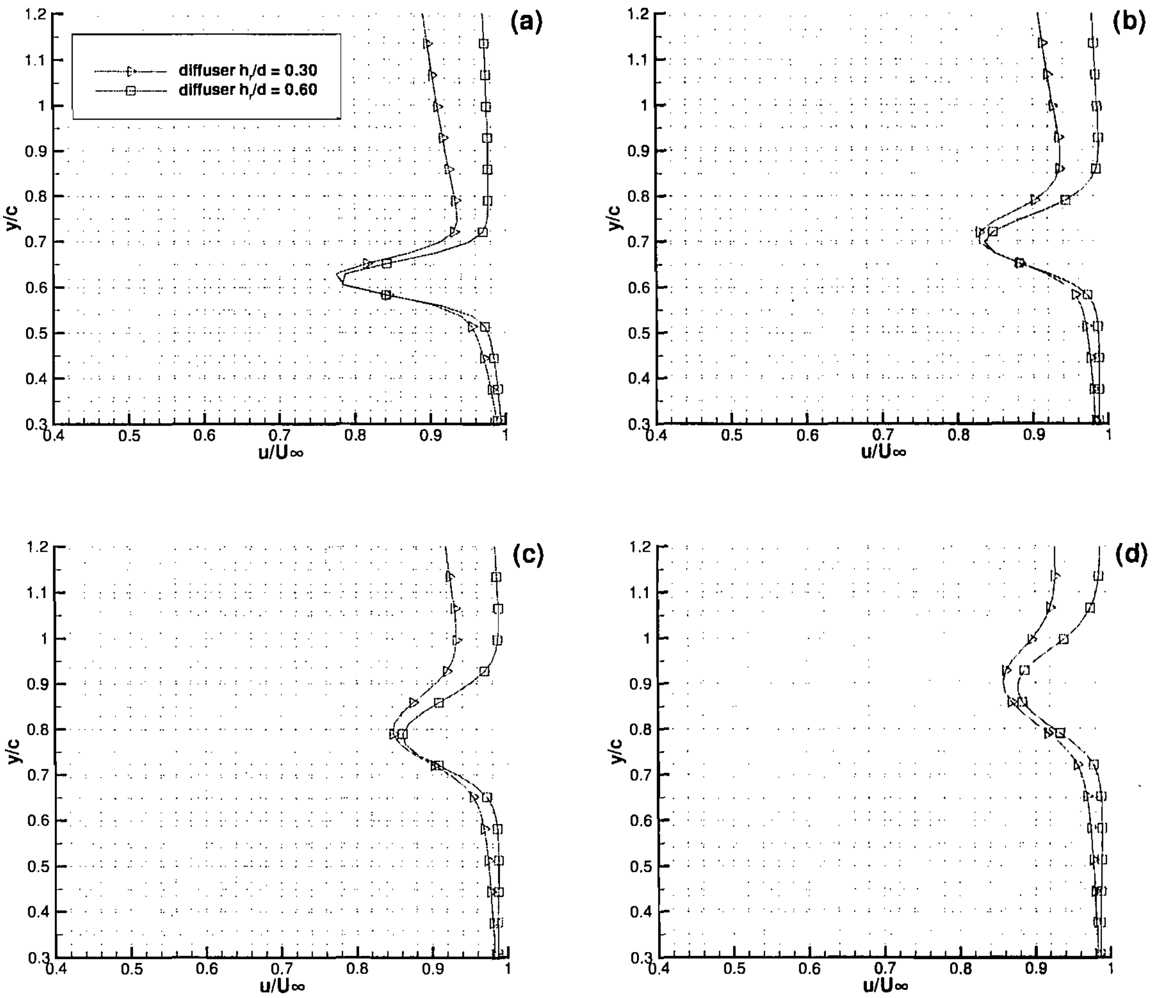

Figure 8.78: A comparison of centreline wing wake profiles for $h_r/c = 0.401$ at x/c = 1.5 (a), x/c = 2.25 (b), x/c = 3 (c) and x/c = 3.75 (d), for two diffuser heights.

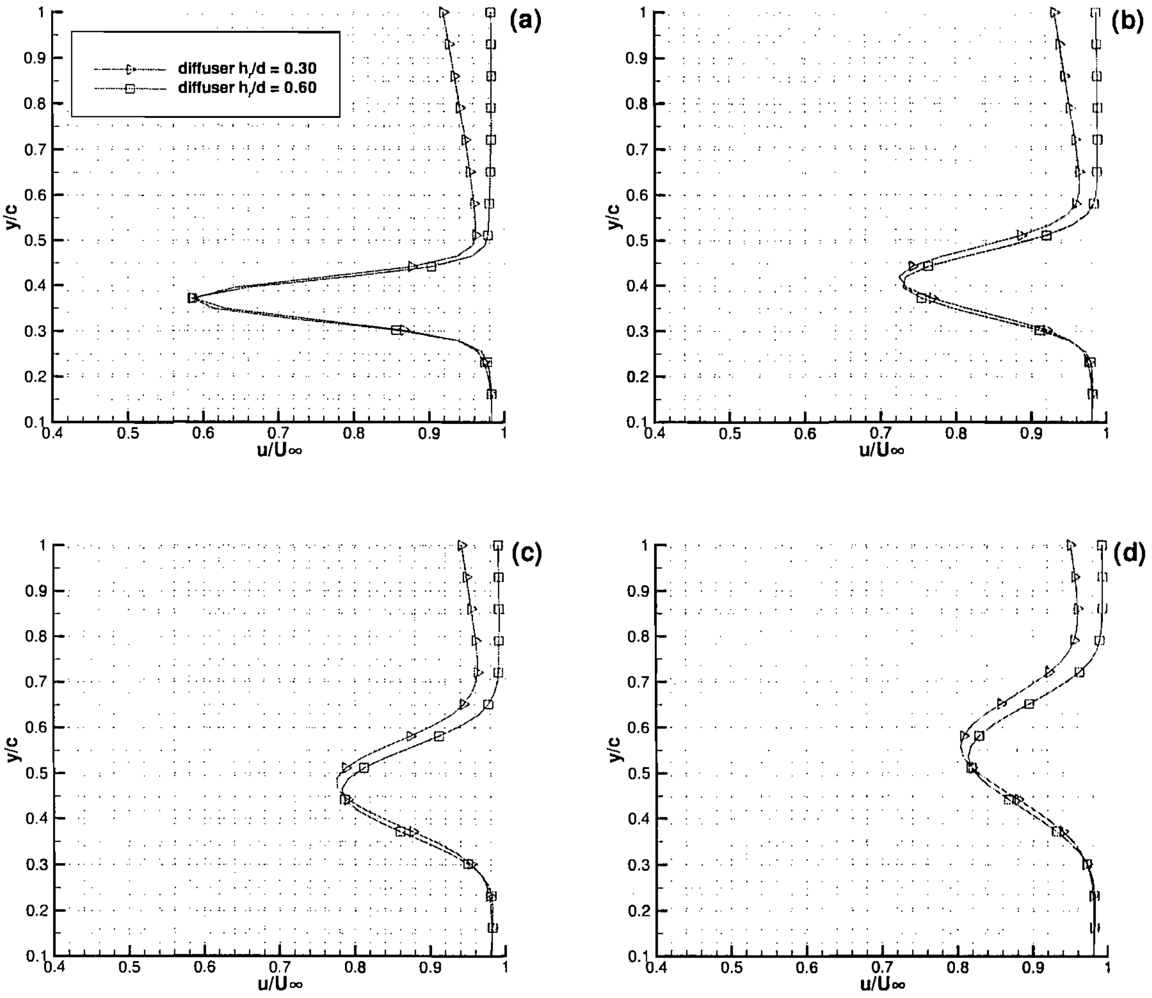

Figure 8.79: A comparison of centreline wing wake profiles for $h_r/c = 0.204$ at x/c = 1.5 (a), x/c = 2.25 (b), x/c = 3 (c) and x/c = 3.75 (d), for two diffuser heights.

8.7 Discussion

The CFD computations have produced results that have predicted the force trends that were uncovered experimentally. In terms of the effect of the upstream diffuser bluff body, the forces showed that the wing experienced less downforce and more drag when in flow condition FC3. This result also held when varying the angle of attack of the wing. Another experimental trend that was predicted was the loss of more downforce when the wing was placed at larger ride heights, as opposed to being placed at lower ride heights. It should be noted that the effect of laminar flow on the surfaces of the wing was not accounted for in the simulations. This result tends to indicate that the trends uncovered experimentally should also occur in cases of little or no laminar flow.

Flow visualisation on the suction surface of the wing at varying ride heights highlighted the delay of trailing edge flow separation in FC3. This delay suggested that the wing may have been operating at a lower angle of attack when placed in this flow condition.

The computational pressure distribution also predicted similar trends to experiment. More downforce was lost from sections closer to the centre of the wing, than was the case for sections closer to the tip of the wing. Also, as the flow changed from FC1 to FC3, the percentage reduction in downforce at each station decreased with decreasing ride height.

The flow field data highlighted the fact that the development of the wake of the wing was influenced by the wake of the upstream body. The computations also suggested that the weaker vortex that emanated from the top of the endplate may be dissipated when in some FC3 conditions. The main endplate vortex was shown to accelerate its horizontal movement and to decelerate its vertical movement as the wing approached the ground boundary. When compared to its position in clean air, the vortex was also predicted to have been displaced closer to the root of the wing at each downstream plane, when in dirty air conditions.

In terms of the effect of a change in the angle of the upstream diffuser, the computations predicted the experimental result that the lift to drag ratio of the downstream wing increased with decreasing diffuser angle. Pressure distribution plots showed that depending on ride height, different sections along the span of the wing generated more downforce when in the flow of the 5 deg ramp diffuser.

Flow visualisation images for this investigation only highlighted a significant change in suction surface flow at the ride height of $h_r/c = 0.204$. At this ride height, in the flow produced by the 5 deg ramp diffuser, a node point was present close to the root of the wing, in the region of flow separation. This feature was previously reported by Winkelmann and Barlow [78] from experiments carried out on rectangular wings beyond stall. The authors surmised that a vortex may have formed at each node point, and propagated downstream. They, however, presented no experimental evidence to support their hypothesis. The computational file was examined to ascertain whether such a vortex had been predicted. Indeed, the velocity vectors on downstream planes parallel to the trailing edge of the wing highlighted the presence of a small vortex that propagated downstream, close to a plane through the midspan of the wing. The vortex rotated in a counter-clockwise manner when viewed from ahead of the wing. The presence of the node vortex was seen to have had an effect on portions of the wake of the wing. Velocity profiles from the plane 2z/b = 0 indicated a slight downward motion as the wake progressed downstream.

In terms of the effect of a change in the height of the upstream diffuser, the computational results predicted negligible change to the downstream wing. The force results were very similar, and the surface flow images and pressure distribution plots provided no significant differences. A possible reason for these results may be the fact that the vortex wakes from each diffuser configuration did not occupy drastically different spatial positions at the plane on which the leading edge of the wing was located ($2.4l$ downstream of the diffuser bluff body).

8.8 Conclusion

The computational simulations that were presented in this chapter were aimed at investigating whether the trends that were uncovered experimentally, could be predicted with CFD. Examination of the data from a number of simulations has allowed the following conclusions to be drawn:

1. A loss in downforce and an increase in drag were predicted for the case of a single element wing placed in the flow produced by an upstream diffuser bluff body.
2. The loss of more downforce at greater ride heights than at lower ride heights was predicted, as was the result that more downforce was lost from sections closer to the midspan of the wing than was the case for sections closer to the tip of the wing.
3. Trailing edge flow separation was delayed in the wake flow, as compared to the undisturbed freestream flow.
4. The trend of an increasing lift to drag ratio of the wing, as the diffuser ramp angle was degreased, was predicted.
5. Changing the height of the diffuser was found to have negligible effect on the downstream wing for the cases simulated.

Chapter 9

Summary and Final Conclusions

9.1 Introduction

This chapter presents a summary of the research undertaken in the last three years. All of the relevant conclusions from the previous chapters are brought together.

9.2 Summary

9.2.1 Research Motivation

Research was carried out in an attempt to shed light on the salient factors that may contribute to the commonly reported lack of sufficient overtaking opportunities, typical of open-wheeled racing series such as Formula 1. Not only do the lack of such opportunities make the racing dull, but pit stop strategies are also influenced as attempts are made to pass competitors while they are being serviced in the pit lane, as opposed to when they are moving on the track.

A review of the available literature showed that although there was some non proprietary data on vehicle interaction, the majority of this data did not pertain to open-wheeled racing cars. The case that most effectively dealt with this type of scenario reported on the overall effects experienced by the downstream vehicle. No detailed measures of methods to counteract the effects were investigated. It followed that the lack of expansive data pertaining to the overtaking of open-wheeled racing cars presented an opportunity to carry out fundamental research aimed at further investigating the interactions experienced during a typical race. It was hoped that any findings would shed light on areas that could possibly be exploited to improve the aerodynamic performance of the downstream car. Additionally, it was also intended to provide a database for this type of aerodynamic flow.

9.2.2 Experimental Replication

The race scenario of one car following another was replicated generically in the wind tunnel by the construction and use of simple experimental models that were selected to represent the salient characteristics of each particular vehicle. The thought process behind this procedure was the following. Starting with simple models allowed for more complexity to be added in the future, as an understanding of the flow field and its inherent interactions were uncovered. Adding more complexity to simple models may allow for the causes of dominant flow features to be identified, and may therefore make it easier to find methods of controlling these features.

As a consequence of the reasons just given, the component of the following car that was chosen to commence the study was the front wing. This device was selected because it was the most forward part of the vehicle that would experience changes in the oncoming flow, because the majority of the downforce was typically lost from this component, and because the remainder of the car operated in the wake that it generated. The component was idealised as a single element wing, scaled to 40% of the dimensions of the front wing of a typical F1 car for the year 2002. It was thought logical to establish baseline data with this configuration before attempting to investigate multi-element devices.

The representation of the leading car evolved though two steps of increasing complexity. Firstly, a wing without endplates was used to idealise the upper elements of the rear wing. Initial tests with this component showed that it produced a measurable effect on the forces experienced by the downstream wing. The effect was reasoned to have been caused by changes to the flow field; changes that were thought to have been induced by the generation and subsequent transmission downstream, of wing tip vortices. Since these vortices were deemed to have had this effect, it was reasoned that even larger vortices would have been produced by a diffuser in ground effect [50, 52]. The decision was therefore taken to incorporate a diffuser into a bluff body shape, so as to better represent the leading car. The idealised rear wing was attached to the diffuser bluff body via endplates.

The height and lateral position of the bluff body were adjustable, as was the angle of the diffuser ramp. Owning to wind tunnel constraints, it was only possible to scale the width of the diffuser (and hence the bluff body) to be 40% of the stipulated width of the diffuser of a typical F1 car for the year 2002.

The bluff body was mounted to a ground board that was positioned just ahead of the rolling road and suction box in the wind tunnel test section. The wing and endplates were mounted to an overhead balance above the rolling road. The tests performed included variations in the height of the wing and variations in its angle of attack. The data taken included force and pressure measurements, flow visualisation images and flow field measurements with PIV and LDA.

9.2.3 Diffuser Bluff Body Flow Field

The flow field generated by the upstream bluff body was examined with smoke trails, surface flow visualisation, PIV and LDA. The smoke trails, which were released from a portable wand, showed that the flow in the vicinity of the rear of the bluff body, close to the diffuser sideplates, was sucked in towards a plane that coincided with the centreline of the test section. The flow then progressed downstream, seemingly concentrated in the middle of the test section as it did so. There was also a significant increase in the amount of audible noise associated with this configuration; an indication of the generation of turbulent flow [79]. Surface flow visualisation on the diffuser ramp highlighted the presence of swirling s-shaped lines that trailed along the edges of the ramp, close to the sideplates. The lines were symmetric about the centreline of the model, and were indicative of vortex generation from the diffuser in ground effect.

An examination of the velocity flow field downstream of the diffuser was carried out with PIV and LDA. The PIV tests were performed in the 2.1 m × 1.5 m facility, while the LDA tests were performed in the larger 3.5 m × 2.5 m facility. In general, the profiles revealed a deficit in the streamwise component of velocity and an upwash in the vertical component of velocity. Both the velocity deficit and the upwash were seen to increase to a maximum and then to decrease, as the height above the ground increased. From the LDA results at the locations of $2z/b = 0.80$ and 0.87, the vertical velocity began to show a downwash in the wake. Altogether, these results pointed to the existence of a vortex in the downstream flow field. The vortex would have rotated in such a manner as to produce an upwash on planes close to the centreline of the tunnel, while producing a downwash on planes closer to the edges of the test section.

The velocity profiles that were presented also indicated that the wake downstream of the bluff body was influenced by the angle of the diffuser ramp and by the height of the bluff body above the ground. It was shown that the 5 and 10 deg diffuser induced the greatest freestream deficit; approximately 6% for the data taken. The 16.7 deg diffuser induced a smaller deficit; approximately 2% to 4% for the data taken. With regard to the upwash in the flow field, decreasing the angle of the diffuser had the effect of decreasing the amount of downstream upwash.

Lowering the height of the diffuser above the ground was also shown to induce a deficit in the freestream flow. The deficit was significantly large for the lowest ride height, ranging from 10% to 19% for the data taken. At the lowest ride height, however, the diffuser may have been operating at a critical point in the transition between the region of force increase and the region of force reduction of its own downforce curve [50].

Between $y/c = 0.08$ and 0.45, the levels of upwash appeared to remain broadly similar, while varying the height of the diffuser. Above this region, the diffuser at the lowest ride height induced significantly lower values of upwash than the others.

9.2.4 Aerodynamic Effects on Downstream Wing

Force measurements carried out on the downstream wing indicated that it experienced a reduction in downforce when in the flow produced by the diffuser bluff body. The reduction was not constant, but varied depending on the ride height of the wing. When compared to the clean air case, more downforce was lost at greater ride heights, than was the case at lower ride heights. This result also held while varying the angle of attack of the wing to generate lift curves. Furthermore, in dirty air conditions, it was proved that the lift curve slope of the wing also increased with decreasing wing ride height. As the wing was moved laterally away from a position directly in front of the bluff body, the downforce values recovered to the clean air levels, and even surpassed these levels at the greatest lateral distance from the bluff body.

The force measurements also showed that it was possible for the force reduction region of the downforce curve to change in character in dirty air at very low ride heights. Instead of a continual decrease in the force, a second region of force increase produced coefficients that were higher than the maximum achieved during the first region of force increase (typically between $h_r/c = 1$ and $h_r/c \approx 0.09$).

With regard to the drag, the force measurements indicated that the wing experienced an increase in this variable when downstream of the diffuser bluff body. The increase was evident throughout the ride height range investigated. Also evident in both the clean air and dirty air measurements were intermittent peaks and dips in the drag coefficient when the wing was positioned below the ride height of $h_r/c = 0.153$.

Confirmation of the physical effects of the bluff body flow on the wing was provided by flow visualisation images. The clean air flow condition indicated that there was laminar to turbulent transition via a laminar separation bubble, visible across the span of both upper and lower surfaces, albeit at different chordwise locations. In contrast, the dirty air flow condition highlighted early transition from laminar to turbulent flow in the middle portion of the span. This earlier formation of the turbulent flow was significant enough to cause the elimination of the separation bubble from the middle portion of both surfaces of the wing.

Flow visualisation at a ride height at which the second region of force increase occurred – in the dirty air conditions – showed that the suction surface experienced massive flow separation in clean air, but that the flow remained attached in the dirty air. Consequently, the wing was able to generate more downforce at that very low ride height. The ride heights at which the phenomenon occurred, however, appeared to be too low to render the effect of any practical importance.

The aerodynamic interactions that were just reported can be linked to the changes in the oncoming flow. The reduction in the downforce of the wing was the result of the generation of lower C_p values, and hence lower total forces. The upwash that was present in the flow field would have served to reduce the effective angle of attack of the wing, hence inducing lower pressures. The increased turbulence in the oncoming flow promoted early laminar to turbulent boundary layer transition on the wing. Consequently, the boundary layer was much thicker from the outset, therefore having a greater decambering effect on the profile. That is, the wing effectively lost camber, which would have resulted in lower pressures. The reduced velocity of the oncoming flow would have also resulted in the generation of lower surface pressures, as the wing was effectively operating at a lower Reynolds number.

The fact that more downforce was lost when the wing was positioned at larger ride heights can be explained by the change in the variables just described. With increasing distance above the ground, for the ride height range tested, there was increased upwash, increased turbulence and a decreasing velocity of the oncoming flow.

The centre of the wing experienced a greater loss in downforce than the tips because the majority of the disturbed flow appeared to be concentrated in that region, and because that region experienced an upwash, while the tips experienced flow with a neutral to slight downward component of velocity, in addition to a slightly higher freestream velocity.

The increase in the drag of the wing can be explained by the resultant interaction of a number of factors. Firstly, flow visualisation in the disturbed conditions highlighted the fact that the laminar separation bubble was eliminated from the middle portion of both the upper and lower surfaces of the wing. This result in itself should have accounted for a decrease in the drag, however, this decrease was seemingly outweighed by drag increments from increased induced drag [80] and the increased extent of the turbulent boundary layer. Increased induced drag resulted from the fact that the wing operated in the upwash of the upstream diffuser bluff body. The increased extent of the turbulent boundary layer caused increased skin friction drag.

9.2.5 Effects of a Change in Diffuser Angle

It was found that the angle of the upstream diffuser affected the lift to drag ratio of the downstream wing. As the stated angle was decreased, the wing operated with increasing efficiency. This result can be linked to a decrease in the amount of upwash generated by diffusers with successively lower ramp angles. The decreased upwash was believed to have contributed to a decrease in the induced drag experienced by the wing, which meant that it would have operated more efficiently at a given ride height.

Observation of the characteristics of the wake of the wing highlighted the fact that the 5 and 10 deg diffusers seemed to induce similar wake development, while the 16.7 deg diffuser induced a different wake development. It is surmised that these differences may have been the result of different types of vortex flow emanating from the diffuser. The 5 and 10 deg diffusers were thought to have produced one type of flow, while the 16.7 deg diffuser was thought to have produced another [51, 52].

9.2.6 Effect of Changes to Bluff Body Height

The effect of changing the height of the upstream bluff body proved more difficult to assess, in terms of the particular treads that may have been uncovered. According to data presented by Senior [50], at $h_r/d = 0.3$ the diffuser was operating in the maximum downforce region of its own downforce curve. Reducing its height above the ground to

$h_r/d = 0.25$, then to $h_r/d = 0.2$, therefore corresponded to shifting its operating point from maximum downforce to the region of the force reduction phenomenon. This change implied that there may have been different flow regimes at each height extreme, and possibly some state of transition between them. There was also an apparent anomaly in one of the drag curves. It was not possible to ascertain whether it was an error or whether it was an unexplained flow feature.

What was concluded with certainty was that diffuser $h_r/d = 0.2$ produced a significant reduction in the lift and drag of the wing, when compared to the other diffuser heights. The reduction was induced mainly by the slow moving fluid in the wake of the diffuser. Essentially, the wing was operating at a significantly lower dynamic pressure. Conversely, it can be stated that the downforce of the downstream wing could be increased if it were possible to inject higher momentum streamwise fluid into the wake produced by the upstream body.

In terms of the development of the downstream wake of the wing, varying the ride height of the diffuser over the stated range induced a similar shape in all cases, with spreading occurring via the lower boundary. The spreading increased as the ride height was reduced, with the maximum wake deficit remaining approximately constant.

9.2.7 CFD

CFD was used to model the wing at one ride height in the clean air conditions in which the experiments were carried out. This case was chosen because the experimental surface flow visualization allowed for the accurate determination of the points of laminar to turbulent flow transition, for use in the simulation. The computations were carried out with the Spalart-Allmaras and RNG $\kappa\epsilon$ turbulence models. It was found that both models predicted premature boundary layer separation on the pressure surface of the wing, indicating that the experimental surface flow was not adequately simulated. Notwithstanding this result, the experimental downforce value was predicted to within 6.5% by the Spalart-Allmaras model, while the experimental drag value was at best, over predicted by 9% with the RNG $\kappa\epsilon$ model.

CFD was also used to perform generic simulations of the clean air and dirty air experimental configurations. The aim was to ascertain whether the trends that were uncovered experimentally could be predicted computationally. No laminar flow was accounted for in these cases. In terms of the effect of the upstream diffuser bluff body, the forces showed that the wing experienced less downforce and more drag in the dirty air. This result also held when varying the angle of attack of the wing. Another experimental trend that was predicted was the loss of more downforce when the wing was placed at larger ride heights, as opposed to being placed at lower ride heights.

Flow visualisation on the suction surface of the wing at varying ride heights highlighted the delay of trailing edge flow separation in the dirty air. This delay suggested that the wing may have been operating at a lower angle of attack when placed in this flow condition.

The computational pressure distribution also predicted similar trends to experiment. More downforce was lost from sections closer to the centre of the wing, than was the case for sections closer to the tip of the wing. The shape of the spanwise load distribution also changed, depending on ride height. At large ride height values the tips of the wing were found to generate more load than the middle of the wing. At low ride heights, the opposite effect occurred.

In terms of the effect of a change in the angle of the upstream diffuser, the computations predicted the experimental result that the lift to drag ratio of the downstream wing increased with decreasing diffuser angle. Pressure distribution plots showed that depending on ride height, different sections along the span of the wing generated more downforce when in the flow of the 5 deg ramp diffuser.

In terms of the effect of a change in the height of the upstream diffuser, the computational results predicted negligible change to the downstream wing. The force results were very similar, and the surface flow images and pressure distribution plots provided no significant differences. A possible reason for these results may be the fact that the vortex wakes from each diffuser configuration occupied similar spatial positions at the plane on which the leading edge of the wing was located, irrespective of the fact that they were initially generated from different ride heights.

9.3 Final Conclusions

From the experiments and computational simulations that were carried out to model the effect that a leading open-wheeled racing car may have on a following open-wheeled racing car, the following can be concluded:

- When in the dirty air flow, the downstream wing that was used to simulate the front wing of the trailing car experienced a decrease in its downforce values and an increase in its drag values, when compared to the clean air case.
- When in the dirty air flow, more downforce was lost from sections closer to the midspan of the wing than was the case for sections closer to the tip of the wing.
- When in the dirty air flow, the shape of the spanwise load distribution altered, depending on ride height. At greater ride heights, the load distribution was lower at midspan than it was towards the wing tips. At lower ride heights, the trend reversed.
- The downstream wing was affected by the upwash flow field from the upstream body. The presence of an upwash appeared to have resulted in an increase in the induced drag experienced by the wing.
- The disturbed flow emanating from the upstream body had the ability to significantly alter the surface flow patterns on the downstream wing. The altered characteristics included earlier laminar to turbulent boundary layer transition, and the elimination of laminar separation bubbles.

- As the angle of the diffuser ramp was decreased, the downstream wing experienced an increase in its lift to drag ratio. The increase in the ratio was at least in part, influenced by the decreasing amount of upwash present in the vicinity of the wing.
- Varying the angle of the diffuser appeared to influence the development of the downstream wake of the wing. The wake showed similar characteristics when behind the 5 deg and 10 deg diffusers, and different characteristics when behind the 16.7 deg diffuser.
- When trying to model a specific experimental configuration in clean air, CFD was not able to entirely match the surface flow conditions on the pressure surface of the wing, owing to premature laminar boundary layer separation.
- When carrying out generic simulations of the clean air and dirty air flow conditions, CFD was able to predict the force and pressure trends that were uncovered experimentally.

9.4 Recommendations for Future Work

In this section, the areas in which further investigations can be carried out will be discussed. The main aim is to provide a more advanced understanding of the aerodynamic interactions. Included in the recommendations are more extensive mappings of the diffuser and wing flow fields and improvements to the experimental models.

9.4.1 Map of Diffuser Flow Field

Given that the flow generated by the different diffuser bluff body configurations was shown to have had wide ranging effects on the downstream wing, it became evident that a detailed experimental investigation of the diffuser wake was needed. The tests should be carried out for the ramp angles considered in this document, as well as for ride heights that are representative of the different diffuser flow states, as outlined in the appropriate references. Data should be taken for varying distances downstream of the diffuser, including any region in which a second test model may be placed. All components of velocity should be measured, as well as the corresponding turbulence statistics, if possible.

9.4.2 Map of Wing Flow Field

The data that was collected in this project indicated that the development of the wake of the wing was influenced by the upstream models. As such, it was thought that a more thorough map of this region would provide further insight regarding the changes to be expected. All components of velocity, as well as turbulence statistics should be collected.

9.4.3 Use of a more Complex Downstream Model

The front wing of the following car was idealized as a single element wing in order to commence this research investigation. The next logical step would be to replace it with a multi-element wing similar to those used on modern cars. After the appropriate measurements were taken with this improved model, it was thought that idealised front wheels could be added. Idealised front wheels may allow for a more accurate representation of the overall drag effects experienced by a following car.

9.4.4 Use of a more Complex Upstream Model

Idealised rear wheels can be added to the upstream bluff body in order to more accurately represent the wake generated by a leading car. This flow field should then be mapped, and the appropriate tests carried out on the downstream model. If possible, the bluff body and wheels should be placed over a rolling road.

Appendix A

Coordinates

A.1 LS(1)–0417 Profile

Table A.1: The Coordinates for the LS(1)-0417 Profile

x-coordinate	y-coordinate
1.000000	-0.000740
0.987266	0.002704
0.967066	0.008207
0.945762	0.014024
0.923608	0.020026
0.900854	0.026160
0.877760	0.032387
0.854545	0.038618
0.831350	0.044771
0.808292	0.050789
0.785403	0.056568
0.762598	0.062150
0.740020	0.067519
0.717710	0.072582
0.695595	0.077308
0.673672	0.081697
0.651937	0.085702
0.630293	0.089303
0.608720	0.092544
0.587234	0.095350
0.565660	0.097708
0.543903	0.099691
0.521989	0.101353
0.499957	0.102692
0.477806	0.103712
0.455524	0.104428

continued on next page

Table A.1: *continued*

x-coordinate	y-coordinate
0.433132	0.104859
0.410681	0.105018
0.388247	0.104912
0.365909	0.104536
0.343704	0.103871
0.321625	0.102910
0.299719	0.101672
0.278119	0.100178
0.256958	0.098425
0.236302	0.096406
0.216233	0.094142
0.196968	0.091685
0.178768	0.089069
0.161719	0.086259
0.145825	0.083338
0.131177	0.080408
0.117814	0.077486
0.105691	0.074568
0.094710	0.071646
0.084755	0.068731
0.075718	0.065849
0.067506	0.063015
0.060044	0.060213
0.053258	0.057430
0.047079	0.054658
0.041453	0.051881
0.036331	0.049072
0.031660	0.046226
0.027387	0.043363
0.023468	0.040504
0.019881	0.037652
0.016617	0.034794
0.013665	0.031920
0.011013	0.029024
0.008664	0.026103
0.006629	0.023158
0.004914	0.020186
0.003512	0.017194
0.002388	0.014212
0.001509	0.011270
0.000850	0.008380
0.000390	0.005539

continued on next page

Table A.1: *continued*

x-coordinate	y-coordinate
0.000112	0.002746
0.000037	0.001378
0.000000	0.000000
0.000105	-0.002740
0.000520	-0.005374
0.001280	-0.007996
0.002411	-0.010573
0.003936	-0.013069
0.005864	-0.015396
0.008184	-0.017513
0.010847	-0.019461
0.013787	-0.021295
0.016960	-0.023061
0.020373	-0.024779
0.024036	-0.026479
0.027957	-0.028198
0.032159	-0.029926
0.036685	-0.031625
0.041592	-0.033250
0.046934	-0.034831
0.052749	-0.036448
0.059069	-0.038151
0.065942	-0.039923
0.073428	-0.041729
0.081617	-0.043533
0.090630	-0.045322
0.100601	-0.047102
0.111669	-0.048889
0.123944	-0.050717
0.137460	-0.052626
0.152197	-0.054528
0.168200	-0.056313
0.185494	-0.057996
0.203952	-0.059583
0.223329	-0.061036
0.243376	-0.062293
0.263964	-0.063305
0.285084	-0.064073
0.306674	-0.064631
0.328584	-0.065000
0.350668	-0.065172
0.372848	-0.065143

continued on next page

Table A.1: *continued*

x-coordinate	y-coordinate
0.395081	-0.064910
0.417317	-0.064469
0.439507	-0.063821
0.461607	-0.062962
0.483575	-0.061881
0.505333	-0.060562
0.526793	-0.058972
0.547991	-0.057036
0.569143	-0.054678
0.590394	-0.051955
0.611749	-0.048861
0.633355	-0.045427
0.655146	-0.041770
0.677003	-0.037944
0.698783	-0.034048
0.720192	-0.030191
0.740996	-0.026271
0.761393	-0.022627
0.781617	-0.019130
0.801636	-0.015591
0.821545	-0.012421
0.841362	-0.009634
0.860952	-0.007192
0.880140	-0.005139
0.898845	-0.003596
0.917153	-0.002681
0.935220	-0.002387
0.953108	-0.002654
0.970648	-0.003571
0.988046	-0.005628
1.000000	-0.007830

Table A.2: The chordwise location of the pressure taps

Suction		Pressure	
Tap	x/c location	Tap	x/c location
1	0.000000	25	0.899870
2	0.006300	26	0.850040
3	0.020000	27	0.800130
4	0.037130	28	0.750000
5	0.055455	29	0.700220
6	0.075220	30	0.650220
7	0.100130	31	0.599830
8	0.149700	32	0.549700
9	0.200040	33	0.499830
10	0.249910	34	0.450090
11	0.299650	35	0.399910
12	0.349910	36	0.349830
13	0.399780	37	0.300040
14	0.449740	38	0.249650
15	0.500040	39	0.199430
16	0.550350	40	0.149610
17	0.600170	41	0.099570
18	0.649960	42	0.061960
19	0.700040	43	0.037260
20	0.750000	44	0.017220
21	0.799870		
22	0.850040		
23	0.900040		
24	0.950260		

A.2 Eppler E420 Profile

Table A.3: The Coordinates for the Eppler E420 Profile

x-coordinate	y-coordinate
1.0000000	0.0000000
0.9965100	0.0016400
0.9869100	0.0067200
0.9727700	0.0148100
0.9548900	0.0245700
0.9329700	0.0348200
0.9064300	0.0453700
0.8753900	0.0565600

continued on next page

Table A.3: *continued*

x-coordinate	y-coordinate
0.8403800	0.0684000
0.8019400	0.0807800
0.7606600	0.0934900
0.7171200	0.1063000
0.6719300	0.1189400
0.6256900	0.1310800
0.5789600	0.1423800
0.5322900	0.1525100
0.4861900	0.1611000
0.4411300	0.1677900
0.3975400	0.1721300
0.3554900	0.1736000
0.3147900	0.1721200
0.2754900	0.1679200
0.2377200	0.1612700
0.2017100	0.1525300
0.1678400	0.1420100
0.1364200	0.1299800
0.1077600	0.1166900
0.0821200	0.1024000
0.0597100	0.0873900
0.0407100	0.0719600
0.0252700	0.0564300
0.0134500	0.0411600
0.0053100	0.0265400
0.0008600	0.0130500
0.0000300	0.0012800
0.0003300	-0.0010700
0.0010200	-0.0039600
0.0016500	-0.0057100
0.0024200	-0.0073100
0.0028700	-0.0080300
0.0033500	-0.0087100
0.0038900	-0.0093100
0.0045200	-0.0098400
0.0052400	-0.0103400
0.0060400	-0.0108200
0.0078600	-0.0116900
0.0099400	-0.0124900
0.0135400	-0.0135400
0.0251600	-0.0154500
0.0449900	-0.0159600

continued on next page

Table A.3: *continued*

x-coordinate	y-coordinate
0.0702400	-0.0141100
0.1009500	-0.0098200
0.1372500	-0.0031700
0.1793800	0.0056500
0.2276900	0.0159300
0.2819900	0.0263700
0.3414800	0.0356900
0.4046800	0.0427100
0.4695800	0.0470200
0.5346600	0.0490100
0.5989100	0.0489100
0.6611800	0.0467300
0.7202200	0.0428200
0.7751100	0.0377200
0.8251700	0.0319000
0.8698200	0.0257000
0.9085000	0.0195000
0.9408200	0.0136400
0.9664200	0.0084200
0.9849900	0.0041100
0.9962400	0.0011200

Appendix B

Error Analysis

B.1 Forces

In order to obtain an estimate of the errors in the force coefficients, the methods outlined by Coleman and Steele [64] have been applied to the experimental data.

$$C_F = \frac{F}{q_\infty S} = \frac{F_{total} - F_{tare}}{q_\infty S} \tag{B.1}$$

$$C_F = \left(\frac{F_{total}}{q_\infty S}\right)_a - \left(\frac{F_{tare}}{q_\infty S}\right)_b \tag{B.2}$$

where a and b refer to the separate experimental configurations, taking into account the stopping and restarting of the wind tunnel to perform the required modifications to the model.

$$C_F = r(X_a, Y_a) - r(X_b, Y_b) \tag{B.3}$$

where X and Y are variables that were measured directly during the experiment and $X_a = F_{total}$, $Y_a = (q_\infty)_a$, $X_b = F_{tare}$ and $Y_b = (q_\infty)_b$.

The random uncertainty in the force coefficients is then given by:

$$P_{C_F} = \sqrt{\left(\frac{\partial C_F}{\partial X_a}\right)^2 P_{X_a}^2 + \left(\frac{\partial C_F}{\partial X_b}\right)^2 P_{X_b}^2 + \left(\frac{\partial C_F}{\partial Y_a}\right)^2 P_{Y_a}^2 + \left(\frac{\partial C_F}{\partial Y_b}\right)^2 P_{Y_b}^2} \tag{B.4}$$

where P_{X_*} is calculated from a large sample population of the measured experimental variables

$$P_{X_*} = 2S_{\overline{X}_i} = \frac{2S_{X_i}}{\sqrt{N_i}} \tag{B.5}$$

and S_X is the standard deviation of the sample consisting of N readings.

The random uncertainty in the lift and drag coefficients of the wing, while behind diffuser $h_r/d = 0.20$, are given in Table B.1. It was felt that this case encompassed the greatest variation in the forces obtained from the balance, so all other configurations were thought to fall within these bounds. In general, the maximum uncertainty in C_L was ±0.002, while the maximum uncertainty in C_D was ±0.0004. Figures B.1 and B.2 provide a graphical representation of the tabular values.

h_r/c	C_L	P_{C_L}	C_D	P_{C_D}
0.833	0.489	0.0006	0.0463	0.00040
0.600	0.553	0.0005	0.0561	0.00042
0.401	0.671	0.0008	0.0647	0.00040
0.289	0.804	0.0008	0.0725	0.00043
0.204	0.968	0.0014	0.0809	0.00041
0.181	1.021	0.0009	0.0847	0.00040
0.153	1.088	0.0012	0.0885	0.00037
0.130	1.123	0.0012	0.0923	0.00044
0.107	1.150	0.0017	0.0949	0.00040
0.100	1.152	0.0012	0.0946	0.00040
0.094	1.145	0.0010	0.0945	0.00044
0.090	1.136	0.0014	0.0928	0.00039
0.085	1.123	0.0007	0.0927	0.00043
0.077	1.026	0.0014	0.0938	0.00039

Table B.1: The random uncertainty values for the case of the wing behind diffuser h_r/d = 0.20.

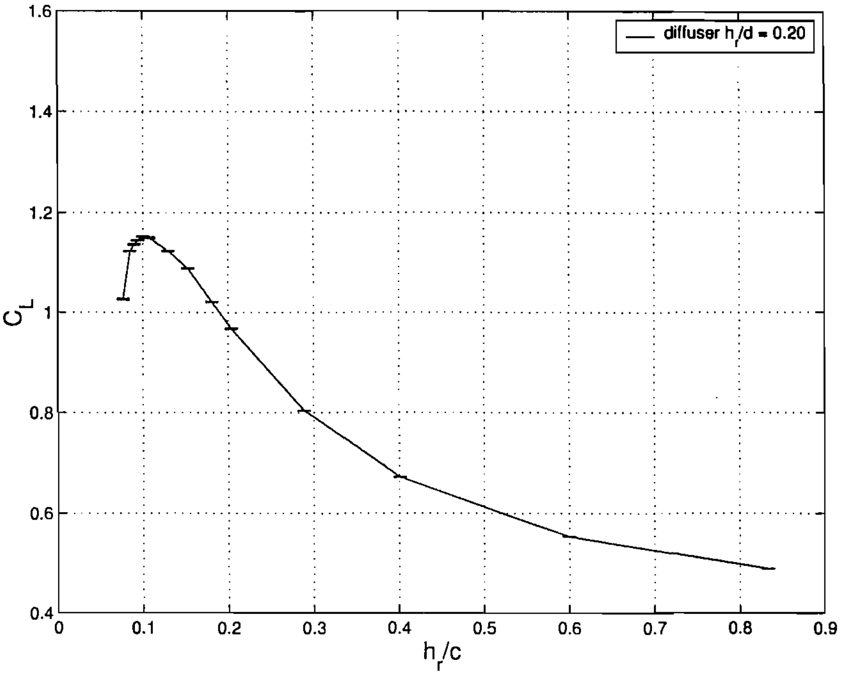

Figure B.1: The random uncertainty in the lift coefficient for the case of the wing behind diffuser $h_r/d = 0.20$.

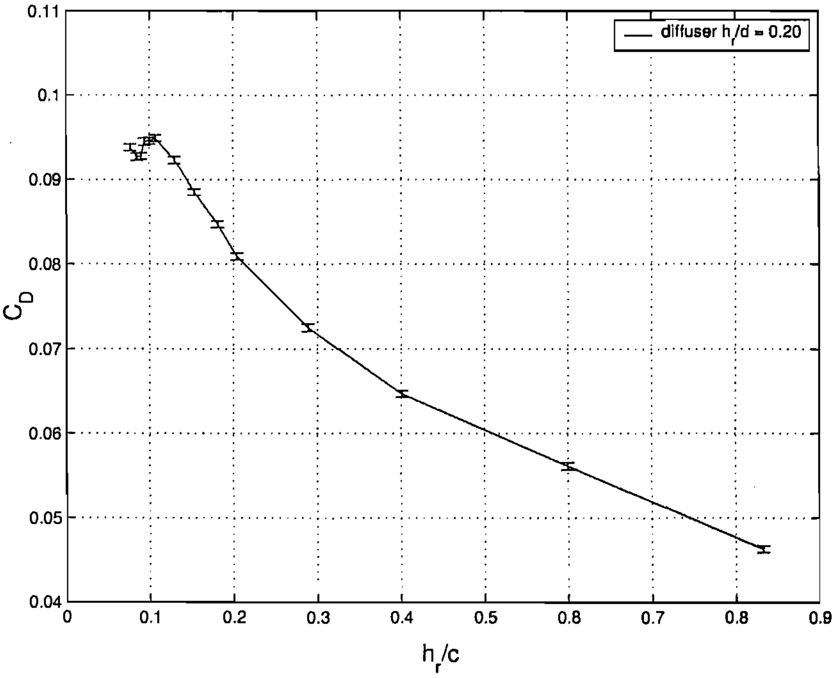

Figure B.2: The random uncertainty in the drag coefficient for the case of the wing behind diffuser $h_r/d = 0.20$.

B.2 Pressures

Table B.2: The estimated worse case uncertainties in the pressure measurements

Suction			Pressure		
Tap	C_L	P_{C_P}	Tap	C_L	P_{C_P}
1	0.710	0.009	25	0.188	0.002
2	-0.286	0.010	26	0.175	0.002
3	-1.070	0.005	27	0.115	0.001
4	-1.504	0.003	28	0.033	0.002
5	-1.692	0.004	29	-0.045	0.001
6	-1.848	0.003	30	-0.111	0.001
8	-1.982	0.004	31	-0.167	0.001
9	-2.099	0.004	32	-0.201	0.001
10	-2.092	0.005	33	-0.232	0.001
11	-2.094	0.003	34	-0.249	0.001
12	-2.076	0.003	35	-0.247	0.001
13	-1.984	0.002	36	-0.240	0.002
14	-1.852	0.002	37	-0.234	0.001
15	-1.671	0.003	38	-0.210	0.001
16	-1.430	0.002	39	-0.157	0.056
17	-1.231	0.002	40	-0.165	0.002
18	-0.964	0.001	41	-0.120	0.002
19	-0.744	0.002	42	-0.074	0.002
20	-0.525	0.002	43	0.020	0.003
21	-0.363	0.001	44	0.257	0.003
22	-0.269	0.002			
23	-0.205	0.006			
24	-0.165	0.002			

Using the methods previously outlined, the random uncertainty in the pressure distribution data was estimated from the samples output at each tap. Data from a case that was considered to have experienced the most measurement fluctuations was used for the calculations. The software only produced a printed version of the pressures, so it was not possible to re-enter (by hand) the output from each configuration. The results are tabulated in Table B.2, and are graphed in Fig. B.3. In general, the uncertainty in the pressure measurements was less than ±0.01, with the exception of one tap, which experienced an uncertainty of ±0.06. From a visual inspection of the raw values that were recorded for all other configurations, the magnitude of the variations that were experienced were comparable to those for the taps showing an uncertainty of ±0.01 or less.

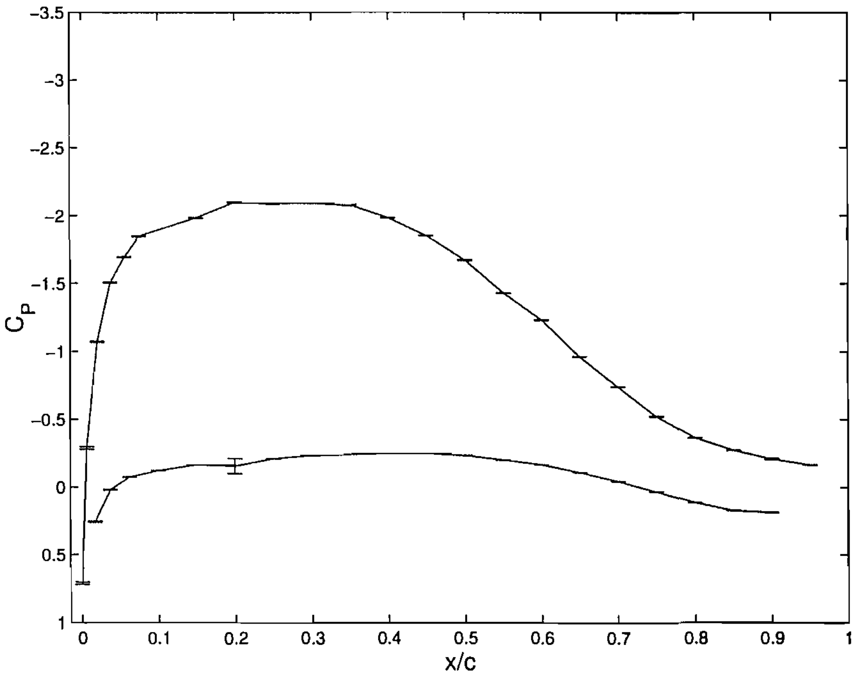

Figure B.3: The random uncertainty in the pressure coefficients for the wing in FC3.

B.3 LDA

The LDA system at the University was used extensively to gather flow field data for wings in ground effect and diffusers in ground effect. The published data from these tests give uncertainty estimates of ±0.09 in u and v [52], and ±0.005 in u/U_∞ and v/U_∞ [34, 36]. To confirm the estimate in the velocity components, an analysis was carried out on the data that was obtained from a point in the region of highest turbulence intensity (approximately 11%) in the wake of the diffuser bluff body. This point was chosen because it was reasoned that the highest velocity fluctuations would occur in the region of highest turbulence intensity. At this particular point, 1372 coincident data measurements were extracted from the LDA post-processing files. Applying the procedures of Coleman and

Steele, the x-velocity was found to be 17.94 ±0.103 m/s, and the y-velocity was found to be 1.040 ±0.097 m/s. A reasonable estimate of the uncertainty in the velocity components is therefore ±0.10 m/s.

B.4 PIV

Data from the PIV system at the University was compared to data from the LDA system by Zerihan [34], and by Webb and Castro [81]. Zerihan compared wing wake profiles that were taken half chord length downstream of the trailing edge of the wing. It was found that the freestream component of the PIV results were generally within ±1% of the freestream component of the LDA results. The PIV profile was also seen to be noisier than the LDA profile.

Webb and Castro investigated the potential of the PIV system for making Reynolds stress measurements in flows of different turbulent intensity and length scale. From their report, it could be deduced that the collection of data to produce mean velocity profiles required less stringent settings of the system parameters, than did the collection of data for the calculation of turbulence quantities. Guidelines regarding pixel size, flow resolution, interrogation area offset and post-processing, among others, were discussed as a best practice for obtaining data for turbulence statistics. The suggested guidelines were applied to the current research.

Consideration of the centreline profiles in the test section of the 2.1 m × 1.5 m wind tunnel can be used as a guide for further estimation of the associated errors. The tests were carried out at 20 m/s. Since the tunnel is in frequent use, both for research and commercially, it is plausible to assume that when the controlling system is set to a required velocity, that velocity is achieved in the test section with reasonably certainty. On this basis, and from the plot for FC1 in Fig. B.4, it can be deduced that there was most likely (barring any unknown tunnel flow irregularities) an uncertainty of 1.6% in u. As a vertical component of velocity is expected to be non-existent in the test section in FC1,

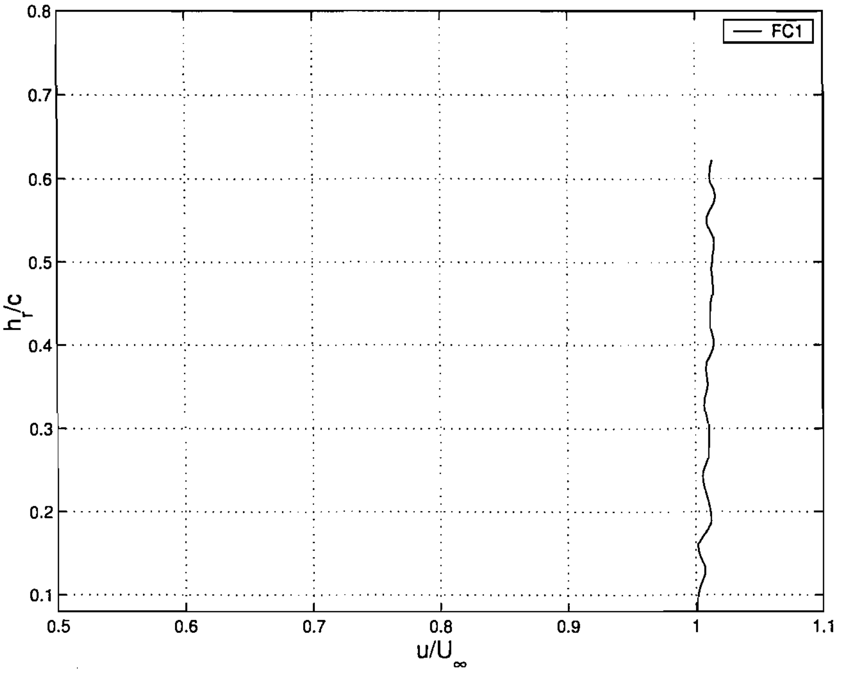

Figure B.4: Wind tunnel centreline profile of u/U_∞, at $x/c = 0.5$, for FC1 in the 2.1 m × 1.5 m wind tunnel.

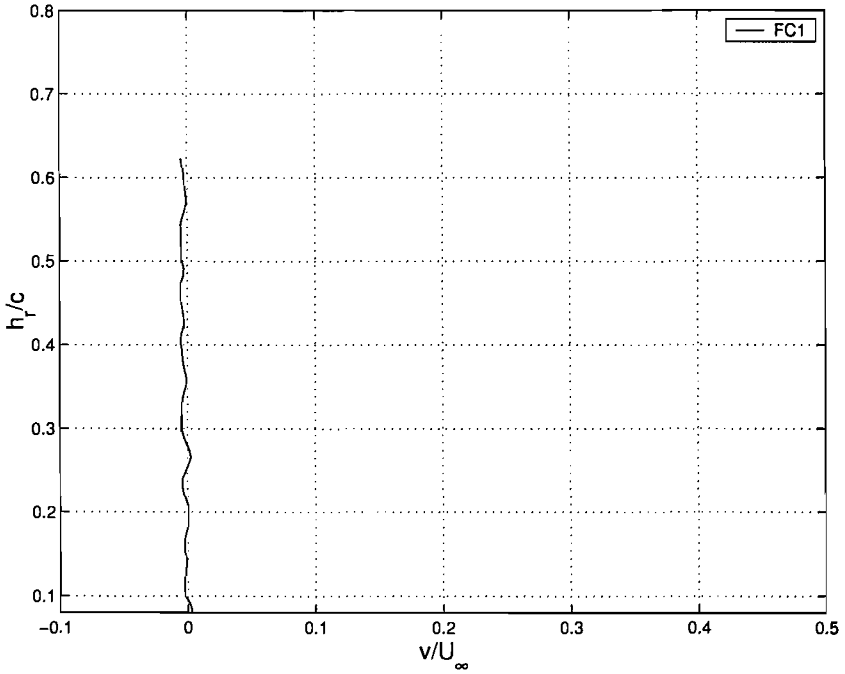

Figure B.5: Wind tunnel centreline profile of v/U_∞, at $x/c = 0.5$, for FC1 in the 2.1 m × 1.5 m wind tunnel.

it can be deduced from Fig. B.5 that the uncertainty in v appeared to be much smaller than the uncertainty in u; plausibly less than 1%. For the data presented in this research, an appropriate estimate of the uncertainty in the PIV measurements is therefore $\pm 1.6\%$ in u, and less than $\pm 1\%$ in v.

References

[1] Wright, P. G., *The influence of aerodynamics on the design of Formula One racing cars*, International Journal of Vehicle Design, Vol. 3, 1982, pp. 383–397.

[2] Dominy, J. A., and Dominy, R. G., *Aerodynamic influences on the performance of the Grand Prix racing car*, Proc Instn Mech Engrs, Vol. 198D, 1984, pp. 87–93.

[3] Gillespie, T. D., *Fundamentals of Vehicle Dynamics*, SAE, Inc., Warrendale, PA, 1992.

[4] Adams, H., *Chassis Engineering*, HPBooks, Los Angeles, CA, 1993.

[5] Wright, P. G., *Formula 1 Technology*, SAE, Inc., Warrendale, PA, 2001.

[6] Romberg, G. F., Chianese, Jr., F., and Lajoie, R. G., *Aerodynamics of Race Cars in Drafting and Passing Situations*, SAE Paper: 710213, 1971.

[7] Howell, J., *Catastrophic Lift Forces on Racing Cars*, Journal of Wind Engineering and Industrial Aerodynamics, Vol. 9, 1981, pp. 145–154.

[8] Wright, P. G., *Cleared for Take-Off*, Racecar Engineering, Vol. 9, No. 7, September 1999, pp. 16–18.

[9] Raymond, A. E., *Ground Influence on Aerofoils*, NACA TN67, 1921.

[10] Reid, E. G., *A Full-Scale Investigation of Ground Effect*, NACA TR265, 1927.

[11] Tonnies, E., *Effect of the Ground on an Airplane Flying Close to it*, NACA TM674, 1932.

[12] Recant, I. G., *Wind-Tunnel Investigation of Ground Effect*, NACA TN705, 1939.

[13] Dominy, R. G., *Aerodynamics of Grand Prix cars*, Proc. Instn. Mech. Engrs., Part D, Journal of Automobile Engineering, Vol. 206, 1992, pp. 267–274.

[14] Gray, W. D. M., *Formula One Wake Flow Simulation*, 3rd Year Project, Dept. of Aeronautics and Astronautics, University of Southampton, 1998–1999.

[15] Dominy, R. G., *The influence of slipstreaming on the performance of a Grand Prix racing car*, Proc. Instn. Mech. Engrs., Part D, Journal of Automobile Engineering, Vol. 204, 1990, pp. 35–40.

[16] Duncan, L. T., *The Effect of Deck Spoilers and Two Car Interference on the Body Pressures of Race Cars*, SAE Paper: 942520, 1994.

[17] Bamsey, I., *Wind of Change*, Race Tech Magazine, No. 45, Dec/Jan 2002/2003, pp. 18–45.

[18] Cooper, K. R., *Bluff-Body Aerodynamics as Applied to Vehicles*, Journal of Wind Engineering and Industrial Aerodynamics, Vol. 49, 1993, pp. 1–22.

[19] Morel, T., *The Effects of Base Slant on the Flow Pattern and Drag of Three-Dimensional Bodies with Blunt Ends*, Aerodynamic Drag Mechanisms of Bluff Bodies and Road Vehicles, Plenum Press, New York, 1978, pp. 191–226.

[20] Ahmed, S. R., *Wake Structure of Typical Automobile Shapes*, Journal of Fluids Engineering, Transactions of the ASME, Vol. 103, March 1981, pp. 162–169.

[21] Ahmed, S. R., *An Experimental Study of the Wake Structures of Typical Automobile Shapes*, Journal of Wind Engineering and Industrial Aerodynamics, Vol. 9, 1981, pp. 49–62.

[22] Hamidy, E., *The Structure of Wakes of 3D Bluff Bodies in Proximity to the Ground*, PhD. Thesis, Department of Aeronautics, Imperial College of Science, Technology and Medicine, London, 1991.

[23] Bearman, P. W., *Near wake flows behind two- and three-dimensional bluff bodies*, Journal of Wind Engineering and Industrial Aerodynamics, Vol. 69, 1997, pp. 33–54.

[24] Lienhard, H., Stoots, C., and Becker, S., *Flow and Turbulence Structures in the Wake of a Simplified Car Model (Ahmed Model)*, Lehrstuhl für Strömungsmechanik (LSTM), Universität Erlangen-Nürnberg, Cauerstr. 4, 91058 Erlangen, Germany.

[25] Alajbegovic, A., Aganost. A., Hill, D., Teixeira, C., and Molvig, K., *Digital Physics - Analysis of the Morel Model*, Document Reference Number: 99448, MIRA Automotive Information Centre, UK. 1997.

[26] Bayraktar, I., Landman, D., and Baysal, O., *Experimental and Computational Investigation of Ahmed Body for Ground Vehicle Aerodynamics*, SAE Paper: 2001-01-2742, 2001.

[27] Basara, B., Przulj, V., and Tibaut, P., *On the Calculation of External Aerodynamics: Industrial Benchmarks*, SAE Paper: 2001-01-0701, 2001.

[28] Krajnovic, S., and Davidson, L., *Large-Eddy Simulation of the Flow Around a Ground Vehicle Body*, SAE Paper 2001-01-0702, 2001.

[29] Ranzenbach, R., and Barlow, J. B., *Two-Dimensional Airfoil in Ground Effect, An Experimental and Computational Study*, SAE Paper 942509, 1994.

[30] Ranzenbach, R., and Barlow, J. B., *Cambered Airfoil in Ground Effect- Wind Tunnel and Road Conditions*, AIAA-95-1909-CP, 1995.

[31] Ranzenbach, R., and Barlow, J. B., *Cambered Airfoil in Ground Effect-An Experimental and Computational Study*, SAE Paper 960909, 1996.

[32] Knowles, K., Donoghue, D. T., and Finnis, M. V., *A Study of Wings in Ground Effect*, Loughborough University Conference on Vehicle Aerodynamics, pp. 22.1–22.13, 1994.

[33] Jasinski, W. J., and Selig, M. S., *Experimental Study of Open-Wheel Race-Car Front Wings*, SAE Paper 983042, 1998.

[34] Zerihan, J. D. C., *An Investigation into the Aerodynamics of Wings in Ground Effect*, Ph.D. Thesis, University of Southampton, April 2001.

[35] Zerihan, J., and Zhang, X., *Aerodynamics of a Single Element Wing in Ground Effect*, Journal of Aircraft, Vol. 37, No. 6, Nov–Dec 2000.

[36] Zhang, X., and Zerihan, J., *Aerodynamics of a Double Element Wing in Ground Effect*, AIAA Journal, Vol. 41, No. 6, June 2003.

[37] Lawson, N. J., Knowles, K., Hart, R. J. E., Wray, J. N., and Eyles, J. M., *An Experimental Investigation Using PIV of the Underflow of a GA(W)-1 Aerofoil Section in Ground Effect*, 4th MIRA International Vehicle Aerodynamics Conference, Session 6B, Warwick, 16-17 October, 2002.

[38] Hoeijmakers, H. W. M, *Vortex Wakes in Aerodynamics*, in: The Characterisation and Modification of Wakes from Lifting Vehicle in Fluids, AGARD Symposium, AGARD-CP-584, Trondheim, Norway, 1996.

[39] Spalart, P. R., *Airplane Trailing Vortices*, Annual Review Fluid Mechanics, Vol. 30, 1998, pp. 107–138.

[40] Rossow, V. J., Sacco, J. N., Askins, P. A., Bisbee, L. S., and Smith, S. M., *Wind Tunnel Measurements of Hazard Posed by Lift-Generated Wakes*, Journal of Aircraft, Vol. 32, No. 2 March - April 1995, pp. 278–284.

[41] Graham-Rowe, D., *Wake-up call*, New Scientist, Vol. 172, No. 2318, 24 Nov 2001, pp. 13.

[42] Corsiglia, V. R., Rossow, V. J., and Ciffone, D. L., *Experimental Study of the Effect of Span Loading on Aircraft Wakes*, Journal of Aircraft, Vol. 13, No. 12, 1976, pp. 968–973.

[43] Ciffone, D. L., and Orloff, K. L., *Far-Field Wake-Vortex Characteristics of Wings*, Journal of Aircraft, Vol. 12, No. 5, June 1974, pp. 464–470.

[44] Rossow, V. J., *Effect of Wing Fins on Lift-Generated Wakes*, Journal of Aircraft, Vol. 15, No. 3, 1977, pp. 160–167.

[45] Jacob. J. D., Liepmann, D., and Savas Ö., *Natural and Forced Growth Characteristics of the Vortex Wake of a Rectangular Airfoil*, in: The Characterisation and Modification of Wakes from Lifting Vehicles in Fluids, AGARD Symposium, AGARD-CP-584, Trondheim, Norway, 1996.

[46] Huenecke, K., *Structure of a transport aircraft-type near field wake*, in: The Characterisation and Modification of Wakes from Lifting Vehicle in Fluids, AGARD Symposium, AGARD-CP-584, Trondheim, Norway, 1996.

[47] De Bruin, A. C., Hegen, S. H., Bernd Rhone, P., and Spalart, P. R., *Flow field survey in trailing vortex system behind a civil aircraft model at high lift*, in: The Characterisation and Modification of Wakes from Lifting Vehicle in Fluids, AGARD Symposium, AGARD-CP-584, Trondheim, Norway, 1996.

[48] Stumpf, E., Rudnik, R., and Ronzheimer, A., *Euler computation of the nearfield wake vortex of an aircraft in take-off configuration*, Aerospace Science and Technology, Vol. 4, 2000, pp. 535–543.

[49] Eaton, J. A., and O'Flaherty, M. P., *Flowfield Prediction of Three-Dimensional Wing Trailing Vortices Using Advanced Turbulence Models*, in: The Characterisation and Modification of Wakes from Lifting Vehicles in Fluids, AGARD Symposium, AGARD-CP-584, Trondheim, Norway, 1996.

[50] Senoir, A. E., and Zhang, X., *The Force and Pressure of a Diffuser-Equipped Bluff Body in Gouund Effect*, Journal of Fluids Engineering, ASME, Vol. 123, Mar 2001, pp. 105–111.

[51] Ruhrmann, A., and Zhang, X., *Influence of Diffuser Angle on a Bluff Body in Ground Effect*, Journal of Fluids Engineering, Transactions of the ASME, Vol. 125, Mar 2003, pp. 332–338.

[52] Zhang, X., Senior, A., and Ruhrmann, A., *Vortices Behind a Bluff Body with an Upswept Aft Section in Ground Effect*, International Journal of Heat and Fluid Flow, Vol. 25, Feb 2004, pp. 1–9.

[53] Hoffmann, J. A., *Effects of Onset Freestream Turbulence on the Performance Characteristics of an Airfoil*, AIAA Paper 90-3025, Aug. 1990.

[54] Devinant, Ph., Laverne, T., and Hureau, J., *Experimental Study of Wind-Turbine Airfoil Aerodynamics in High Turbulence*, JWEIA 90, 2002, pp. 689–707.

[55] http://www.fia.com, *2003 Formula One Technical Regulations*, FIA.

[56] McGhee, R. J., and Beasley, W. D., *Low Speed Aerodynamic Characteristics of a 17–Percent–Thick Airfoil Section Designed for General Aviation Applications*, NASA TN D–7428, Dec 1973.

[57] Barlow, J. B., Rae, W. H., Jr., and Pope, A., *Low–Speed Wind Tunnel Testing*, John Wiley & Sons, 1999.

[58] Braslow, A. L., Hicks, R. M., and Harris, R. V., *Use of Grit Type Boundary Layer Transition Trips on Wind Tunnel Models*, NASA TN D–3579, 1966.

[59] Braslow, A. L., and Knox, E. C., *Simplified Method for Determination of Critical Height of Distributed Roughness Particles for Boundary Layer Transition at Mach Numbers from 0 to 5*, NACA TN 4363, Sept 1958.

[60] Burgin, K., Adey, P. C., and Beatham, J. P., *Wind Tunnel Tests on Road Vehicle Models using a Moving Belt Simulation of Ground Effect*, Journal of Wind Engineering and Industrial Aerodynamics, Vol. 22, 1986, pp. 227–236.

[61] Axon, L., Jaguar Racing, *Private Communications*, University of Illinois, 2001.

[62] ESDU, *Blockage Corrections for Bluff Bodies in Confined Flows*, ESDU 80024, Issued Nov 1980, with Ammendment Mar 1998.

[63] http://www.windtunnels.soton.ac.uk

[64] Coleman, Hugh W., and Steele, W. Glenn, *Experimentation and Uncertainty Analysis for Engineers*, John Wiley & Sons, 1999.

[65] *ZOC22B and ZOC23B Instruction and Service Manual*, Scanivalve Corporation.

[66] *Wind Tunnel Instrumentation and Control System, Software Version 2*, Pi Research Ltd.

[67] *FlowMap Particle Image Velocimetry Instrumentation, Installation and User's Guide*, Dantec Measurement Technology, 1998.

[68] http://www.dantecdynamics.com

[69] Goldstein, R. J., *Fluid Mechanics Measurements, Second Edition*, Taylor & Francis, 1996.

[70] Anderson, John D., Jr., *Computational Fluid Dynamics – The Basics with Applications*, McGraw–Hill International Editions, Mechanical Engineering Series, 1995.

[71] Tannehill, John C., Anderson, Dale A., and Pletcher, Richard H., *Computational Fluid Mechanics and Heat Transfer, Second Edition*, Taylor & Francis, 1997.

[72] Pope, Stephen B., *Turbulent Flows*, Cambridge University Press, 2000.

[73] http://www.iss.soton.ac.uk/research/iridis/

[74] *Fluent 5 Solver Training Notes*, TRN-1998-006, Dec 1998.

[75] Drela, M., *XFOIL 6.6 User Primer*, MIT Aero & Astro, MIT, Cambridge Mass., 1996.

[76] *Fluent User's Guide*, Fluent Inc.

[77] Harvey, J. K., and Perry, F. J., *Flowfield Produced by Trailing Vortices in the Vicinity of the Ground*, AIAA Journal, Vol. 9, 1971, pp. 1659–1660.

[78] Winkelmann, A. E., and Barlow, J. B., *Flowfield Model for a Rectangular planform Wing beyond Stall*, AIAA Journal, Vol. 8, 1980, pp. 1006–1007.

[79] Gad-el-Hak, M., *Flow Control - Passive, Active and Reactive Flow Management*, Cambridge University Press, 2000.

[80] McCormick, B. W., Jr., *Aerodynamics of V/STOL Flight*, Dover Publications, Inc., 1967.

[81] Webb, S., and Castro, I. P., *PIV, LDA & HWA comparative measurements in various turbulent flows*, Report No. AFM-03/01, School of Engineering Sciences, University of Southampton, 2003.